# PRINTABLE ELECTROCHEMICAL BIOSENSORS FOR THE DETECTION OF NEUROTRANSMITTER AND OTHER BIOLOGICAL MOLECULE

by

**Tran Ngoc Huyen Nguyen**

**A Dissertation**

*Submitted to the Faculty of Purdue University*

*In Partial Fulfillment of the Requirements for the Degree of*

**Doctor of Philosophy**


Weldon School of Biomedical Engineering

West Lafayette, Indiana

August 2020

## THE PURDUE UNIVERSITY GRADUATE SCHOOL
## STATEMENT OF COMMITTEE APPROVAL

Dr. Hyowon (Hugh) Lee, Chair
Weldon School of Biomedical Engineering

Dr. Jenna Rickus
Weldon School of Biomedical Engineering,
School Agricultural and Biological Engineering

Dr. Riyi Shi
Weldon School of Biomedical Engineering,
Department of Basic Medical Sciences

Dr. Muhammad Ashraful Alam
School of Electrical and Computer Engineering

**Approved by:**

Dr. George R. Wodicka
Dane A. Miller Head of Biomedical Engineering
Weldon School of Biomedical Engineering

To

Anh Tung Thiên

and

My Beloved Parents

# ACKNOWLEDGMENTS

This thesis is a result of many experiences I have encountered at Purdue from dozens of remarkable individuals whom I wish to acknowledge. First and foremost, I would like to express my sincere gratitude to my advisor, Professor Hyowon (Hugh) Lee. I thank him for graciously accepting me into his lab. Ever since, he has supported me not only by providing a research assistantship over the past five years, but also academically throughout all this time. His enthusiasm and persistence have motivated me and allowed me to accomplish more than I expected as a graduate student. I will always be grateful for his guidance.

I would also like to express my sincere appreciation to my thesis committee members. I am indebted to Professor Riyi Shi for his patience, helpful advice, and support throughout this research. I am particularly grateful for his generosity in sharing and making available his lab setup and animal resources to make this work possible. I am also incredibly thankful to Professor Muhammad A. Alam for his valuable scientific and career advice. I thank him for his support and many insightful discussions that bring our collaboration into success. I would also like to extend my sincere gratitude to Professor Jenna Rickus for her comments and encouragement. Her support and valuable suggestions at the beginning of my graduate research help jump-start my project that resulted in this work.

I also wish to thank my collaborator, Dr. Jessica Page, for her dedication and support. Her knowledge of and experience with animal setup and spinal cord injury research was an integral part of this work. I would also like to thank my collaborators on my other project, Professor Alexander Chubykin, and Professor Shriram Ramanathan, on the in vivo glutamate study. I am also very grateful to James K. Nolan for our collaboration and the stimulating discussions that we have had over the years. I thank him for his tremendous help in all the biosensors and electrochemical issues.

Thank you to the rest of the Laboratory of Implantable Microsystems Research Lab members. They have helped me at all stages of this work. A special acknowledgment goes to my office mate since the beginning: Dr. Hyunsu Park. Hyunsu is a truly wonderful friend. I thank him for his support and for always listening to my concerns with patience and understanding. I also thank Dr. Qi Yang and Bahar Dhowan, who have been very supportive in every way. I am incredibly grateful for my fellow graduate students, friends I have met at Purdue, and my longtime friends. I would not have

made it, sanely, through graduate school without their friendships and constant support. I am also thankful to the Weldon School of Biomedical Engineering and all its member's staff for all the considerate support and guidance. Furthermore, I would like to thank the rest of the undergraduate research team, especially Stephanie Lam and Yi Wang, for their collaborative effort during data collection.

A significant part of this accomplishment is due to the support of my family and my extended family. I would like to express my deepest gratitude to my parents, Trong Nhan, and Ngoc Nga, for their unconditional love, countless sacrifice and unparalleled support throughout my life. I would not have made this far without them. My sisters, Minh Nguyen, and Phuc Nguyen have been my best friends all my life. I thank them for all the pieces of advice, encouragement, and unwavering supports during this challenging period.

And finally, to my husband, Dr. Thien Nguyen, who has been by my side throughout this Ph.D. I want to express my most profound appreciation for his dedication, unconditional love, and patience for all these years. I cannot thank him enough for willing to commute for four hours every weekend in the last five years. He always has faith in me and my intellect, and without him by my side and his loving support, I could never have achieved this goal.

# TABLE OF CONTENTS

# LIST OF TABLES

# LIST OF FIGURES

# ABSTRACT

**Author:** Nguyen, Tran Ngoc Huyen. Ph.D
**Institution:** Purdue University
**Degree Awarded:** August 2020
**Title:** Printable Electrochemical Biosensors for the Detection of Neurotransmitter and other Biological Molecules
**Committee Chair:** Dr. Hyowon Lee

Glutamate is the principal excitatory neurotransmitter in the central nervous system. As one of the most abundant neurotransmitters, glutamate plays an essential role in many processes of the central nervous system and beyond. As a result, any disruption that causes an abnormal glutamate level can significantly impact the central nervous system's neurological functions. Glutamate excitotoxicity is a neuropathology that persists in many neurodegenerative disorders such as Parkinson's and Alzheimer's disease as well as in the traumatic brain and spinal cord injuries. Thus, the ability to obtain precise information about the extracellular glutamate level in the living brain and spinal cord tissue may provide new insights into the fundamental understanding of glutamate in neurological disorders and neurophysiological phenomena.

Conventional bioanalytical techniques that characterize glutamate levels *in vivo* have a low spatiotemporal resolution that has impeded our understanding of this dynamic event. The electrochemical sensor has emerged as a promising solution that can satisfy the requirement for highly reliable and continuous monitoring methods with an excellent spatiotemporal resolution for the characterization of extracellular glutamate concentration. In this thesis, I present various amperometric biosensors fabricated using a simple direct ink writing technique for *ex vivo* and *in vivo* glutamate monitoring.

The amperometric biosensor is fabricated by immobilizing glutamate oxidase on nanocomposite electrodes made of platinum nanoparticles, multiwalled carbon nanotubes, and a conductive polymer. The biosensors demonstrate good sensitivity and selectivity that can be inserted into a spinal cord and measure extracellular glutamate concentration. Additionally, another type of glutamate biosensor is fabricated from commercially available activated carbon with platinum microparticles. We utilize

astrocyte cell culture to demonstrate our biosensor's ability to monitor the glutamate uptake process. We also present a direct measurement of glutamate release from optogenetic stimulation in mouse primary visual cortex brain slides.

Moreover, we explore a new type of material, perovskite nickelate-Nafion heterostructure, to fabricate biosensors and measure glutamate inside the mouse brain. Finally, by utilizing the nanocomposite ink and direct ink writing technique, we also fabricate the gold-ruthenium non-enzymatic glucose biosensor. We apply a modified Butler-Volmer non-linear model to evaluate the impact of geometrical and chemical design parameters of non-enzymatic biosensor performance.

# CHAPTER 1. INTRODUCTION

## 1.1 The Motivation for Neurotransmitter Sensing

Glutamate, or glutamic acid, is the principal excitatory neurotransmitter in the central nervous system (CNS). As one of the most abundant neurotransmitters in the brain and the spinal cord, it plays an essential role in many processes of the CNS Platt (2007). Moreover, glutamate plays a significant role in maintaining and regulating the bioenergetics process Hertz (2006) and acts as a precursor to synthesize gamma-aminobutyric acid (GABA), a critical inhibitor neurotransmitter in the hippocampus L. Peng et al. (1993). Glutamate is also a part of the synthesis process of proteins and small peptides. It is involved in the fatty acid synthesis cycle, detoxification of ammonia, and maintaining osmotic/anionic balance Melorose, Perroy, and Careas (2015). Additionally, glutamate facilitates the production of cytokine, a crucial protein in neuronal development, maturation, survival, and regeneration, as well as in the mechanism of pain transduction and neural cell injury Melorose et al. (2015). Fig. 1.1 summarizes the crucial roles of glutamate in the brain tissue.

In normal physiological conditions, glutamate is deliberately secreted from glutamatergic nerve terminals in response to depolarization, passed through the synaptic cleft, and is rapidly bound to postsynaptic receptors Doble (1999).These receptors are membrane ion channels, and their activation allows the transfer of cations into the postsynaptic neurons and subsequent depolarization Nicholls and Attwell (1990). This process is highly effective that keeps the extracellular concentration of glutamate approximately 1 mM for less than 10 ms during action potential and quickly returns to less than 20 nM Dzubay and Jahr (1999). On the other hand, the intracellular concentration of glutamate is approximately 10 mM, which is up to 10,000-fold of the extracellular concentration Danbolt (2001); Featherstone and Shippy (2008). As a result, any disruption that causes an abnormal glutamate level can significantly impact the CNS's neurological functions. Fig. 1.2 illustrates a classical regulation of glutamate neurotransmission, as well as estimating the concentration of glutamate at different areas in normal conditions Moussawi, Riegel, Nair, and Kalivas (2011).

### 1.1.1 Glutamate Excitotoxicity

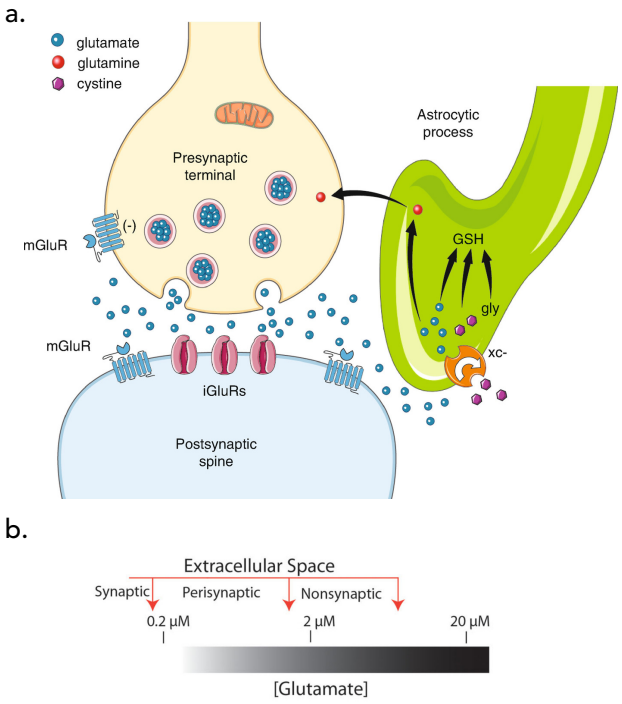


*Figure 1.1.* (a) Schematic of classical glutamatergic neurotransmission. Glutamate releases from presynaptic terminals and glial cells. Glutamate then binds and activates receptors, which allows the influx of $Ca^{2+}$ and $Na^{+}$ ions into the postsynaptic spine (Reprinted by permission from Springer Nature, The Therapeutic Use of N-Acetylcysteine (NAC) in Medicine, Ref Foster Olive et al. (2018). Copyright 2019). (b) Estimated the extracellular glutamate concentration at different locations: synaptic, perisynpatic, and nonsynaptic areas. (Reprinted with permission from Moussawi et al. (2011)).

Glutamate excitotoxicity (GET) is a neuropathology that persists in many neurodegenerative disorders such as Parkinson's and Alzheimer's disease as well as in the traumatic brain and spinal cord injuries (SCI) Caudle and Zhang (2009); Oyinbo (2011); E. Park, Velumian, and Fehlings (2004). According to Dr. John Olney, a pioneer who first examined this catastrophic event in the brain and the spinal cord, GET is a process in which excessive flow of glutamate in the extracellular space constantly depolarizes neurons. Eventually, it leads to neuronal death by a cascade of cellular events Doble (1999); Olney and Sharpe (1969).

Many studies have suggested that sodium entry is responsible for early necrotic events due to the activation of voltage-dependent sodium channels by persistent depolarization. This event disturbs the osmotic balance of the cells causes cell swelling and lysis along with the increasing flow of calcium into the cells Doble (1999); Kiedrowski, Wroblewski, and Costa (1994). This initiates many deleterious events such as free radical generation, harmful enzyme activation, mitochondria dysfunction Farooqui and Horrocks (1991); J. Wang (2005), which ultimately leads to neuronal death. Finally, a high intracellular calcium concentration can lead to the exocytosis event of glutamate-containing vesicles Doble (1999). Fig. 1.3 presents some of the processes involved in the excitotoxic cascade. Despite extensive research in neurodegeneration, the mechanism that triggers the increase in extracellular glutamate remains unclear. Thus, a better understanding of GET in neurodegenerative disorders and neurotrauma may lead to novel therapeutic interventions to minimize GET-related damages Lau and Tymianski (2010).

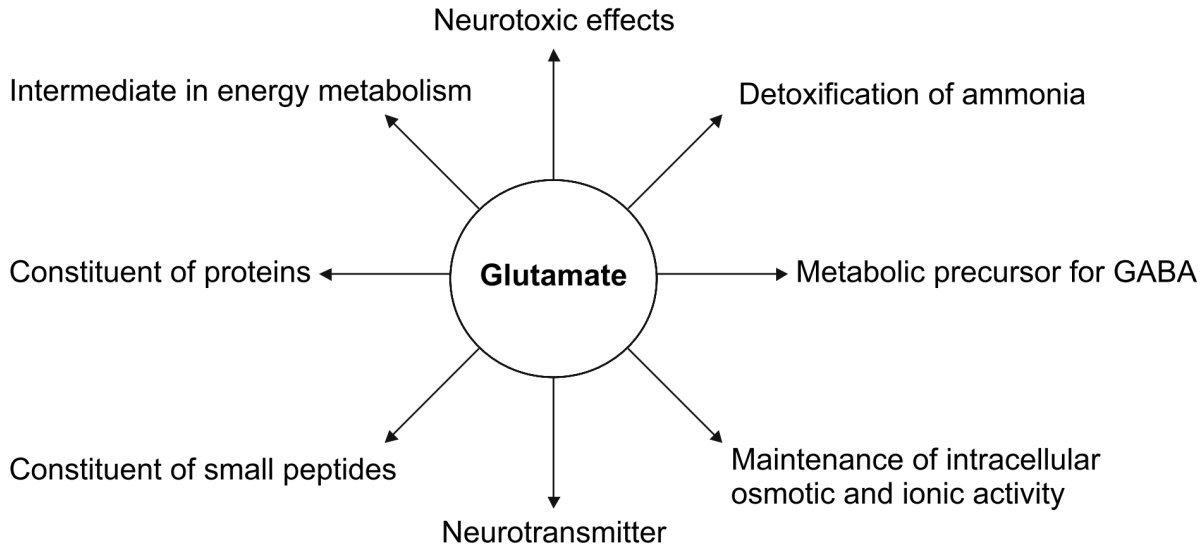


*Figure 1.2.* Different roles of glutamate in the central nervous system. (Reprinted by permission from Springer Nature, Neurochemical Aspects of Excitotoxicity, Ref Melorose et al. (2015). Copyright 2008).

## 1.2 Methods to Quantify Extracellular Glutamate Concentration

A critical step in developing a treatment for GET is having a reliable method to measure the extracellular concentration of glutamate. Many techniques, both invasive and non-invasive, are used to monitor neurotransmitters in complex biological environments.

### 1.2.1 Nuclear Magnetic Resonance Spectroscopy

Nuclear magnetic resonance spectroscopy (NMR) has become a popular method for analyzing metabolic compounds. It is a non-invasive technique that uses labels atomic nuclei such as $^{1}H$ or $^{13}C$. Magnetic properties of these specific atomic nuclei are the physical foundation of NMR spectroscopy Wong (1996). When a magnetic field with specific frequency is applied, nuclei can be excited to re-emit electromagnetic radiation. The radiation determines the physical and chemical properties of compounds that they contain. Different compounds can be detected based on the resonance frequency shift for different chemical structures De Graaf (2007); Wong (1996).

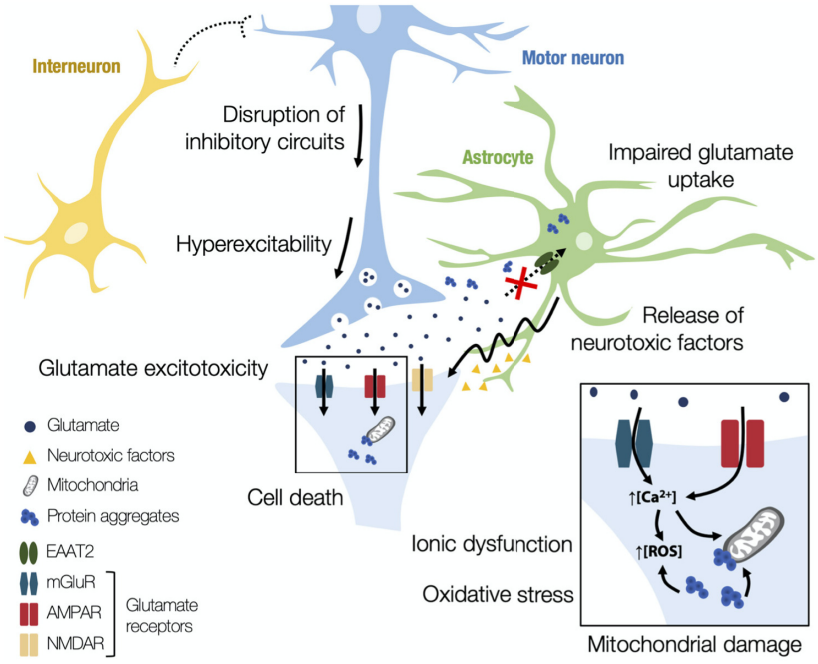


*Figure 1.3.* A schematic representation of proposed biochemical mechanisms of glutamate excitotoxicity. (Reprinted with permission from Armada-Moreira et al. (2020)).

Through this technique, a variety of metabolites such as glutamate can be rapidly detected *in vivo* based on their chemical structures. However, in complex biological environments, many compounds exist with very similar structures and functional groups. For example, it is impossible to distinguish glutamate, glutamine, gamma-aminobutyric acid (GABA) under a low magnetic field Soares and Law (2009). As a result, it is challenging to identify individual compounds from the recorded spectrum. Moreover, it is impossible to separate between intracellular and extracellular concentration, because NMR is only capable of measuring from a bulk tissue, and evaluating through voxels of several cubic centimeters square. Thus, it is not possible to measure at a cellular scale Müller et al. (2020); Ramadan, Lin, and Stanwell (2013). Furthermore, it has a poor temporal resolution ranging from 5 to 60 min. Hence, it is incapable of measuring the fast change of analytes, such as extracellular glutamate Boumezbeur et al. (2010); Rothman et al. (1999). Finally, this method requires large and expensive equipment that may not be widely available Weltin (2015).

### 1.2.2 Positron Emission Tomography

Positron emission tomography (PET) is another non-invasive imaging technique. It examines the metabolism of organ/tissue, pathological conditions, or biochemical properties. By administering a small amount of radiotracer into an organism, the tracer undergoes positive beta decay and breakdown by a radionuclide and emits positrons. The positrons then create gamma radiation. PET scanner detects the gamma radiation and constructs a three-dimensional image Muehllehner and Karp (2006). PET usually target glutamate receptor (mGluR) to help establish the condition of glutamate inside an organism. Glutamate receptor (mGluR) is usually targeted in PET to help establish the concentration of glutamate inside an organism Kagedal et al. (2013); S. Li and Huang (2014).

While PET is a common non-invasive method, it still has disadvantages in measuring metabolic analytes. The tracers have relatively short half-life ranging from several minutes to hours. Thus, it is challenging to conduct long and continuous measurements. PET also has a low spatial resolution in the range of millimeters, and temporal acquisition rate in the range of minutes Muehllehner and Karp (2006). Moreover, available tracer concentration strongly affects the analytical detection limit. PET is also limited in measuring integral synthesis and mapping regional metabolic

activity. Thus, it is unable to measure extracellular or intracellular metabolites levels. Finally, PET also requires large and expensive equipment.

### 1.2.3 Microdialysis

Microdialysis is an invasive technique commonly used to analyze and monitor neurotransmitters *in vivo* Van Der Zeyden, Oldenziel, Rea, Cremers, and Westerink (2008). Many studies examined the role of glutamate in neurotrauma used microdialysis to monitor glutamate change McAdoo, Xu, Robak, and Hughes (1999); Miele, Berners, Boutelle, Kusakabe, and Fillenz (1996); G. Y. Xu, Hughes, Ye, Hulsebosch, and McAdoo (2004a); G. Y. Xu, Hughes, Zhang, Cain, and McAdoo (2005); G. Y. Xu, Liu, Hughes, and McAdoo (2008); G. Y. Xu, McAdoo, Hughes, Robak, and De Castro (1998). Microdialysis consists of a probe that inserts into the tissue of interest. The probe is typically made of a semipermeable hollow fiber membrane, connecting to inlet and outlet tubing. The probe continuously perfused, and analytes from interested tissue or body-fluid are exchanged at the membrane and transported outside. The collected analytes are then analyzed using a different quantitative method Chaurasia et al. (2007). Fig. 1.4 presents the schematic of microdialysis.

Microdialysis has a significant advantage in measuring neurotransmitters. For example, microdialysis can extract information from freely moving or anesthetized animals. Additionally, it can measure directly from a specific brain region and be used to deliver drugs Cifuentes Castro et al. (2014a). Nevertheless, there are many disadvantages. Microdialysis needs to be accompanied by another analytical process such as high-performance liquid chromatography, electrophoresis, or mass spectroscopy to analyze the collected sample M. Perry, Li, and Kennedy (2009); W. C. Tseng, Hsu, Shiea, and Huang (2015). Therefore, there is a significant time lapse between the sampling process *in vivo* and the external analysis. This procedure can lead to misinterpretation of data for the neurotransmitter with a short half-life Van Der Zeyden et al. (2008). Therefore, microdialysis is not capable of providing timely information on the dynamic neurotransmitter concentration *in vivo*. It also has a low temporal resolution, typically ranging from 1 to 30 min. For the small concentration analytes, such as extracellular glutamate, the response time may be even longer Moussawi et al. (2011).

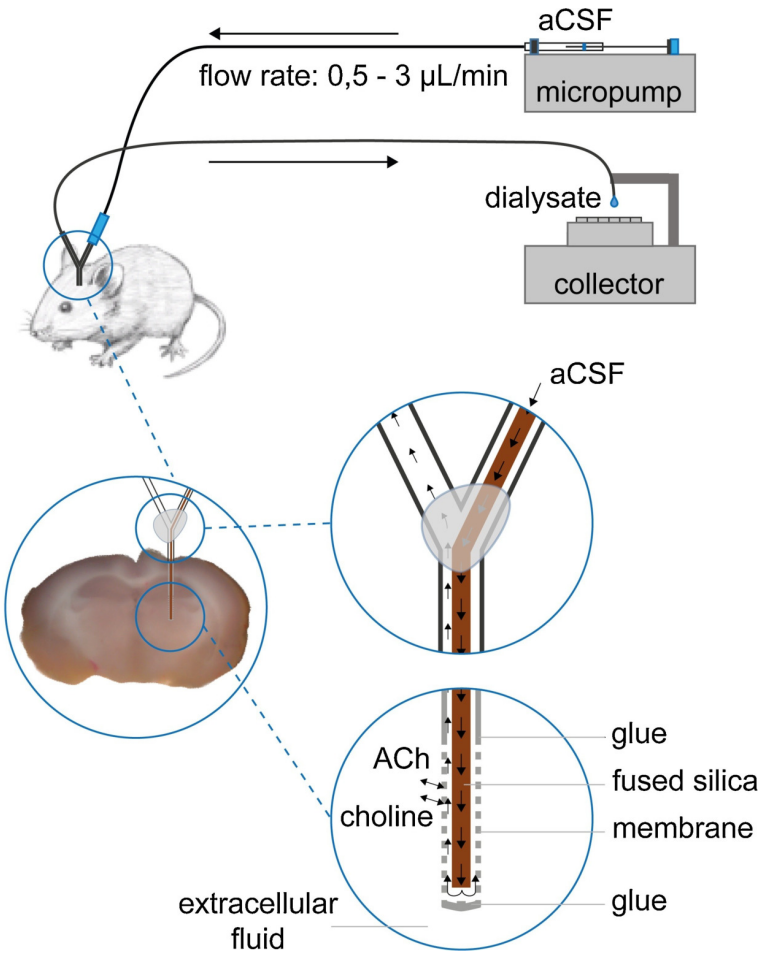


*Figure 1.4.* An example presents a microdialysis procedure. ACSF is continuously perfused through the probe using a micropump. The analytes are collected and analyzed by different analytical techniques. (Reprinted with permission from König et al. (2018). Copyright 2018 Elsevier).

Microdialysis is also quite invasive. It has a relatively large probe size of 1-4 mm in length and 250-500 $\mu$m in diameter Connelly (2011). Therefore, the probe limits the spatial resolution of the system and causes extensive damage to the surrounding tissues. Consequently, despite possessing the lowest detection limit, the low spatiotemporal of microdialysis proves less attractive options in measuring extracellular glutamate concentration *in vivo*.

### 1.2.4 Electrochemical Microsensor

To effectively measure extracellular glutamate *in vivo*, a less invasive analytical method with accurate detection and better spatiotemporal resolutions is necessary. Many studies have underscored the significance of detecting rapid and short-term events, usually in a second or millisecond time scale Pellerin and Magistretti (2004). Furthermore, continuous monitoring capability is crucial since it will grant immediate access to the dynamic change along with the recovering effect Weltin (2015). An electrochemical implantable microbiosensor provides a promising alternative. Specifically, enzymatic biosensor provides a solution for continuous monitoring of neurotransmitters Villagrán, Pérez, and Ibarra (2008).

The biosensor comprises of a biological component such as an enzyme or antibody and an electrochemical transducer. Electrochemical microsensor has become a valuable tool for detecting neurotransmitters *in vitro* and *in vivo* due to several reasons. They are capable of measuring extracellular analytes directly in the tissue with potentially minimal damage to the surrounding tissues Ispas, Crivat, and Andreescu (2012). They have a relatively simple design suitable for miniaturizing. The microscale array of these biosensors allow high spatiotemporal resolutions. Yao *et al*. compared the temporal resolution of a miniature implantable electrochemical sensor with a response about 5 s in contrast with the microdialysis study with a temporal response of 1-2 min Yao, Yano, and Nishino (2004). Additionally, Astra-Zeneca G. S. Wilson and Gifford (2005) demonstrated the advantage of temporal response in glutamate biosensor compared to microdialysis. They observed multiple glutamate spikes concentration in 30-60 s follows stimulation, whereas microdialysis showed response often $>$ 10 min G. S. Wilson and Gifford (2005). Electrochemical microsensor is also highly sensitive and selective Oldenziel et al. (2007); Ryan, Lowry, and O'Neill (1997); T. T. C. Tseng, Yao, and Chan (2013); Weltin et al. (2014). Finally, this approach is relatively cost-effective, which makes it ideal for mass production.

Using conventional microelectromechanical systems (MEMS) techniques, several groups have developed microscale biosensors for measuring glutamate levels in the brain or the spinal cord Cao, Li, Nguyen, Peng, and Chiao (2012); Govindarajan, McNeil, Lowry, McMahon, and O'Neill (2013); Weltin et al. (2014). However, most MEMS-based glutamate biosensors are rigid, expensive, and time-consuming to fabricate. Fig. 1.5 shows examples of different MEMS-based *in vivo* microsensors.

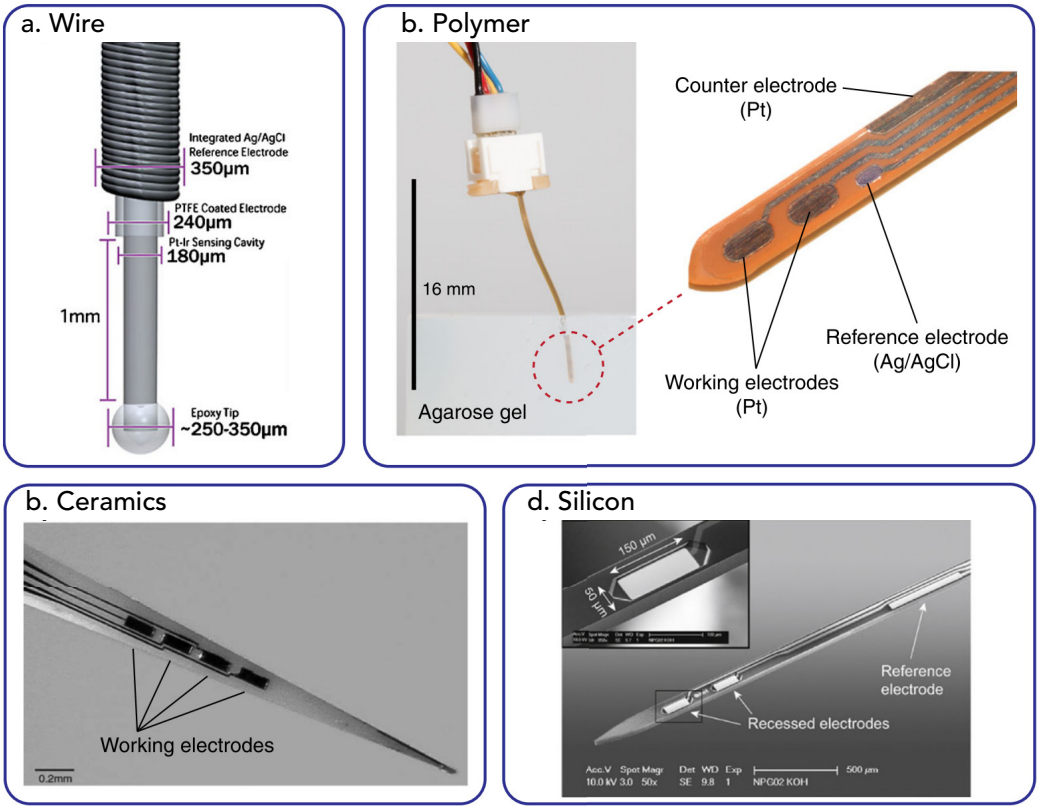


*Figure 1.5.* MEMS-based *in vivo* microsensor platforms. (a) Microsensors construct using Pt wires or fibres Naylor et al. (2011). Microsensors are fabricated on (b) polymer Weltin et al. (2014), (c) ceramic Burmeister et al. (2005), (d) silicon substrates Frey et al. (2010). (Reprinted with permission from Weltin et al. (2016). All images reprinted with permission from Elsevier).

Printed electronics can address many of the shortcomings of conventional MEMS fabrication processes by enabling the rapid production of low-cost, flexible devices Ahn et al. (2009); Lewis (2006). Specifically, there has been significant efforts to use various printing techniques to develop devices for biological, medical, and optical applications Hon, Li, and Hutchings (2008). Flexible electrochemical biosensors and other electronic devices are now commonly fabricated using screen-printing and ink-jet printing techniques Cinti et al. (2015); Hondred, Stromberg, Mosher, and Claussen (2017); H. Lee et al. (2012). Another additive manufacturing technique is direct ink writing that is particularly useful for printing high-aspect-ratio features on any planar or non-planar substrate Hon et al. (2008); Kadara, Jenkinson, Li, Church, and Banks (2008); Lewis (2006).

## 1.3 Direct Ink Writing

Direct ink writing (DIW) has an excellent potential for applications such as microelectronics K. Sun et al. (2013), biofuel cells and batteries K. Sun et al. (2013), sensors Hardin, Ober, Valentine, and Lewis (2015), photonics Gratson et al. (2006), advanced ceramics Q. Li and Lewis (2003), and biological applications Kolesky et al. (2014). DIW is an extrusion-based printing technique that creates three-dimensional (3D) shapes through a computer-controlled system Ahn et al. (2009); Hao et al. (2020). Fig. 1.6 shows an example of a DIW platform. Different materials such as hydrogels, electrolyte solutions, and pastes are deposited through extrusion nozzles by force of a screwing system, a piston, or pneumatic pressure Hao et al. (2020). After printing, the printed structures solidify through liquid evaporation, gelation, phase change by thermal energy, or a solvent driven reaction to form 3D structures Cheng, Deivanayagam, and Shahbazian-Yassar (2020).

DIW consists of two main types: (1) continuous filament writing and (2) aerosol jet printing, as presented in Fig. 1.7. The aerosol jet printing process prints the ink drop-by-drop on-demand Jabari and Toyserkani (2016); M. Wei et al. (2017). On the other hand, continuous filament writing allows

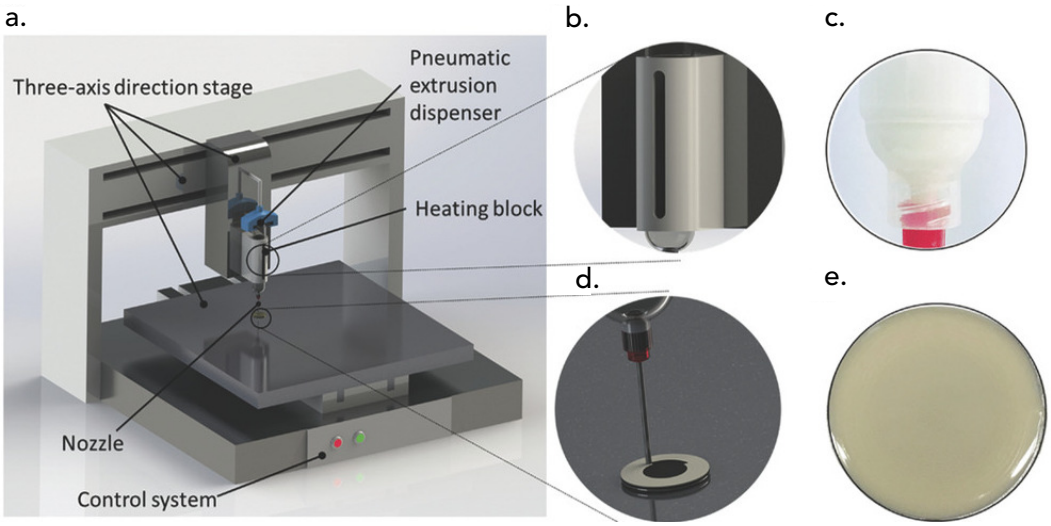


*Figure 1.6.* Schematic of a direct ink writing platform. (a) Illustration of the robotic deposition system. (b) An example of heating chamber that is equipped in some platform. (c) An examples of printable ink stores in a syringe barrel. (d) Schematic showing that the printable ink is printed on a fix substrate. (e) An image of the printed structure that is solidified onto the substrate at room temperature. (Reprinted with permission from Cheng et al. (2018). Copyright 2018 John Wiley and Sons).

the ink to extrude continuously from a nozzle onto a fixed substrate Q. Xu et al. (2015); Y. Zhang et al. (2019). This process directly writes continuous ink from a fine nozzle with a diameter ranging from 0.1 to 250 $\mu$m at a controlled speed Ahn et al. (2009); Q. Xu et al. (2015). Presently, DIW can achieve a very high resolution ($\sim$ 100 nm) Q. Xu et al. (2015). Furthermore, DIW offers other advantages, including low cost, precision, and construction of complex geometry parts without additional masks or dyes. The ability to fabricate with high-precision matches the needs of many significant applications, such as cell-bioprinting for medical applications or microscale and nanoscale electronic devices. DIW can fabricate complex structures with internal pores, thus better manipulating physical and chemical properties than the conventional processes Hao et al. (2020); Hon et al. (2008).

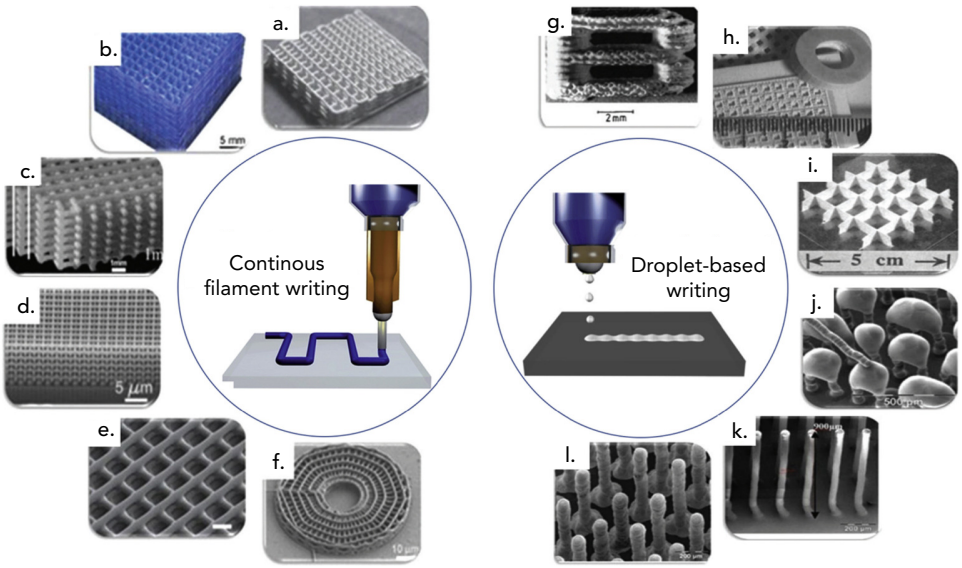


*Figure 1.7.* Continuous filament writing: (a) Biomaterial inks, (b) Fugitive organic inks, (c) Colloidal inks, (d) Sol-gel inks, (e). Hydrogel inks, (f). Polyelectrolyte inks. Droplet-based writing: (g) 3D ceramic components, (h). Unfired ceramic, (i) Structure made via 3D printing, (j) 3D micro-periodic structures made via sol-gel inks, (k) SEM micrographs of 3D pHEMA scaffolds, (l) 3D radial array. (Adapted with permission from M. Wei et al. (2017). Copyright 2017 Elsevier. Adapted with permission from Ref Q. Xu et al. (2015) with permission from The Royal Society of Chemistry. Copyright 2015).

Printable ink is a crucial factor in DIW as it determines not only the possible printable geometries but also the performances and internal structure of the final products Y. Zhang et al. (2019). Printable ink should have shear-thinning behavior, which decreases the viscosity of fluids and increases the shear rate to print devices with high resolution Cheng et al. (2020). With shear-thinning behavior,

the fluid can flow through the nozzle smoothly under pneumatic or mechanical forces because of a reduction in viscosity. Moreover, ink material can affect the flexibility, electrical conductivity, and mechanical robustness of printed devices Y. Zhang et al. (2019). Thus, the rheology of inks should be optimized to improve their electrochemical and mechanical properties. The addition of nanomaterials such as nanoparticles K. Sun et al. (2013), nanowires R. Z. Li, Hu, Zhang, and Oakes (2014), carbon nanotubes Shin et al. (2016), and graphene Secor, Ahn, Gao, Lewis, and Hersam (2015) can modify the inks' rheological properties. Fig. 1.8 shows an overview process of ink preparation for DIW. In addition to conductive filler, binders, and solvent, other additives can also facilitate DIW. For example, humectants help promote the hydrophilicity of ink, while surfactant reduces the surface tension of inks Daalkhaijav, Yirmibesoglu, Walker, and Mengüç (2018); K. Sun et al. (2013). DIW technology is a novel printing technique that can fabricate compact and multifunctional products with broad raw material selections and different feature sizes. The 3D structures fabricated by DIW may also find potential applications as sensors, microfluidic networks, scaffolds for tissue engineering, drug-delivery devices, and photonic-band gap materials Cheng et al. (2020).

## 1.4 Overview of the thesis

This thesis consists of six chapters. Chapter 1 introduces the motivation and methods that I used to detect extracellular neurotransmitter and other biological molecules. It presents the current methods to quantify the extracellular glutamate concentration and their challenges. Moreover, chapter 1 discusses the fabrication technique and the requirements to construct printable electrochemical biosensors.

Chapter 2 focuses on the design and development of the nanocomposite ink used to fabricate flexible glutamate biosensors using direct ink writing. Additionally, this chapter discusses the electrochemical and electrical characteristics of the functional ink and the biosensors. Finally, it presents the application of the biosensor in measuring glutamate *ex vivo*.

Chapter 3 investigates another type of ink that used to fabricate glutamate biosensor using direct ink writing. This chapter considers the mechanical, electrical, and electrochemical characteristics of the glutamate biosensors. Chapter 3 also goes over the application to monitor glutamate uptake in astrocyte cell culture, and glutamate release from optogenetic stimulation in mouse primary visual

cortex slices.

Chapter 4 showcases an application of a new type of material, perovskite nickelate-Nafion heterostructure, in measuring glutamate inside the mouse brain.

Chapter 5 presents the work of using the nanocomposite ink and direct ink writing technique to fabricate the AuRu non-enzymatic glucose sensor. This chapter discusses the surface and electrochemical characterization of the biosensors. Moreover, Chapter 5 presents a modified Butler-Volmer non-linear model to evaluate the impact of geometrical and chemical design parameters of non-enzymatic biosensor performance.

Chapter 6 summarizes the work presented in this thesis and outlines areas for potential future research.

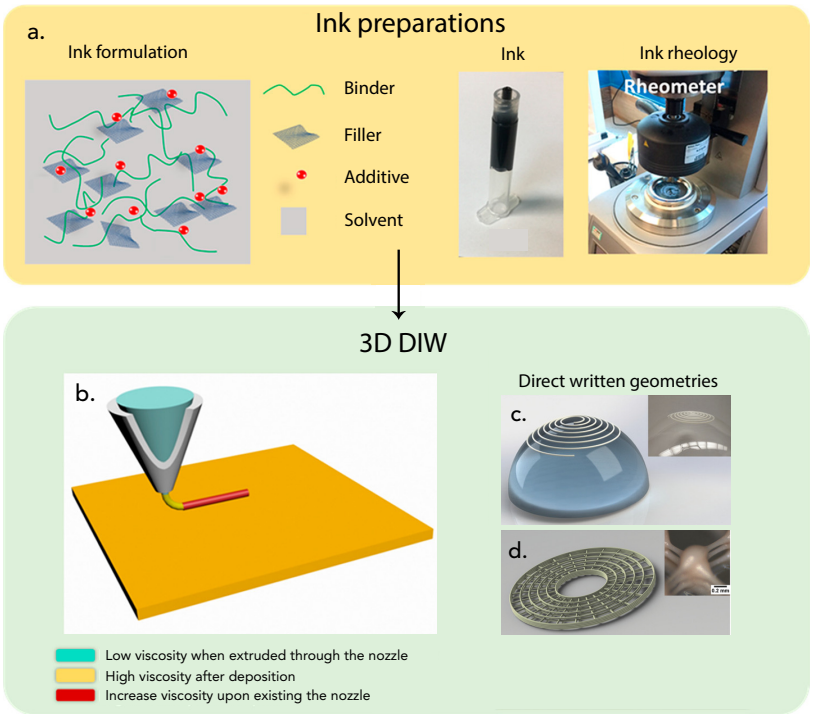


*Figure 1.8.* (a) An overview of ink preparation, ink preparation consists of ink formulation and ink rheology. The printable ink usually contains filler, additives, binder, and solvents. Ink rheology can be measured using a rheometer. (b) Stable and controllable ink flows to construct complex 3D assemblies, such as (c) an example of printable ink that prints onto a hemispherical surface, and a digital image of the printable ink (inset), (d) an example of the printable ink with 3D radial array structure, and optical image of a 3D net (inset). (Adapted with permission from Y. Zhang et al. (2019). Copyright 2019 American Chemical Society. Adapted with permission from Cheng et al. (2018). Copyright 2018 John Wiley and Sons).

# CHAPTER 2. FACILE FABRICATION OF FLEXIBLE GLUTAMATE BIOSENSOR USING DIRECT WRITING OF PLATINUM NANOPARTICLE-BASED NANOCOMPOSITE INK

## 2.1 Introduction

In this study, we used direct ink writing as a simple, low-cost method to rapidly fabricate microscale electrodes by printing conductive, flexible nanocomposite ink on thin-film polymer substrates. The nanocomposite ink consisted of platinum nanoparticles (PtNPs), multi-walled carbon nanotubes (MWCNT), conductive polymer—poly (3,4-ethylenedioxythiophene) polystyrene sulfonate (PEDOT: PSS), and Ecoflex™ silicone rubber. We immobilized glutamate oxidase on top of printed PtNPs-MWCNT-PEDOT:PSS-Ecoflex (PtNPs nanocomposite) electrodes to make microscale implantable glutamate sensors with high sensitivity, linearity and selectivity. Finally, we used our sensors to measure glutamate release from an excised spinal cord segment of a rat following a SCI. Our ultimate goal is to use our easy-to-fabricate implantable glutamate sensors to better characterize the dynamic process of GET during a neurotrauma.

## 2.2 Experimental Section

### 2.2.1 Materials

PEDOT: PSS (5 wt.%), Nafion 117 solution (5 wt.%), platinum nanoparticles ($<$ 50 nm particle size) were obtained from Sigma Aldrich (St. Louis, MO). Carboxylic functionalized multi-walled carbon nanotube (MWCNT) were generously donated by Cheap Tubes Inc. (Grafton, Vermont). L-Glutamic acid, bovine serum albumin (BSA, min 96%), glutaraldehyde (50% in deionized water), hydrogen peroxide (30%), 0.1 M phosphate buffer solution (PBS, pH 7), and dimethyl sulfoxide (DMSO) were obtained from Fisher Scientific (Walham, MA). Ascorbic acid (AA) and uric acid (UA), and acetaminophen (AC) were purchased from Alfa Aesar (Thermo Fisher Scientific, Walham, MA). Glutamate oxidase (GluOx) from Streptomyces, with a rated activity of 25 units per mg protein was purchased from Cosmo Bio USA (Carlsbad, CA). Ag (CI-1001) and Ag/AgCl (CI-4001) were generously donated by Engineered Conductive Materials Inc. (Delaware, OH). Ecoflex (00-30) was obtained from Smooth-On (Macungie, PA). Elastomeric polydimethylsiloxane (PDMS, Sylgard 184) was purchased from Dow Corning (Midland, MI).

### 2.2.2 Nanocomposite ink preparation

To create the PtNPs nanocomposite, 30 mg of carboxylic functionalized MWCNT (1 wt.%) and 30 mg PtNPs (1 wt.%) were first mixed with 582.75 $\mu$l (22 wt.%) of DMSO in a sonication bath for 2 h. The mixture then was added to 2000 mg PEDOT:PSS ink, and sonicated again for 10 min to re-disperse the nano materials. Finally, 520 mg (16 wt.%) Ecoflex was added and mixed using a homogenizer Ultra-Turrax T 25, IKA, Wilmington, NC) at 10000 rpm overnight. The final mixture was dried at 60 °C in vacuum for 1 h to remove excess DMSO and to create desired viscosity for printing. MWCNT-PEDOT:PSS nanocomposite and PEDOT:PSS ink were also prepared for electrochemical characterization using a similar procedure except without PtNPs. The PEDOT:PSS ink was modified with DMSO (22 wt.%) to improve conductivity.

### 2.2.3 Direct writing of biosensors

Fig. 2.1a shows the fabrication process of a flexible glutamate biosensor using direct ink writing on a flexible polymer substrate. A commercial 3-axis microfluid dispensing robot (Pro-EV 3, Nordson EFD, East Providence, RI) was used to print the conductive ink. To achieve microscale features, pulled glass capillary pipettes with 30 $\mu$m-diameter tips were used as the dispensing nozzle. PtNPs nanocomposite ink was used to define the working electrode, counter electrode, and conductive traces. Silver/silver chloride (Ag/AgCl) ink was used as the reference electrode and contact pads. To insulate the device, PDMS was printed over the conductive traces leaving only the electrodes and contact pads exposed.

### 2.2.4 Micromachining of implantable biosensor

To complete the implantable biosensor, we used two different rapid prototyping techniques. In the first type, a femtosecond laser (CARBIDE, Altos Photonics, USA) was used to machine the probe outline from a 40-$\mu$m-thick PDMS film on Parylene C-coated glass slide. The laser was operated with a wavelength of 1030 nm, a laser pulse duration of 290 fs, an output power of 2 W, a pulse repetition rate of 100 kHz, and a scanning speed of 1 mm/s. After laser micromachining, the biosensor was released from the surface by submersion in deionized water.

In the second type, a custom maskless photolithography and a reactive ion etcher were used to pattern and machine the probe outline Y. Li et al. (2015); H. Park, Raffiee, John, Ardekani, and Lee (2018). For this micromachining technique, a commercially available 50 $\mu$m-thick LCP sheet (Ultralam 3850, Rogers corporation, Chandler, AZ, USA) was used as the sensor substrate. The probe outline was designed and projected using Microsoft PowerPoint. The exposed LCP was etched using a reactive ion etcher (STS ICP Advanced Oxide Etch, Surface Technology System, Newport, United Kingdom) with 50 sccm of $O_2$ and 10 sccm of $SF_6$ at 2000 W in 2 mTorr for 7 min. After fabricating the desired probe structure, the sensor elements were printed on the LCP probe and glutamate oxidase was immobilized to complete the biosensor.

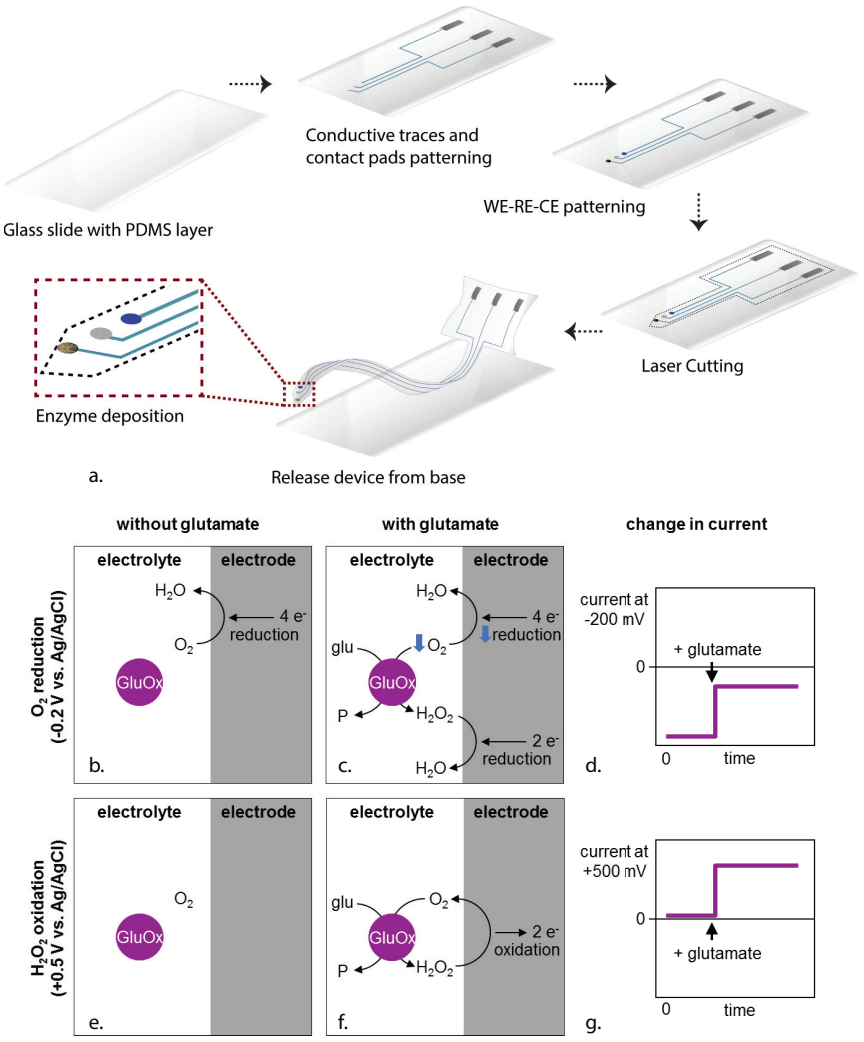


*Figure 2.1.* (a) Schematic of fabrication process of PtNPs-nanocomposite-based glutamate biosensor on a PDMS substrate. The glutamate biosensor works by one of two first-generation mechanisms depending on the bias potential (−0.2 V or 0.5 V vs. Ag/AgCl). In both cases, the enzymatic reaction is L-glutamate + $O_2$ + $H_2O$ → $\alpha$-ketoglutarate + $H_2O_2$ + $NH_3$. In the figure, some species have not been shown for concision. P stands for alpha-ketoglutarate and NH3; glu, for glutamate (and $H_2O$); GluOx for glutamate oxidase. (b) At 0.5 V vs. Ag/AgCl, the working electrode oxidizes $H_2O_2$ ($H_2O_2 \rightarrow O_2 + 2H^+ + 2e^-$). Because the calibration electrolyte initially has no $H_2O_2$, the current starts near zero. (c) When glutamate is added, the enzymatic reaction produces $H_2O_2$, which then oxidizes on the electrode. This creates an anodic current. (d) Therefore, the current at 0.5 V vs. Ag/AgCl also appears more positive when glutamate is added. (e) At −0.2 V vs. Ag/AgCl, the working electrode reduces $O_2$ dissolved in the electrolyte ($O_2 + 4H^+ + 4e^- \rightarrow 2H_2O$). Because of $O_2$ reduction, the sensor starts with a negative cathodic current. (f) When glutamate is added, the enzymatic reaction consumes and depletes $O_2$, and therefore $O_2$ reduction at the electrode decreases. Although $H_2O_2$ reduction ($H_2O_2 + 2H^+ + 2e- \rightarrow 2H_2O$) increases, the net effect is a decrease in cathodic current. (g) Therefore, the current at −0.2 V vs. Ag/AgCl becomes more positive when glutamate is added. (Reprinted with permission from T. N. Nguyen et al. (2019a). Copyright 2019 Elsevier).

### 2.2.5 Enzyme and perm-selective membrane immobilization

After printing the electrodes, the working electrode was coated with an enzyme matrix to complete the glutamate biosensor. When the sensor needed a permselective layer, Nafion was deposited before coating with the enzyme matrix. For Nafion coating, 0.5 $\mu$l of 0.5 wt.% Nafion® was dropped on the surface and was dried at room temperature. For all working electrodes, the enzyme was immobilized using a solution of GluOx (100 U/ml), BSA (1 wt.%) and glutaraldehyde (0.15%). A 0.5 $\mu$l drop of solution was formed on a pipette tip and deposited on the working electrode under a microscope. Enzyme droplets were lowered on the working electrode. This was repeated 5 times with each application consisting of four depositions on top of the working electrode. Devices were left at room temperature for 24 h and then stored at 4 °C before use.

### 2.2.6 Surface investigation and characterization

The surface morphology of the PtNPs nanocomposite was observed using a field-emission scanning electron microscopy (FESEM, S-4800, Hitachi, Japan). The elemental composition was determined using energy dispersive X-ray spectroscopy (EDX) attached to the FESEM system. The morphology of the carbon nanotubes and PtNPs was further characterized by transmission electron microscopy (TEM, Tecnai G2 20, FEI Company, OR).

### 2.2.7 Electrochemical analysis of fabricated biosensor

Electrochemical analysis of the sensors was performed using a SP-200 potentiostat (Bio-logic USA, LLC, Knoxville, TN, USA). All electrochemical experiments were performed in a conventional three-electrode cell configuration in 0.01 M PBS (pH 7.0) as the supporting electrolyte (50 mL for all experiments). A scan rate of 100 mV/s and sampling interval of 1 mV/s were used for cyclic voltammetry (CV). All amperometry data (i.e., *i-t* curve) were collected at 0.5 V or $-0.2$ V vs. Ag/AgCl with a 0.3 s sampling interval after 20 min of settling time unless stated otherwise. All amperometric calibrations were done in a solution, stirred by a magnetic bar at 200 rpm, in a Faraday

cage. The glutamate sensor stability was evaluated by comparing sensitivity to glutamate before and after 7-weeks storage in 0.01 M PBS (pH 7.0) at 4 °C.

### 2.2.8 *Ex vivo* evaluation

Spinal cord segments were surgically extracted from male Sprague-Dawley rats from 200-400 g Page, Park, Chen, Cao, and Shi (2017) and placed on a double sucrose gap recording chamber for *ex vivo* evaluation Jensen and Shi (2003); R. Shi and Blight (1996); W. Sun et al. (2010); R. Yan, Page, and Shi (2010). While in the recording chamber, spinal cord segments were in Krebs solution kept at pH 7.2-7.4 by bubbling continuously with 95% $O_2$, 5% $CO_2$ Page et al. (2017). The *ex vivo* experiments were performed by inserting the glutamate sensor vertically into the gray matter of the spinal cord either before or after SCI. SCI was simulated by squeezing the spinal cord with metal tweezers for 5-10 s near the glutamate sensor. The change in glutamate concentration was measured with our biosensor at 0.5 V vs. Ag/AgCl.

## 2.3 Results and Discussion

### 2.3.1 Characterization of PtNPs nanocomposite

We used FESEM and TEM to examine the morphology of the PtNPs nanocomposite. The FESEM images showed a rough surface morphology (Fig. 2.2a), which is likely due to incorporation of PtNPs on the surface. For amperometric sensors, the additional surface area from roughness often corresponds to a higher sensitivity Z. Li, Leung, Gao, and Gu (2015); Tiwari, Vij, Kemp, and Kim (2016). TEM images showed clustering of PtNPs with MWCNT (Fig. 2.2b).

We also characterized the elemental composition of the nanocomposite using EDX (Fig. 2.2c). The weight percentage of each material is averaged from four different spots on the sample surface. The EDX spectrum had large peaks corresponding C and O, Si, which indicates the presence of PEDOT:PSS, MWCNT and Ecoflex. A peak for S corresponds to PSS in PEDOT:PSS. The spectrum

also featured a peak for Pt. According to EDX data, PtNPs nanocomposite was 1.49 wt.% Pt, which closely matches our expectation. DMSO evaporates out of 1%-PtNPs nanocomposite ink as it dries after being printed, so the final fraction of Pt should be about 1.28 wt.%. The Al peak is likely from the Al substrate upon which PtNPs nanocomposite was printed for EDX characterization.

We used the conductive polymer PEDOT:PSS as the base material of the PtNPs nanocomposite. PEDOT:PSS lowers inter-particle resistance via $\pi$ - $\pi$ interactions. By these interactions, PEDOT:PSS promotes conductive phases between the polymer matrix and nanofillers (PtNPs and MWCNTs) and connects nanoparticle clusters together Patole and Lubineau (2015); Zhou and Lubineau (2013). According to literature, the combination of carbon nanotubes and metallic nanoparticles results in novel hybrid nanoassemblies that improve adsorption of biomolecules and facilitate electron transfer (Fig. 2.2b) P. C. Ma, Tang, and Kim (2008). MWCNTs improved the robustness and performance of our glutamate sensors thanks to their high electrical conductivity, mechanical strength and excellent chemical stability Rathod, Dickinson, Egan, and Dempsey (2010). Others have reported weak interaction and high contact resistance between nanoparticles and carbon nanotubes in mixtures Dong et al. (2007). However, adding PtNPs improved the electrocatalytic activity of our nanocomposite.

### 2.3.2 Fabricated biosensors and electrochemical evaluations

Figs. 2.2d- 2.2e show the fabricated devices on PDMS and LCP. The PDMS device was laser cut, and the LCP device was printed directly on micromachined LCP H. Park et al. (2018). Both thin-film devices were highly compliant upon release and required delicate handling. The flexible biosensor maintained good sensitivity even when bent at 45° (Fig. 2.3). The PDMS based sensors could be stiffened if needed by using polyethylene glycol, silk, saccharose, gelatin or other biodegradable coating materials Weltman, Yoo, and Meng (2016). On the other hand, the LCP based sensors with 50 $\mu$m thickness were stiff enough for insertion to the spinal cord tissue without buckling in our *ex vivo* measurements.

Fig. 2.5a shows the CV of a PtNPs nanocomposite electrode compared to MWCNT-PEDOT:PSS and PEDOT:PSS electrodes. The voltammogram of PEDOT:PSS was rectangular due to non-Faradaic charging current. This charging current is a product of capacitive behavior between the conductive electrode surface and the electrolyte Gerwig et al. (2012). The voltammogram of MWCNT-PEDOT:PSS showed a slightly higher current density than PEDOT:PSS electrode, which is in agreement with literature González-Gaitán, Ruiz-Rosas, Morallón, and Cazorla-Amorós (2017); J. Park, Lee, Yim, and Han (2011); J. Zhang et al. (2012). A more distinct voltammogram was generated when PtNPs were added. PtNPs nanocomposite (PtNP-MWCNT-PEDOT:PSS) exhibited superior catalytic behavior (i.e., higher current density) compared to the other composite materials. Therefore, we used PtNPs nanocomposite as our sensor material.

We evaluated the amperometric responses of our nanocomposite biosensors using two different biasing potentials, 0.5 V and $-0.2$ V vs. Ag/AgCl (Figs. 2.1b- 2.1g). At either potential, GluOx produces $H_2O_2$ and consumes $O_2$ in proportion to the glutamate it catalyzes. At 0.5 V vs. Ag/AgCl, PtNPs nanocomposite oxidizes $H_2O_2$, so the current generated by this can be correlated to the glutamate concentration (Figs. 2.1b- 2.1d) Cui, Barford, and Renneberg (2007); Hamdi, Wang, Walker, Maidment, and Monbouquette (2006). Fig. 2.5b shows a voltammogram from our glutamate sensors in 100 $\mu$M glutamate, 0.01 M PBS (pH 7.0). The voltammograms demonstrate oxidation of enzymatically produced $H_2O_2$ shown as an increase in current starting around 0.3 V with the highest oxidation peak around 0.5 V. Thus, we chose 0.5 V as our potential for amperometric glutamate sensing via $H_2O_2$ oxidation.

PtNPs-nanocomposite glutamate biosensor was made to be flexible in order to minimize the damage to the tissue as well as withstanding the insertion force. Fig. 2.3 presents the photographs of flexible glutamate biosensor bending on the surface at 45°. CV and amperometry were run in both normal, non-bending condition, and bending condition to compare the functionality of glutamate nanocomposite biosensors.

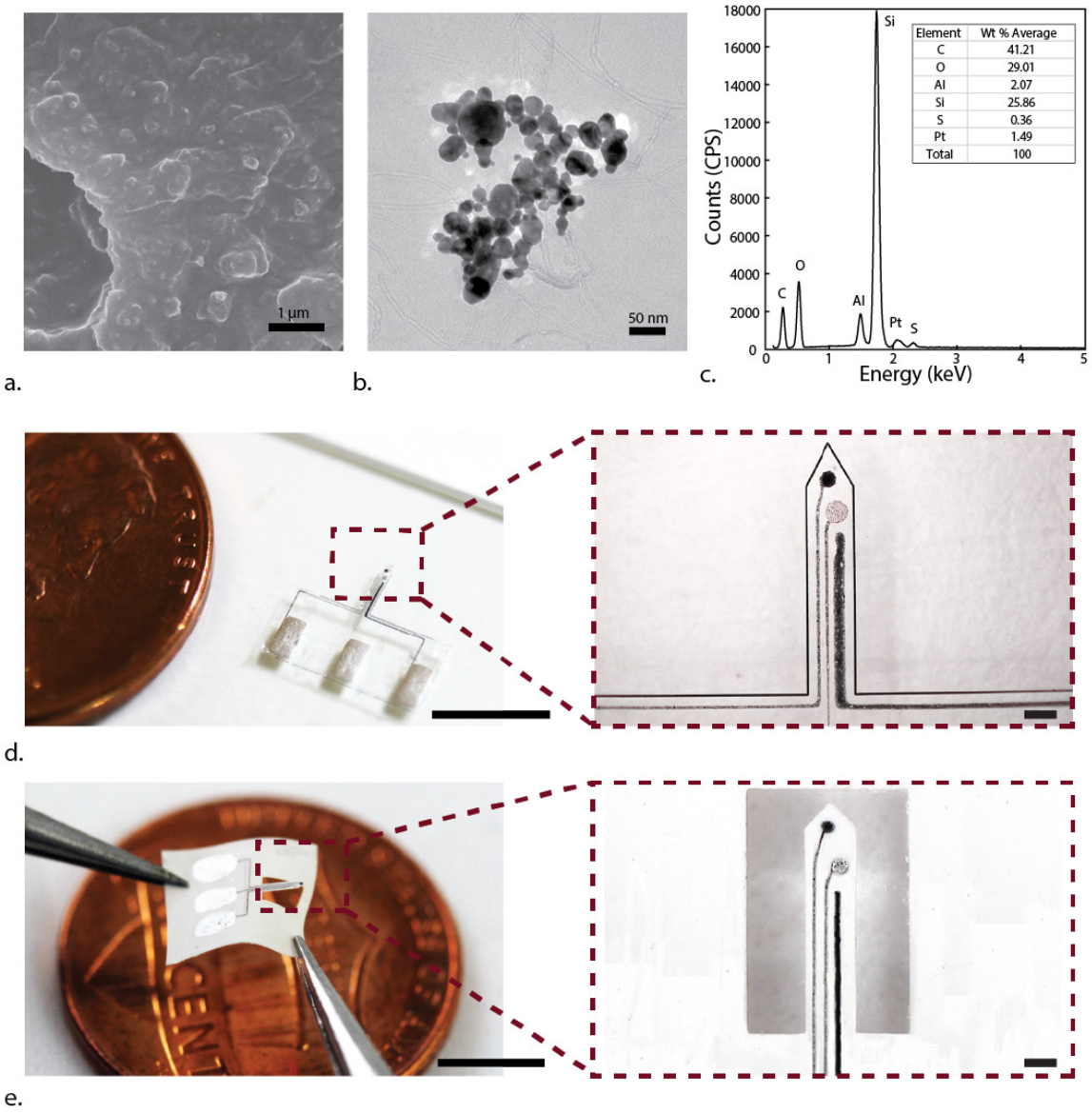


*Figure 2.2.* (a) Scanning electron micrographs of PtNPs nanocomposite. The rough nanoscale texture is most likely due to the embedded PtNP clusters. (b) Transmission electron micrographs of PtNPs nanocomposite. Note the clustered nanocomposite linked with MWCNT. (c) EDX spectrum of fabricated PtNPs nanocomposite. The Al peak is most likely due to the Al substrate used to image the nanocomposite sample. (d) Photograph of a flexible micro-glutamate biosensor on PDMS substrate (scale bars: 5 mm and 200 $\mu$m). (e) Photograph of a flexible micro-glutamate biosensor on LCP sheet (scale bars: 5 mm and 200 $\mu$m). (Reprinted with permission from T. N. Nguyen et al. (2019a). Copyright 2019 Elsevier).

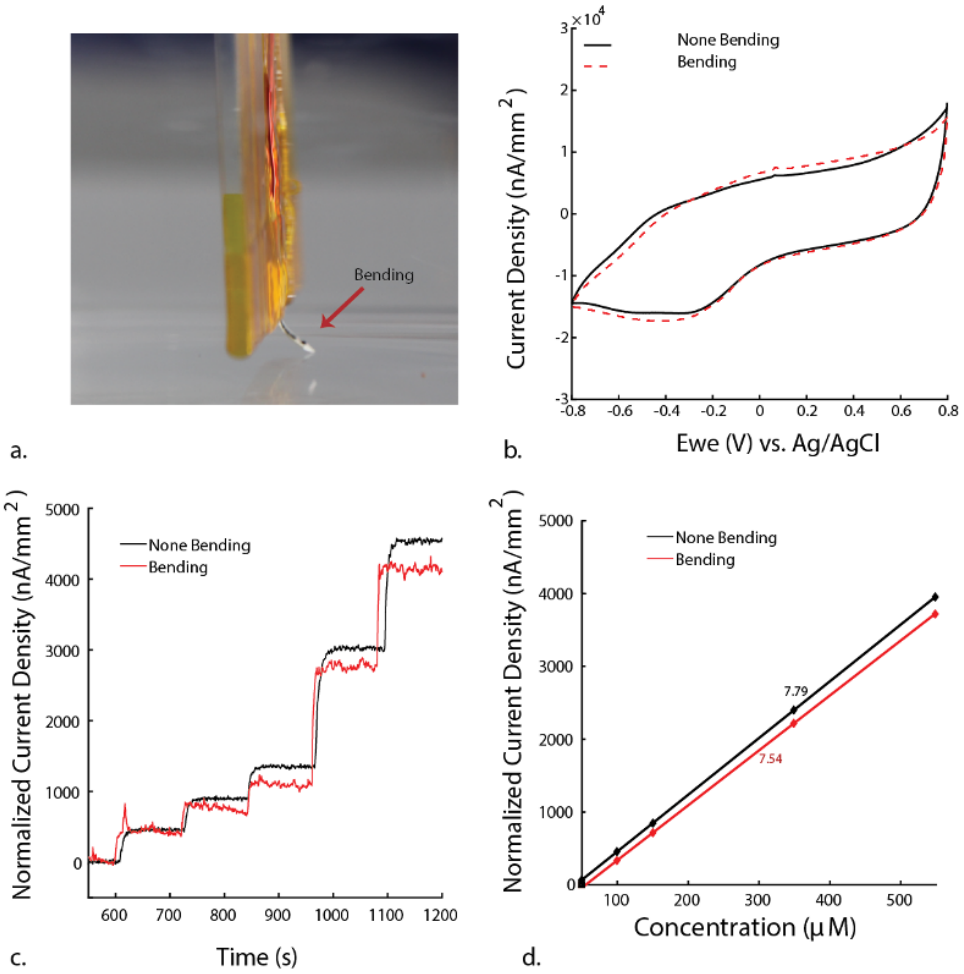


*Figure 2.3.* (a) Photograph of a flexible micro-glutamate biosensor on LCP sheet bending on the surface an angle of 45°. (b) Cyclic voltammetry of glutamate biosensors made from PtNPs-nanocomposite-Nafion-GluOx in 0.01 M PBS (pH 7) in none-bending condition and bending condition (as shown in a). Scan rate = 100 mV $s^{-}1$. (c). Amperometric curves for PtNPs-nanocomposite-Nafion-GluOx biosensors at applied potential of 0.5 V vs. Ag/AgCl in 0.01 M PBS (pH 7.0) with various concentration of glutamate in none-bending condition and bending condition (as shown in a). (d) The corresponding calibration curve and the sensitivity of glutamate biosensor none-bending condition and bending condition. (Reprinted with permission from T. N. Nguyen et al. (2019a). Copyright 2019 Elsevier)

It is also possible to sense glutamate via $O_2$ reduction (Fig. 2.1e- 2.1g). At $-0.2$ V vs. Ag/AgCl, PtNPs nanocomposite reduces $O_2$, generating a cathodic current. When GluOx consumes $O_2$ along with glutamate, $O_2$ is depleted near the PtNPs nanocomposite, so $O_2$ reduction and cathodic current decrease. As can be seen in Fig. 2.5b, the PtNPs nanocomposite-GluOx displayed a large reduction peak around $-0.2$ V. Thus, we chose $-0.2$ V as another potential for amperometric detection of glutamate via the reduction of $O_2$. However, it is worth noting that when the sensors are operated at low negative potential, the background noise coming from the reduction of $O_2$ also increase in the signal. Thus, it is likely to cause the signal resolution at $-0.2$ V to be less stable than the signal resolution at 0.5 V You et al. (2004).

### 2.3.3 Amperometric responses of printed glutamate biosensor

We characterized the glutamate biosensor performance using chronoamperometry at 0.5 V and $-0.2$ V vs. Ag/AgCl. As shown in Fig. 2.5c- 2.5d, PtNP nanocomposite-Nafion-GluOx was more sensitive to glutamate than the other composite materials at 0.5 V vs. Ag/AgCl. The calibration plot (Fig. 2.5d) shows that PtNPs nanocomposite-Nafion-GluOx had a linear response with a sensitivity of $2.60 \pm 0.15$ nA $\mu M^{-1}$ $mm^{-2}$ ($n = 3$, each). These results are comparable to other MEMS-fabricated glutamate sensors, which suggests that our simple fabrication method can yield high performing glutamate sensors (Table 2.1).

We then evaluated the performance of our glutamate sensor at $-0.2$ V vs. Ag/AgCl) (Fig. 2.5e). Again, PtNP nanocomposite-Nafion-GluOx had the highest sensitivity compared to the other composite materials. The calibration plot (Fig. 2.5d) shows a linear response with a higher sensitivity of $12.81 \pm 1.18$ nA $\mu M^{-1}$ $mm^{-2}$ ($n = 3$), which is more sensitive than glutamate sensing via $H_2O_2$ oxidation at 0.5 V vs. Ag/AgCl.

### 2.3.4 Linear range, limit of detection and response time

We calibrated our biosensors with successive additions of glutamate from 1 $\mu$M to 1400 $\mu$M to determine the linear range (Fig. 2.4). When biased at 0.5 V, the linear range was between 1 $\mu$M and 800 $\mu$M. The detection limit was 0.5 $\mu$M, and the response time was $< 3$ s. When biased at $-0.2$ V,

the linear range was smaller, from 10 $\mu$M to 600 $\mu$M. At $-0.2$ V, the detection limit, 0.2 $\mu$M, was slightly lower than it was at 0.5 V, but the response time (15 s) was much longer.

Taken together, these results suggest that we are able to successfully fabricate glutamate biosensor using our nanocomposite with good sensitivity and detection limit. The normal background extracellular glutamate concentration is reported to be in the micromolar range (i.e., $< 20$ $\mu$M) Moussawi et al. (2011). In a SCI rat model, the extracellular glutamate concentration has previously been measured to be as high as 530 $\mu$M G. Y. Xu et al. (2004a). Therefore, regardless of biasing potential, our biosensors are more than capable of detecting glutamate in normal physiological conditions as well as in a SCI model.

### 2.3.5 Selectivity and stability of the printed glutamate biosensor

For successful *in vivo* electrochemical detection of glutamate, the biosensor must be selective against other electroactive species present in the body. Three possible interfering substances (i.e., AA, UA, AC) that are thought to be present in the spinal cord were identified to evaluate the selectivity of the electrodes Kotanen, Moussy, Carrara, and Guiseppi-Elie (2012). The current obtained for each interfering substance at a concentration of 100 $\mu$M in the presence of 200 $\mu$M glutamate was used as an indicator for the biosensor selectivity in comparison with the glutamate reading alone.

When biased at 0.5 V, other electroactive species can also be directly oxidized at the electrode surface. Thus, we added a Nafion permselective layer, which electrostatically repels anions, on the electrode surface before enzyme immobilization to enhance the biosensor selectivity S. Pan and Arnold (1996). Fig. 2.7a shows the amperometric response of PtNPs-based glutamate biosensor against AA, UA, and AC. At 0.5 V the current ratio between glutamate and AA is 0.2, and 0.05 between glutamate and UA. However, the current ratio between glutamate and AC is approximate 0.59, which suggests that our Nafion membrane cannot fully prevent interference from AC. However, this may be improved in future studies by using another type of permselective layer such as m-Phenylenediamine dihydrochloride Stephens, Quintero, Pomerleau, Huettl, and Gerhardt (2011), or by annealing Nafion to improve its selectivity Burmeister and Gerhardt (2001).

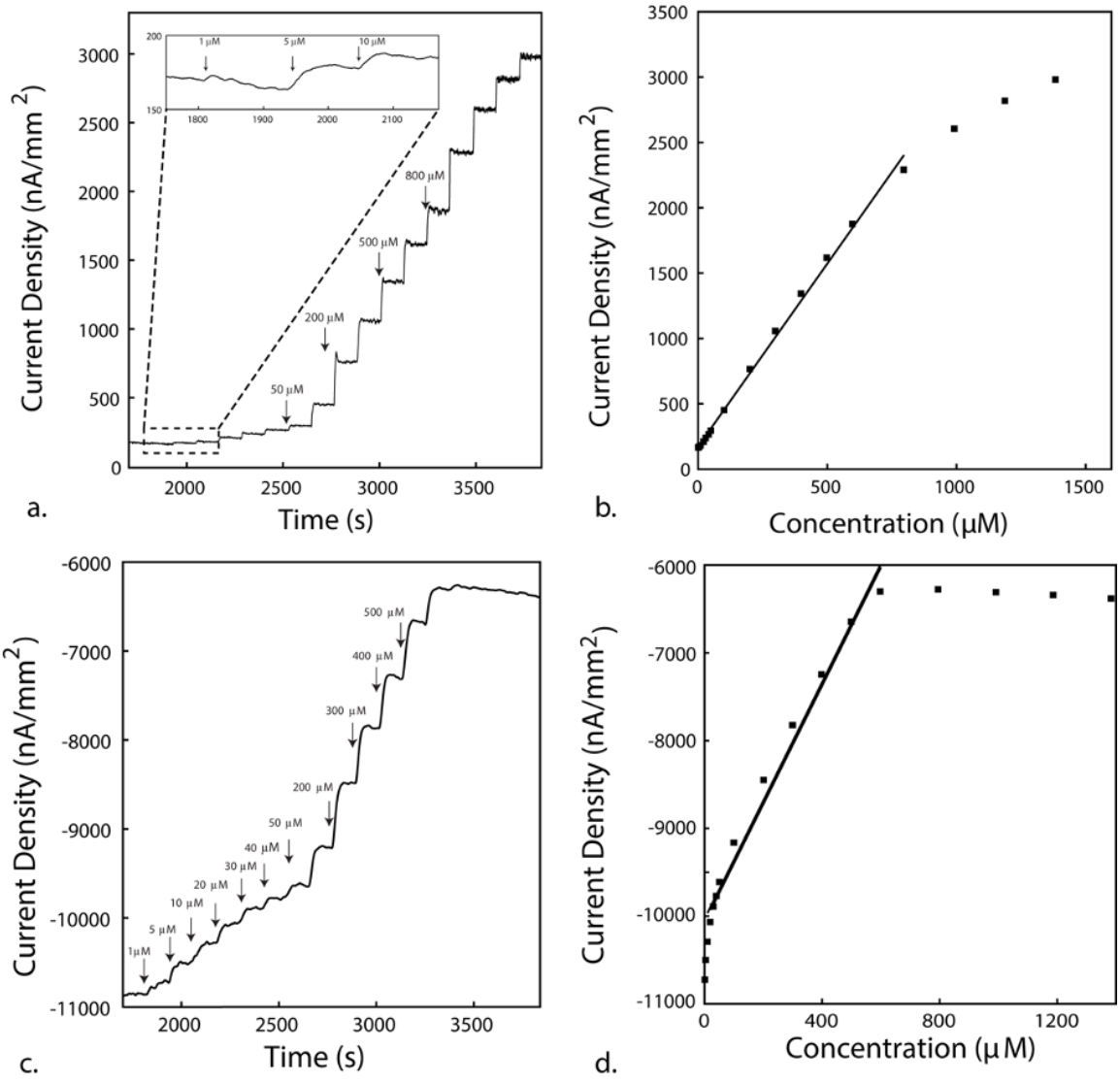


*Figure 2.4.* (a) Amperometric curve of different concentration of glutamate in 0.01 M PBS solution (pH 7.0) of PtNPs nanocomposite-Nafion-GluOx printing electrode at applied potential of 0.5 V. (b) The corresponding calibration curve of response current versus the concentration of glutamate at applied potential of 0.5 V. (c) Amperometric curve of different concentration of glutamate in 0.01 M PBS solution (pH 7.0) of PtNPs nanocomposite-Nafion-GluOx printing electrode at applied potential of − 0.2 V. (d) The corresponding calibration curve of response current versus the concentration of glutamate at applied potential of − 0.2 V.(Reprinted with permission from T. N. Nguyen et al. (2019a). Copyright 2019 Elsevier)

We also evaluated the selectivity of our biosensor against AA, UA, and AC at $-0.2$ V. Fig. 2.7b shows the amperometric response of our glutamate biosensor to these molecules. The ratio current between glutamate and interference species are 0.013, 0.026 and 0.006 for AA, UA, AC, respectively. Even without a permselective layer, our glutamate biosensor exhibited excellent selectivity against these common interfering molecules. This suggests that at $-0.2$ V, it is possible to obtain a more sensitive and interference-free measurement of glutamate concentration when a longer sampling interval is acceptable.

Next, we evaluated the long-term stability of our glutamate biosensor by comparing the sensitivity before and after storing them at 4 °C in 0.01 M PBS (pH 7.0) for 7 weeks. Figs. 2.7c- 2.7d show the amperometric responses of our biosensors before and after the storage period ($n = 3$, each). The sensor maintained $79.66 \pm 2.718\%$ of its initial sensitivity at 0.5 V (Fig. 2.7c). Similarly, the sensor maintained $80.56 \pm 1.71\%$ of its initial sensitivity at $-0.2$ V (Fig. 2.7d). The decrease in current response may be due to enzyme inactivation or electrode fouling during the storage period.

### 2.3.6 $O_2$ dependence

Because $O_2$ is a co-substrate of glutamate oxidase, the response of our glutamate sensor depends on the presence of $O_2$. This may present a challenge for *in vivo* application, in which the concentration of $O_2$ may not be constant Y. Zhang and Wilson (1993). Thus, we calibrated our sensors at $-0.2$ V in air (oxygenated) and nitrogen-purged (deoxygenated) 0.01 M PBS (pH 7.0) ($> 60$ min each). As expected, the sensitivity to glutamate decreased by 30.91% in nitrogen-purged PBS compared to air-purged PBS, and decreased by 18.54% compared to normal PBS (Fig. 2.6). The fact that nitrogen-purging did not completely eliminate glutamate response may be trace amounts of oxygen remaining in PBS to facilitate glutamate oxidase catalysis. It is also possible that some $O_2$ had dissolved in to the sensor 's PtNP nanocomposite prior to nitrogen purging, which can still facilitate glutamate oxidation in $O_2$-depleted bulk solution. Nevertheless, these results confirm the $O_2$ dependence of the enzymatic biosensors at $-0.2$ V.

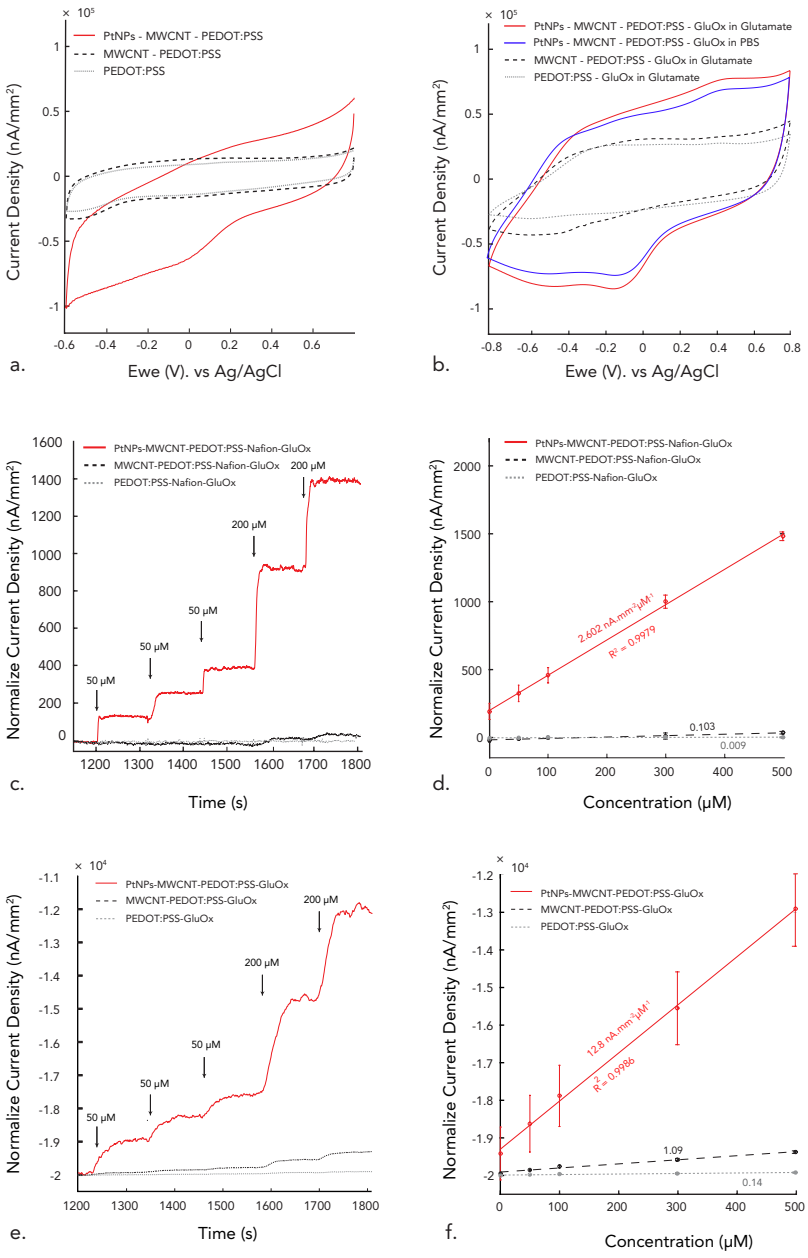


*Figure 2.5.* (a) Cyclic voltammetry of various nanocomposite materials in 0.01 M (pH 7.0). Scan rate = 100 mV $s^{-1}$. (b) Cyclic voltammetry of glutamate biosensors made from various materials in 0.01 M PBS (pH 7.0) solution and 100 $\mu$M glutamate. Note that the PtNP nanocomposite exhibited highest catalytic activity. Scan rate = 100 mV $s^{-1}$. (c) Representative amperometric curves for various nanocomposite glutamate biosensors at applied potential of 0.5 V vs. Ag/AgCl in 0.01 M PBS (pH 7.0). (d) The corresponding calibration curve and the sensitivity of each glutamate biosensor material (n = 3). (e) Representative amperometric curves for various nanocomposite glutamate biosensors at applied potential of $-0.2$ V vs. Ag/AgCl in 0.01 M PBS. Note that the response time for each glutamate addition is much slower. (f) The corresponding calibration curve and the sensitivity of each glutamate biosensor material (n = 3). Note that the PtNP nanocomposite glutamate biosensor is approximately 5 times more sensitive using this method. (Reprinted with permission from T. N. Nguyen et al. (2019a). Copyright 2019 Elsevier).

Highly sensitive enzymatic detection of glutamate ($> 90\%$) is possible when partial pressure of $O_2$ in the tissue is maintained $> 30$ torr Hu, Mitchell, Albahadily, Michaelis, and Wilson (1994). In a normal cerebral cortex, the partial pressure of $O_2$ is typically $> 40$ torr Silver (1965), however, it is not yet clear how SCI impacts oxygenation of the spinal cord. Therefore, it may be necessary to perform additional experiments to correlate oxygenation of the SCI model prior to using our glutamate sensor.

### 2.3.7 *Ex vivo* measurements

In order to demonstrate the capability of our biosensors for monitoring glutamate release in a physiologically-relevant environment, we implanted pre-calibrated sensors into a half segment of a rat spinal cord, onto which we administered injuries to induce glutamate release (Fig. 2.8a). Fig. 2.8b shows the injury-induced glutamate release with the sensor already implanted in the spinal cord. The initial peak corresponds to the glutamate released by the biosensor insertion whereas the second peak corresponds to the glutamate release due to SCI. In the second experiment, we applied SCI prior to inserting the biosensor (Fig. 2.8c). As such, the first peak corresponds to the device insertion, and the second peak likely corresponds to the change in glutamate concentration due to induced SCI.

These preliminary results confirms previously reported results to suggest that SCI can significantly increase extracellular glutamate concentration, and that our glutamate biosensor can monitor this change in glutamate concentration. Although the response time of our biosensor at 0.5 V is $< 3$ s, we found that the current spike due to SCI occurred between 10-20 s after the injury. This may be due to physical distance between the SCI site and the location of our implanted biosensor. To better characterize this dynamic process, we may need to improve the response of our biosensors. We also found that the increase in glutamate concentration is relatively transient following an SCI. The elevated glutamate concentration seem to only last $< 10$ s before settling down to pre-injury levels. Additional experiments are needed to confirm this transient behavior of extracellular glutamate concentration. Nevertheless, these results highlight the capability of our biosensors in examining the relatively rapid glutamate response following an SCI that cannot be resolved using conventional microdialysis. By using these simple biosensors that can be rapidly be fabricated at low cost, we may be able to better elucidate the effects of GET in SCI *in vivo* at a higher spatiotemporal resolution.

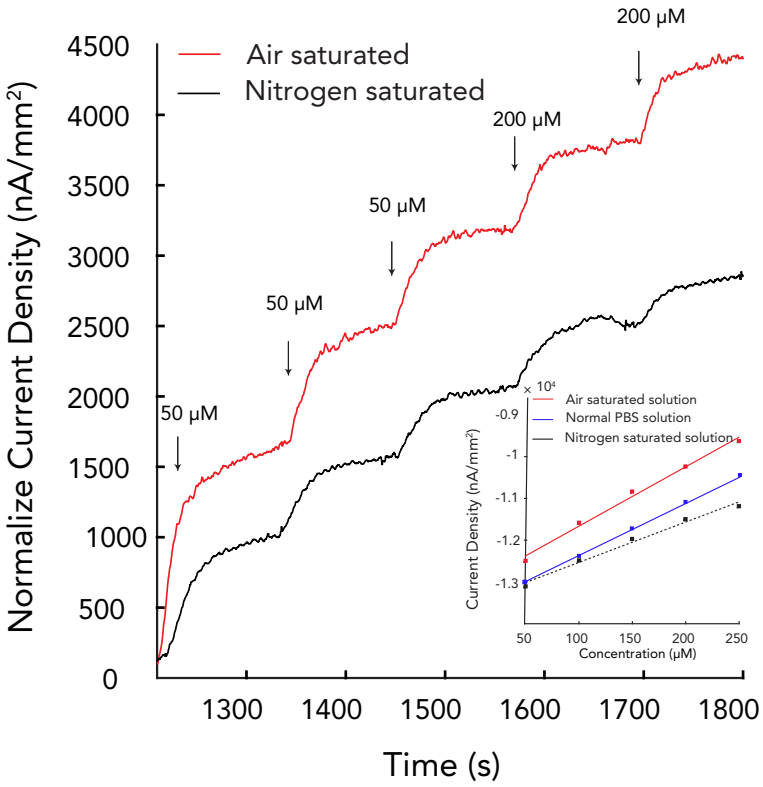


*Figure 2.6.* Amperometric response of PtNPs nanocomposite-GluOx to glutamate in air saturated and $N_2$ saturated 0.01 M PBS solution (pH 7.0) at $-$ 0.2 V. Inset: the corresponding calibration curve of response current versus the concentration of glutamate in different solution. It also included the calibration curve from PtNPs-nanocomposite-GluOx in normal 0.01 M PBS solution (pH 7.0). (Reprinted with permission from T. N. Nguyen et al. (2019a). Copyright 2019 Elsevier)

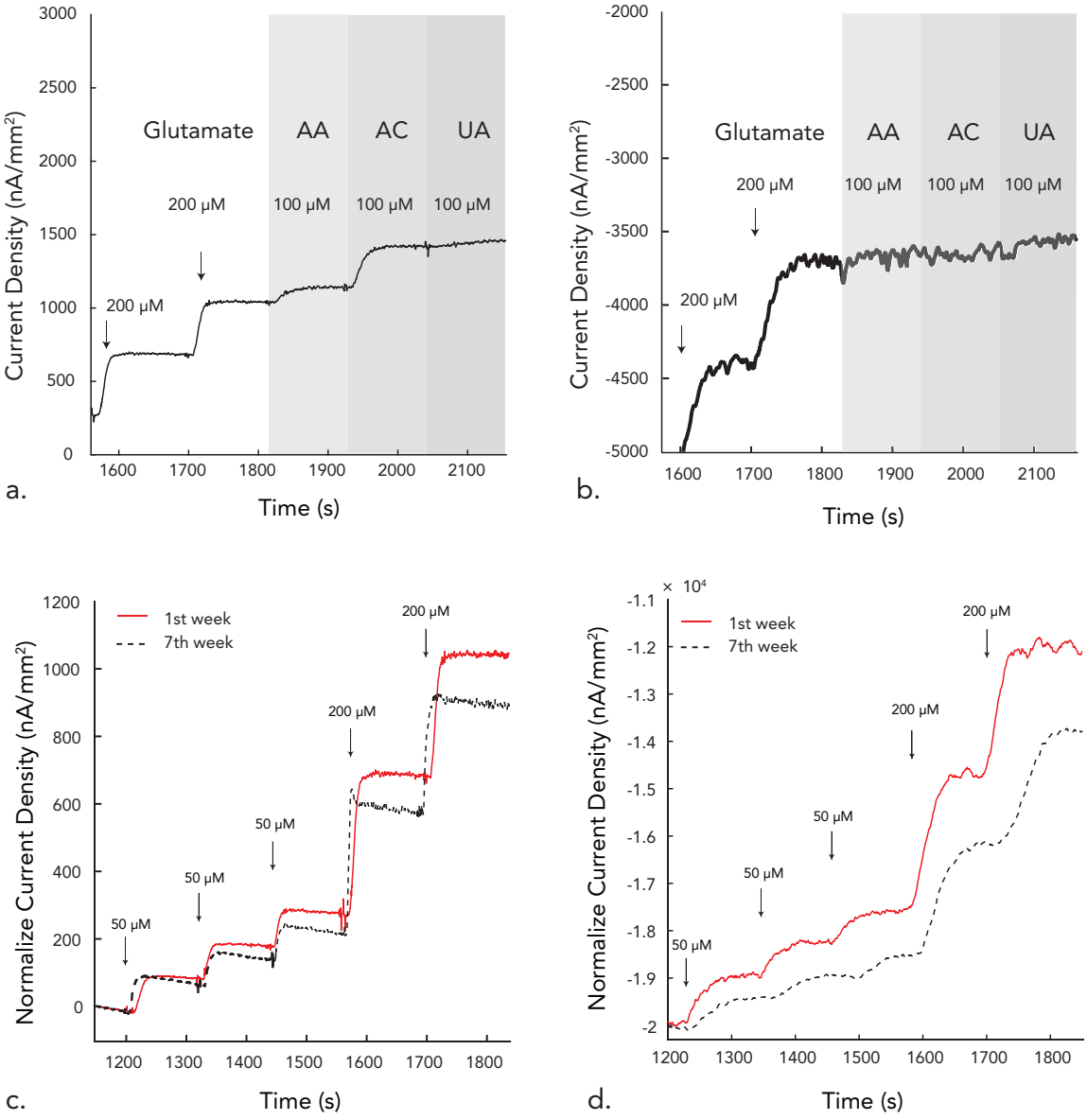


*Figure 2.7.* (a). Amperometric response of PtNPs nanocomposite-Nafion-GluOx upon sequential addition of 200 $\mu$M glutamate, 100 $\mu$M of AA, 100 $\mu$M of AC and 100 $\mu$M of UA into constantly stirred PBS solution at +0.5 V. (b) Amperometric response of PtNPs nanocomposite-GluOx upon sequential addition of 200 $\mu$M Glutamate, 100 $\mu$M of AA, 100 M of AC and 100 $\mu$M of UA into constantly stirred 0.01 M PBS (pH 7.0) solution at −0.2 V. (c) Amperometric *i-t* curve of different concentration of glutamate in 0.01 M PBS solution (pH 7.0) of PtNPs nanocomposite-Nafion-GluOx at +0.5 V before and after 7 weeks of storage. (d) Amperometric *i-t* curve of different concentrations of glutamate in 0.01 M PBS solution (pH 7.0) of PtNPs nanocomposite-GluOx at −0.2 V before and after 7 weeks of storage. (Reprinted with permission from T. N. Nguyen et al. (2019a). Copyright 2019 Elsevier).

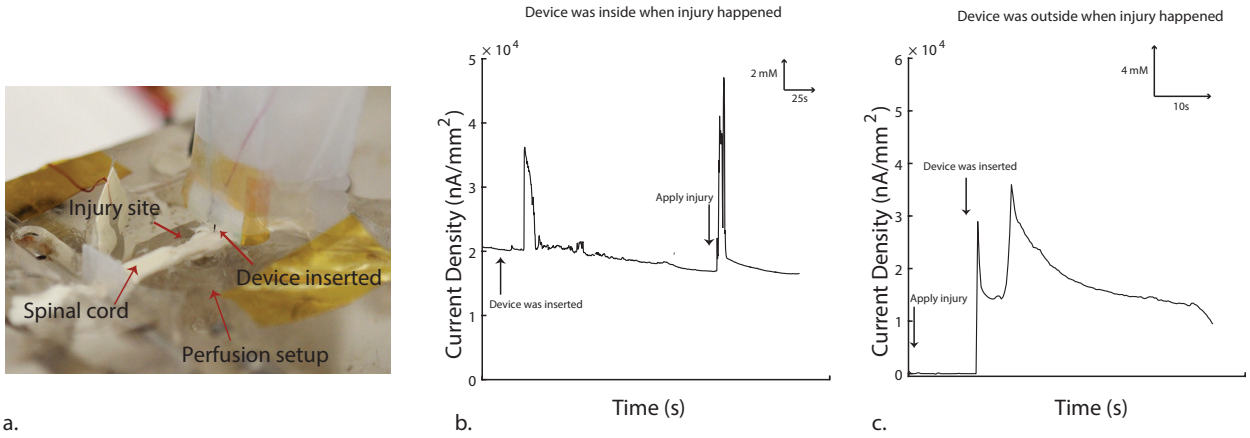


*Figure 2.8.* A representative result of current changes corresponding to injury-induced glutamate release in the spinal cord segment of a rat. (a). Photograph of sensor inserted in the spinal cord segment of a rat. (b). Device was inserted into the spinal cord before injury was applied to the spinal cord. (c). Injury was applied to the spinal cord before the device was inserted to the spinal cord. (Reprinted with permission from T. N. Nguyen et al. (2019a). Copyright 2019 Elsevier)

## 2.4 Conclusion

In this study, we presented a nanocomposite ink that consists of PtNPs, MWCNT, PEDOT:PSS, and Ecoflex to print microscale glutamate sensors using a direct-writing process. The biosensor featured an onboard Ag/AgCl reference and counter electrode. We demonstrated a relatively simple, economic, and rapid method to fabricate a sensor capable of sensing glutamate with a high sensitivity and low limit of detection for *in vivo* applications. Our glutamate sensor also had an adequate linear range and response time, which are suitable for glutamate measurement in the spinal cord to investigate the impact of GET during SCI.

Although these glutamate biosensors demonstrated good bench-top and *ex vivo* performance, our ultimate goal is measuring glutamate *in vivo*. To this end, additional *ex vivo* and *in vivo* work may be needed to verify the functionality in a more complex biological environment. Of particular interest is characterizing the effects of biofouling and foreign body reaction on biosensor sensitivity and stability over the course of implantation. Moreover, we plan to create a biosensor array to better characterize glutamate concentration flux, which will improve our understanding of how GET may propagate to exacerbate SCI.

*Table 2.1.* Comparison of various electrochemical glutamate biosensors. (Reprinted with permission from T. N. Nguyen et al. (2019a). Copyright 2019 Elsevier)

| **Electrode material** | **Area** ($mm^2$) | **Fabrication method** | **Sensitivity** (nA $\mu M^{-1} mm^{-2}$) | **Permselective membrane** | **Detection limit** | **Response time** | **Linear range** | **Reference** |
|---|---|---|---|---|---|---|---|---|
| Pt | 0.0491 | Commercial Pt wire | 0.32 | poly(o-phenylenediamine)- PPD | N/A | N/A | 0- 150 $\mu$M | McMahon and O'Neill (2005) |
| Pt | 0.0491 | Commercial Pt wire | 0.80 | polypyrrole- PPY | 2 $\mu$M | 2 s | 0- 250 $\mu$M | Hamdi et al. (2006) |
| Pt/Chitosan | 8.0425 | Commercial Pt disk | 0.85 | poly(o-phenylenediamine)- PPD | 0.7 $\mu$M | 2 s | 200 $\mu$M | M. Zhang, Mullens, and Gorski (2006) |
| Pt | 0.0491 | Commercial Pt wire | 0.71 | poly(o-phenylenediamine)- PPD | 2.5 $\mu$M | $<$ 5 s | N/A | Govindarajan et al. (2013) |
| Pt | 0.0075 | MEMS | 0.95 | m-phenylenediamine-mPD | 0.5 $\mu$M | 10 s | 150 $\mu$M | Frey et al. (2010) |
| Pt | 0.0050 | MEMS | 1.26 | Nafion-Polypyrrole- PPY | 2.1 $\mu$M | 1 s | $>$ 630 $\mu$M | T. T. C. Tseng and Monbouquette (2012) |
| Pt | 0.0040 | MEMS | 1.83 | Nafion | 0.32 $\mu$M | N/A | 5- 300 $\mu$M | Tolosa, Wassum, Maidment, and Monbouquette (2013) |
| Pt | 0.095 | MEMS | 2.16 | m-phenylenediamine- mPD | 0.22 $\mu$M | 5 s | 150 $\mu$M | Weltin et al. (2014) |
| Pt | 0.0075 | MEMS | 7.47 | Nafion | 0.5 $\mu$M | $<$ 8 s | N/A $\mu$M | W. Wei et al. (2015) |
| Pt | 0.0085 | MEMS | 2.04 | PPY/Nafion | 0.5 $\mu$M | $<$ 3 s | 1- 800 $\mu$M | Hoa, Chen, and Tseng (2018) |
| Pt/MWCNT | 0.7800 | Electrodeposition | 3.84 | Polypyrrole OPP | 0.3 $\mu$M | 7 s | 0- 150 $\mu$M | Ammam and Fransaer (2010) |
| Glassy carbon | 7.0680 | Electrodeposition | 2.10 | Nafion | 0.7 $\mu$M | N/A | 0.1-100 $\mu$M | Karyakin, Karyakina, and Gorton (2000) |
| Carbon fiber | 0.0095 | Commercial carbon fiber | 0.36 | Nafion | 3 $\mu$M | 20-30 s | 0- 100 $\mu$M | Kulagina, Shankar, and Michael (1999) |
| Carbon fiber | 0.00007 | Comercial carbon fiber - Prussian blue | 1.35 | poly-o-phenylenediamine-PoPD | $<$ 2 $\mu$M | N/A | 150 $\mu$M | Salazar, Martín, O'Neill, and González-Mora (2016) |
| Carbon nanofibers | 98300 | PECVD | 0.18 | N/A - low oxidation potential | 0.000767 $\mu$M | 0.05 s | 20 - 500 $\mu$M | Isoaho et al. (2017) |
| CNT composite | 7.0000 | CNT coated on glassy carbon | 0.10 | N/A - low oxidation potential | 2 $\mu$M | 4 s | N/A | Chakraborty and Retna Raj (2007) |
| MWCNT/AuNP/CHIT | 36.000 | Electrodeposition | 1.55 | N/A - low oxidation potential | 1.6 $\mu$M | 5 s | 5 - 500 $\mu$M | Batra and Pundir (2013) |
| PtNPs/AuNP | 0.2000 | Electrodeposition | 0.11 | Nafion | 14 $\mu$M | $<$ 5 s | 0.8 $\mu$M | Jamal, Xu, and Razeeb (2010) |
| PtNPs/MWCNT/PEDOT:PSS | 0.0314 | Direct writing | 2.6 (0.5 V) | Nafion | 0.5 $\mu$M | $<$ 3 s | 1- 800 $\mu$M | This work |
| PtNPs/MWCNT/PEDOT:PSS | 0.0314 | Direct writing | 12.8 ($-$0.2 V) | N/A - low oxidation potential | 0.2 $\mu$M | 15-20 s | 10- 600 $\mu$M | This work |

# CHAPTER 3. FABRICATION AND *EX VIVO* EVALUATION OF ACTIVATED CARBON–PT MICROPARTICLE BASED GLUTAMATE BIOSENSOR

## 3.1 Introduction

In this work, we introduce an economical yet functionally superior composite material for biosensor fabrication based on commercially available activated carbon with Pt microparticles (C-Pt). Here we optimized the sensor performance to demonstrate that the C-Pt based glutamate biosensors have a superior performance compared to the MEMS-fabricated and the Pt nanoparticle-based glutamate biosensors T. N. Nguyen et al. (2019a). C-Pt was mixed with conductive polymer, PEDOT:PSS, to create a dispensable composite ink that can be printed on any soft or hard substrate including PDMS and LCP. The new C-Pt glutamate biosensors have better sensitivity, limit of detection, response time, linear range, and stability compared to our previous Pt nanoparticle-based version. Using an astrocyte cell culture, we demonstrate the capability to monitor extracellular glutamate consumption. Additionally, we present a direct *ex vivo* measurement of glutamate release from optogenetic stimulation in mouse primary visual cortex (V1) brain slices.

## 3.2 Methods

### 3.2.1 Reagents

Ascorbic acid (AA), acetaminophen (AC), and uric acid (UA) were purchased from Alfa Aesar (Thermo Fisher Scientific, Waltham, MA). Glutamate oxidase (GluOx) from Streptomyces was purchased from Cosmo Bio USA (Carlsbad, CA) with a rated activity of 25 units/mg of protein. PEDOT:PSS (5 wt.%), Nafion® 117 solution (5 wt.%), 3,4-Dihydroxyphenylacetic acid (DOPAC) and 5-hydroxyindoleacetic acid (5-HIAA) were purchased from Sigma Aldrich (St. Louis, MO). Bovine serum albumin (BSA, $>$ 96%), hydrogen peroxide (30%), glutaraldehyde (25% in deionized water), L-glutamic acid, dimethyl sulfoxide (DMSO), 0.1 M phosphate buffer solution (PBS, pH 7.0), C-PT paste (10% Pt) were purchased from Fisher Scientific (Waltham, MA). Ag/AgCl (CI-4001), Ag (CI-1001) and were purchased from Engineered Conductive Materials Inc. (Delaware, OH). Carboxylic functionalized multi-walled carbon nanotube (MWCNT) were purchased from Cheap Tubes Inc. (Grafton, Vermont). Ag/AgCl/NaCl (3.5 M) reference electrode for astrocyte measurement was purchased from (Bio-logic USA, LLC, Knoxville, TN, USA). Human cerebral cortex astrocytes, astrocyte medium and cell freezing medium were obtained from ScienCell Research Laboratories (Carlsbad, CA). Astrocyte medium consisted of 500 ml of basal medium, 10 ml of fetal bovine serum (FBS, Cat. No. 0010), 5 ml of penicillin/streptomycin solution (P/S, Cat. No. 0503), and 5 ml of astrocyte growth supplement (AGS, Cat. No. 1852).

### 3.2.2 Ink Preparation

Two different composite inks were used to complete the fabrication of the new glutamate biosensors. The first ink formulation was for the working and the counter electrodes. It was prepared by modifying conductive polymer (PEDOT:PSS) with C-Pt. The polymer composite consisted 1 wt.% of Pt, which was constructed by mixing 100 mg of C-Pt paste and 400 mg of PEDOT: PSS in a planetary centrifugal mixer (ARE-310, Thinky U.S.A., Inc, Laguna Hills, CA) for 30 min and degassing for additional 10 min.

Because C-Pt-modified PEDOT:PSS exhibited high resistance, a second ink was developed to create a more conductive electrical traces. It consisted of PEDOT:PSS modified with 1 wt.% of MWCNT and 22 wt.% of DMSO to improve its conductivity J. Park et al. (2011). Ecoflex (20 wt.%) was also added to improve the flexibility of the ink Bandodkar, Nuñez-Flores, Jia, and Wang (2015). MWCNT was first mixed with DMSO in sonication bath for 2 h. The mixture then was added to PEDOT:PSS ink and transferred to the planetary centrifugal mixer and mixed for 1 h. Next, Ecoflex was added, and mixed for 10 min. Finally, the composite was degassed using the planetary centrifugal mixer for another 1 h. The final mixture was dried at 60 °C in vacuum for 1 h to remove excess DMSO and to create desired viscosity for printing.

Commercially available Ag (CI-1001, Engineered Materials Solutions, Inc., Delaware, OH) and Ag/AgCl (CI, 4001, Engineered Materials Solutions, Inc., Delaware, OH) pastes were used to print the contact pads and the reference electrodes. Lastly, PDMS was applied as an insulating layer leaving only the electrode areas open.

### 3.2.3 Fabrication and Direct Ink Writing Process

Fig. 3.1 shows the construction of our DIW glutamate biosensor. A three-axis automated microfluidic dispensing system (Pro-EV3 and Ultimus V, Nordson EFD, East Providence, RI) was used as the DIW platform that can position the dispensing tip with $\pm$ 8 $\mu$m accuracy within the working space of 400 mm$^2$. A pressurize 3 cc syringe barrel (Nordson EFD, East Providence, RI) was used as the ink reservoir. A custom glass capillary pipette with 30 $\mu$m-diameter tip was fabricated using micropipette puller (Sutter Instrument, Novato, CA) to dispense microscale features. Here, an input pressure ranged from 10–40 psi, and the printing speed was varied from 1–5 mm/s. The biosensors were printed on either PDMS or LCP (Ultralam 3850, Rogers Corporation, Chandler, AZ, USA) substrate. PDMS was prepared by spin coating PDMS on a glass slide. The glass slide was pre-coated with 1 $\mu$m layer of Parylene C to promote device release. The biosensors were also printed on a 100-$\mu$m-thick LCP sheet. To complete the glutamate biosensor with good selectivity, Nafion and glutamate oxidase were deposited using a previously described method T. N. Nguyen et al. (2019a). After the enzyme immobilization, the samples were stored in room temperature for 48–72 h, and in 4 °C until testing.

### 3.2.4 Biosensor Evaluation

A field-emission scanning electron microscopy (FESEM, S-4800, Hitachi, Japan) was used to examine the physical structure and surface morphology of the C-Pt–PEDOT:PSS composite. Cyclic voltammographs (CV) and chronoamperometry measurements were obtained using a conventional three-electrode cell to evaluate the electrochemical characteristics of the fabricated biosensors. A commercial potentiostat (SP-200, Bio-logic USA, LLC, Knoxville, TN, USA) was used to perform all electrochemical analysis. All CV measurements were performed in the potential range of $-0.6$ – 0.8 V using the scan rate of 100 mV/s and the sampling interval of 1 mV/s. All amperometry data were obtained at 0.5 V vs. Ag/AgCl after 20 min of settling time with a 0.3 s sampling interval. The supporting electrolyte solution was 50 ml of 0.01 M PBS (pH 7.0) for all experiments unless stated otherwise. During the amperometry experiments, a stir bar was placed at 180 rpm in the electrolyte solution. A Faraday cage was used for reduce the background noise. The stability of our printed sensors were evaluated by comparing their glutamate sensitivity before and after 3 weeks of storage in 0.01 M PBS (pH 7.0) at 4 °C. Electrochemical impedance spectroscopy (EIS) was performed by deliver 10 mV sinusoid excitation voltage to the working electrode. The magnitude and phase of electrode impedance was measured from 10 to 100 kHz in 0.01 M PBS (pH 7.0). All current signal from amperometry experiments were normalized to specific surface area of tested electrodes.

### 3.2.5 Cell Cultures Preparation

Human cerebral cortex astrocytes were obtained from Sciencell (Carlsbad, CA). Astrocytes were cultured to near confluency (until the cell population grows to the point that cells nearly cover culture surface), and then removed from the culture plate by treatment with Trypsin-EDTA, centrifuged, and resupsended to $>$ 1 x 106 cells/mL. They were frozen in a medium containing DMSO in liquid nitrogen. Astrocytes were expanded and maintained per Sciencell′s protocol. Astrocytes were cultured in 12-well, tissue culture-treated plates, with $10^5$ cells seeded per well. These cultures were then incubated until confluency ($\sim$2 d) in a humidified atmosphere with 5 % $CO_2$ at 37 °C. The medium was replaced 1 d after seeding. Prior to the amperometric measurements, the cultures were washed twice with 0.01 M PBS (pH 7.0), and then placed in 1.5 ml of 0.01 M PBS (pH 7.0).

The glutamate biosensor was then lowered until its end touched the cell culture well surface, so the sensor electrode was $\sim$100 $\mu$m away and therefore about the same distance away from cultured astrocytes. We applied 0.5 V versus reference to the glutamate sensor and waited 20 min for the non-faradaic current to settle. Then, we added 0.5 ml of 0.9 mM glutamate ($n = 3$), resulting in a final concentration of 225 $\mu$M in 2 ml of 0.01 M PBS (pH 7.0). As a control, this same procedure was repeated in wells without cells ($n = 3$).

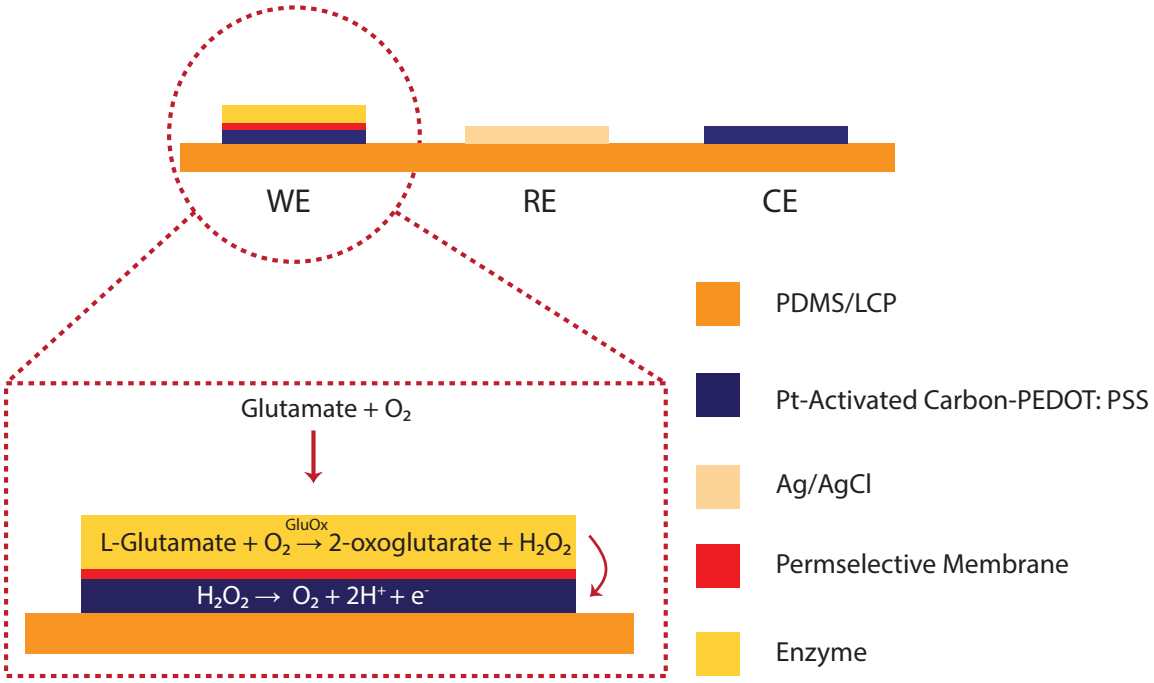


*Figure 3.1.* Cross-sectional view of the C-Pt–PEDOT:PSS based glutamate biosensor. The conventional three-electrode construction allows amperometric measurement of glutamate concentration continuously. Briefly, the glutamate oxidase converts glutamate into $H_2O_2$, which is then oxidized on the electrode surface to generate current. (Reprinted with permission from T. N. Nguyen et al. (2020). Copyright 2020 Elsevier)

### 3.2.6 Glutamate Consumption Measurement

Prior of each recording measurement, glutamate sensors were calibrated in 0.01 M PBS (pH 7.0) electrolyte solution to determine their baseline sensitivity. For glutamate consumption measurement, the glutamate biosensor, Ag/AgCl reference electrode, and Pt-wire counter electrode were placed in the culture well with astrocytes and 1.5 ml of 0.01 M PBS (pH 7.0). The glutamate

biosensor was oriented perpendicular to the cell culture well surface.

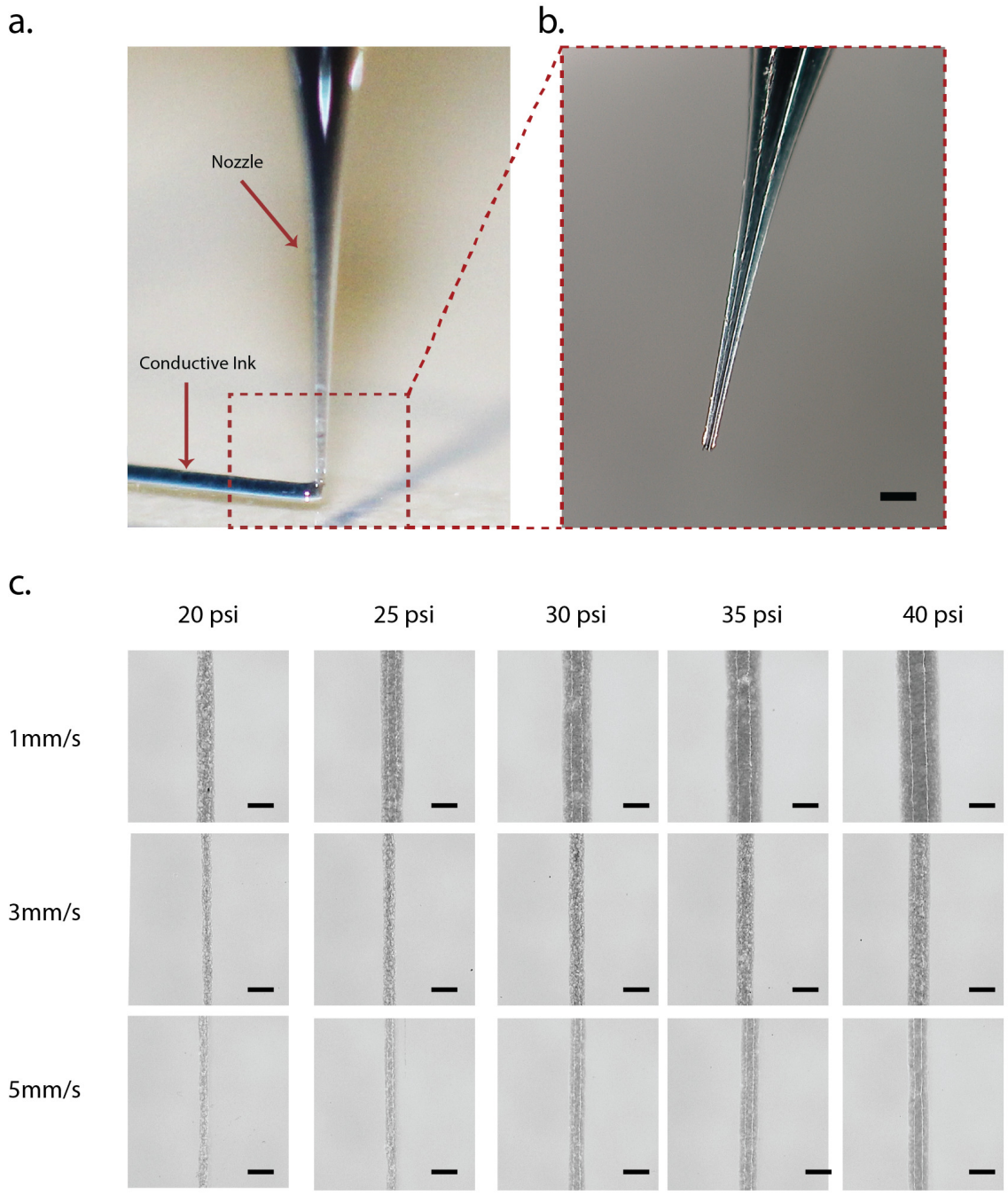


*Figure 3.2.* Resolution of our direct ink writing platform. (a–b) Photographs of a custom pulled-pipette dispensed tip (scale bar = 200 $\mu$m). (c) Photographs of dispensed of conductive ink at various speeds and pressures (scale bars = 100 $\mu$m., SI Table. 3.1). (Reprinted with permission from T. N. Nguyen et al. (2020). Copyright 2020 Elsevier)

### 3.2.7 Animal and Acute Brain Slice Experiments

All animal experiments were reviewed and approved by the Purdue University Animal Care and Use Committee. Brain slices preparation was followed as in previous study Wu et al. (2016). Male B6.Cg-Tg(Thy1-COP4/EYFP)18Gfng/J (Thy1-ChR2-YFP) mice of 3-4 months old from Jackson Lab were anesthetized by intraperitoneal injection with a mix of 90 mg/kg ketamine and 10 mg/kg xylazine. Trans-cardiac perfusion was carried out with oxygenated (carbogen from Airgas: 95% $O_2$, 5% $CO_2$) choline chloride artificial cerebrospinal fluid (choline chloride ACSF, composition in mM: 1.25 $NaH_2PO_4$, 25 $NaHCO_3$, 110 choline chloride, 10 dextrose, 2.5 KCl, 0.5 $CaCl_2$, 7 $MgCl_2$, 3.1 pyruvic acid, 11.6 ascorbic acid). The brain was dissected immediately after finishing perfusion. Once collected, the brain was shaped and fixed in the cutting chamber of the vibratome (Leica VT1000), which was filled with the ice-cold choline chloride ACSF and oxygenated continuously with carbogen flow. Three hundred micron thick coronal brain slices containing the visual cortex were collected and placed immediately to a 32 °C incubation chamber with oxygenated ACSF (composition in mM: 1.25 $NaH_2PO_4$, 26 $NaHCO_3$, 10 dextrose, 124 NaCl, 2.5 KCl, 2 $CaCl_2$, 0.8 $MgCl_2$) for at least 30 min. The brain slices were then placed at room temperature (25 °C) for at least 1 h before use.

### 3.2.8 Optogenetic Stimulation of Brain Slices

The Thy1-ChR2-YFP mice express a light-gated cations channel protein, channelrhodopsin-2 (ChR2) on the Layer V Thy1 positive pyramidal neurons of visual cortex. During the experiment, oxygenated ACSF was perfused over the slice at $\sim$1 ml/min. The working electrode was placed on the experiment platform underneath the brain slice for direct contact. Ag/AgCl and Pt wire were functioned as reference and counter electrode, respectively. The slice was kept in place by a slide hold-down to prevent movement of slice during the experiment. The focal blue light of 470 nm was shed on the layer V of the visual cortex of the brain slice through objective len of the microscope, which would stimulate influx of cations through ChR2 to depolarize the neurons. Depolarized presynaptic neurons would release glutamate to synaptic clefts and glutamate would perfuse to the sensor below the brain slice. The light-emitting diode (LED) source (8.1 mW, Mightex Toronto,

Ontario M3A) was controlled through its analog port using BioLED Analog and Digital I/O Control Module from the same company as the LED source. We applied light stimulation of 20 Hz, 5 ms in width, for 1 s every 15 s (Fig. 3.14d).

## 3.3 Results and discussion

According to literature, PEDOT:PSS exhibits superior electrical conductivity and chemical stability G. Yang, Kampstra, and Abidian (2014), as well as high degree of porosity to allow rapid ionic exchange between material and electrolyte surrounding environment Kergoat et al. (2014). In this study, a low-cost commercial C-Pt was utilized to improve the catalytic properties of the conductive ink. Pt is used widely in construction of many microscale electrochemical biosensors Govindarajan et al. (2013); Kergoat et al. (2014); T. N. Nguyen et al. (2019a). Activated carbon is also well-known for its porosity and high surface area that are advantageous as electrocatalytic/adsorbent material for oxidation of $H_2O_2$ Bach and Semiat (2011); Biniak, Swiatkowski, and Pakuła (2001); Harry Marsh and Rodríguez-Reinoso (2006). By using a commercially available C-Pt paste, we were able to create a highly sensitive electrode surface upon which to build our enzymatic glutamate biosensors. The resulting conductive ink can be processed using DIW with necessary flexibility that enabled us to rapidly prototype microscale glutamate biosensors. Fig. 3.1 shows the schematic of the printed C-Pt based glutamate biosensor.

### 3.3.1 Fabrication Results and Surface Characterization

We first characterized the resolution limit of our dispensing process to optimize our printing parameters. The dispensing pressure and the printing speed were varied with $\sim$30-$\mu$m-wide custom glass capillary dispensing tip to optimize the line width of the conductive polymer (Fig. 3.2a–b). Fig. 3.2c presents the resulting lines with different printing parameters. We were able to print lines as small as 35 $\mu$m by applying a higher writing speed with a lower pneumatic pressure (Table 3.1). The conductive traces made using C-Pt–PEDOT:PSS ink had high resistance (20–140 k$\Omega$) that prevented us from using the composite (Fig. 3.3-3.4). Thus, we modified PEDOT:PSS with MWCNT, which

significantly improved the conductivity (Fig. 3.5). For consistent fabrication of our biosensor, we kept the width of our conductive trace to be $\leq$100 $\mu$m. We also characterized the composites by EIS.

EIS measurements (Fig. 3.6a) show that the impedance of MWCNT-PEDOT:PSS electrodes was about 4.5 orders of magnitude lower than the impedance of C-Pt-PEDOT:PSS electrodes at 1 kHz. At 1 kHz, the impedances were 2.62 ± 0.88 k$\Omega$ and 12.02 ± 0.17 k$\Omega$ for MWCNT-PEDOT:PSS and C-Pt-PEDOT:PSS respectively. The results supported the choice of using MWCNT- PEDOT:PSS composite as the trace material over C-Pt-PEDOT:PSS composite.

Fig. 3.6b present additional data for estimated charge transfer resistance and double layer capacitance of the composites. C-Pt-PEDOT:PSS showed lower charge transfer resistances in comparing to MWCNT-PEDOT:PSS, which made it more appropriate to be used as working electrode material, and MWCNT-PEDOT:PSS as conductive trace material M. Ma, Liu, Shen, Kas, and Smith (2018); Olivé-Monllau, Esplandiu, Bartrolí, Baeza, and Céspedes (2010); A. Sun, Venkatesh, and Hall (2016). Figs. 3.7a–b show the printed glutamate biosensors. The diameter of the fabricated sensor surface was about 200 $\mu$m. The PDMS-based sensor was approximately 25-$\mu$m-thick. The thin-film device was highly compliant upon released and conformed well to the underlying surface, which highlighted the possibility of creating flexible and wearable sensor arrays using this approach Hsieh, Hsu, and Chen (2018). Fig. 3.7c presents another type of printed biosensor on a 100-$\mu$m-thick LCP substrate. This thin-film device was stiff enough to be vertically positioned into a cell culture plate or placed flat underneath brain slices.

Finally, we utilized FESEM to examine the surface morphology of the C-Pt–PEDOT:PSS composite (Figs. 3.7d–e). We saw that the polymer composite electrodes had rough and porous surface with Pt microparticles embedded in PEDOT:PSS. The rough surfaces have been shown to have greater catalytic activity for $H_2O_2$, thus corresponding to a higher sensitivity for amperometric oxidase-based biosensors S. C. Perry, Gateman, Sifakis, Pollegioni, and Mauzeroll (2018). In addition, the relative rough surface may help improve the response time and lower the limit of detection for enzymatic electrochemical biosensors S. C. Perry et al. (2018).

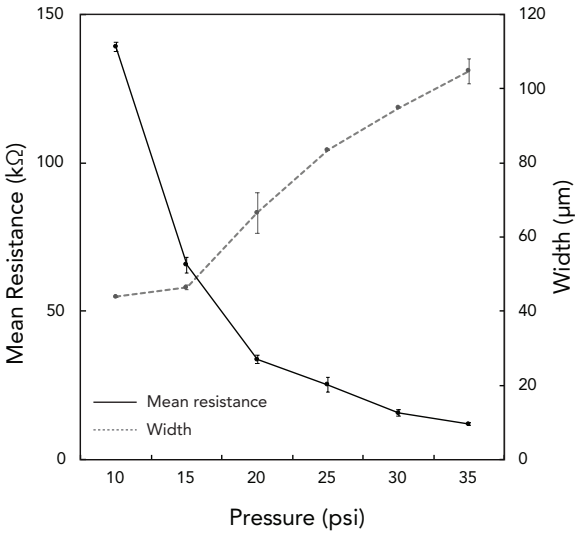


*Figure 3.3.* Results of the direct ink writing experiments with composite ink regarding the pressure variation and its impact on printing. The graph represents the width and the mean resistance of dispensed lines as function of pressure (n = 10). While the pressure was varied, the dispensed speed was kept at 1 mm/s for the entire experiment. The length of each dispensed lines was 10 mm. (Reprinted with permission from T. N. Nguyen et al. (2020). Copyright 2020 Elsevier)

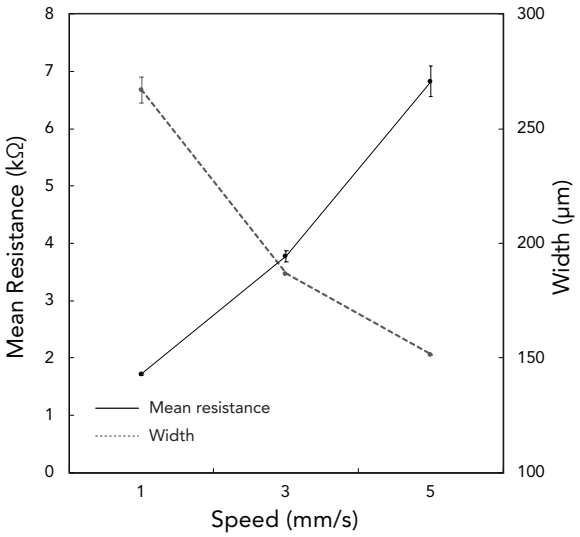


*Figure 3.4.* Results of the direct ink writing experiments with composite ink regarding the speed variation and its impact on printing. The graph represents the width and the mean resistance of dispensed lines as function of speed (n = 10). While the speed was varied, the dispensing pressure was kept at 40 psi for the entire experiment. The length of each dispensed line was 9 mm. (Reprinted with permission from T. N. Nguyen et al. (2020). Copyright 2020 Elsevier)

| | | Pressure (psi) | | | | | |
|---|---|---|---|---|---|---|---|
| | | 20 | 25 | 30 | 35 | 40 | |
| | **1** | 75.4 | 95.2 | 119.2 | 140.5 | 163.2 | |
| **Speed (mm/s)** | **3** | 34.3 | 48.5 | 62.6 | 75.3 | 82.5 | **Line width ($\mu$m)** |
| | **5** | 35.7 | 41.4 | 61.2 | 71.1 | 75.5 | |

*Table 3.1.* Width of dispensed lines as a function of different dispensing parameters. (Reprinted with permission from T. N. Nguyen et al. (2020). Copyright 2020 Elsevier).

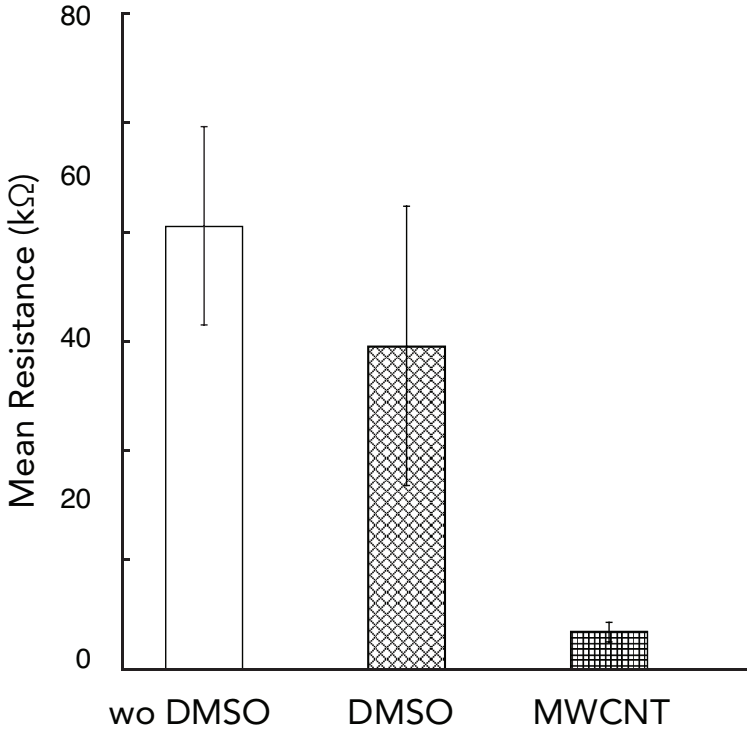


*Figure 3.5.* The mean resistance of different type of inks. The resistance of PEDOT:PSS ink embedded with MWCNT compared with PEDOT:PSS ink modified with DMSO and PEDOT:PSS ink without any modification. The dispensed speed was kept at 1 mm/s for the entire experiment. The length of each dispensed line was 10 mm. In this comparison, data includes all lines with dispensed pressure ranging from 10 to 45 psi for each individual ink type. (Reprinted with permission from T. N. Nguyen et al. (2020). Copyright 2020 Elsevier)

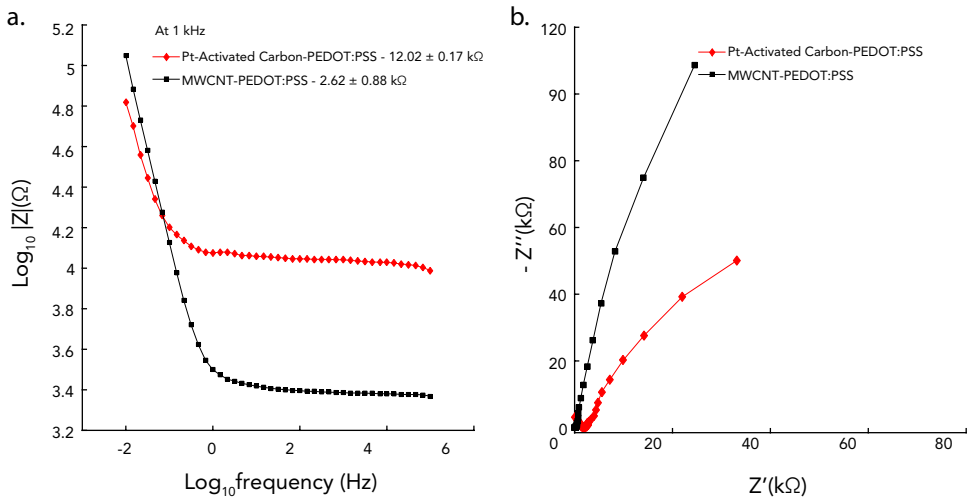


*Figure 3.6.* (a) Representative impedance spectra of the microelectrodes with two different types of materials, C-Pt-PEDOT:PSS and MWCNT-PEDOT:PSS. The impedance spectra of microelectrodes were tested in PBS (pH 7.0). (b) Nyquist plots of microelectrodes with two different types of materials, C-Pt-PEDOT:PSS and MWCNT-PEDOT:PSS. (Reprinted with permission from T. N. Nguyen et al. (2020). Copyright 2020 Elsevier)

### 3.3.2 Cyclic Voltammetry

Fig. 3.8a shows the CV of an activated C-Pt–PEDOT:PSS composite compared to PEDOT:PSS alone. An electrode made of PEDOT:PSS exhibited rectangular voltammogram because of its non-Faradaic charging current. It is a product of the conductivity of this polymer material and capacitive behavior between the electrode surface and 0.01 M PBS (pH 7.0) Gerwig et al. (2012). When PEDOT:PSS was modified with C-Pt, the voltammogram of electrode exhibited a much higher current density than PEDOT:PSS alone. As such, the electrochemical response of C-Pt–PEDOT:PSS composite electrode was expected to be superior than PEDOT:PSS electrode alone. The function of glutamate oxidase biosensor is based on the detection of enzymatically generated $H_2O_2$. The use of Pt together with carbon materials is known to enhance the detection of $H_2O_2$ Hrapovic, Liu, Male, and Luong (2004); Wen et al. (2009). Thus, we examined the electrocatalytic property of the Pt-C composite using cyclic voltammetry in both buffer and $H_2O_2$ solutions. Fig. 3.8b shows the CV of the C-Pt–PEDOT:PSS composite in different concentration of $H_2O_2$.

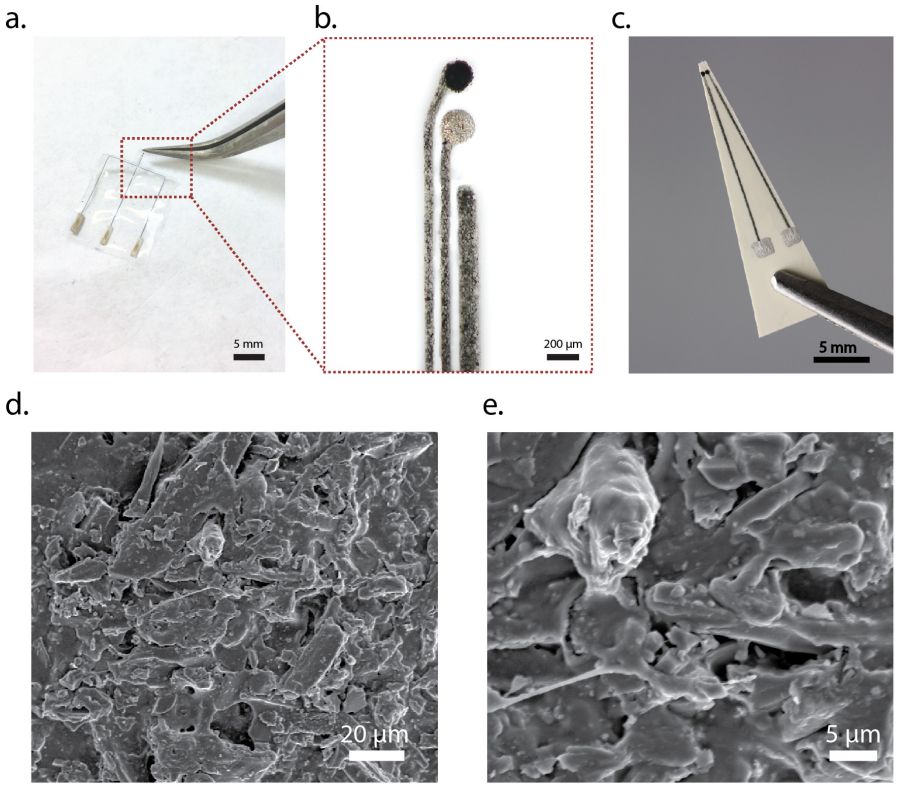


*Figure 3.7.* Printed glutamate biosensor. (a) A photograph of a fully-released glutamate biosensor printed on a PDMS substrate. (b) A close up view of the three electrodes (i.e., working, reference, and counter electrodes). (c) A photograph of a printed glutamate biosensor printed on an LCP substrate for recording with astrocyte cells. (d–e) Scanning electron micrographs of C-Pt–PEDOT:PSS composite at different magnifications. (Reprinted with permission from T. N. Nguyen et al. (2020). Copyright 2020 Elsevier)

The C-Pt–PEDOT:PSS electrode exhibited good electrocatalytic activity against $H_2O_2$, which suggests that these electrodes could serve as a first generation electrochemical platform for detection of glutamate via oxidase-based mechanism. Electrochemical behavior of $H_2O_2$ starts at around 0.1 V and can go up of 0.7 V vs. Ag/AgCl in the positive direction. In this case, an oxidation wave starts to display at around 0.2 V with increasing current due to addition of $H_2O_2$. At 0.5 V, the difference in current between 100 $\mu$M and 1000 $\mu$M of $H_2O_2$ is reaching its peak. Therefore, we selected 0.5 V as the potential for glutamate detection.

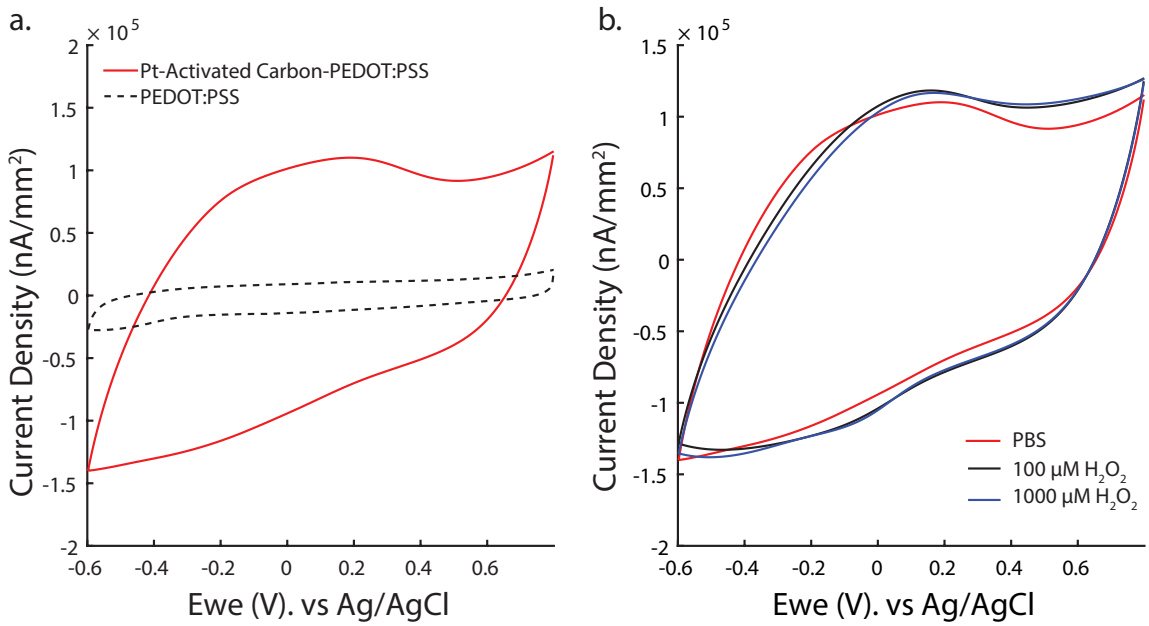


*Figure 3.8.* (a) Cyclic voltammetry of C-Pt–PEDOT:PSS compare to PEDOT:PSS alone in 0.01 M PBS (pH 7.0). Scan rate = 100 mV $s^{-1}$. Note that the C-Pt–PEDOT:PSS exhibited higher catalytic activity compared to PEDOT:PSS alone. (b) Cyclic voltammetry of C-Pt–PEDOT:PSS composite in 0.01 M PBS (pH 7.0), 100 $\mu$M and 1000 $\mu$M $H_2O_2$. Scan rate = 100 mV $s^{-1}$. (Reprinted with permission from T. N. Nguyen et al. (2020). Copyright 2020 Elsevier)

### 3.3.3 Amperometric Responses of the Glutamate Biosensor

Fig 3.9a shows the *i-t* responses of C-Pt–PEDOT:PSS composite sensors against $H_2O_2$ and glutamate. The calibration plot (Fig. 3.9d) shows that C-Pt–PEDOT:PSS composite had a linear response with a sensitivity of 5.73 $\pm$ 0.08 nA $\mu M^{-1}$ $mm^{-2}$ ($n = 3$) for glutamate and 15.17 $\pm$ 0.12 nA $\mu M^{-1}$ $mm^{-2}$ for $H_2O_2$ ($n = 3$). As a comparison, we also utilized MEMS-fabricated Pt microelectrodes (50-$\mu$m-diameter) as glutamate biosensors and characterized their performance. We immobilized glutamate oxidase and Nafion on e-beam evaporated microscale Pt-disc. Fig 3.9c-d shows the amperometric responses and the calibration curve of the MEMS glutamate biosensor against $H_2O_2$ and glutamate. The MEMS biosensor had a sensitivity of 2.07 $\pm$ 0.02 nA $\mu M^{-1}$ $mm^{-2}$ ($n = 3$) for glutamate and 6.28 nA $\mu M^{-1}$ $mm^{-2}$ $\pm$ 0.51 for $H_2O_2$ ($n = 3$).

Additionally, we examined the dynamic range of our printed biosensors with successive addition of glutamate from 1 $\mu$M to 2000 $\mu$M (Fig. 3.9e). We found that our C-Pt–PEDOT:PSS composite biosensor exhibited a linear range from 1 $\mu$M and 925 $\mu$M ($R^2$ = 0.996) at 0.5 V vs. Ag/AgCl (Fig. 3.9f). The detection limit was 0.03 $\pm$ 0.003 $\mu$M ($n = 3$), and the response time $\leq$ 1 s. Thus, we concluded that our C-Pt-based printed glutamate biosensor has high sensitivity, good linearity, low detection limit and fast response time as comparing to the MEMS biosensor as well as previously reported glutamate biosensors (Table 3.4).

The printed glutamate biosensors showed 65% higher sensitivity compared to the MEMS-fabricated glutamate biosensor. These results are encouraging because they demonstrate the possibility of fabricating high-quality biosensor using commercially available low-cost materials and direct-writing technology. For small-batch fabrication, this approach would be more economical and efficient than conventional microfabrication techniques. Furthermore, we may be able to increase the sensitivity of these rapid prototyped biosensors using C-Pt matrix with higher Pt composition (i.e., $> 1\%$).

### 3.3.4 Biosensor Specificity and Stability

Although enzymes are well-known for their specificity, oxidase biosensors are often affected by non-specific signals from electroactive species present in the milieu. For example, ascorbic acid (AA), uric acid (UA), and acetaminophen (AC) are often found in cell culture media and in the body, and they can be oxidized at the electrode surface. To improve our biosensor specificity, we used Nafion as a permselective membrane. Fig. 3.11a shows that our biosensor can effectively block signals from AA (100 $\mu$M) and UA (100 $\mu$M) without affecting glutamate sensitivity. However, we were not able to block the signal from AC (100 $\mu$M). We tested the selectivity of our glutamate biosensors against 3,4-Dihydroxyphenylacetic acid (DOPAC) and 5-hydroxyindoleacetic acid (5-HIAA). A 0.5 % Nafion layer deposited at room temperature was able to block ascorbic acid and uric acid (Figure 6), however, it was not able to block DOPAC and 5-HIAA. Therefore, we tried to anneal 5 % Nafion at 160-170$^\circ$ for 4 min to test its ability to block DOPAC and 5-HIAA (Fig. 3.10). The annealing Nafion was able to effectively block DOPAC and 5-HIAA, however, the current density response of this biosensor to 200 $\mu$M of glutamate dropped about 68% compared to the non-annealed biosensor. In

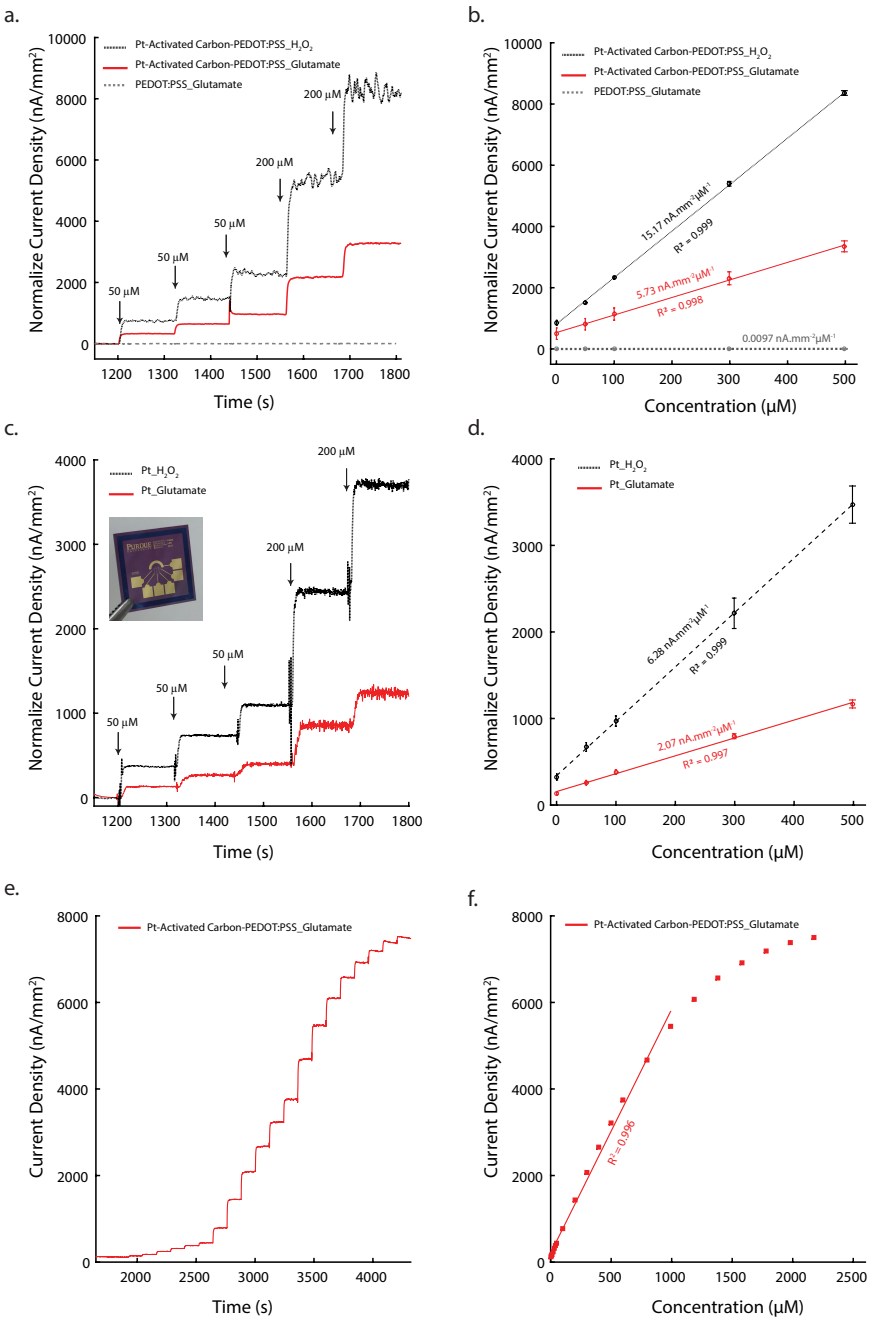


*Figure 3.9.* (a) Representative amperometric curves for C-Pt–PEDOT:PSS and PEDOT:PSS in 0.01 M PBS to glutamate and $H_2O_2$ ($n = 3$, each). (b) The corresponding calibration curves and the sensitivity of each glutamate biosensor materials to glutamate and $H_2O_2$ ($n = 3$, each). (c) Representative amperometric curves for MEMS–fabricated biosensors in 0.01 M PBS (pH 7.0) to glutamate and $H_2O_2$ ($n = 3$, each). Inset: a photograph of a MEMS glutamate biosensor. (d) The corresponding calibration curves and the sensitivity of MEMS–fabricated sensor to glutamate and $H_2O_2$ ($n = 3$, each). (e) An amperometric curve of C-Pt–PEDOT:PSS to large range of different concentrations of glutamate in 0.01 M PBS (pH 7.0) solution. (f) The corresponding calibration curve for C-Pt–PEDOT:PSS biosensor to glutamate up to 925 $\mu$M ($R^2 = 0.996$). (Reprinted with permission from T. N. Nguyen et al. (2020). Copyright 2020 Elsevier)

the future, we would like to further address this issue by using a different type of permselective membrane such as o-aminophenol or m-phenylenediamine dihydrochloride. We also measured the stability of our glutamate biosensors by quantifying the change in their sensitivities before and after storage at 4 °C in 0.01 M PBS (pH 7.0) for 3 weeks. The *i-t* responses and calibration curves of our glutamate biosensors before and after the storage period were presented in Figs. 3.11b and 3.11c. When the sensors were refrigerated, they retained 97.9 % of their initial sensitivities ($n = 3$).

### 3.3.5 Experiments to test the reusability of the C-Pt-PEDOT:PSS composite glutamate biosensors

We also characterized the reusability of our glutamate biosensor by quantifying the change in their sensitivities before and after bending 100 times and 1000 times (Figs. 3.12). The conductive traces of our C-Pt–PEDOT:PSS composite glutamate biosensors were made by MWCNT-PEDOT:PSS composite, which was modified by Ecoflex (Methods: Ink preparation). This modification increased the reusability of the biosensor even after multiple bending cycles. Fig. 3.12 presents the photographs of the flexible glutamate biosensor at non-bending position and bending on the surface at an angle of ¿ $45^o$. The amperometry experiments were run in both normal, non-bending condition, and after bending for 100 times and 1000 times to compare the functionality of the glutamate composite biosensors. The glutamate biosensors had average sensitivity of 5.08 $\pm$ 0.69 nA $\mu$M$^{-1}$ mm$^{-2}$ (n = 3) before bending process. After bending for 100 times, the sensitivity was 5.20 $\pm$ 0.62 nA $\mu$M$^{-1}$ mm$^{-2}$ (n = 3), which is $\sim$2.5 % compare to the original value. After bending for 1000 times, the sensitivities were 5.43 ± 0.8 nA $\mu$M$^{-1}$ mm$^{-2}$ (n = 3), which is $\sim$6 % compare to the original value.

### 3.3.6 Experiments to test the durability of the C-Pt–PEDOT:PSS composite glutamate biosensors

In order to test the durability of the C-Pt–PEDOT:PSS composite glutamate biosensors, we tested the sensors multiple times and compared the sensitivities of the sensors after each experiment (n = 3). Fig. 3.13 demonstrates the amperometric responses and calibration curves of the glutamate biosensors. Table 3.2 represents the sensitivities of glutamate biosensors for three devices. The average sensitivities after 8 runs were 5.11 $\pm$ 0.21 $\mu$M$^{-1}$ mm$^{-2}$, 5.96 $\pm$ 0.15 $\mu$M$^{-1}$ mm$^{-2}$and 4.65

$\pm$ 0.21 $\mu M^{-1}$ $mm^{-2}$ for device 1, device 2 and device 3, respectively. Overall, there was about 3 % change in sensitivities between runs. Additional evaluations are required to determine how well these enzymatic biosensors can maintain functionality *in vitro* and *in vivo*.

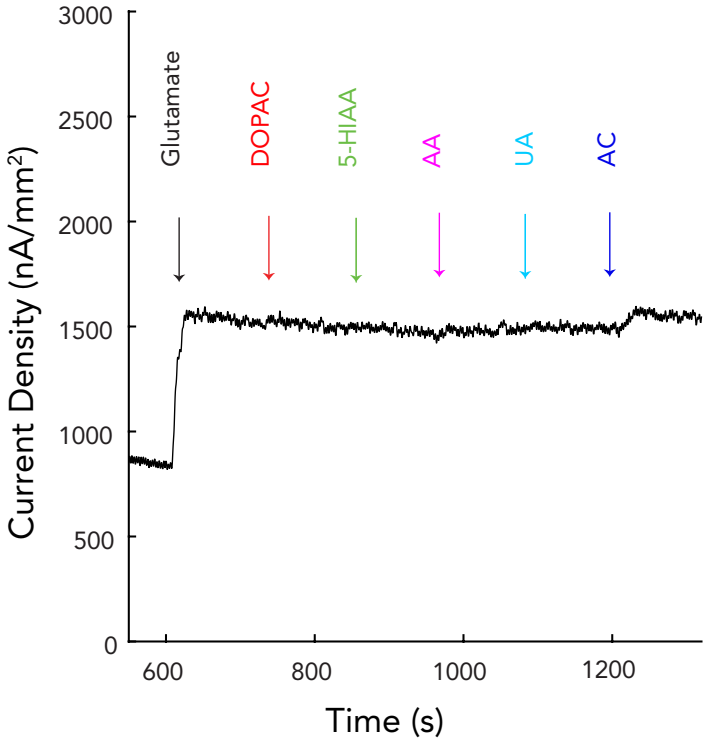


*Figure 3.10.* A response of C-Pt-PEDOT:PSS composite biosensor using annealing Nafion as permselective membrane upon sequential addition of 200 $\mu$M glutamate, 100 $\mu$M of DOPAC, 100 $\mu$M of 5-HIAA, 100 $\mu$M of AA, 100 $\mu$M of UA and 100 $\mu$M of AC into constantly stirred 0.01 M PBS (pH 7.0) solution. (Reprinted with permission from T. N. Nguyen et al. (2020). Copyright 2020 Elsevier)

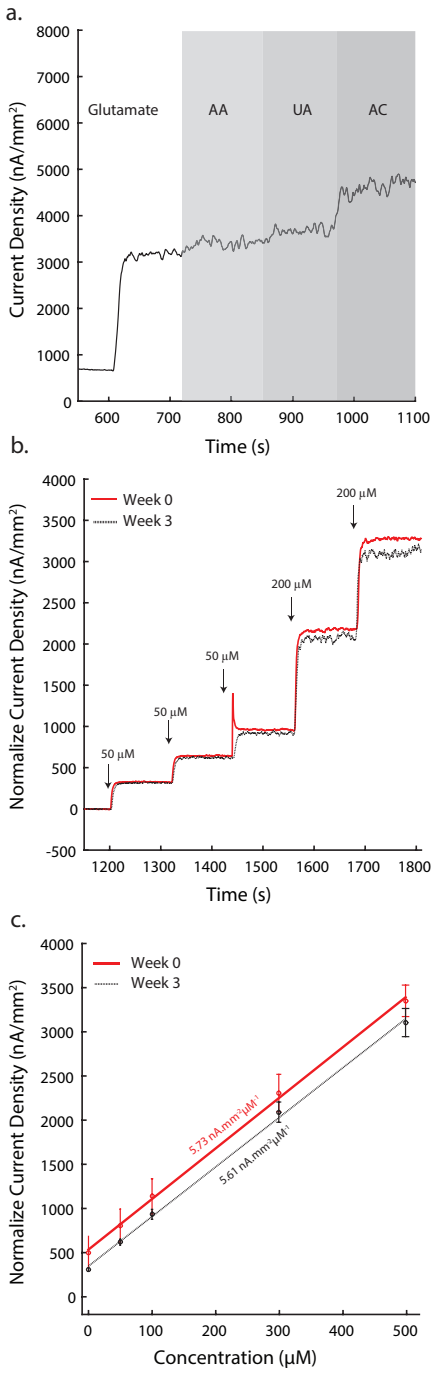


*Figure 3.11.* (a) A response of C-Pt–PEDOT:PSS composite upon sequential addition of 200 $\mu$M glutamate, 100 $\mu$M of AA, 100 $\mu$M of UA and 100 $\mu$M of AC into constantly stirred 0.01 M PBS (pH 7.0) solution. (b) An amperometric response of different concentrations of glutamate in 0.01 M PBS solution (pH 7.0) of C-Pt–PEDOT:PSS composite before and after 3 weeks of storage ($n = 3$). (c) The corresponding calibration curve and sensitivity of C-Pt–PEDOT:PSS composite before and after 3 weeks of storage ($n = 3$). (Reprinted with permission from T. N. Nguyen et al. (2020). Copyright 2020 Elsevier)

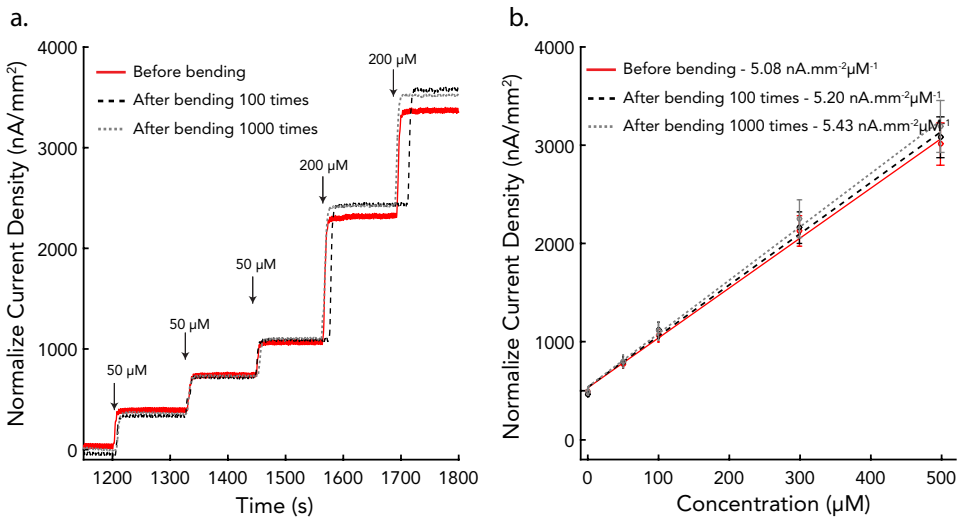


*Figure 3.12.* (a) Amperometric curves for C-Pt–PEDOT:PSS glutamate composite biosensors at applied potential of 0.5 V vs. Ag/AgCl in 0.01 M PBS (pH 7.0) to various concentrations of glutamate in none-bending condition and after bending 100 times and 1000 times. (b) The corresponding calibration curves and the sensitivities of glutamate biosensors in none-bending condition and after bending 100 times and 1000 times. (Reprinted with permission from T. N. Nguyen et al. (2020). Copyright 2020 Elsevier)

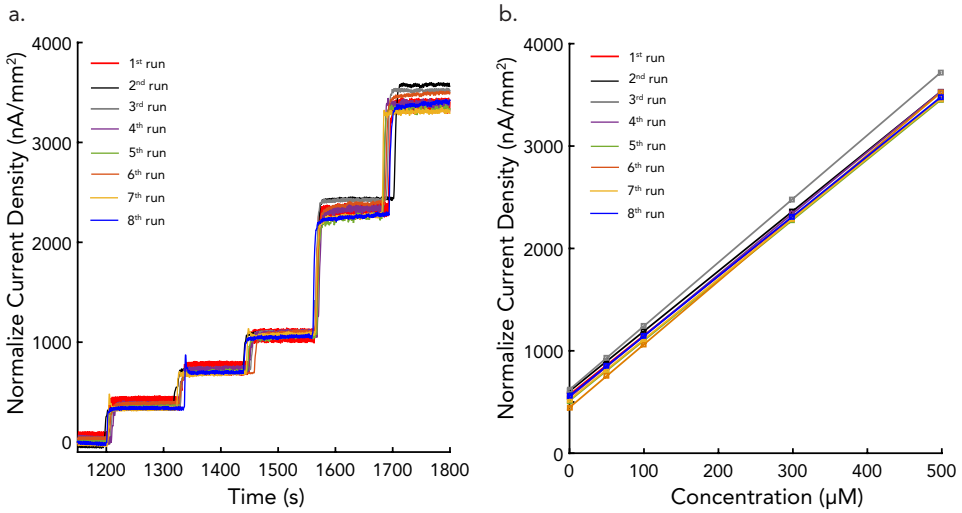


*Figure 3.13.* (a) Representative of amperometric curves for C-Pt-PEDOT:PSS composite glutamate biosensors at applied potential of 0.5 V vs. Ag/AgCl in 0.01 M PBS (pH 7.0) to various concentrations of glutamate at multiple runs. (b) Representative of the corresponding calibration curves of glutamate biosensors at multiple runs. (Reprinted with permission from T. N. Nguyen et al. (2020). Copyright 2020 Elsevier)

*Table 3.2.* Summary the sensitivity of each device after each run. (Reprinted with permission from T. N. Nguyen et al. (2020). Copyright 2020 Elsevier).

| | | **$1^{st}$ run** | **$2^{nd}$ run** | **$3^{rd}$ run** | **$4^{th}$ run** | **$5^{th}$ run** | **$6^{th}$ run** | **$7^{th}$ run** | **$8^{th}$ run** |
|---|---|---|---|---|---|---|---|---|---|
| **Sensitivity (nA $\mu$M$^{-1}$ mm$^{-2}$)** | **Device 1** | 5.07 | 5.13 | 5.49 | 5.13 | 4.73 | 4.98 | 5.28 | 5.1 |
| | **Device 2** | 5.79 | 5.87 | 6.21 | 5.99 | 5.89 | 6.17 | 5.9 | 5.85 |
| | **Device 3** | 4.39 | 4.63 | 4.61 | 4.95 | 4.93 | 4.53 | 4.44 | 4.76 |

### 3.3.7 Measuring Glutamate Uptake from Astrocytes

To further demonstrate the sensor functionality, we measured changes in glutamate concentration using primary human astrocyte culture. Fig. 3.14a shows our printed glutamate biosensor in astrocyte culture $\sim$100 $\mu$M away. When a bolus of glutamate (225 $\mu$M) is added, the biosensor responded rapidly with a current spike, which ultimately settled in about 10 min (Fig. 3.14b). The glutamate concentration was estimated to be about 125 $\mu$M after 10 min in astrocyte culture, which is likely due to glutamate consumption by astrocytes (Fig. 3.14c) at the density of electrode surface. Measurements from the astrocytes had greater standard deviation than the control, which may be due to different levels of cell density at the time of experiment.

One of the limitations of using a single channel biosensor is that it is not possible to ascertain concentration gradient of the analyte. In the future, we may be able to further elucidate on the characteristics of astrocyte-mediated glutamate concentration gradient by printing a linear array of glutamate biosensors and measuring at specific distances simultaneously. The measurement from biosensor array may be useful for quantifying the relationship between the glutamate concentration at the cell surface and the glutamate uptake rate McLamore et al. (2010); Rivera et al. (2018); Sridharan et al. (2018).

### 3.3.8 Measuring Glutamate Release from Mouse Visual Cortex by Optogenetic Stimulation

To further demonstrate the potential use of these biosensors for real-time biological applications, we measured glutamate from optogenetic-induced release in mouse brain slices. Working electrodes were calibrated before and after tissue experiments. Extracellular glutamate changes were quantified during light activation at visual cortex in mice. Light pulses of 5 ms width were applied as described in method section (Fig. 3.14d), 1 s duration every 15 s at 20 Hz. Fig. 3.14e shows a representative of precise optical control of glutamate release. There were pronounced increase in peak current density right after the stimulation. Furthermore, the temporal dynamic of glutamate release in this stimulation was very robust with less than 1s after each stimulation. The dashed red lines in Fig. 3.14e indicated where stimulations were applied. The peak current density per $mm^2$ was average over 40 trials of light stimulation in three samples, indicated average concentration recorded per stimulation was $11.43 \pm 2.00$ $\mu$M ($n = 3$). The results suggest that the ChR2-control of glutamate release was robust and can be successfully measured by using the C-Pt glutamate biosensor.

## 3.4 Conclusion

In this work, we presented a simple manufacturing technique for creating a highly sensitivity glutamate biosensors using low-cost C-Pt–PEDOT:PSS composite ink. The biosensor can be rapidly prototyped using DIW on various substrate. The printed biosensors performed better than MEMS-fabricated and Pt nanoparticle-based glutamate biosensors in terms of their sensitivity. The sensor had high sensitivity of $5.73 \pm 0.08$ nA $\mu M^{-1}$ $mm^{-2}$, a good linear range from 1 $\mu$M up to 925 $\mu$M ($R^2$ = 0.996), a low detection limit of with 0.03 $\mu$M, and a fast response time $\leq$ 1 s. Furthermore, our sensor demonstrated good specificity for glutamate when tested against AA and UA. Additional work is needed to optimize permselective layer to prevent oxidation of AC. In the future, we plan to perform additional experiments to better quantify the dynamic extracellular glutamate concentration in various *in vitro* and *in vivo* models. Furthermore, we plan to apply the similar fabrication techniques for other sensing applications using different recognition elements.

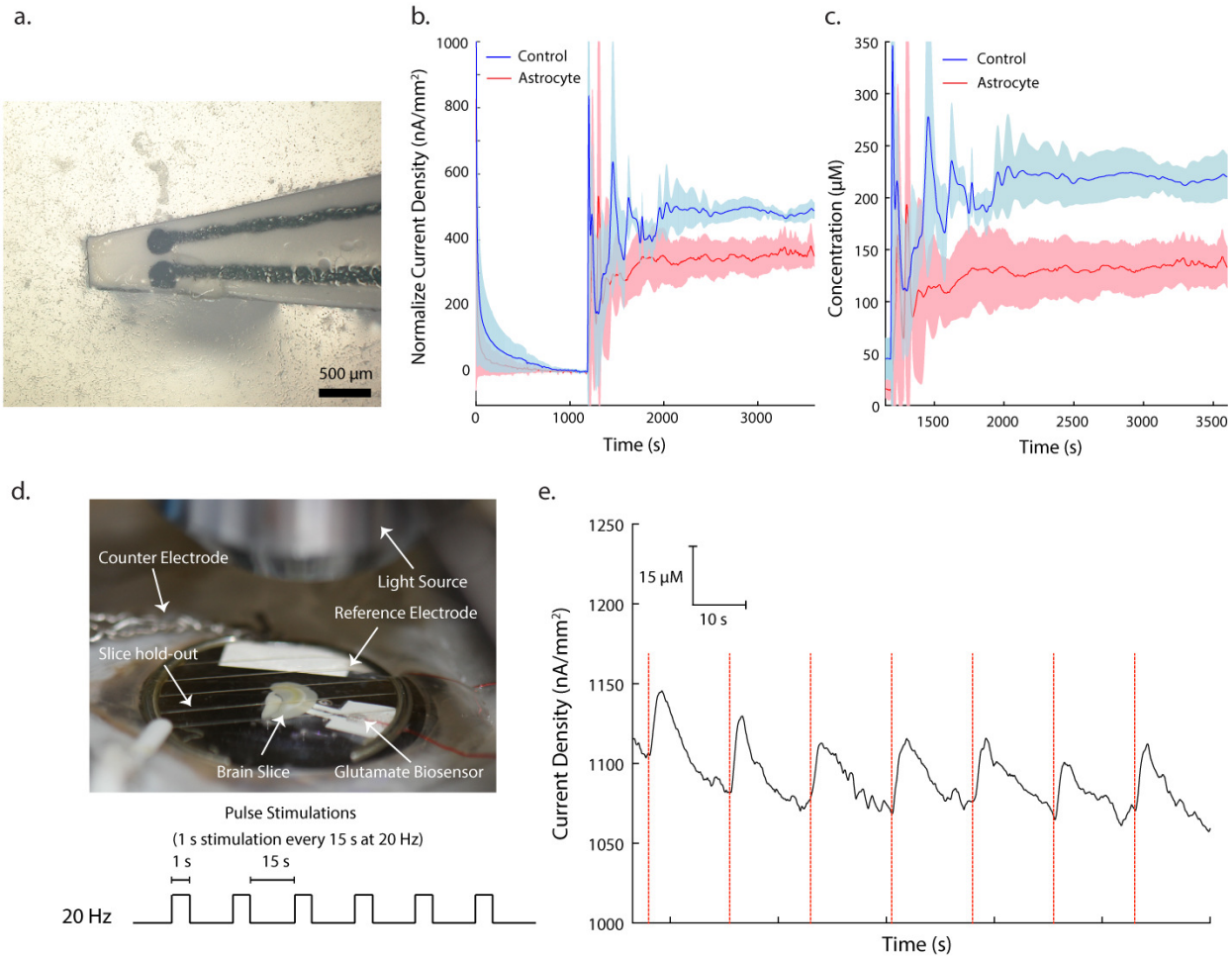


*Figure 3.14.* (a) A photograph of glutamate biosensor (foreground) over an astrocyte cell culture (background). (b) Measurement of glutamate consumption by astrocyte cells. Blue: mean current response 100 $\mu$m from the surface of culture well following addition of 225 $\mu$M glutamate without astrocytes (control, n = 3). The blue shading indicates the standard deviation of the three samples. Red: mean current response 100 $\mu$m from the surface of culture well following addition of 225 $\mu$M glutamate into the astrocyte cell culture. The red shading indicates the standard deviation of three measurements with astrocytes. (c) Estimated glutamate concentration during the glutamate consumption experiments with and without astrocytes. (d). Optogenetic-induced glutamate release setup using a visual cortex brain slice from a mouse (top). Light pulses of 5ms width,1s duration every 15 s at 20 Hz (bottom). (e) Representative of an *ex vivo* light-induced glutamate sensing curve. The dashed red lines indicated the time when stimulations were applied. (Reprinted with permission from T. N. Nguyen et al. (2020). Copyright 2020 Elsevier)

*Table 3.3.* Different methods for in vivo measurement of glutamate. (Reprinted with permission from T. N. Nguyen et al. (2019a). Copyright 2020 Elsevier)

| Method | Temporal resolution | Spatial resolution | Detection limit | Additional quantification method/requirement | Reference |
|---|---|---|---|---|---|
| Microdialysis | >minutes | $\geq 0.6\,mm^2$ | $\sim 1\,\mu M$ | High Performance Liquid Chromatography | Cifuentes Castro et al. (2014b); van der Zeyden, Oldenziel, Rea, Cremers, and Westerink (2008); Weltin et al. (2016) |
| Nuclear magnetic resonance spectroscopy | >minutes | $mm^3$(non-invasive) | ~mM | Large equipment | Behar and Rothman (2001); Ramadan et al. (2013) |
| Positron emission tomography | seconds to minutes | $mm^3$ (non-invasive) | $<1\,\mu M$ | Large equipment | Kagedal et al. (2013); Muehllehner and Karp (2006) |
| Optical sensors | ms | $<100$ nm | $<1$ nM | Optical access | Issberner, Schauer, Trimmer, and Walt (2002); Pospíšilová, Kuncová, and Trögl (2015) |
| Electrochemical microsensor | $\leq 1$ s | $<100\,\mu m$ | $<0.1\,\mu M$ | N/A | Salazar, Martín, O'Neill, and González-Mora (2016); T. T. C. Tseng and Monbouquette (2012); Weltin et al. (2014) |



*Table 3.4.* Different type of glutamate biosensors. (Reprinted with permission from T. N. Nguyen et al. (2020). Copyright 2020 Elsevier)

| Type of electrode | Fabrication method | Sensitivity (nA $\mu M^{-1}\,mm^{-2}$) | Limit of detection ($\mu M$) | Response time (s) | Linear range ($\mu M$) | Flexibility | Estimated cost | Reference |
|---|---|---|---|---|---|---|---|---|
| Pt | Commercial Pt wire | 0.85 | 0.7 | 2 | 200 | N/A | | M. Zhang et al. (2006) |
| Carbon fiber | Commercial carbon fiber | 1.35 | <2 | N/A | 150 | N/A | | Salazar, Martín, O'Neill, and González-Mora (2016) |
| Polyimide base/Pt | MEMS | 2.16 | 0.22 | 5 | 150 | Flexible (base only) | | Weltin et al. (2014) |
| Silicon/Pt | MEMS | 2.07 | 0.12 | 3 | N/A | Rigid | | This study |
| Pt/MWCNT | Electrodeposition | 3.84 | 0.3 | 7 | 0-150 | Rigid | | Ammam and Fransaer (2010) |
| Screen-printed/CNT | Commercial screen-printed | 0.057 | 0.01 | 5 | 0.01-10 | Rigid | | Khan, Gorski, and Garcia (2011) |
| Pt-C-PEDOT:PSS | Direct ink writing | 5.73 | 0.03 | $\leq 1$ | 1-925 | Flexible | | This study |

# CHAPTER 4. *IN VIVO* GLUTAMATE SENSING INSIDE THE MOUSE BRAIN WITH PEROVSKITE NICKELATE-NAFION HETEROSTRUCTURES

## 4.1 Introduction

Perovskite oxides (formula of $ABO_3$) are an important materials family with a diverse range of physical properties and functionalities of interest to multiple disciplines in science and engineering. Among this class, rare-earth nickelates ($RNiO_3$ (RNO)), where R represents rare-earth lanthanide elements, have attracted significant interest in the fields of electronics, catalysis, and energy Catalano et al. (2018); Scherwitzl et al. (2010); L. Wang et al. (2018). Perovskite nickelates are strongly correlated systems with electronic properties highly sensitive to the microstructure, strain, and defects Catalan (2008); Middey et al. (2016). The ground state at room or body temperature can be insulating or metallic depending on the steric effect due to the A-site cation, for instance, $NdNiO_3$ is a correlated metal at room temperature Alsaqqa et al. (2017); Catalan, Bowman, and Gregg (2000); Hauser et al. (2015). The highly tunable electronic properties of nickelates have served as motivation to exploit them as electrocatalysts in energy technologies L. Wang et al. (2019) and bio-sensors H. T. Zhang et al. (2019). There exists a great need for bio-sensing inside brain tissue in living animals for *in vivo* measurements of neurotransmitters. Advancing *in vivo* techniques to monitor neurotransmitter release in the brain is of great interest and significance to neuroscience, disease therapy, and bio-engineering fields, because these neurotransmitters play an essential role in critical brain functions such as information transmission, learning and memory Behar and Rothman (2001); D. Liu, Thangnipon, and McAdoo (1991); Okumoto et al. (2005); Weltin et al. (2016).

Furthermore, neurotransmission is known to be impaired in neurodegenerative disorders such as Parkinson's and Alzheimer's Disease Shen (2010). However, the precise measurements of neurotransmitters in the studies of these disorders are often lacking. Current technologies are being used to measure glutamate such as high-performance liquid chromatography, gas chromatography,

mass spectrometry, and microdialysis. While these techniques result in a high level of accuracy, they require external analysis, and longer measurement time Bouatra et al. (2013); Moraes et al. (2012); Schultz, Uddin, Singh, and Howlader (2020). On the other hand, genetically encoded glutamate sensors require genetic modification of the target cells. Thus, electrochemical sensors are well-suited for *in vivo* measurements, in which direct and continuous measurements in deep brain tissue can be carried out without the need for artificial labels or gene therapy Burmeister et al. (2013, 2020); Y. Wang et al. (2019); Wassum et al. (2012). Indeed, benchtop experiments exploring oxide electrodes for sensing of bio-molecules have been reported B. Wang et al. (2013); L. Wang et al. (2017). However, multiple disciplines across natural sciences and engineering have to be brought together and numerous hurdles crossed to go from material-level sensing experiments to their use in implanted electrode devices for *in vivo* brain recording from live animals.

In recent years, several candidates for amperometric glutamate biosensors have been developed such as noble metals (e.g., Pt, Au, Pd Lowry and O'Neill (1994); O'Neill, Chang, Lowry, and McNeil (2004)), glassy carbon, carbon fiber or carbon nanotubes (CNTs Ammam and Fransaer (2010); Huffman and Venton (2009)), polymersRahman, Kwon, Won, Choe, and Shim (2005), binary metal oxides (e.g., $TiO_2$ and $CeO_2$ Dalkıran, Erden, and Kılıç (2017); Özel, Ispas, Ganesana, Leiter, and Andreescu (2014)) and perovskite oxides (e.g., titanates) Dai et al. (2018); L. Wang et al. (2017). Additionally, several studies have been presented for implantation of glutamate sensors into brain matter for real-time recording Mattinson et al. (2011); Rutherford, Pomerleau, Huettl, Strömberg, and Gerhardt (2007); Y. Wang et al. (2019); Wassum et al. (2012). However, improving both response time scale and detection limit simultaneously motivates the discovery of new platforms for sensing. We report such a biosensor using a cross-linking immobilizing method with nafion-coated perovskite nickelate thin films. Glutamate oxidase (GluOx), an enzyme that metabolizes glutamate and releases $H_2O_2$, was immobilized on nafion-coated NNO film. The as-generated $H_2O_2$ molecules penetrate through the nafion and released protons and electrons catalyzed by NNO film. The released charge carriers were monitored using a three-electrode setup amperometrically. Here, for the first time, we present experimental demonstration of fast detection of low concentration (nM range) of the glutamate in phosphate buffer saline (PBS) using benchtop measurements, followed by *ex vivo* in mouse brain slices and *in vivo* in awake head-fixed mice using a correlated material system of perovskite nickelate (i.e., $NdNiO_3$ (NNO)) heterostructured with nafion, a polymeric ion-permeable membrane.

## 4.2 Methods

### 4.2.1 Fabrication of $NdNiO_3$ (NNO)/Nafion/Enzyme heterostructures

4.2.1.1 $NdNiO_3$ film deposition: Perovskite nickelate $NdNiO_3$ (NNO) thin films were grown on single crystal (001) $LaAlO_3$ (LAO) substrates (MTI corp) using a AJA UHV magnetron sputtering at room temperature. All substrates were rinsed by toluene, acetone, and isopropanol, and dried with high purity $N_2$ before deposition. The optimized growth condition was calibrated using Phenom SEM equipped with energy-dispersive X-ray spectroscopy (EDS). The deposition gas atmosphere is mixture of 40/10 sccm $Ar/O_2$ at total deposition background pressure of 5 mTorr. Two metallic Ni (DC, 66W) and Nd (RF, 145W) targets were used for deposition. The film growth rate is $\sim$ 2.5 nm per minute. After deposition, the samples were treated by post-annealing in air at 500 °C for 24 h in a tube furnace with ramping and cooling rate of 1.5 °C $min^{-1}$. Films with thickness of $\sim$50 nm were used in this work.

4.2.1.2 Nafion coating synthesis Perovskite nickelate $NdNiO_3$ (NNO) thin films were used as a working electrode for neurotransmitter detection. The films were connected using magnetic wire (34 AWG, Digi-Key Corp, MN) by silver paste. The contact was insulated using polydimethylsiloxane (PDMS) leaving only the working area open for electrochemical activity. The thin-film electrode was then coated with a thin layer of Nafion as permselective membrane to improve selectivity for glutamate over other interferences such as ascorbic acid (AA), acetaminophen (AC) and uric acid (UA). Prior to coating, thin-film electrodes were baked at 175 °C for 4 minutes to remove any moisture. They were then removed from oven and lowered into the amber vial containing Nafion solution, such that the recording sites were submerged in the solution. The films were rotated in a circular motion 5 times ($\sim$ 1 s per rotation). The films were removed from the Nafion solution and baked at 175 °C for 4 minutes. They were removed from the oven and cooled down for at least 10 min at room temperature before coating with GluOx enzyme for glutamate sensing.

4.2.1.3 Enzyme immobilization After Nafion coating, the films were functioned with glutamate oxidase (GluOx), bovine serum albumin (BSA) and glutaraldehyde protein matrix. BSA (2.5 %) and glutaraldehyde (0.4 %) were added to the microcentrifuge tube containing glutamate oxidase (500 U/ml). The solution was mixed by centrifuging for 30 s. The resulting solution was 1 % BSA, 0.15 % glutaraldehyde and 100 U/ml GluOx. GluOx was crosslinked with BSA and glutaraldehyde to be immobilized on the surface of Nafion coated film. The protein matrix solution was used immediately. A 0.1-10 $\mu$l micropipette was used to coat the NNO sensor. 2 $\mu$l of glutamate matrix was drawn up. A small droplet of the solution was formed at the pipet tip without completely releasing the droplet. The solution droplet was then lowered to briefly contact the film surface and is raised straight up and off the NNO sensor surface. This was repeated 4 times with at least 1min wait in between. The coating film were cured at room temperature from 48-72 h and then stored at 4 °C before first measurement Burmeister et al. (2013); T. N. Nguyen et al. (2019b).

4.2.1.4 Chemical agent procurement Glutamate oxidase (GluOx) from Streptomyces, with a rated activity of 25 units per mg protein was obtained from Cosmo Bio USA (Carlsbad, CA). Nafion perfluorinated resin solution (5 wt.% in water and alcohol), glutaraldehyde (25% in water) were obtained from Sigma Aldrich (St. Louis, MO). L-Glutamic acid, 0.1 M phosphate buffer saline (PBS, pH 7.4) were obtained from Fisher Scientific (Waltham, MA). Ascorbic acid (AA), uric acid (UA), acetaminophen (AC) were purchased from Alfa Aesar (Fisher Scientific, Waltham, MA). Elastomeric polydimethylsiloxane (PDMS, Sylgard 184) was purchased from Dow Corning (Midland, MI). Water was purified by Milli-Q (Millipore, Bedford, MA). Ag/AgCl/NaCl (3.5 M) reference electrode was acquired from (Bio-logic USA, LLC, Knoxville, TN, USA) for three-electrode measurements.

4.2.1.5 Microscopy Cross-sectional area images of NNO/LAO film were obtained using a Cs and Cc aberration-double corrected FEI Titan transmission electron microscopy (TEM) at 200 keV. The TEM specimen was prepared by focused ion beam (FIB) lift-out and subsequently milled in a Gatan PIPS at 200 eV to remove any excess damage layers introduced by the FIB. The scanning TEM energy dispersive X-ray spectroscopy (STEM-EDS) data was collected using an FEI Talos equipped with a Super X EDS at 200keV.

4.2.1.6 Electrical conduction measurements After each glutamate treatment, the NNO film (without nafion coating) was rinsed with DI water and dried with high-purity $N_2$ gas. Two Pd pads with the thickness of 100 nm were deposited onto film as contact using magnetron sputtering from Pd target. The current-voltage (I-V) curves were measurement between two Pd contact by using a Keithley 2635A Source Measure Unit. For measurements of in-plane conductivity of the film, the cyclic voltammetry measurement was performed using a three-electrode setup on a Solatron 1260 potentiostat. A silver paste was scratched into a corner of the NNO film (5mm ×10mm), and a stainless steel wire was in contact with Ag paste and baked at 50 °C until the paste become solid. Thereafter, the back and sides and Ag paste area were sealed with inert epoxy (Locite 9460) leaving NNO film ($\sim$ 0.3 $cm^2$) exposed to the electrolyte only. In our measurement, the NNO film served as working electrode, and the Pt wire and Ag/AgCl in 3.5 M KCl served as counter electrode and reference electrode, respectively. 5 × 10-3 M each of $K_3Fe(CN)_6$ and $K_4Fe(CN)_6{\cdot}3H_2O$ (Sigma, $>$ 99 %) were added to the 0.1 M KCl electrolyte. Before measurement, the electrolyte was bubbled with ultra-high purity $N_2$ for 30 min.

4.2.1.7 Synchrotron X-ray measurements The X-ray measurements were carried out on beamline 33-ID-D at Advanced Photon Source, Argonne National Laboratory. A 6-circle Newport Kappa diffractometer was used for the X-ray diffraction measurement near the substrate (002) Bragg peak. The nominal incident X-ray photon energy of 8.333 keV was used for the XRD measurements, which is lower than the measured Ni absorption edge of $\sim$ 8.345 keV. XRD and XANES measurements were done on the same spot of the sample. For XAS measurement, a single element Vortex detector was used to collect the fluorescence signal from the sample as the incident X-ray energy was scanned through the Ni-K absorption edge (8.31 - 8.56 keV).

Two different incident angles of X-rays were chosen for the XAS measurements: one at 5.2 degree to survey whole depth of the film; another at 0.3 degree, i.e., below the critical angle, where the X-ray extinction depth is reduced to less than ten nanometers, to probe the Ni cation valence state of the surface layer. O K-edge X-ray absorption spectroscopy was conducted at beamline 29-ID IEX at the Advanced Photon Source, Argonne National Laboratory. Data were collected in a pressure better

that 1×10$^{-}$8 Torr in total fluorescence yield (TFY) using a micro-channel plate with 7° angular acceptance located at $2\theta = 20^{o}$. We used circular polarization with an overall energy resolution better than 100 meV. The incidence angle was set to theta = 5°, as to limited the penetration depth to 10 nm at the O K- edge. The total fluorescence yield was normalized by the incident x-ray intensity (I0) using the drain current from a gold mesh upstream of the sample.

4.2.1.8 Atomic Force Microscopy (AFM) The topographic AFM mapping of the NNO films upon different glutamate treatments were performed using an Asylum MFP3D stand-alone atomic force microscope using Asylum ASYELEC-01 conductive tips (Si coated with Ti/Ir).

### 4.2.2 *Ex vivo* glutamate sensing experiments on brain slices

4.2.2.1 Needle shape NNO/LAO electrode fabrication The needle shape NNO/LAO electrodes used in the *ex vivo* experiments were fabricated by using a wafer saw to cut the NNO/LAO wafer into 1x10 mm needle like structures. The electrodes were then mechanically polished with 3 $\mu$m polishing paper such that the width was approximately the same as the original wafer thickness (250 $\mu$m) resulting in a 0.25×0.25×10 mm final structure.

4.2.2.2 Animals and acute brain slices preparation All animal procedures were approved by Purdue University Animal Care and Use Committee. Brain slices were prepared as described 64. P28-P35 female C57BL/6 mice were anesthetized with the mix of 90 mg/kg ketamine and 10 mg/kg xylazine delivered by intraperitoneal injection. After confirmation of deep anesthesia, trans-cardiac perfusion was performed with oxygenated (carbogen from Airgas: 95% $O_2$, 5% $CO_2$) high sucrose dissection buffer (HSDB, composition in mM: 1.25 $NaH_2PO_4$, 25 $NaHCO_3$, 212.7 sucrose, 10 dextrose, 2.5 KCl, 0.5 $CaCl_2$, 7 $MgCl_2$, 1.3 ascorbic acid). After the perfusion has completed, the brain was quickly isolated by dissection. The brain was trimmed to desirable shape and fixed in the cutting chamber of the vibratome (Leica VT1000) filled with the HSDB while constantly oxygenated with carbogen flow.

The coronal brain slices containing the striatum and primary visual cortex (V1) were cut into 300 $\mu$m of thick sections. The brain slices were transferred immediately to a 32 °C incubation chamber containing oxygenated artificial cerebrospinal fluid (ACSF, composition in mM: 124 NaCl, 2.5 KCl, 2 $CaCl_2$, 0.8 $MgCl_2$, 1.23 $NaH_2PO_4$, 26 $NaHCO_3$, and 10 glucose) and incubated there for 30 min. The slices were then kept at room temperature (about 25 °C) for a least 1 h before use.

4.2.2.3 Electrical stimulation of brain slices The electric current was generated by a stimulation isolator (WPI A365) and output to a bipolar electrode (FHC CE2C55). The thin tip of the bipolar electrode was placed on the surface of the target brain areas. To induce glutamate release in V1, 5 s or 10 s constant 40 Hz stimulations were applied, and the width of one pulse was 0.1 ms, the amplitude was 500 $\mu$A.

4.2.2.4 *Ex vivo* experiment setup For *ex vivo* experiments shown in Fig. 4.7a, a piece of NNO/LAO was fixed on the experiment platform, on which the brain slide was placed. Pt wire and Ag/AgCl were served as a counter electrode and a reference electrode, respectively. During the experiment, the recording chamber was continuously perfused with an oxygenated ASCF solution. A slide hold-down was placed in order to avoid slice movement during measurements. The *ex vivo* experiment shown in Fig. 4.7d shared the same setup. Alternatively, a needle shape NNO/LAO connected via magnetic wire (30 AWG, Digi-Key Corp, MN) by solder served as a working electrode. PDMS was used as an insulation layer over the solder connection to prevent any contact with the solution. The device was then attached to a stainless tube for insertion.

4.2.2.5 *Ex vivo* electrochemical evaluation Electrochemical sensing experiments were carried out using SP-200 potentiostat (Bio-logic USA, LLC, Knoxville, TN, USA). Investigation of glutamate detection was done through the chronoamperometry i-t curve technique. All chronoamperometry data were collected after 20 min of settling time unless stated otherwise. A conventional three-electrode cell was used for chronoamperometry measurements with Ag/AgCl/NaCl (3.5 M) as a reference electrode and graphite rod as a counter electrode for all evaluations. Parameters for chronoamperometry were at 0.6 V vs. Ag/AgCl with 0.1 s sampling interval. All chronoamperometry was performed in a stirring solution of 0.01 PBS (pH 7.4) as supporting electrolyte and rotation rate of 180 rpm.

### 4.2.3 *In vivo* glutamate sensing experiments on awake mice

4.2.3.1 Fabrication of *in vivo* sensors A complete three electrode chemical sensor system was prepared for *in vivo* brain implantation experiments. The shank was prepared by spin-coating SU-8 2050 resin (Microchem, Newton, MA) on a 4-inch silicon wafer substrate with 3500 rpm of spin-speed to obtain 50 $\mu$m of thickness. The sample was soft baked for 3 min in 65 $^{o}$C, and 6 min in 95 $^{o}$C. UV light (dose: 160 mJ/cm$^2$) was exposed using a mask aligner (Suss MA6, Suss Microtech, Garching, Germany). Post-exposure bake was done for 1 min in 65 $^{o}$C, and 6 min in 95 $^{o}$C. The sample was developed in the SU-8 developer (Microchem, Newton, MA) for 5 min, and rinsed with isopropyl alcohol. Hard bake was done at 200 $^{o}$C for 10 min. Shanks were released from the silicon wafer by etching the natural oxide with buffered oxide etch followed by rinsing in DI water for 5 times.

After fabricating the desired SU-8 shank structure, platinum nanoparticle nanocomposite was printed on the backside of the shank as CE, and as a conductive trace for RE on the front side T. N. Nguyen et al. (2019b). Ag/AgCl ink was used to print RE on top of the conductive trace in the front of the shank. Silver ink was printed as contact pads, and PDMS was printed as an insulated layer exposing only the electrodes and contact pads. A 3-axis microfluid dispensing robot (Pro-EV 3, Nordson EFD, East Providence, RI) was used for the printing process. The needle shape NNO/LAO was then attached right below the reference electrode and connected via magnetic wire (34 AWG, Digi-Key Corp, MN) by silver ink. The whole system was placed on a bared LAO substrate (1 cm×1 cm) before attached to a stainless-steel tubing, which helps guide the insertion (Fig. 4.8a).

4.2.3.2 Mice and Surgical Procedures Surgical procedures were performed as described previously Kissinger, Pak, Tang, Masmanidis, and Chubykin (2018). C57BL/6 mice were housed on a 12 hr light/dark cycle. P55 old mice were anesthetized with 5% inhaled isoflurane (in oxygen) and maintained at 1.5% during surgery. Once deep anesthesia was confirmed the mice were affixed with ear bars to a NeurostarTM stereotaxic surgery frame and ophthalmic ointment was applied to the eyes. The scalp was shaved and sterilized with DynarexTM ethanol wipes before a midline incision was made and expanded to uncover the lambda and bregma skull sutures. The skull was sterilized using 3% $H_2O_2$, and the periosteum was removed. Once the skull was dry, coordinates for the binocular

visual cortex (from lambda: AP 0.8 mm, ML +/- 3.2 mm) were marked using NeurostarTM stereodrive software. A 9.5 mm long head post was glued in place with cyanoacrylate to a point on the midline of the skull 3.5 mm anterior to bregma. A reference pin made from a 1.5 mm tungsten wire soldered to the end of a 0.79 mm diameter gold plated pin was also glued into place with cyanoacrylate after insertion through the skull at a point on the midline 0.2 mm anterior of bregma. MetabondTM bone cement was used to seal the skull under a head cap.

Habituation of the mice to the head-fixation apparatus began after a day of recovery from the initial surgery. Habituation lasted for a minimum of three days for 90 min/day. When attached to the head-fixation apparatus via the implanted head post, the mice stood on a vertical treadmill facing the center of a 47.63 cm x 26.99 cm monitor screen placed 16.51 cm in front of them. After the last day of habituation, the following day, a craniotomy was performed at one of the marked coordinates. The same method of anesthesia was used for this surgery, as for the initial head post-implantation. Once affixed to the head-fixation apparatus, the biosensor was inserted normal to the surface of the now exposed binocular area of the primary visual cortex. Once inserted, the sensor was allowed to settle, and the mouse allowed to fully awaken from anesthesia over 30 minutes before recording. For the electrophysiology data, the process was the same as with the biosensor, but instead, a 64 channel silicon electrode was inserted. After a recording session, the craniotomy was re-sealed with Kwik-CastTM Silicone Elastomer and Ortho-JetTM orthodontic acrylic resin.

4.2.3.3 Visual Stimulation To generate and present the visual stimuli, the open-source psychology software PsychoPy was used. During the habituation of the mice, they were shown a control screen made with the color space “gray” on a monitor with a mean luminance of 73 cd/m$^2$. The visual stimuli provided to promote a neural response were single 10 s sinusoidal drifting gratings (spatial frequency (SF) = 0.03 cycles per degree of visual angle, temporal frequency (TF) = 3 Hz, speed = 100 deg/s, oriented and drifting at an angle of 150 degrees) with an inter-trial interval of 8s, a drifting checkerboard pattern (temporal frequency (TF) = 3 Hz, speed = 100 deg/s, oriented and drifting at an angle of 150 degrees) displayed for 10 s with an inter-trial interval of 8 s as well as a 10 s display time with an inter-trial interval of 30 s, a full contrast modulation following a 2.5 Hz square wave displayed for 10 s with an inter-trial interval of 60 s.

4.2.3.4 Perfusions and Histology Before starting the perfusion, the mice were anesthetized with intraperitoneal injections of a 90 mg/kg ketamine and 10 mg/kg xylazine solution. The inner cavity of the peritoneum was exposed with an incision under the rib cage before cutting the lateral sides of the rib cage and removing the diaphragm. The heart was then exposed by peeling back the rib cage and any other connective tissue. 1X PBS was gravity-fed through a 25-gauge needle inserted into the left ventricle to force blood out of an incision made in the right atrium. Perfusion of 4 % PFA was then used to fix the tissue. To remove the brain, the animal was decapitated, and the head cap sealing the skull was removed. Then cuts were made up the midline and along the lambda and bregma sutures in order to remove the skull and expose the brain enough to remove it from the skull. Once extracted the brain was placed in 4 % PFA for 24 h before slicing it into 100 $\mu$m thick coronal sections. The slices were carefully attached on slides and mounted by NPG-Glycerol. The sensor track was then visualized by light microscopy.

4.2.3.5 Analysis of electrophysiological data Raw traces were digitized at 30 kHz and acquired with OpenEphys acquisition hardware and software. For LFP analysis, the raw signal traces were filtered (1–300 Hz) and downsampled to 1 kHz, manually inspected for artifacts, and filtered with a notch filter removing 60 Hz noise. In order to compare LFPs between mice, the first and strongest trial-averaged visually evoked potential (VEP) from a visual stimulus (putative layer 4 VEPs) from each column of a silicon probe was used. For spike analysis, raw traces were bandpass-filtered (300-6000 Hz). Spikes were detected and sorted with the use of Kilosort, a template-based clustering algorithm implemented in Matlab Pachitariu, Steinmetz, Kadir, Carandini, and Harris (2016). The default Kilosort parameters were used except for a 6 SD threshold for spike detection and initializing the templates from data. Manual inspection of the resulting clusters for unit quality was performed using the Phy template GUI, based on criteria Rossant et al. (2016) that have been previously described Kissinger et al. (2018).

4.2.3.6 Single unit analysis To analyze single unit activity, they were put into peristimulus time histograms (PSTHs) with a 10ms bin size and were smoothed with a Gaussian smoothing kernel (width = 100ms). Z-score heatmaps were made by normalizing to the mean firing rate (FR) across time, so z = (FR – mean FR)/(SD FR), and the z-scores of the population time course line plots were

made by normalizing FR to the baseline period preceding stimuli presentation, so z = (FR – mean baseline FR)/(SD baseline FR).

## 4.3 Results

Fig. 4.1a shows the schematic pathway for the glutamate sensing mechanism using NNO as a biosensor device. The electrical stimulus leads to an increased level of glutamate (path (1) in Fig. 4.1b), which gets transported to the device interface. The glutamate oxidase (GluOx) enzyme is immobilized on the film surface, which consumes the glutamate with oxygen and water to produce $H_2O_2$. The GluOx biosensor is $O_2$-dependent, as suggested in Eq. 4.1. However, it operates well in the brain under normal conditions without being limited by oxygen concentrationClay and Monbouquette (2017):

$$\mathrm{L-glutamate} + \mathrm{H_2O} + \mathrm{O_2} \longrightarrow \mathrm{alpha-ketoglutarate} + \mathrm{NH_3} + \mathrm{H_2O_2} \tag{4.1}$$

The $H_2O_2$ selectively penetrates through the nafion film (path (3) in Fig. 4.1b). $H_2O_2$ is then catalytically oxidized at the working electrode of NNO according to Eq. 4.2 at an appropriate polarization potential and monitored by the electrochemical station.

$$\mathrm{H_2O_2} \longrightarrow \mathrm{O_2} + 2\mathrm{H^+} + 2\mathrm{e^-} \tag{4.2}$$

The protons intercalate into the nickelate lattice in which the proton is weakly bonded with oxygen anions and occupies interstitial sites in $NiO_6$ octahedra, and the extra electron is filled into the ligand hole in $Ni_{3d}$-$O_{2p}$ hybridized orbital Oh, Jo, and Son (2019); J. Shi, Zhou, and Ramanathan (2014). After the intercalation of proton and electron, the electron-electron repulsion in Ni site orbital leads to the localization of electrons and an increase of resistivity, as a feedback mechanism.

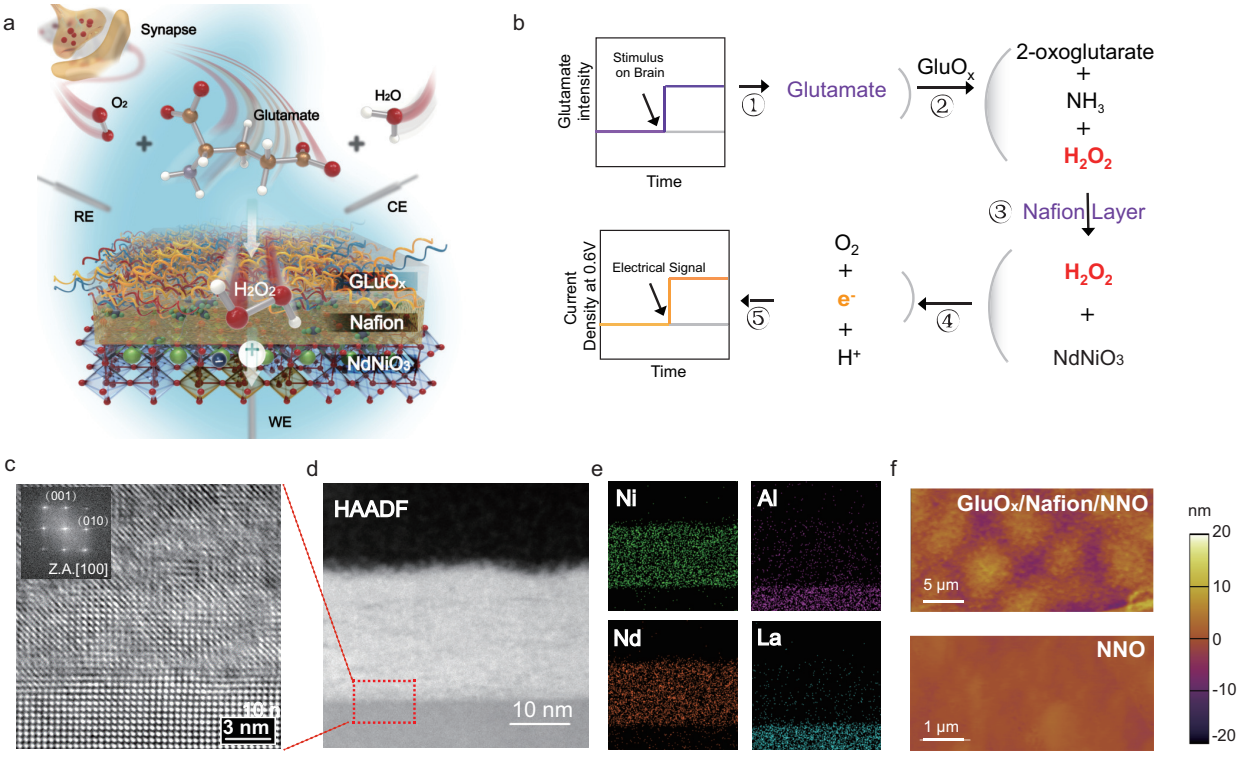


*Figure 4.1.* $NdNiO_3$/Nafion heterostructure as a glutamate biosensor. (a) Schematic of glutamate sensing with nickelate-nafion sensor. The $NdNiO_3$ (NNO) thin film was coated with nafion followed by GluOx enzyme. The nafion serves as a ion selective permeable membrane while GluOx enzyme is immobilized on top of nafion. (b) Bio-sensing reaction mechanism of glutamate by NNO. Electrical stimulus application led to the release of glutamate. The GluOx enzyme coated on NNO catalyzes the enzymatic reaction to form $\alpha$-ketoglutarate, $NH_3$ and $H_2O_2$. The $H_2O_2$ diffuses through the nafion to reach surface of NNO. Under applied bias (i.e., 0.6 V vs. Ag/AgCl), the $H_2O_2$ oxidation is catalyzed by NNO, which is monitored by electrochemical station. (c) High resolution TEM image of NNO/LAO cross-section. The Fast Fourier Transform (FFT) image of interface is shown in inset. (d) HAADF-STEM, and (e) STEM-EDX image of cross-section of NNO/LAO film. The selected area diffraction pattern is shown in inset of Fig. 4.1c. The epitaxially grown NNO film on LAO substrate with uniformly dispersed Nd and Ni across film thickness could be observed. (f) The surface morphology of GluOx/Nafion/NNO and NNO characterized by atomic force microscopy (AFM). The surface of NNO is quite smooth. In comparison, the GluOx coating has a rough morphology of round-shaped particles with the diameter of $\sim 5\ \mu$m which is distinguishable from bare NNO surface as well as Nafion/NNO surface. (Reprinted with permission from H. Sun et al. (2020). Copyright 2020 American Chemical Society.)

The top-view and cross-section morphology of NNO/LAO (NdNiO3 thin film deposited on $LaAlO_3$ substrate) film were analyzed by transmission electron microscopy (TEM). The interface between NNO film and LAO substrate is sharp without any secondary phases (Fig. 4.1c-d). The NNO film is epitaxially oriented along [001] direction, parallel to the c-axis of LAO (001) substrate. The zone axis of the specimen is [100] for imaging and can be seen by the symmetry in the FFT image shown in the inset of Fig. 4.1c. STEM-EDX analysis shown in Fig. 4.1e illustrates the uniform distribution of Nd and Ni elements across film thickness. The NNO film was coated with nafion (a widely used ion permeating membrane) and the GluOx enzyme. Atomic force microscopy (AFM) measurements were then performed to verify the surface decoration (Fig. 4.1f). The pristine NNO surface has a surface roughness of $\sim$ 0.76 nm. In comparison, the first layer of nafion coating leads to the increase of surface roughness to 8.54 nm (Table 4.1). Further GluOx coating shows up as a bright spot with diameter of 5 $\mu$m.

### 4.3.1 Glutamate Biosensor Performance

The chronoamperometric method for the determination of glutamate utilizes the oxidation response of $H_2O_2$, a byproduct of enzymatic oxidation. From CV scan results (representative result shown in Fig. 4.2), 0.6 V vs. Ag/AgCl is chosen as an optimal potential for amperometric detection of glutamate via oxidation of $H_2O_2$, which is also typically used in literature Burmeister et al. (2020). Prior to sensing measurements, the NNO film was confirmed to have sufficient conductivity for reliable electrocatalytic activity. In the presence of oxygen, GluOx catalyzes successive reaction of glutamate to form $H_2O_2$, which can be oxidized at the electrode. As shown in Fig. 4.4a, the perovskite nickelate film coated with Nafion-GluOx exhibits prominent electrocatalytic activity toward increasing levels of glutamate. The successive addition of glutamate (50 $\mu$M each dosage) leads to a significant jump up of current density of 18 nA $mm^{-2}$ per dosage. In comparison, the nickelate without Nafion-GluOx demonstrates no current density variation upon addition of glutamate at 0.6 V vs. Ag/AgCl, suggesting that there is no occurrence of Faradaic reaction ($H_2O_2 \rightarrow O_2 + H^+ + 2e^-$) without the enzyme.

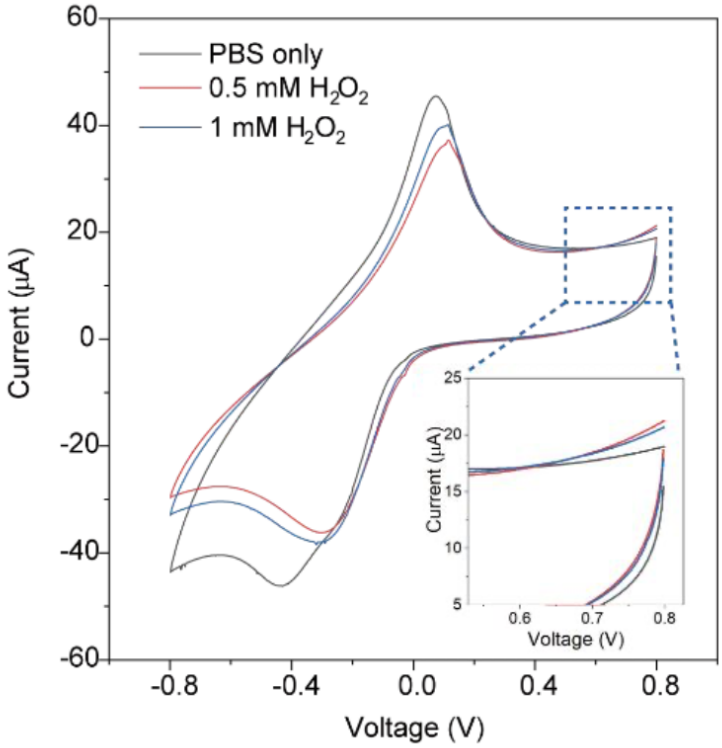


*Figure 4.2.* Cyclic voltametry (CV) scan of NNO based glutamate biosensor in different solutions. We assessed the electrocatalytic property of NNO film using cyclic voltammetry in $H_2O_2$ (0.5 mM and 1 mM) containing PBS solutions. The redox peaks between $-$ 0.4V and 0.2V is related to the reversible proton intercalation-deintercalation in NNO film Z. Zhang et al. (2018). The electrocatalytic activity of $H_2O_2$ oxidation starts to show increase in current at potential higher than 0.5 V (shown in inset). As result, we selected 0.6 V as a suitable potential for glutamate detection to maximize oxidation of $H_2O_2$ and minimize other interferences at higher over-potential, which is also typically seen in literature Danbolt (2001). (Reprinted with permission from H. Sun et al. (2020). Copyright 2020 American Chemical Society).

A calibration plot is presented in Fig. 4.4b, which presents a linear kinetic reaction with a sensitivity of 0.327 ± 0.07 nA $\mu M^{-1}$ $mm^{-2}$ (n = 3) toward glutamate. For sensor selectivity, a Nafion layer which electrostatically repels anions was deposited onto the perovskite nickelate film before the immobilizing of GluOx enzyme layer. Fig. 4.3a shows the amperometric response of our glutamate biosensor against AA, UA, AC. Fig. 4.3b presents the current ratio between glutamate and AA, UA and AC.

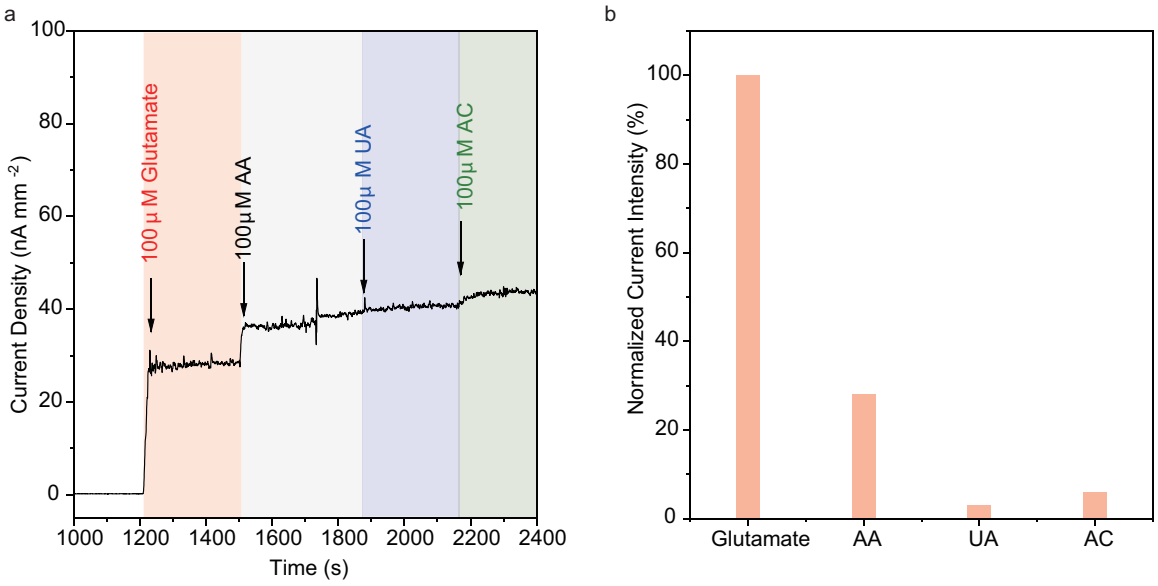


*Figure 4.3.* Amperometric sensing and interference (selectivity) studies of nickelate- nafion heterostructure. (a) Amperometric response of GluOx/Nafion/NNO biosensor upon sequential addition of 100 $\mu$M of glutamate, 100 $\mu$M of ascorbic acid (AA), 100 $\mu$M of uric acid (UA) and 100 $\mu$M of acetaminophen (AC) into constantly stirred 0.01 M PBS (pH 7.4) solution at 0.6 V vs. Ag/AgCl. (b) Summary of normalized current intensity of different species (glutamate, AA, UA, AC). For successful detection of glutamate *in vivo*, the biosensor must be highly selective toward glutamate and against other electroactive species present in the body. When biased at 0.6 V vs. Ag/AgCl, other electroactive species can also be directly oxidized at the electrode surface, and contributed to the increase of current density. Therefore, for sensor selectivity, a Nafion layer which electrostatically repels anions was deposited onto the perovskite nickelate film before the immobilizing of GluOx enzyme layer. There is very slight response from the sensor to UA and AC. The current ratio of AA/Glutamate is 28% with negligible ratio of UA/glutamate and AC/glutamate of 4% and 7%, respectively. The results suggested that the Nafion membrane can prevent about 80% interference signal from AA. (Reprinted with permission from H. Sun et al. (2020). Copyright 2020 American Chemical Society).

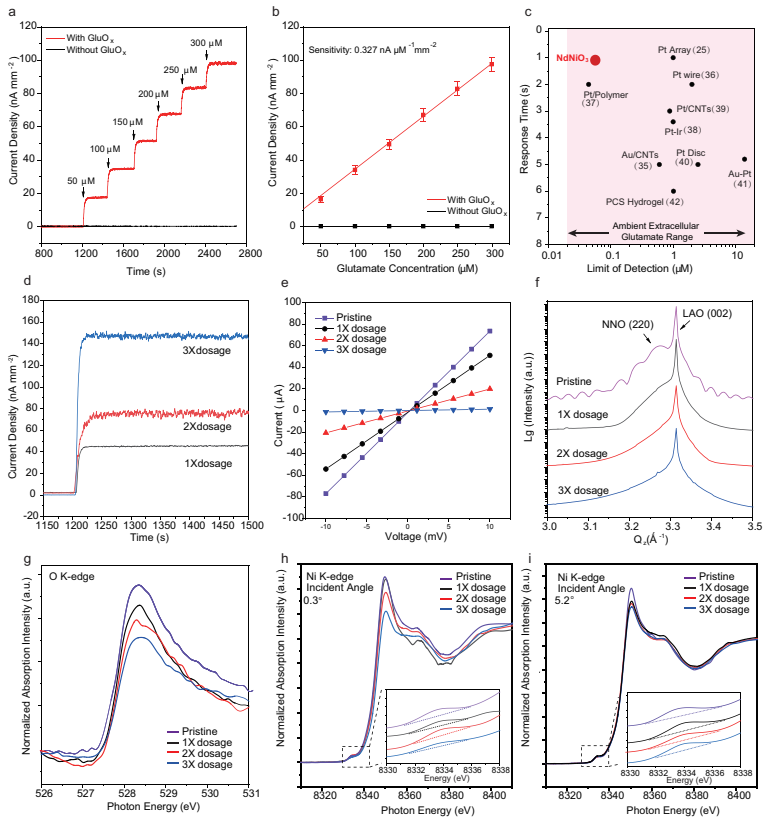


*Figure 4.4.* Benchtop experiments and nickelate characterization post-glutamate dosage. (a) Representative amperometric curves for NNO as a glutamate biosensor at applied potential of 0.6 V vs. Ag/AgCl in 0.01 M PBS (pH 7.4) with and without the presence of GluOx enzyme (control). (b) The corresponding calibration curves and the sensitivity is shown. (c) Comparison of the performance metrics in terms of response time and detection limit of various representative glutamate biosensors from literature. The light pink regime indicates the ambient extracellular glutamate level without any external stimulus. (d) Representative amperometric curves for NNO as a glutamate biosensor for different dosages of glutamate (100 $\mu$M per dosage) at applied potential of 0.6 V vs. Ag/AgCl in 0.01 M PBS (pH 7.4). (e) The i-V curves taken from NNO films after treatment with 0× (pristine), 1×, 2×, 3× dosages of glutamate. The evolution of resistivity of the films is shown in inset. For instance, 3× dosage treatment of glutamate led to the increase of film resistivity by 2 orders of magnitude due to proton-electron incorporation. (f) Synchrotron X-ray diffraction scans of identical NNO films upon the treatment of pristine film and films subjected to 1×, 2×, 3× dosage of glutamate. The scans are along Qz direction around the (002) diffraction peak of LaAlO3 (LAO) substrate (pseudocubic notation). (g). X-ray absorption curves of the O K-edge of NNO films after treatment of 0× (pristine), 1×, 2×, 3× dosages of glutamate. (h-i) Angle-dependent X-ray absorption spectra of the Ni K-edge of NNO films upon the treatment of 0× (pristine), 1×, 2×, 3× dosages of glutamate at the incident angle of (h) 0.3 o and (i) 5.2 o. The zoom-in feature of pre-edge area spectra are shown in inset. The glutamate treatment leads to the gradually decreased intensity of O K-edge absorption peak, pre-edge hump area and white line intensity of Ni K-edge XANES, due to the intercalation of proton and electron into NNO lattice from the hydrogen peroxide oxidation.(Reprinted with permission from H. Sun et al. (2020). Copyright 2020 American Chemical Society.)

There is very slight response from the sensor to UA and AC. The current ratio of AA/Glutamate is 28 % with negligible ratio of UA/glutamate and AC/glutamate of 4 % and 7 %, respectively. The results suggested that the Nafion membrane can only prevent about 80 % interference signal from AA. Therefore, in future studies, another type of permselective layer such as m-Phenylenediamine dihydrochloride can be applied to better block interferent signal from AA and other species such as Dopamine and 5-hydroxytryptamine Burmeister and Gerhardt (2001); Ganesana, Trikantzopoulos, Maniar, Lee, and Venton (2019); Miele et al. (1996); Stephens et al. (2011); Weltin et al. (2014). One can also include a final layer of ascorbate oxidase enzyme (200 U/ml) to further prevent the interference of AA Ganesana et al. (2019).

A comparison of the parameters for response time and limits of detection of various glutamate biosensors is shown in Fig. 4.4c Batra and Pundir (2013); Ganesana et al. (2019); Govindarajan et al. (2013); Hamdi et al. (2006); Jamal et al. (2010); Kwong, Gründig, Hu, and Renneberg (2000); Maity and Kumar (2019); Sirca, Vardeu, Pinna, Diana, and Enrico (2014); Wassum et al. (2008). The light pink regime in Fig. 4.4c represents ambient extracellular glutamate ranging from 20 nM to 20 $\mu$M Moussawi et al. (2011); Y. Wang et al. (2019). The NNO film demonstrates a fast response time of $\sim$ 1.2 s and low detection limit of 16 nM with a linear range between 1 to 700 $\mu$M (Fig. 4.5). These metrics are comparable to state-of-the-art glutamate sensors suggesting their potential as in-vivo sensors as described further. Additionally, it is important for our glutamate sensor to maintain the balance between sensitivity, selectivity and temporal resolution. Thus, the existence of the permselective membrane is also significant to keep our sensor selective, which increases the response time as comparing to ultra-fast glutamate sensor Y. Wang et al. (2019). Furthermore, as described in more detail later, the sensor is implanted at the layer 4 of the visual cortex next to the direct thalamocortical projection, where small concentration of glutamate is released by different types of visual stimulation. In this case, the response time and low detection limit of our sensor are suitable to detect the glutamate release. However, even faster response times, sensitivity and better resolution for transient glutamate detection can be achieved by optimizing the Nafion layer dimensions in future studies as shown theoretically by Clay and Monbouquette (2018).

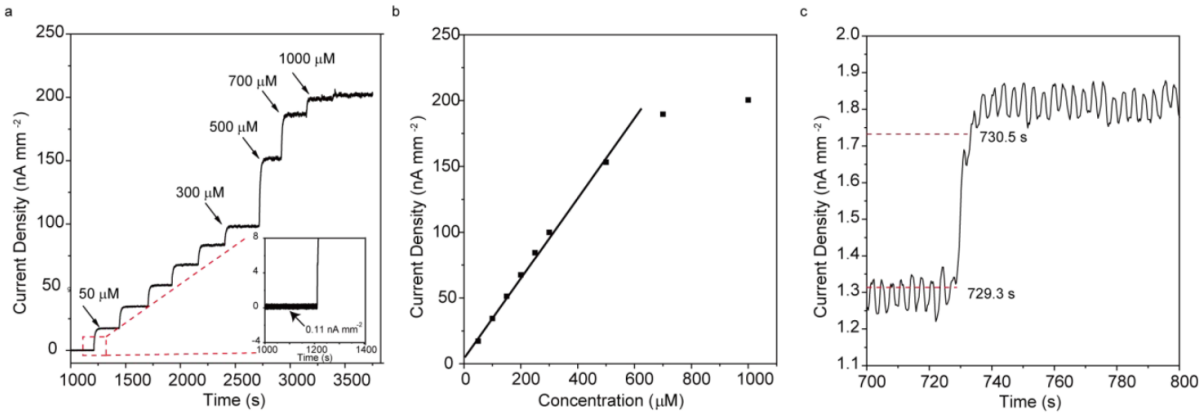


*Figure 4.5.* (a). Sensor performance measurements. Amperometric curves for different concentrations (up to 1000 $\mu$M) of Glutamate in 0.01 M PBS solution (pH 7.4) taken from GluOx/Nafion/NNO biosensor at applied potential of 0.6 V vs. Ag/AgCl. The baseline current (no glutamate added) was utilized to calculate the limit of detection of NNO film by applying the equation 5 as follows:
Limit of detection (signal: noise (s–n) =3) = 3 × Stdev of noise current/linear slope from figure b (b) The corresponding calibration curve of response current versus the concentration of glutamate at applied potential of 0.6 V vs. Ag/AgCl. c. The response time of NNO biosensor. The response time is defined as the delay time between the rise of the increase in analyte concentration and the rise of the current signal taken at 90 % of the total change. In our experiments, 1 $\mu$M glutamate was added to the reaction system, and the measurement response time is estimated to be $\sim$ 1.2 s. (Reprinted with permission from H. Sun et al. (2020). Copyright 2020 American Chemical Society).

### 4.3.2 Phase evolution in nickelate sensors after exposure to glutamate dosages

The hydrogen peroxide oxidation reaction at the nickelate electrode can be monitored via the electrochemical station. Separately, the nickelate thin film can be studied post-reaction by ex-situ methods using high energy resolution synchrotron radiation. The resistance evolution of the films (i-v curves) after treatment with different dosages of glutamate in 0.01 M PBS (pH 7.4) solution (Fig. 4.4d) is shown in Fig. 4.4e. The pristine metallic NNO film has a low resistivity of $\sim$ 0.18 m$\omega$ cm. The 1× dosage of glutamate leads to a slight increase to around 0.25 m$\omega$ cm. The 2× and 3× dosage treatment further results in substantial change in resistivity by $\sim$ 5X and $\sim$ 2 orders of magnitude. Such PBS-mediated conductivity reduction due to electron filling is non-volatile at ambient conditions.

To investigate the mechanism of sensor response to glutamate, microstructural and electronic structure studies were performed on representative samples. Synchrotron X-ray diffraction curves taken from films after different dosage treatments are shown in Fig. 4.4f. The pristine NNO was epitaxially grown on single crystalline LAO substrate, which shows a shoulder (220) diffraction peak (orthorhombic notation) at Qz $\approx$ 3.27 Å-1. The substrate LAO (002) diffraction peak (in pseudocubic notation) is located at 3.31 Å-1, indicating the NNO films' larger out-of-plane lattice parameter. Upon 1× dosage glutamate treatment, the diffraction peak of NNO becomes broader and shows a shift toward lower Qz position, which arises from the proton/electron doping induced lattice expansion and distortion. The XRD pattern of NNO after further 2× dosage and 3× dosage treatments demonstrates no apparent diffraction peak which indicates a decrease in film crystallinity due to the greater concentration of protons that are intercalated through the film. Synchrotron X-ray absorption near-edge spectroscopy (XANES) measurements near the O K-edge of NNO films after different dosages are shown in Fig. 4.4g.

The gradual suppression of the O K-edge absorption peak at 529 eV occurs upon different dosage treatment, suggesting a decrease in oxygen-projected density of unoccupied states owing to the electron injection into $O_{2p}$-$Ni_{3d}$ hybridized orbitals. Synchrotron XANES measurements near the Ni K-edge of NNO films after different dosages measured at different incidence angles are shown in Fig. 4.4h-i, respectively. The choice of incidence angles allows us to determine if there are any significant changes occurring only near the surface as opposed to a significant fraction of the film thickness. The pre-edge region (shown in inset of Fig. 4.4h-i) of XANES can be regarded as the fingerprint of the covalence status between $O_{2p}$-$Ni_{3d}$ hybridized orbital. The intensity of white line peak depends on the occupancy of the bound final states. Both spectra at incidence angles of 0.3° and 5.2° show similar evolution trend that the white line peak amplitude significantly gets weaker and the effective integrated area underneath the pre-edge peak apparently suppressed after the glutamate treatment. Both reductions indicate electron filling into hybridized d-orbital due to the neurotransmitter. The reduction in integrated pre-edge peak area of glutamate treated NNO is normalized by the area of pristine NNO. For an incidence angle of 0.3°, the pre-edge area decreases by 48 % for 3× dosage treatment (Table 4.2). In comparison, such change is estimated to be 28 % for incidence angle of 5.2°, (Table 4.3).

Previous work using $SmNiO_3$ thin films for spontaneous transfer of hydrogen from glucose (with no electrical stimuli) showed only near-surface doping to a few unit cells H. T. Zhang et al. (2019). In this work, we can see that electron filling from a neurotransmitter could be a bulk effect across the film thickness under the electrochemical bias used in the amperometric sensing methodology, confirmed by both synchrotron XRD and XANES measurements as shown above. To verify reproducibility, we annealed the sensor devices to remove the doped hydrogen, started the fabrication process from scratch for subsequent re-use (Fig. 4.6).

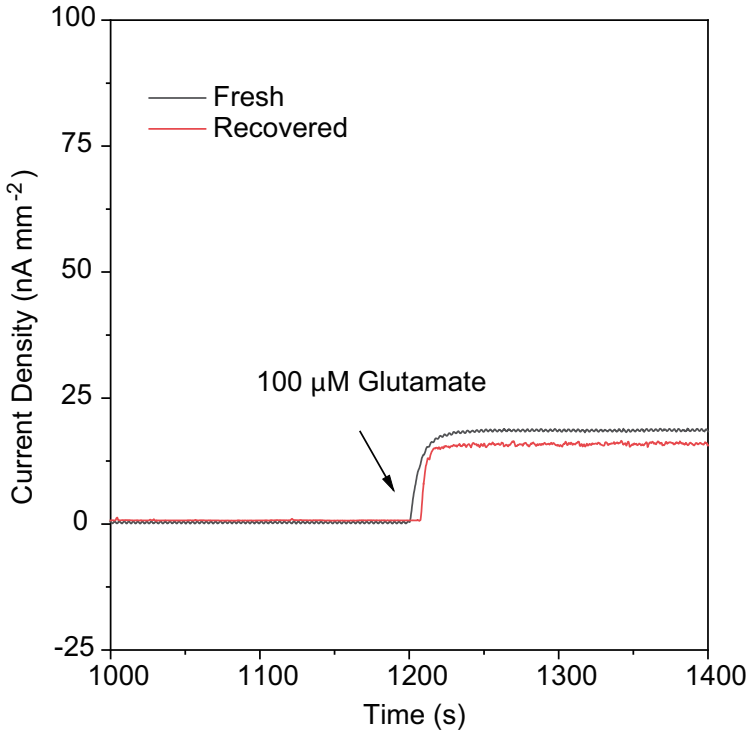


*Figure 4.6.* Recovery and re-use of the treated NNO biosensor. To demonstrate repeatability, the $NdNiO_3$ sensor was annealed in air at 500 °C for 24 h. The redecoration of Nafion and GluOx were performed onto recovered NNO film. It can be observed that the sensitivity of the film could be recovered close to fresh sample, indicating reproducibility.(Reprinted with permission from H. Sun et al. (2020). Copyright 2020 American Chemical Society).

### 4.3.3 *Ex vivo* studies of neurotransmitter release from mouse visual cortex

Prior to demonstrating the use of these biosensors for real-time monitoring of neurotransmitter glutamate released from neuronal tissue of living animals, we first measured glutamate release in acute mouse brain slices *ex vivo*. Brain slices were prepared from the primary visual cortex (V1) of mice. In each experiment, a glutamate NNO sensor was placed underneath a brain slice and secured by a slice holder for glutamate measurement. To stimulate glutamate release from the presynaptic terminals within the slice, a bipolar stimulus electrode was placed on the surface of the layer 4 of the cortical slice. Electrical pulses were applied as described in Methods (Fig. 4.7a-b).

Stimulation of layer 4, the main recipient of the thalamic input, was justified by the anatomical organization of the V1 microcircuit and the extensive previous studies of the long-term synaptic plasticity at the layer 4 to layer 2/3 synapse61. Furthermore, this layer 4 to layer 2/3 synapse represents one of the strongest feedforward inputs in the cortical column. To achieve full contact of brain tissue with the biosensor, we made sure that the sensor was about twice as large as the brain slice (0.46×0.76 $cm^2$) (Fig. 4.7a). When the glutamate reached the glutamate oxidase layer of the biosensor, the redox current was captured by the perovskite nickelate biosensor. The sampling rate for the redox current recording was 10 Hz and all the current density shown in Fig. 4.7c and f is normalized to square millimeter in order to compare the data obtained with sensors of different surface areas. About 8 s following the onset of electrical stimulation (500 $\mu$A 0.1ms width pulse, 40Hz for 10s), the peak current density per $mm^2$ is up to 20 nA (baseline subtracted), indicated the highest glutamate concentration recorded is about 60 $\mu$M (Fig. 4.7f). The baseline is the average current density value when no prominent current peak is detected in consecutive 20 s of a recording trial. The results suggest that NNO can be successfully used for sensing glutamate signal *ex vivo*.

The large surface area of the sensor increased the sensitivity of glutamate detection, but its size limited the spatial resolution. Furthermore, the size of the sensor was prohibitively large for *in vivo* recordings from the live mouse. To develop a more compact sensory design that could be inserted into the brain of a live mouse, we developed a needle-like prototype of the biosensor with the 250×300 $\mu m^2$ dimensions. Although it is larger than the latest state-of-the-art silicon probe for electrophysiological recordings, this design represented a major improvement compared to the benchtop version and could be successfully used for the recordings.

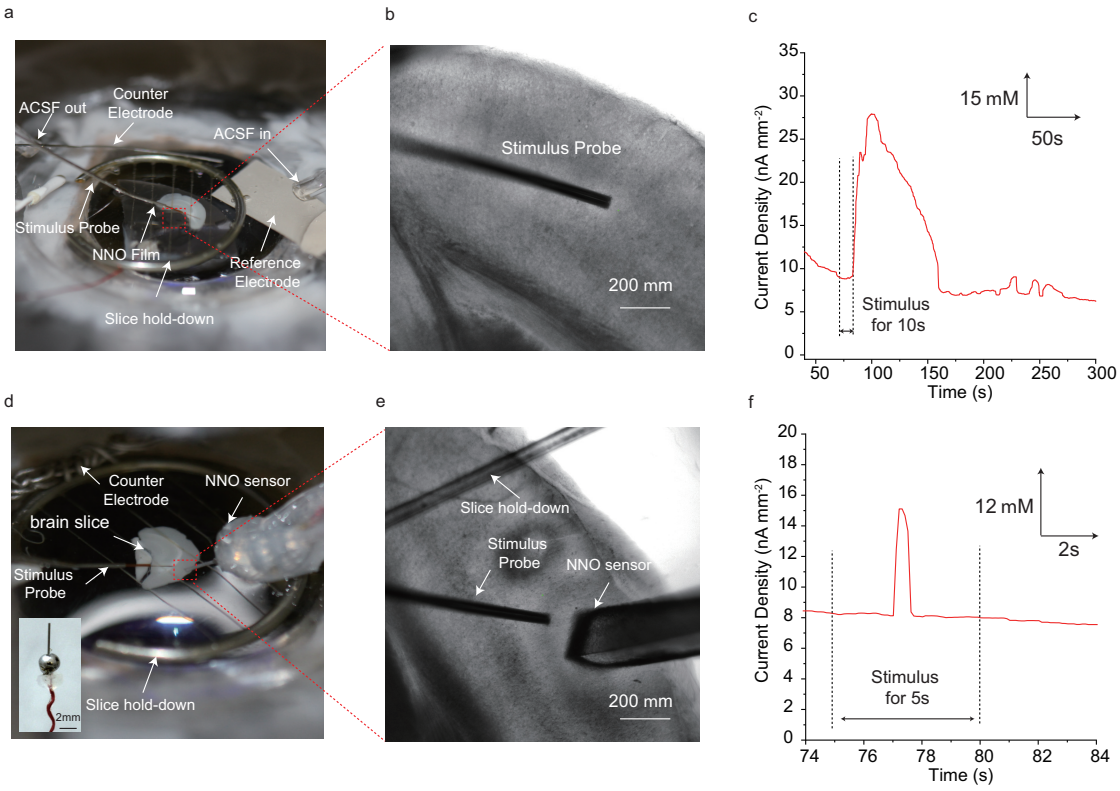


*Figure 4.7. Ex vivo* studies of glutamate release in stimulated brain slices. (a) *Ex vivo* stimulated glutamate sensing setup using a visual cortex brain slice of a mouse. The size of the visual cortex brain slice is $\sim$ 0.46 cm×0.76 cm. (b) Zoom-in image of brain slice with the electrical stimulus probe is attached. (c) Representative *ex vivo* stimulated glutamate sensing curve is shown. The glutamate sensing experiment was performed using a three-electrode setup at 0.6 V vs. Ag/AgCl. A sharp current peak was observed $\sim$ 8 s after the electrical stimulus (500 $\mu$A 0.1 ms width pulse 40Hz for 10 s) was applied to the brain slice. (d) The same setup shown in d is identical to a. Here, the glutamate sensor was machined into a needle-shape probe and was inserted into the brain slice. (e) The zoom-in image of the brain slice with the stimulus probe and the glutamate sensor. (f) Representative *ex vivo* stimulated glutamate sensing curve recorded by the needle-shape sensor. The recording and stimulation protocol is the same as in a-c, but the stimulation time is 5 s. The peak was detected $\sim$ 2 s after the electrical stimulus was turned on.(Reprinted with permission from H. Sun et al. (2020). Copyright 2020 American Chemical Society).

Before using the new design *in vivo*, we first tested it in brain slices. We had placed the new needle-shape sensor on top of layer 2/3 and successfully recorded glutamate release when applying the same high-frequency stimulation (500 $\mu$A 0.1s width pulse, 40 Hz for 5 s) of layer 4 in V1 as described earlier (Fig. 4.7d-f). The current density peak was detected about 2s after the stimulation began, the peak is up to 7 nA/mm$^2$, which corresponds to $> 21$ $\mu$M of glutamate during this experiment (Fig. 4.7f). The faster and more transient response detected by the needle-shape sensor compared to the large baseplate sensor could be explained by the closer proximity of the needle-shape sensor to the presynaptic terminals in layer 2/3 releasing glutamate directly compared to the slow excessive glutamate spillover required to reach the baseplate sensor. The results indicate that the needle-like sensor is more precise and sensitive and is promising for glutamate monitoring in living animals.

### 4.3.4 *In vivo* studies of neurotransmitter release from mouse brain

In order to demonstrate the potential for real-time biological applications, the nickelate-nafion sensors were used to record glutamate release *in vivo* in awake, head-fixed mice. A needle-shaped version of the sensor was inserted into the binocular region of the visual cortex to record the release of glutamate in response to visual stimulation (Fig. 4.8). The experiment setup and mouse brain atlas (from Allen Brain Institute Lein et al. (2007)) are shown in Fig. 4.8a and b, respectively. Fig. 4.8d shows the measured response to the Fig. 4.8d shows the measured response to the drifting sinusoidal grating (spatial frequency = 0.03 (cpd), temporal frequency = 3 Hz, speed = 100 deg/s) presented for 10s. The sensor with the coating shows a stimulus-induced peak suggesting it is detecting extracellular glutamate.

Recordings made in response to other visual stimuli patterns are shown in Fig. 4.9. Some differences in the amount of glutamate detected may be potentially explained by the differences in the ability of different visual stimulation protocols to activate presynaptic terminals in the visual cortex and release glutamate. To compare *in vivo* glutamate release in response to visual stimulation to the standard electrophysiological recordings performed in mice, we performed extracellular recordings of visually evoked potentials (VEPs) and neuronal unit responses as described previously (Fig. 4.10) Kissinger et al. (2018).

There was a temporal delay between stimulation and glutamate detection both *ex vivo* and *in vivo*. This delay was higher than the response latency in extracellular electrophysiological recordings of local field potentials and neuronal spikes (Fig. 4.10). The distinct behavior may be potentially explained by the action of the glutamate transporters in the presynaptic terminal and astrocytes, which can swiftly remove glutamate from the synaptic cleft and extracellular space following visual stimulation. Consequently, we may be able to detect only excess glutamate released following extensive, prolonged electrical stimulation in brain slices or visual stimulation *in vivo*. The slow diffusion of this excess glutamate may also explain the latency between the stimulation and the glutamate signal detection by the biosensor compared to electrophysiological methods. Future studies can include further miniaturization of electrode devices for multiplexed long-term *in vivo* brain research and bio-compatibility analysis.

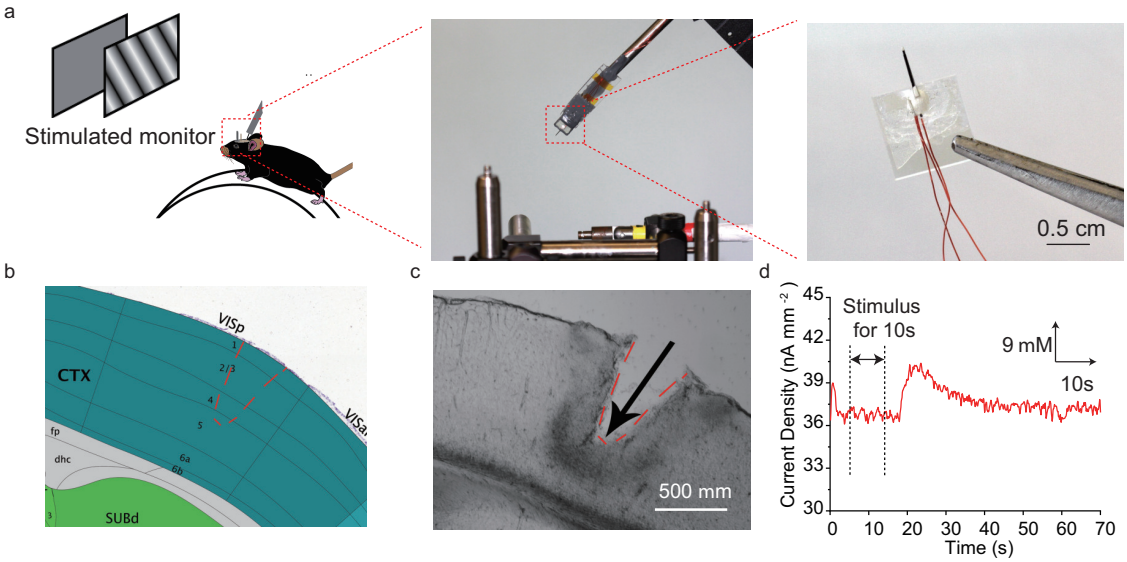


*Figure 4.8. In vivo* glutamate release studies on awake mice. (a) Setup for the *in vivo* glutamate sensing from awake, head-fixed mouse and close-up images of the sensor used. The visual stimulus presented was drifting sinusoidal grating (Spatial frequency = 0.03 (cpd), temporal frequency = 3 Hz, speed = 100 deg/s) presented for 10s with an inter-trial delay of 8s where a gray screen was displayed. (b) Mouse brain atlas (from Allen Brain Institute) showing the sensor was inserted into the binocular V1 region of the primary visual cortex (V1) outlined in red dashed line. (c) Slice histology showing the insertion path of the sensor in V1. (d) Representative *in vivo* glutamate recording is shown during visual stimulus made by the glutamate sensor (red). (Reprinted with permission from H. Sun et al. (2020). Copyright 2020 American Chemical Society).

## 4.4 Conclusion

We have presented the demonstration of an amperometric biosensor using a correlated metallic perovskite nickelate (i.e.,$NdNiO_3$ (NNO)) for neurotransmitter sensing in both *ex vivo* brain slices and *in vivo* inside the brain of awake mice. The biosensor consists of a NNO/nafion/GluOx hetero-structure with high selectivity towards glutamate, fast response time (1.2 s) and low detection limit (16 nM). Correlated metallic systems interfaced with polymers can therefore contribute to design of components for neurotransmitter sensing and brain-machine interfaces.

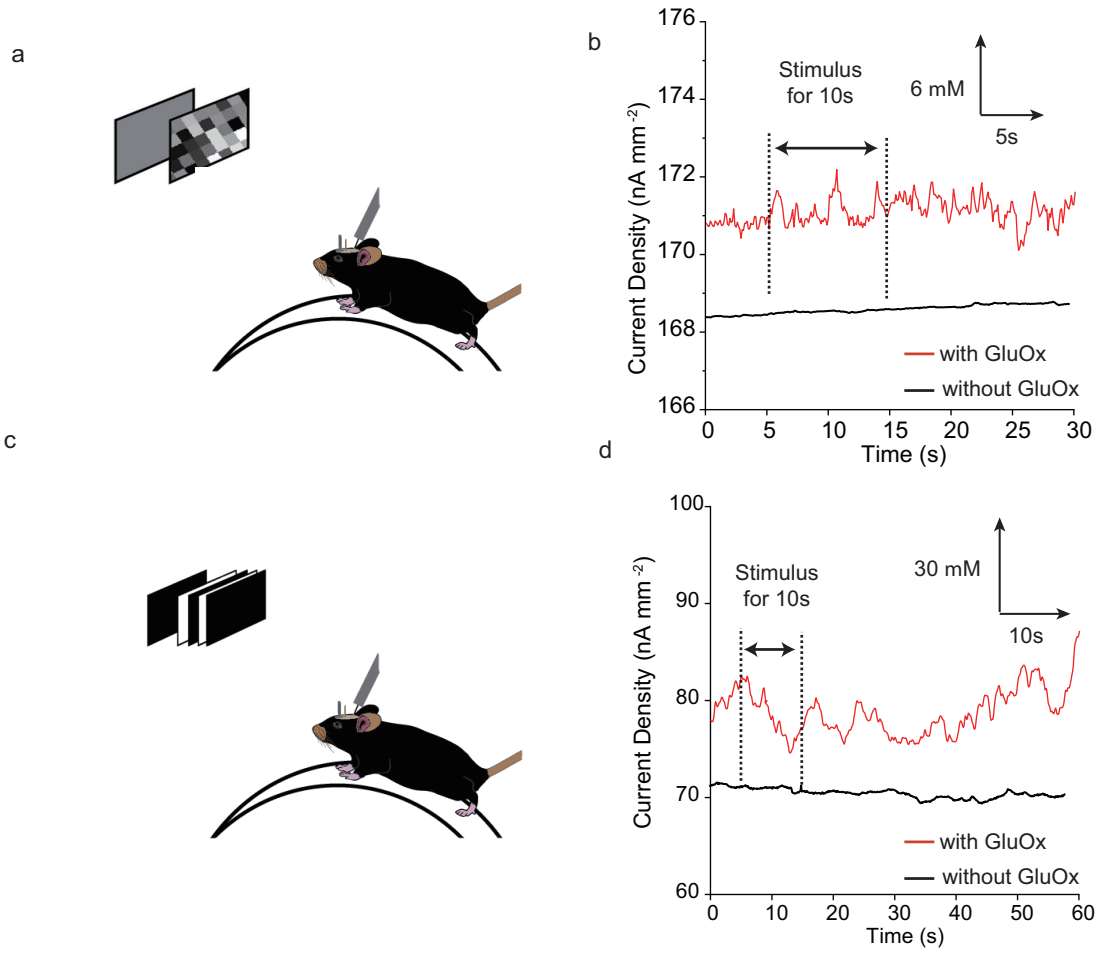


*Figure 4.9. In vivo* glutamate sensing in awake mice exposed to various visual stimuli. (a) Setup for *in vivo* glutamate measurements and the checkerboard visual stimulus presented for 10 s with a 30 s inter-trial delay. (b) Average of 10 trials of the recordings during checkerboard visual stimulus. The control experiment (without GluOx coating) is also shown. (c) Setup for the *in vivo* recordings using full contrast modulation following a 2.5 Hz square wave displayed for 10 seconds with an inter-trial interval of 60 seconds. (d) Average of 5 trials of the recordings during full contrast modulation following a 2.5 Hz square wave visual stimulus. The control experiment (without GluOx coating) is also shown.(Reprinted with permission from H. Sun et al. (2020). Copyright 2020 American Chemical Society).

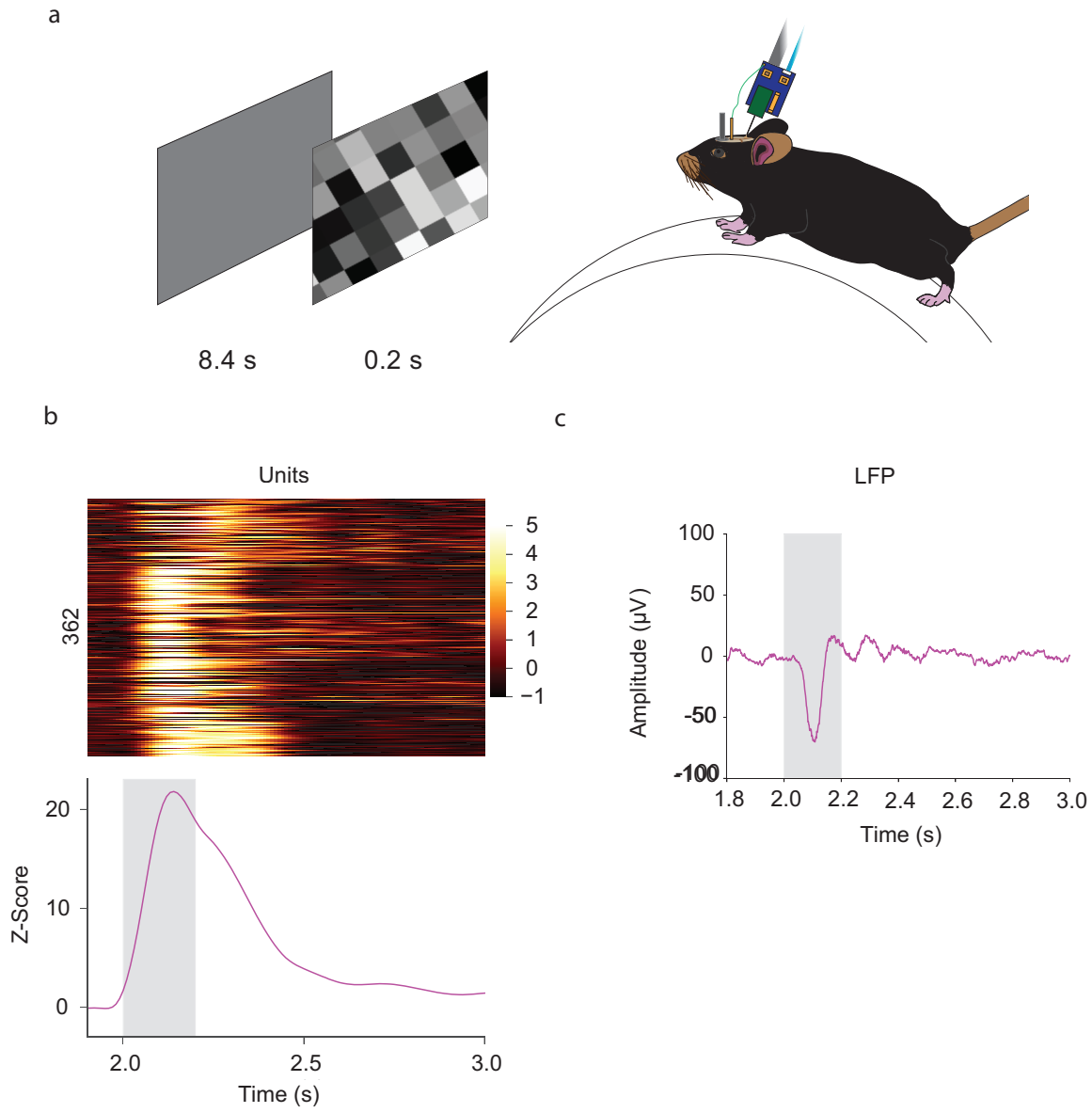


*Figure 4.10.* Electrophysiology experiments in awake mice with silicon probes (control). (a) Experimental setup for the *in vivo* electrophysiology experiments in head fixed, awake mice using 64 channel silicon probes (control data). The visual stimulation of a drifting checkerboard displayed for 0.2s per trial with an inter-trial interval of 8.4s. (b) Unit analysis from electrophysiology experiments. Z-score firing rate heatmap of 362 units from 6 mice showing response to the checkerboard stimulus. (c) Local field potential (LFP) response to checkerboard stimuli. Visually evoked potentials (VEPs) averaged across trials from 6 mice. (Reprinted with permission from H. Sun et al. (2020). Copyright 2020 American Chemical Society).

*Table 4.1.* Summary of film roughness. (Reprinted with permission from H. Sun et al. (2020). Copyright 2020 American Chemical Society).

| Film Name | Roughness (nm) |
|---|---|
| NNO | 0.768 |
| Nafion/NNO | 8.547 |
| GluOx/Nafion/NNO | 2.682 |

*Table 4.2.* Summary of normalize pre-edge area of Ni K-edge XANES at incident angle of 0.3°. (Reprinted with permission from H. Sun et al. (2020). Copyright 2020 American Chemical Society).

| Sample | Normalized Pre-edge area |
|---|---|
| Pristine | 100% |
| 1X dosage | 85.2% |
| 2X dosage | 80.1% |
| 3X dosage | 52.3% |

*Table 4.3.* Summary of normalize pre-edge area of Ni K-edge XANES at incident angle of 5.2°. (Reprinted with permission from H. Sun et al. (2020). Copyright 2020 American Chemical Society).

| Sample | Normalized Pre-edge area |
|---|---|
| Pristine | 100% |
| 1X dosage | 84.1% |
| 2X dosage | 76.3% |
| 3X dosage | 72.1% |

# CHAPTER 5. PRINTABLE NON-ENZYMATIC GLUCOSE BIOSENSORS USING CARBON NANOTUBE-PTNPS NANOCOMPOSITE MODIFIED WITH AURU FOR IMPROVED SELECTIVITY

## 5.1 Introduction

Over the years, enzymatic electrochemical biosensors based on glucose oxidase (GOx) have been popularized for the management of diabetes mellitus owing to their good selectivity and high sensitivity. However, most of these enzyme-based glucose biosensors are disposable with limited functional lifetime Diabetes (2009); Nichols, Koh, Storm, Shin, and Schoenfisch (2013); Shaw, Sicree, and Zimmet (2010); Zhu, Yang, Li, Du, and Lin (2015). One of the most recognized problems for limited sensor lifetime is related to the intrinsic instability of enzymes. Although GOx is quite stable compared to others, enzymatic glucose biosensors are continuously exposed to the risk of thermal and chemical deformation during fabrication, storage, and usage. GOx rapidly loses activity below pH 2 or above pH 8, and it completely loses its functionality above 40 °C S. Park, Boo, and Chung (2006); R. Wilson and Turner (1992). Consequently, biosensor fabrication including enzyme immobilization and device sterilization requires a careful planning to prevent chemical and temperature-induced enzyme inactivation S. Park et al. (2006).

To circumvent the issue of enzyme degradation, significant efforts has been focused on investigating the electrocatalysis of glucose without using an enzyme as the biorecognition molecule Si, Huang, Wang, and Ma (2013). The majority of non-enzymatic electrochemical glucose sensors generate electrical current by directly oxidizing glucose on the electrode surface D. W. Hwang, Lee, Seo, and Chung (2018). Nanoscopic electrodes, especially nanoporous electrocatalysts, are frequently employed due to their high active surface areas Bae, Han, and Chung (2012). These are ideal for a kinetically controlled, surface-bound reaction such as direct glucose oxidation Gollas, Elliott, and Bartlett (2000); Si et al. (2013); Toghill and Compton (2010). Noble metal nanoparticles are often used for their excellent conductivity, catalytic properties, and large surface area to promote a good

matrix for bio-adsorption of molecule onto the surface J. Yang, Jiang, Zhang, and Gunasekaran (2010); Zhao, Zhang, Bai, Yang, and Sun (2006). However, a major drawback of using single-metal metallic catalysts is that they oxidize various other endogenous interference species, such as L-ascorbic acid (AA), uric acid (UA), and 4-acetamidophenol (AP), in the potential range similar to direct glucose oxidation, resulting in poor selectivity.

Bimetallic alloys of nanoparticles are promising alternatives to achieve better selectivity because they oxidize glucose at a lower potential Holt-Hindle, Nigro, Asmussen, and Chen (2008); Nantaphol et al. (2017); J. Wang, Thomas, and Chen (2008). In addition, they are known for their superior electrocatalytic activity compared to single metal catalysts Duan and Wang (2013); Ferrando, Jellinek, and Johnston (2008); Guisbiers et al. (2014); J. Yang, Chen, Yang, and Ying (2012). Thus, here we used electrodeposition of gold-ruthenium alloy nanoparticles (Au-RuNPs) to create a bimetallic coating to fabricate a more selective non-enzymatic glucose biosensor. Electrodeposition is a simple modification process that can produce a high-purity surface with controllable particle size C. B. Hwang et al. (2000). The combination of Au and Ru in Au-RuNPs synergistically enhances the oxidative current from glucose and improves the selectivity compared to single-metal system. Their synergistic effect is due to their surface electronic states, which are greatly affected by changes in geometric parameters Mueller, Krtil, Kibler, and Jacob (2014); X. Wang et al. (2018).

Moreover, the supporting materials also play a major role in the performance of electrocatalysts due to their interactions, which facilitates the catalytic activities between metallic catalysts and support materials Hsu, Chien, and Jeng (2008). To achieve a fine dispersion and high utilization, nanocatalysts are usually supported on high-surface area materials such as carbon nanotubes (CNT), carbon nanofibers, graphene, or activated carbon Gallego et al. (2017); T. N. Nguyen et al. (2020); Nolan, Nguyen, Le, DeLong, and Lee (2020); Steigerwalt, Deluga, and Lukehart (2002); Z. Sun et al. (2011). This is due to the distinctive characteristics of such new carbon nanomaterials, such as more crystalline structures, high electrical conductivities, excellent corrosion resistances, and high purities Kim, Nam, Ma, and Kim (2006); Kingston et al. (2014); Tian, Prestgard, and Tiwari (2014). Hence, in this study, we employed our previously developed high-surface-area Pt-nanoparticle (PtNPs) CNT-based nanocomposite electrodes as an effective supporting material for one step electrodeposition of AuNPs and RuNPs for direct oxidation of glucose T. N. Nguyen et al. (2019b).

We used field-emission scanning electron microscopy (FESEM), X-ray photoelectron spectroscopy (XPS), energy dispersive X-ray spectroscopy (EDX), cyclic voltammetry (CV), and amperometry to verify the structural and electrochemical properties of Au-RuNPs catalysts. We also investigated the effects of different electrodeposition times and Au-RuNPs catalyst compositions on electrocatalytic activity and sensitivity to glucose. We found that our bimetallic system simultaneously has a good sensitivity and a wider dynamic range than previously developed non-enzymatic sensors. We employed a non-linear model to correlate the geometrical and chemical design parameters to the amperometric response of the sensor. This model confirmed our choice of using Au-RuNPs catalyst rather than other types of electroactive surfaces including Pt-Ru or PtNPs-based (single metal catalyst) biosensors. Finally, we showed that this new non-enzymatic glucose biosensor has good stability, reproducibility, and selectivity, which may be suitable for *in vivo* glucose detection in the future.

## 5.2 Experimental section

### 5.2.1 Chemicals

Gold (III) chloride hydrate ($HAuCl_4 \cdot xH_2O$, $\sim$50 % Au basis), Ruthenium (III) Chloride hydrate ($RuCl_3 \cdot xH_2O$, 99.98% trace metals basis), Chloroplatinic acid hydrate ($H_2PtCl_6 \cdot xH_2O$, $>$99.9 % trace metal basis), and PEDOT:PSS (5 wt.%), platinum nanoparticles ($<$50 nm particle size) were obtained from Sigma Aldrich (St. Louis, MO). Carboxylic functionalized multi-walled carbon nanotube (COOH-MWCNT, outer diameter: 10-20 nm, length: 10-30 $\mu$m, purity: $>$95 wt.%) were bought from Cheap Tubes Inc. (Grafton, Vermont). Sulfuric Acid ($H_2SO_4$, 95-98 %), 0.1 M phosphate buffer solution (PBS, pH 7.4), and dimethyl sulfoxide (DMSO), D-glucose, sucrose, lactose, fructose were obtained from Fisher Scientific (Waltham, MA). Ascorbic acid (AA) and uric acid (UA), and 4-acetamidophenol (AP) were purchased from Alfa Aesar (Thermo Fisher Scientific, Waltham, MA). Ag and Ag/AgCl ink (CI-1001) were purchased from Engineered Conductive Materials Inc. (Delaware, OH). Elastomeric polydimethylsiloxane (PDMS, Sylgard 184) was purchased from Dow Corning (Midland, MI). Ecoflex (00-30) was purchased from Smooth-On (Macungie, PA). The deionized water (DI) used was purified using Milli-Q (Millipore, Bedford, MA). Basal glucose concentrations from the whole blood and human serum were measured with test strips and glucometer (DS-W, Auvon, Peachtree Corners, GA). Whole porcine fresh blood ([glucose] = 2.585 mM) was collected from the animal facility of Biomedical Engineering Department at Purdue University. It was mixed with 10 USP units of heparin/ml and stored at 4 °C until measurements. Human serum ([glucose] = 4.785 mM) from human male AB plasma was obtained from Sigma-Aldrich (H4522, St. Louis, MO).

### 5.2.2 Apparatus and electrochemical measurements

Electrochemical preparation of the sensors and *in vitro* experiments were conducted using a commercial bench-top potentiostat (SP-200, Bio-logic USA, LLC, and Knoxville, TN, USA). All electrochemical evaluations were performed in 0.01 PBS (pH 7.4, 50 mL for all experiments).

A conventional three-electrode cell was used in electrodeposition, with the prepared nanocomposite as the working electrode, the silver/silver chloride (Ag/AgCl/NaCl (3M) (Bio-logic USA, LLC, Knoxville, TN, USA) as reference electrode, and a graphite rod as counter electrode. Two separated reference electrodes were used for electrodeposition and CV experiments. The scan rate of 20 mV/s or 100 mV/s were used for CV with 1 mV/s sampling interval. All CV experiments were performed in quiescent solution. Investigation of glucose sensing was done by using chronoamperometry. All amperometry data (i-t curve) were collected after 10 min of settling period unless stated otherwise. The amperometry was performed at a specified potential vs. Ag/AgCl/(3 M NaCl) with 0.3 s sampling interval. All amperometry was performed in a solution stirred at 240 rpm and in a Faraday cage. Amperometry was also used to test stability of the fabricated biosensors. The biosensors were stored dry in an oven at 37 °C when not in use.

For the experiment in biological fluids, Au-RuNPs-nanocomposite was used as the working electrode. Ag/AgCl ink and PtNPs nanocomposite ink were printed as reference and counter electrode, respectively, as shown in Fig. 5.1a. For each measurement, the three-electrode system was completely covered by 50 $\mu$l of sample.Márquez, Jiménez-Jorquera, Domínguez, and Muñoz-Berbel (2017) For each sample, 40 $\mu$l of whole blood or serum was mixed with 10 $\mu$l of DI water with varying glucose concentration, which produced different final glucose concentration in whole blood and human serum.

### 5.2.3 Surface characterization

The surface morphology of the nanocomposite and Au-RuNPs-nanocomposite was observed using a field-emission scanning electron microscopy (FESEM, S-4800, Hitachi, Japan). The morphology of the MWCNT and PtNPs base was also characterized by transmission electron microscopy (TEM, Tecnai G2 20, FEI Company, OR). The elemental composition was determined using an energy dispersive X-ray spectroscopy (EDX) attached to the FESEM system. The element and chemical composition of Au-RuNPs surface was further characterized by X-ray photoelectron spectroscopy (XPS) using a Kratos AXIS Ultra DLD Imaging X-ray Photoelectron Spectrometer.

### 5.2.4 Synthesis of PtNPs-MWCNT-based nanocomposite

To create the MWCNT-based nanocomposite, 25.32 mg of carboxylic functionalized MWCNT (1 wt.%) and 126.58 mg PtNPs (5 wt.%) were first mixed with 582 $\mu$l (11 wt.%) DMSO in a sonication bath for 2 h. The mixture then was added to 2000 mg PEDOT:PSS ink. The mixture was then transferred to a planetary centrifugal mixer (ARE-310, Thinky U.S.A., Inc, Laguna Hills, CA) and mixed for 1 h. Finally, 379.75 mg (16 wt.%) Ecoflex was added, mixed for 10 min, and degassed using the planetary centrifugal mixer for another 1 h. The final mixture was dried at 60°C in a vacuum for 1 h to remove excess DMSO and to reach the desired viscosity for printing.

### 5.2.5 Direct ink writing of the nanocomposite electrode

The fabrication process utilized direct ink writing of conductive inks by using a commercial automated fluid dispensing system (Pro-EV 3, Nordson EFD, East Providence, RI). A custom glass capillary pipette with a 30-$\mu$m-diameter tip was fabricated to dispense microscale features. The nanocomposite ink was used to define the working electrode, and the conductive traces. The silver Ag ink was used to print the contact pads. PDMS was then printed over the device to insulate the biosensor leaving only the working electrode exposed for electrochemical activity. By using a direct ink writing technique and our nanocomposite ink, the non-enzymatic glucose biosensor can be printed on any available substrate. Fig. 5.1a shows an example of a non-enzymatic biosensor, which was printed on a liquid crystal polymer (LCP) substrate. The nanocomposite working electrode was then used for one step electrodeposition of Au-RuNPs for direct oxidation of glucose. Fig. 5.1b on the left presents the nanocomposite surface before the electrodeposition of Au-RuNPs.

### 5.2.6 Synthesis of 1:3 Au-Ru alloy nanoparticles on PtNPs nanocomposite surface

The electrochemical deposition of Au-RuNPs on the nanocomposite was performed in 2.5 mM $HAuCl_4$ and 7.5 mM $RuCl_3$ in 0.2 M $H_2SO_4$ aqueous solution. Prior to the experiment, $H_2SO_4$ solution was deoxygenated with high purity nitrogen gas for 30 min to remove oxygen. $HAuCl_4$ and

$RuCl_3$ were added to the $H_2SO_4$ solution and then sonicated in an ice bath for complete dissolution ($\sim$ 5 h). The electrodeposition of Au-RuNPs was carried our for 180 s at $-0.2$ V vs. Ag/AgCl. The temperature of the solution was controlled at 4 °C using an ice bath in order to obtain smaller particles. The obtained Au-RuNPs was washed with distilled water and then dried at room temperature. Fig. 5.1b on the right presents the surface of Au-RuNPs after electrodeposition on the nanocomposite electrode. This method was modified from work by Xiao et al.'s Xiao, Zhao, Mei, Mo, and Zeng (2009). A different concentration, 3:1 $HAuCl_4$:$RuCl_3$ was also tested to optimize the best condition. As result, 1:3 $HAuCl_4$:$RuCl_3$ was chosen (Fig. 5.2). Electrodeposition time was also optimized between 120 s, 180 s and 300 s (Fig. 5.3). We explored different bimetallic systems such Pt-RuNPs before deciding on Au-RuNPs as the catalyst for non-enzymatic glucose sensor (Fig. 5.4).

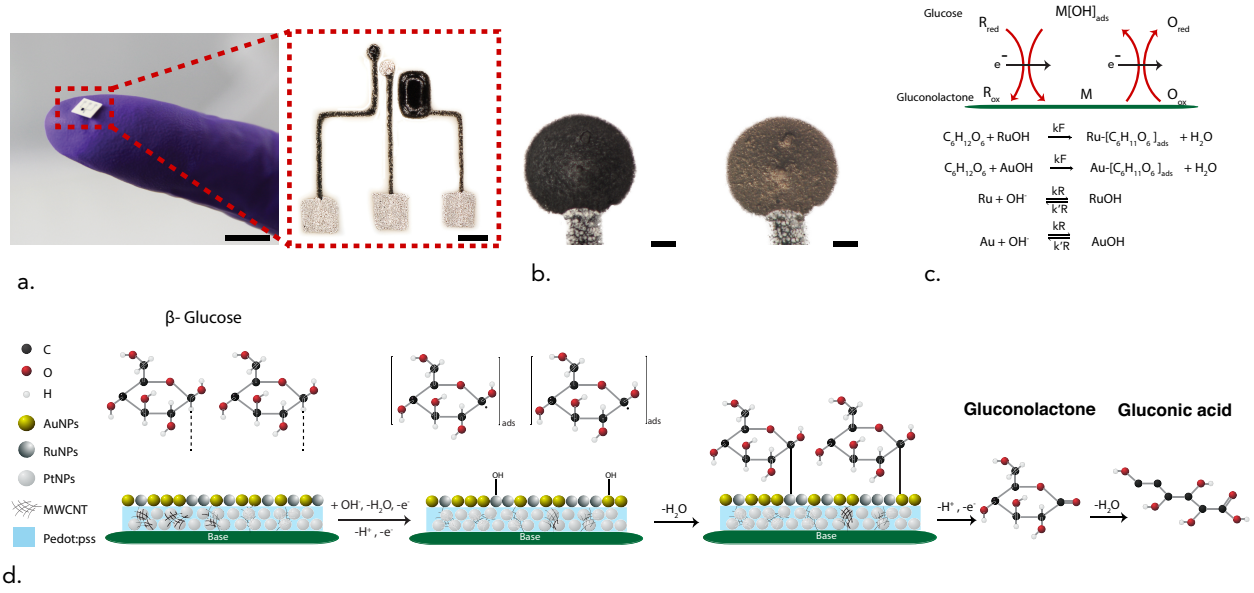


*Figure 5.1.* (a) Photographs of a flexible non-enzymatic glucose biosensor on LCP sheet (scale bars: 10 mm and 500 $\mu$m). (b) Photographs of the nanocomposite before (left side) and after electrodeposition of Au-RuNPs on the surface (right side) (scale bars: 200 $\mu$m). (c) (d) Schematic illustration of the possible mechanism for the electrocatalytic oxidation of glucose at Au-RuNPs on MWCNT-based nanocomposite surface along with possible chemical reactions between the metal nanoparticle surface and glucose molecules. (Reprinted with permission from T. Nguyen et al. (2020). Copyright 2020 American Chemical Society).

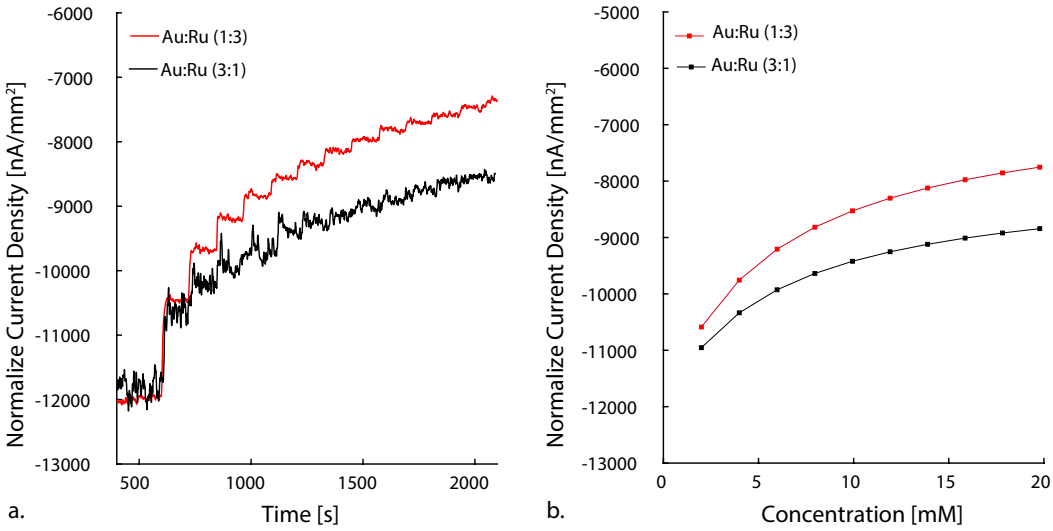


*Figure 5.2.* (a) Current-time curve obtained at Au-RuNPs biosensor with two different electrodepositing concentration of gold(III) chloride hydrate (HAuCl4) and ruthenium(III) chloride hydrate ($RuCl_3$) with successive addition of glucose with every 2 mM increment in 0.01 M PBS (pH 7.4) at − 0.1 V. (b) Non-linear feature of the steady-state response for glucose at Au-RuNPs biosensor with two different electrodepositing concentration of $HAuCl_4$ to $RuCl_3$ in 0.01 M PBS (pH 7.4) at − 0.1 V. (Reprinted with permission from T. Nguyen et al. (2020). Copyright 2020 American Chemical Society).

*Table 5.1.* Key fitting parameters in the simulation for experiment with two different electrodepositing concentrations of $HAuCl_4$ and $RuCl_3$. (Reprinted with permission from T. Nguyen et al. (2020). Copyright 2020 American Chemical Society).

| | Au:Ru (1:3) | Au:Ru (3:1) |
|---|---|---|
| N0 (mol/$m^2$) | 2.49E-05 | 1.85E-05 |
| kF ($m^3$ /s/mol) | 0.0867 | 0.0862 |
| kR (1/s) | 0.455 | 0.455 |
| k'R (1/s) | 0.044 | 0.044 |

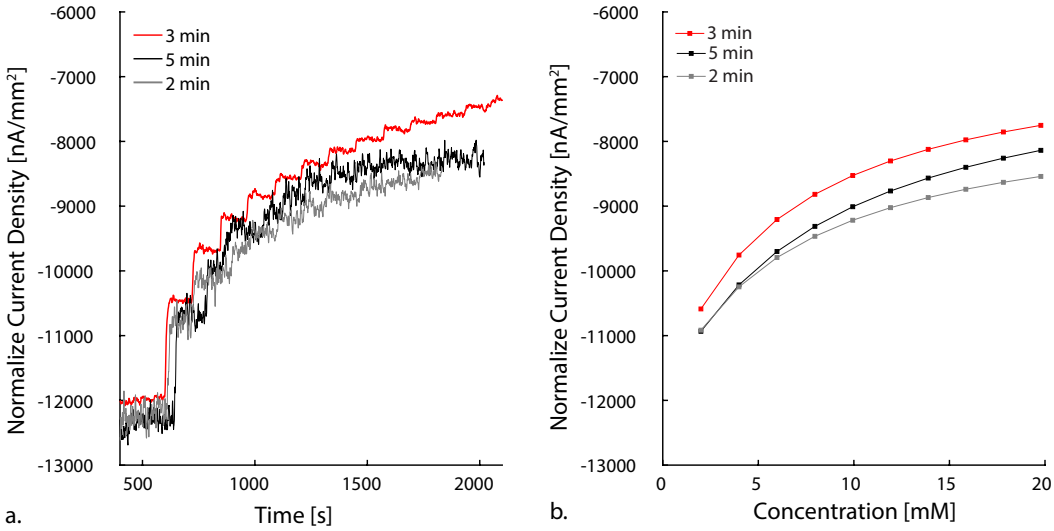


*Figure 5.3.* (a) Current-time curve obtained at Au-RuNPs biosensor with different electrodepositing time using 1:3 ratio of$HAuCl_4$ to $RuCl_3$ solution with successive addition of glucose with every 2 mM increment in 0.01 M PBS (pH 7.4) at − 0.1 V. (b) Non- linear feature of the steady-state response for glucose at Au-RuNPs biosensor with different electrodepositing time using 1:3 ratio of HAuCl4 to RuCl3 solution in 0.01 M PBS (pH 7.4) at − 0.1 V. (Reprinted with permission from T. Nguyen et al. (2020). Copyright 2020 American Chemical Society).

*Table 5.2.* Key fitting parameters in the simulation for experiment with different electrodepositing time using 1:3 ratio of $HAuCl_4$ to $RuCl_3$ solution. (Reprinted with permission from T. Nguyen et al. (2020). Copyright 2020 American Chemical Society).

| | Au:Ru (1:3) - 2 min | Au:Ru (1:3) - 3 min | Au:Ru (1:3) - 5 min |
|---|---|---|---|
| N0 ($mol/m^2$) | 2.08E-05 | 2.49E-05 | 2.48E-05 |
| kF ($m^3$ /s/mol) | 0.0774 | 0.0867 | 0.0605 |
| kR (1/s) | 0.455 | 0.455 | 0.455 |
| k'R (1/s) | 0.044 | 0.044 | 0.044 |

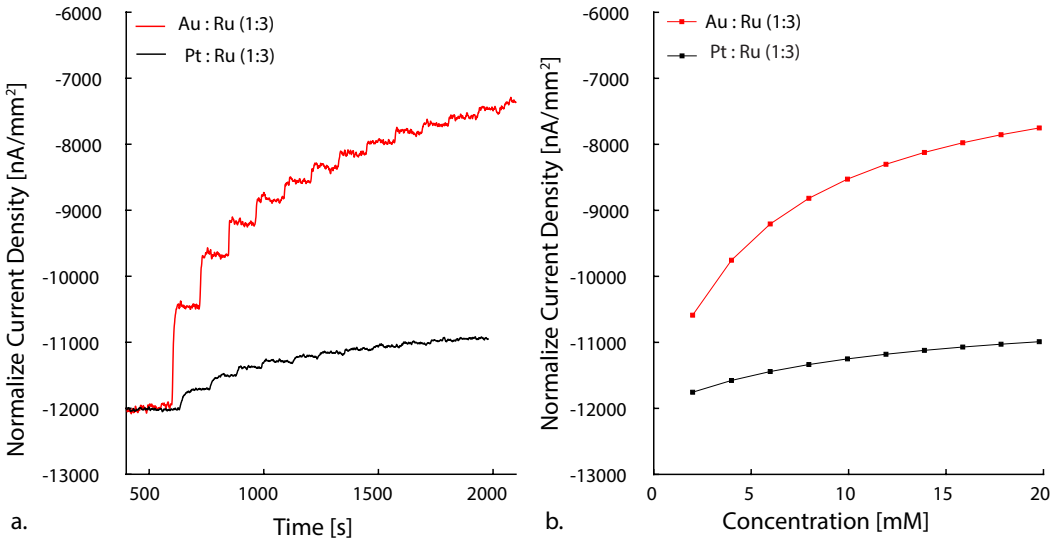


*Figure 5.4.* (a) Current-time curve obtained at Au-RuNPs biosensor with two different bimetallic systems, Au:Ru (1:3) and Pt:Ru (1:3), with successive addition of glucose with every 2 mM increment in 0.01 M PBS (pH 7.4) at − 0.1 V. (b) Non-linear feature of the steady-state response for glucose at two different bimetallic systems, Au:Ru (1:3) and Pt:Ru (1:3) in 0.01 M PBS (pH 7.4) at − 0.1 V. (Reprinted with permission from T. Nguyen et al. (2020). Copyright 2020 American Chemical Society).

*Table 5.3.* Key fitting parameters in the simulation for experiment with two different bimetallic systems, Au:Ru (1:3) and Pt:Ru (1:3). (Reprinted with permission from T. Nguyen et al. (2020). Copyright 2020 American Chemical Society).

| | Au:Ru (1:3) | Pt: Ru (3:1) |
|---|---|---|
| N0 (mol/m$^2$) | 2.49E-05 | 7.05E-06 |
| kF (m$^3$/s/mol) | 0.0867 | 0.0467 |
| kR (1/s) | 0.455 | 0.455 |
| k'R (1/s) | 0.044 | 0.044 |

## 5.3 Results and discussion

### 5.3.1 Morphological analysis

We used FESEM and TEM to examine the morphology of the MWCNT-based nanocomposite and the Au-RuNPs modified surface. Fig. 5.7a presents the surface morphology of the resulting nanocomposite before electrodeposition. It displayed a rough morphology, which is likely due to incorporation of PtNPs into the conductive polymer. We also used TEM to examine the composition of the nanocomposite ink. The inset of Fig. 5.7a presents the morphology of PtNPs in the MWCNT framework. TEM confirmed that PtNPs were aggregates of particles less than 50 nm in diameter. After the electrodeposition of Au-RuNPs on the surface of nanocomposite, we used FESEM again to re-examine the modified surface. Fig. 5.7b shows the deposition of Au-RuNPs on the surface. The nanoparticles were well dispersed with average size around 50 nm. One of the key attributes associated with superior electrocatalytic properties is high surface area because it increases molecular adsorption, $O_2$ reduction, and pseudo-capacitive behavior Lang, Hirata, Fujita, and Chen (2014); Sokolov, Tschulik, Batchelor-McAuley, Jurkschat, and Compton (2015). As such, the nanoporous morphology of our nanocomposite aggregate may improve the sensor performance Jiao et al. (2017); Lim, Tan, Sofer, and Pumera (2015).

Next, we characterized the elemental composition of the Au-RuNPs modified surface using EDX (Fig. 5.7c), which showed the weight percentage of each material. The EDX spectrum shows large peaks corresponding to Au (35.8 wt.%), Ru (0.8 wt.%) and Pt (13.7 wt.%). The spectrum also has peaks corresponding to C, O, S, and Si, which indicates the presence of PEDOT:PSS and MWCNT in the sample. The XPS also confirmed the presence of Au and Ru (Fig. 5.7d-f). The survey scan contains graphitic C1s peak at 282.1 eV, which overlap with Ru3d peaks. The XPS spectrum of Au4f core displays major peaks at 81.5 eV corresponding to the binding energy of $Au4f_{7/2}$ and 85.2 eV corresponding to the binding energy of $Auf_{5/2}$ (Fig. 5.7d). XPS analysis is consistent with reports for Au4f Govindasamy et al. (2018) and indicates the successful formation of Au on the surface Xue, Ma, Zhou, Zhang, and He (2015). XPS spectra for C1s-Ru3d core appear in Fig. 5.7e.

The C1s peak corresponds to the $sp^2$ carbon atom, which occurs at 282.1 eV Agnès et al. (2009); Y. Peng, Pan, Wang, Lu, and Chen (2018). This peak consists of several overlapping individual peaks belonging to C1s and $Ru3d_{3/2}$ photoelectrons. The other distinct peak at 279 eV corresponds to the binding energy of $Ru3d_{5/2}$ of metallic $Ru^0$ Y. Peng et al. (2018). These results suggest successful deposition of AuRu on the surface of the nanocomposite.

Although the amount of Ru nanoparticles was small at the surface of the biosensors (Fig. 5.7e), their presence was critical in creating the synergistic effects with Au nanoparticles to enable glucose measurements at $-0.1$ V and prevent electroactive interferences.Si et al. (2013) As shown in Fig. 5.5, the nanocomposite surfaces that was deposited with only Au nanoparticles was not able to detect glucose at $-0.1$ V. Moreover, we varied the $RuCl_3$ concentration in electrodeposited solution and assessed the biosensors catalytic performances to further analyze the role of RuNPs. Fig. 5.6a and b exhibit CVs of the AuNPs nanocomposite, Au-RuNPs (1:3) nanocomposite, and Au-RuNPs (1:5) nanocomposite in a solution of 0.01 M PBS (pH 7.4) and 2 mM glucose at a scan rate of 20 mV/s, respectively. Au-RuNPs (1:5) electrode showed the highest currently density compared to the other electrodes in PBS solution. However, in glucose-spiked samples, the anodic peak at $-0.1$ V, which is considered to be related to the direct electrooxidation of glucose, was the highest for Au-RuNPs (1:3). Thus, we used this composition as our electrode material to fabricate our non-enzymatic glucose biosensor.

### 5.3.2 Electrocatalytic activity for glucose oxidation in neutral media

We assessed the catalytic performance of Au-RuNPs toward glucose oxidation in neutral media. Fig. 5.8a shows CVs of the nanocomposite and Au-RuNPs modified electrode in a solution of 0.01 M PBS (pH 7.4) at a scan rate of 20 mV/s. Au-RuNPs electrode exhibited higher current density values and greater catalytic behavior than samples without Au-RuNPs. We also compared the CV profile of the nanocomposite in the presence of glucose at scan rate of 20 mV/s (Fig. 5.8b). The nanocomposite exhibited anodic peaks at approximately $-0.4$ V, $+0.2$ V, and $+0.6$ vs. Ag/AgCl, which can be attributed to multi-electron transfer of glucose oxidation on the nanocomposite surface Rathod et al. (2010); G. Wei, Xu, Li, and Jandt (2011).

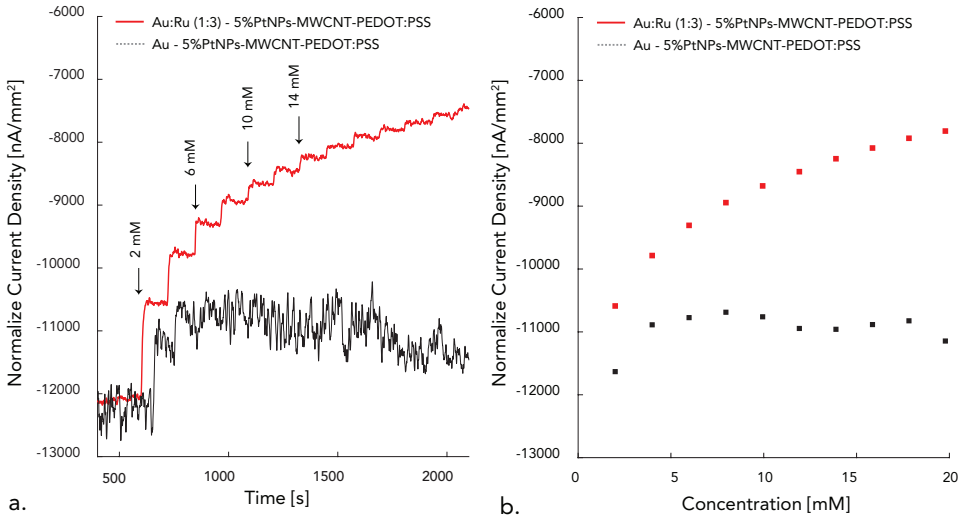


*Figure 5.5.* (a) Current-time curve obtained at Au-RuNPs nanocomposite biosensor and Au nanocomposite biosensor with successive addition of glucose with every 2 mM increment in 0.01 M PBS (pH 7.4) at − 0.1 V vs. Ag/AgCl. (b) Non-linear feature of the steady-state response for glucose at Au-RuNPs biosensor and Au nanocomposite biosensor in 0.01 M PBS (pH 7.4) at − 0.1 V vs. Ag/AgCl. (Reprinted with permission from T. Nguyen et al. (2020). Copyright 2020 American Chemical Society).

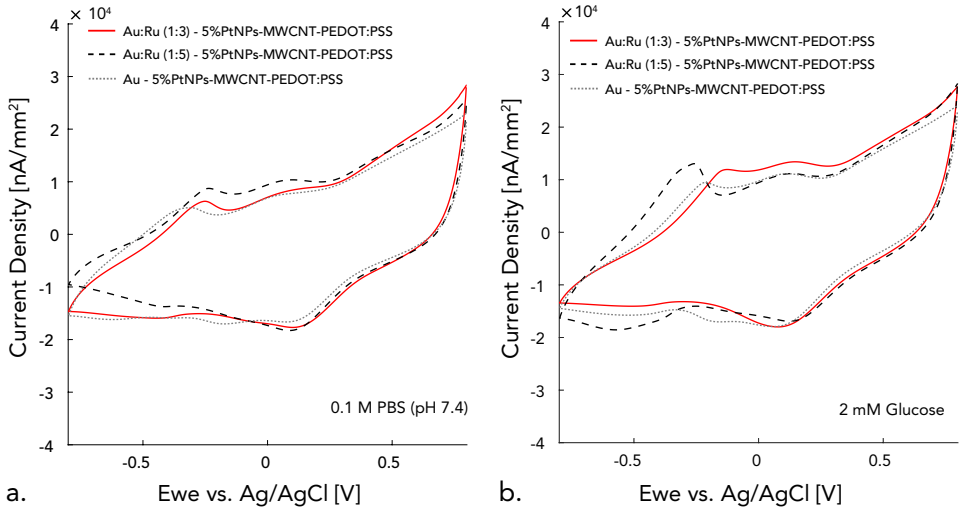


*Figure 5.6.* (a) Cyclic voltammetry of the Au-RuNPs (1:3)-nanocomposite, Au-RuNPs (1:5)-nanocomposite and Au-nanocomposite biosensors in 0.01 M PBS (pH 7.4). Scan rate = 20 mV/s. (b) Cyclic voltammetry of the Au-RuNPs (1:3)-nanocomposite, Au-RuNPs (1:5)- nanocomposite and Au-nanocomposite biosensors in 2 mM glucose. Scan rate = 20 mV/s. (Reprinted with permission from T. Nguyen et al. (2020). Copyright 2020 American Chemical Society).

After depositing Au-RuNPs, we saw two distinct cathodic reduction peaks at +0.05 V and −0.5 V. Previous studies on the electrocatalytic oxidation of organic molecules on bimetallic systems of noble metals have proposed a "bi-function mechanism," in which Ru dissociates water leaving adsorbed OH species ($Ru(OH)_{ads}$) H. Liu et al. (2006); Seland, Tunold, and Harrington (2008); Yi, Yu, and Niu (2010). As such, we predicted that $Ru(OH)_{ads}$ reacted with Au to form gold hydroxide in the solution Yi et al. (2010). Fig. 5.8c shows that in 2 mM glucose in 0.01 M PBS (pH 7.4), Au-RuNPs show high electroactivity toward glucose oxidation. We observed a large anodic peak around +0.2 V from the forward scan, which suggests that electrooxidation of glucose at Au-RuNPs may consist of multi-step electrode reactions Si et al. (2013); Yi et al. (2010). In addition, there is an anodic peak around −0.1 V, which is generally considered to be related to direct electrooxidation of glucose adsorbed onto the catalyst. Fig. 5.1c and Fig. 5.1d show a possible mechanism of direct glucose oxidation on the surface of Au-RuNPs.

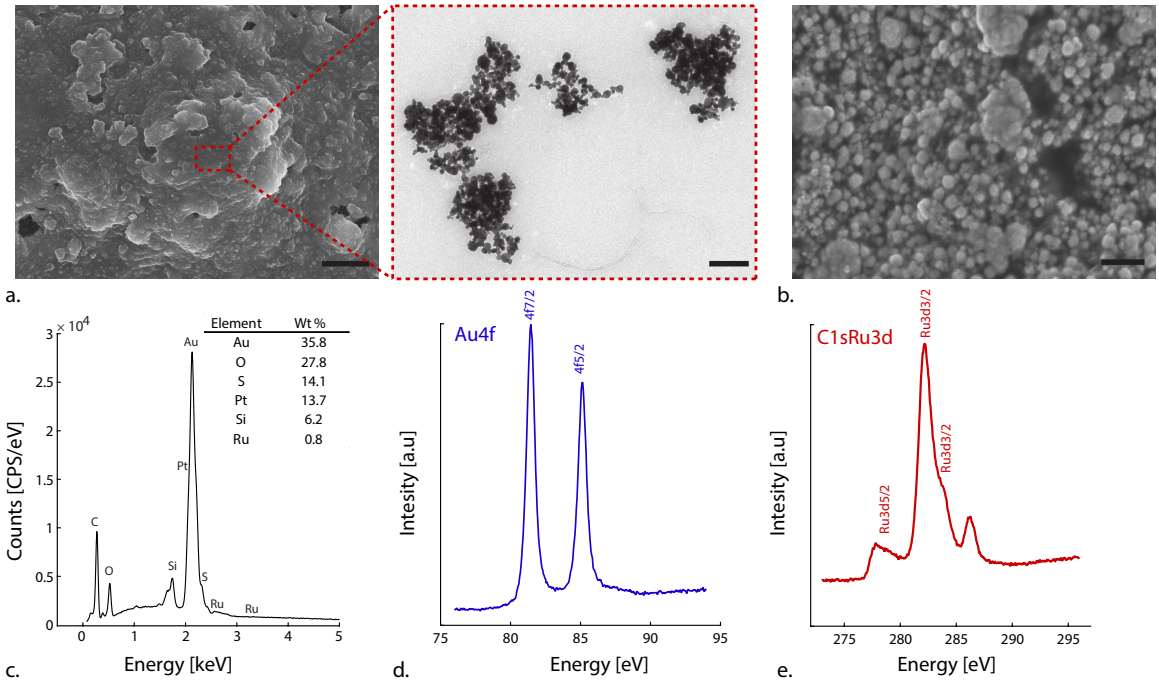


*Figure 5.7.* (a) Scanning electron micrographs of the nanocomposite (scale bars: 5 $\mu$m). Inset: transition electron micrographs of MWCNT-based nanocomposite (scale bar 200 nm). (b) Scanning electron micrographs of Au-Ru nanoparticles on MWCNT-based nanocomposite (scale bar: 250 nm). (c) EDX spectrum of fabricated Au-RuNPs-nanocomposite. XPS spectra of Au-RuNPs-nanocomposite (d) Au4f, (e) C1s-Ru3d. (Reprinted with permission from T. Nguyen et al. (2020). Copyright 2020 American Chemical Society).

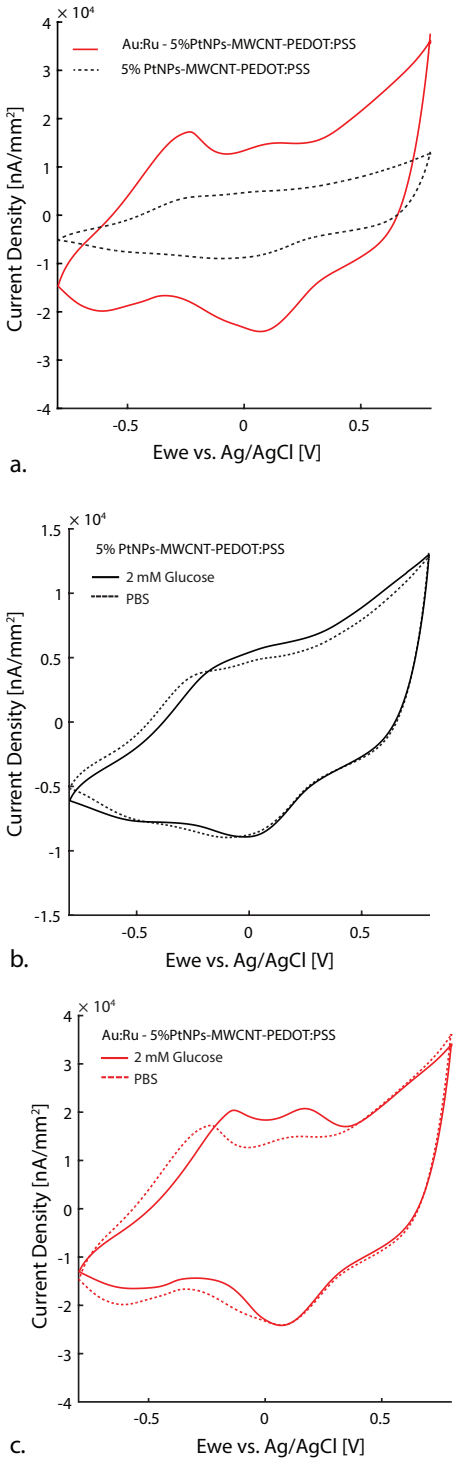


*Figure 5.8.* (a) Cyclic voltammetry of PtNPs-MWCNT-based nanocomposite and Au-RuNPs-nanocomposite biosensors in 0.01 M PBS (pH 7.4). Scan rate = 20 mV/s. (b) Cyclic voltammetry of the nanocomposite biosensors in 2 mM glucose. Scan rate = 20 mV/s. (c) Cyclic voltammetry of Au-RuNPs-nanocomposite biosensors. Scan rate = 20 mV/s. (Reprinted with permission from T. Nguyen et al. (2020). Copyright 2020 American Chemical Society).

Eq.5.1-5.4 describe possible chemical reactions between the metal nanoparticle surface and glucose molecules. $Ru(OH)_{ads}$ species with many active sites on their surfaces would reduce the energy of $OH^-$ adsorption onto Au, leading to enhancement of direct electrooxidation of glucose corresponding to the anodic peak around $-0.1$ V.

$$C_6H_{12}O_6 + RuOH \overset{kF}{\rightarrow} Ru[C_6H_{11}O_6]_{ads} + H_2O \tag{5.1}$$

$$C_6H_{12}O_6 + AuOH \overset{kF}{\rightarrow} Au[C_6H_{11}O_6]_{ads} + H_2O \tag{5.2}$$

$$Ru + OH^- \underset{k'R}{\overset{kR}{\rightleftharpoons}} RuOH + e^- \tag{5.3}$$

$$Au + OH^- \underset{k'R}{\overset{kR}{\rightleftharpoons}} AuOH + e^- \tag{5.4}$$

### 5.3.3 Non-linear analytical model

A linear approximation does not hold for a two-step reaction of the electrocatalytic oxidation of glucose, which includes oxidative adsorption of intermediates and follows with their oxidation. Furthermore, the geometrical and chemical features of sensors greatly impacts the linearity of biosensor response. Therefore, it is necessary to have an accurate non-linear model to explain the sensitivity of non-enzymatic glucose sensors. Recently, an analytical model has been developed, which attributed the linear range to the intrinsic properties of different reaction mechanisms Jin and Alam (2019).

In this study, a modified Butler-Volmer model was used and applied to our specific nanostructure surface. Au-RuNPs non-enzymatic glucose detection is modeled as two-step process described above (Eq.5.1-5.4). In this case, $k_F$ represents the forward reaction rate, while $k_R$ and $k'_R$ represent the forward and reverse reaction constants in equation Eq.5.2 and 5.3. $k_R$ and $k'_R$ follow the Butler-Volmer equation with electrode bias potential.

The model applies classical diffusion in eq.5.5. Eq.5.5 and 5.6 quantify the mass transport of glucose, which is a diffusion-limited process in bulk solution, before they reach the electrode surface. In this case, natural convection from secondary transport phenomena is not considered. Since Au-RuNPs are immobilized on the nanocomposite electrode surface, the oxidation reaction only happens when glucose molecules diffuse near the electrode surface. Reaction flux is described in eq.5.6 and the surface glucose absorption flux is defined as:

$$\frac{\mathrm{d}G}{\mathrm{d}t} = D\nabla^2 G \tag{5.5}$$

$$J_{rec} = k_F \cdot N_M \cdot G_s \tag{5.6}$$

with the glucose diffusion coefficient in the bulk sample solution D, glucose concentration G, the surface density of metal nanoparticles $N_M$, and the bulk glucose concentration near the nanoparticle surface $G_s$. In eq.5.7, the reaction flux $J_{rec}$ was coupled with electrode surface density of Au(OH)$_{ads}$-Ru(OH)$_{ads}$, which can be presented as the sum of forward and reverse reaction flux:

$$\frac{\mathrm{d}N_{M-OH}}{\mathrm{d}t} = k_F N_M G_s - (k'_R N_{M-OH}) \tag{5.7}$$

where $N_M$ represents Au-Ru (M) and $N_{M-OH}$ represents Au(OH)$_{ads}$-Ru(OH)$_{ads}$ (M-OH), which follow the total metal elements conservation $N_0$:

$$N_M + N_{M-OH} = N_0 \tag{5.8}$$

It is worth mentioning that pH plays an important role in non-enzymatic glucose sensing systems. Many studies have been conducted at pH $> 9$ to ensure sufficient $OH^-$ supply for the chemical reactions. Consequently, the concentration of $OH^-$ is not the rate-limiting factor but the surface density of $M(OH)_{ads}$ - $N_{M-OH}$. Therefore, in our model, pH-dependence is not included. Moreover, all of the experiments in this study were conducted in PBS at pH 7.4. The model can be solved analytically to find the coupled diffusion and surface reaction rates from eq.5.5-5.8. By applying "diffusion equivalent capacitance" Nair and Alam (2006), the steady-state diffusive flux of glucose in bulk solution can be written as:

$$J_{diff} = C_D \cdot \frac{G_0 - G_s}{A_e} \tag{5.9}$$

Where $C_d$ is the equivalent diffusion capacitance for the nanostructured electrode. $G_s$ is glucose concentration near the electrode surface and $G_0$ is bulk glucose concentration Jin and Alam (2019); Nair and Alam (2013). $A_e$ represents the surface area of a single nanoelectrode. Sensor response can be obtained by solving eq.5.5-5.9 and rewriting the equations in normalized form with unitless variables: $N_M^* = \frac{N_M}{N_0}$, $N_{M-OH}^* = \frac{N_{M-OH}}{N_0}$, $G_s^* = \frac{G_s}{G_0}$, $\gamma = \frac{C_D}{A_e k_F N_0}$, $\alpha = \frac{k_R}{k_F G_0'}$, $\beta = \frac{k_R'}{k_F G_0}$. More information on the exact solution can be find in a recent study from Jin et al., 2019 Jin and Alam (2019).

Unknown variables $N_M^*$, $N_{M-OH}^*$ and $G_s^*$ can be solved with approximated expression for $N_M^*$ and $N_{M-OH}^*$:

$$N_M^* \approx \frac{\alpha}{(\alpha + \beta + 1) - \frac{\alpha}{\gamma}} \tag{5.10}$$

$$N_{M-OH}^* = 1 - N_M^* \approx \frac{G_0 + (\frac{k_R'}{k_F} - \frac{A_e k_R N_0}{C_D})}{G_0 + (\frac{k_R + k_R'}{k_F} - \frac{A_e k_R N_0}{C_D})} \tag{5.11}$$

The final amperometric response of the glucose sensor can be expressed as a function of $N_{M-OH}$:

$$j = i/A_eff = q \cdot N_A \cdot (k_R N_{M-OH} - k_R' N_M) \approx q \cdot N_A \cdot (k_R + k_R') \cdot N_0 \cdot (N_{M-OH}^* - \frac{k_R'}{k_R + k_R'}) \tag{5.12}$$

$A_{eff}$ describes effective electrode surface area. $N_A$ is the Avogadro constant. Based on this model, the steady-state amperometric response of the Au-RuNPs non-enzymatic sensors was modeled and is presented as solid lines in Fig. 5.9b, Fig. 5.9d, and Fig. 5.9f.

### 5.3.4 Amperometric response of fabricated biosensors for non-enzymatic glucose detection

We first investigated amperometric glucose sensing using the nanocomposite electrode (Fig. 5.9a and Fig. 5.9b). The nanocomposite at $+0.5$ V was able to non-enzymatically sense glucose in 0.01 M PBS (pH 7.4). Fig. 5.9b takes this calibration data and compares a linear fit to the non-linear model. Root-mean-square error (RMSE) of the physic-based model is 0.0596, much less than the RMSE of a conventional linear fit, 0.1292. However, at this operating potential, the nanocomposite oxidizes interferents such as AA and AP much faster than it oxidizes glucose. We predicted that Au-RuNPs modified electrode would have better selectivity than the nanocomposite alone.

In order to find an optimum operating potential, we calibrated the Au-RuNPs biosensor at various potentials from $-0.15$ V to $+0.15$ V to glucose in 0.01 M PBS (pH 7.4) (Fig. 5.9c). We found that the bias potential of $-0.1$ V vs. Ag/AgCl resulted in the greatest sensitivity. Fig. 5.9d shows the impact of electrode voltage bias by fitting the data from Fig. 5.9c to the non-linear model. In this case, surface density of Au-Ru, $N_0$, and forward reaction constant remain the same, while the voltage dependent reaction constants $k_R$ and $k'_R$ change as shown in Table 5.4. At the optimum electrode bias potential, $-0.1$ V, $k_R$ is maximized and $k'_R$ is minimized. Therefore, we chose $-0.1$ V as the optimal potential for amperometric glucose sensing by Au-RuNPs biosensor.

Fig. 5.9e shows the current response of Au-RuNPs and the nanocomposite to glucose while calibrated at $-0.1$ V vs. Ag/AgCl. Fig. 5.9f shows the steady-state amperometric response for both catalysts at $-0.1$ V potential and the effect of adding Au-RuNPs on the surface of the nanocomposite. Au-RuNPs had a higher sensitivity compare to the nanocomposite alone. Table 5.4 shows that adding Au-RuNPs increases the total metal catalyst density $N_0$ and the forward reaction constant $k_F$.

Eq.5.12 may be used for calibrations over the full range of glucose concentration, estimating uncertainty or saturation limit of output current. On the other hand, a reasonable linear relationship between steady state current and glucose concentration can be established between 1 and 10 mM with a sensitivity of 0.2347 nA $\mu\text{M}^{-1}$ $\text{mm}^{-2}$ $\pm$ 0.0198 (n=3). The limit of detection was calculated to be 0.068 mM (S/N=3). Table 5.5 compares our non-enzymatic glucose biosensor to previously reported non-enzymatic glucose biosensors.

*Table 5.4.* List of key fitting parameters in the simulation for each respective experiment. (Reprinted with permission from T. Nguyen et al. (2020). Copyright 2020 American Chemical Society).

| | Type | $N_0$ | $k_F$ ($m^3$/s/mol) | $k_R$(1/s) | $k'_R$(1/s) |
|---|---|---|---|---|---|
| **Figure 4b** | Nanocomposite only at 0.5 V | $2.5\text{x}10^{-5}$ | $2.6\text{x}10^{-2}$ | 0.064 | 0.075 |
| **Figure 4d** | Au-RuNPs at 0.15 V | $2.5\text{x}10^{-5}$ | $8.5\text{x}10^{-2}$ | 0.085 | 0.819 |
| | Au-RuNPs at 0.1 V | $2.5\text{x}10^{-5}$ | $8.5\text{x}10^{-2}$ | 0.176 | 0.357 |
| | Au-RuNPs at 0 V | $2.5\text{x}10^{-5}$ | $8.5\text{x}10^{-2}$ | 0.435 | 0.443 |
| | Au-RuNPs at $-0.1$ V | $2.5\text{x}10^{-5}$ | $8.5\text{x}10^{-2}$ | 0.435 | 0.059 |
| | Au-RuNPs at $-0.15$ V | $2.5\text{x}10^{-5}$ | $8.5\text{x}10^{-2}$ | 0.435 | 0.044 |
| **Figure 4f** | Au-RuNPs at $-0.1$ V | $2.5\text{x}10^{-5}$ | $8.5\text{x}10^{-2}$ | 0.455 | 0.044 |
| | Nanocomposite only at $-0.1$ V | $1.4\text{x}10^{-5}$ | $7.7\text{x}10^{-3}$ | 0.455 | 0.044 |

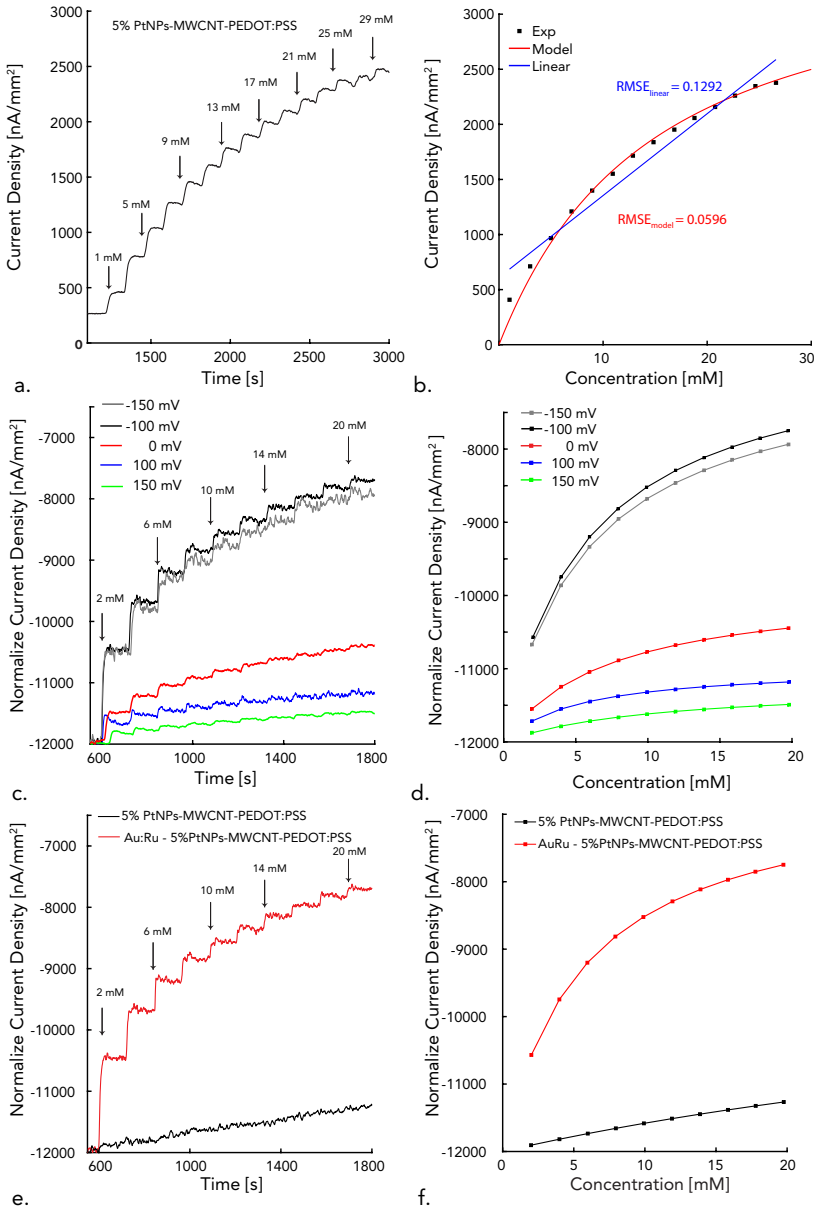


*Figure 5.9.* (a) Current-time curve obtained using our nanocomposite biosensor with successive addition of glucose from 1 mM up to 29 mM of glucose with every 2 mM increment in 0.01 M PBS (pH 7.4). (b) Linear fit for glucose using the nanocomposite electrode compared to the non-linear model of the steady-state response of the nanocomposite glucose sensor. (c) Current-time curve obtained with Au-RuNPs-nanocomposite biosensor with successive addition of glucose with every 2 mM increment in 0.01 M PBS (pH 7.4) at different potentials. (d) Non-linear feature of the steady-state response for glucose with Au-RuNPs-nanocomposite electrode at different potentials. (e) Current-time curve obtained at Au-RuNPs-nanocomposite biosensor and the nanocomposite with successive addition of glucose at 2 mM increments in 0.01 M PBS (pH 7.4) at $-0.1$ V. (f) Non-linear feature of the steady-state response for glucose with Au-RuNPs-nanocomposite biosensor and the nanocomposite with successive addition of glucose in 0.01 M PBS (pH 7.4) at $-0.1$ V. (Reprinted with permission from T. Nguyen et al. (2020). Copyright 2020 American Chemical Society).

### 5.3.5 Selectivity, reproducibility, stability, reusability and performance in biological fluids

The selectivity of non-enzymatic based glucose sensors is a challenge due to the lack of a specific biorecognition agent. Fig. 5.11a shows that the Au-RuNPs biosensor was selective to glucose over other sugars including fructose, sucrose, and lactose. We also evaluated the response of our biosensor physiological levels of ascorbic acid (AA), uric acid (UA), 4-acemitadophenol (AP). As seen in Fig. 5.11b, there is negligible interference from AA, UA, or AP. The selectivity of the non-enzymatic glucose sensor is a result of the lower operating potential used, below the peak oxidation potentials of the interferents.

Next, we evaluated the reproducibility and stability of our non-enzymatic glucose sensors. We tested the amperometric responses of 5 different Au-RuNPs biosensors to 2 mM of glucose independently and measured a relative standard deviation (RSD) value of 3.87%. We investigated the long-term stability of the sensors by monitoring the changes in biosensor sensitivity over three weeks. We stored the biosensors in an oven at 37 °C when not in-use. Our results showed that biosensors maintained more than 87% of their sensitivity to 2 mM glucose after three weeks (Fig. 5.10). This suggests that our non-enzymatic glucose sensor has a long-term stability at body temperature. Thus, we concluded our Au-RuNPs-modified electrode is suitable for the fabrication of sensitive, repeatable, and stable non-enzymatic amperometric glucose sensors.

We also evaluated the reusability of the biosensor by calibrating the device multiple times at various glucose concentrations. In general, we observed decreased current responses with each calibration. However, we were also able to electrochemically regenerate the biosensor using five cycles of CVs (0 and 1.5 V in 0.5 M $H_2SO_4$ with scan rate = 100 mV $s^{-1}$)W. C. Lee et al. (2019); Márquez et al. (2017). Fig. 5.12 shows the comparison of the normalized current density between the first and the seventh calibration of our biosensor ($n = 5$). We believe this result demonstrates the stability of our low-cost biosensor (Table 5.6-5.7) and their potential application in a closed system that allows surface regeneration (i.e., lab-on-a-chip) Economou, Kokkinos, and Prodromidis (2018); Márquez et al. (2017).

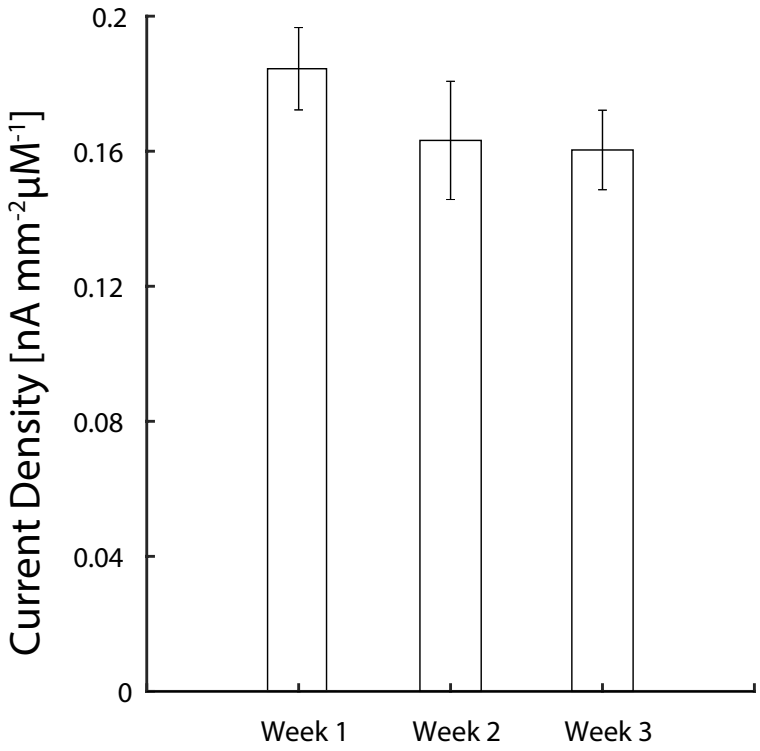


*Figure 5.10.* Biosensor lifetime measurement where the glucose sensitivity for Au-RuNPs biosensors were monitored over a period of 3 weeks (n=4). The sensors were stored in an oven at 37 °C when they were not in use. (Reprinted with permission from T. N. H. Nguyen et al. (n.d.). Copyright 2020 American Chemical Society).

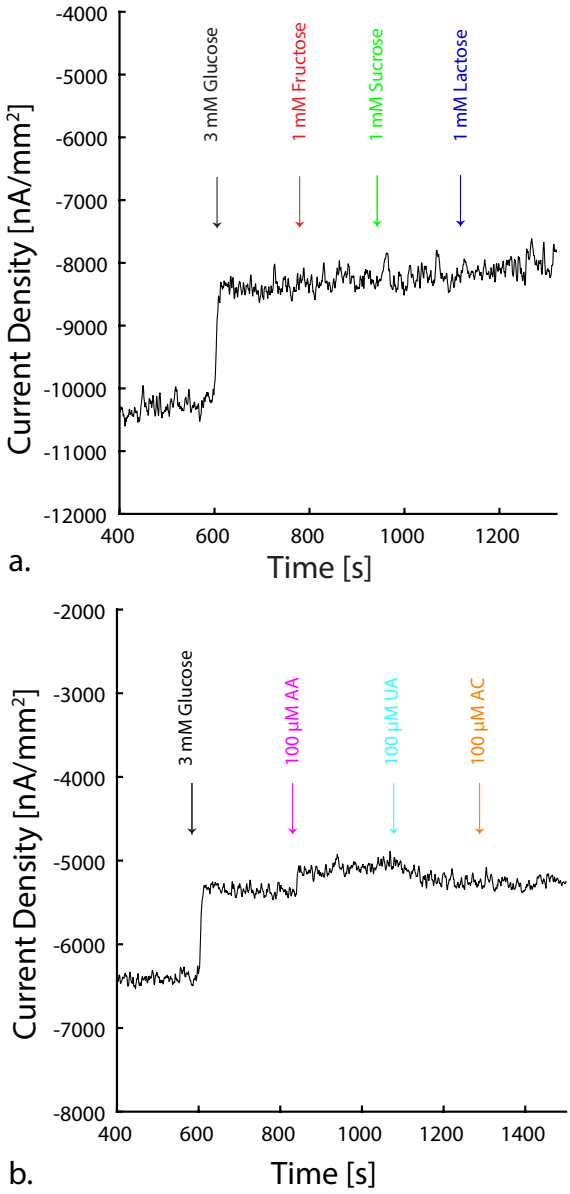


*Figure 5.11.* (a) Interference study for Au-RuNPs-nanocomposite in 0.01 M PBS (pH 7.4) with successive addition of glucose, fructose, sucrose, and lactose. (b) Interference study for Au-RuNPs-nanocomposite in 0.01 M PBS (pH 7.4) with successive addition of glucose, AA, UA, AP. (Reprinted with permission from T. Nguyen et al. (2020). Copyright 2020 American Chemical Society).

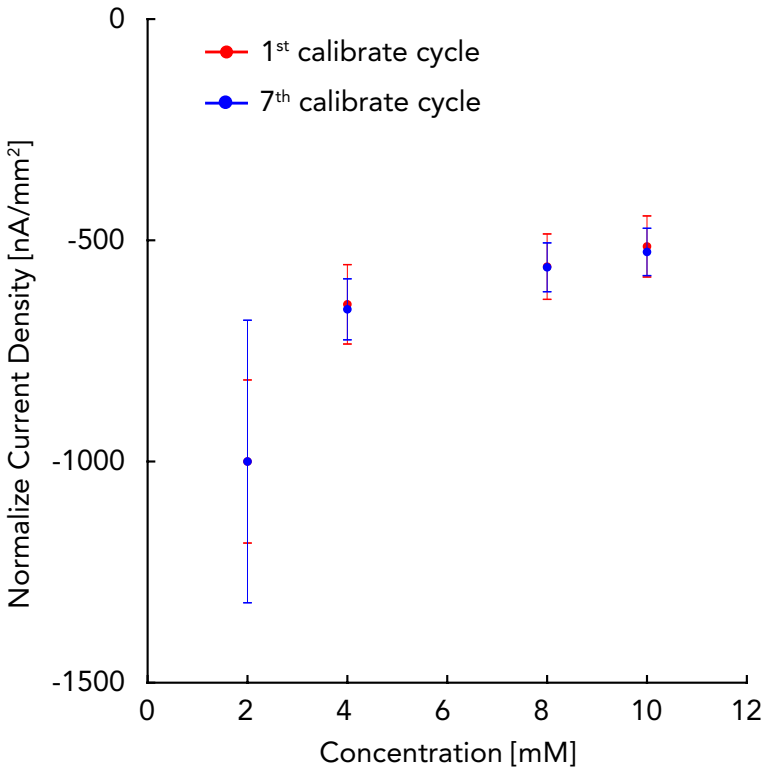


*Figure 5.12.* Non-linear feature of the steady-state response for glucose with Au-RuNPs-nanocomposite biosensor to different glucose concentration at detection potential of −0.1 V vs. Ag/AgCl through continuous calibration cycles. The sensor was washed with DI water between calibrations and cleaned electrochemically with 5 cyclic voltammetries between 0 and 1.5 V in 0.5 M H2SO4. Scan rate = 100 mV $s^{-1}$ W. C. Lee et al. (2019); Márquez et al. (2017). (Reprinted with permission from T. Nguyen et al. (2020). Copyright 2020 American Chemical Society).

Finally, we measured glucose concentration from human serum and porcine whole blood samples directly using our biosensors at various simulated pre-diabetic and diabetic conditions. Fig. 5.13 shows the amperometric responses for various glucose concentrations at −0.1 V potential in human serum and porcine whole blood ($n = 4$ each). We saw substantial changes in current responses between health an pre-diabetic ranges in both serum and blood. We believe these results demonstrate the capability of our biosensors to differentiate physiologically-relevant glucose concentrations in biological media. By taking the non-linear responses of these non-enzymatic biosensors into account, we may also be able to improve the range and performance of these biosensors for future in vitro and in vivo diagnostic applications.

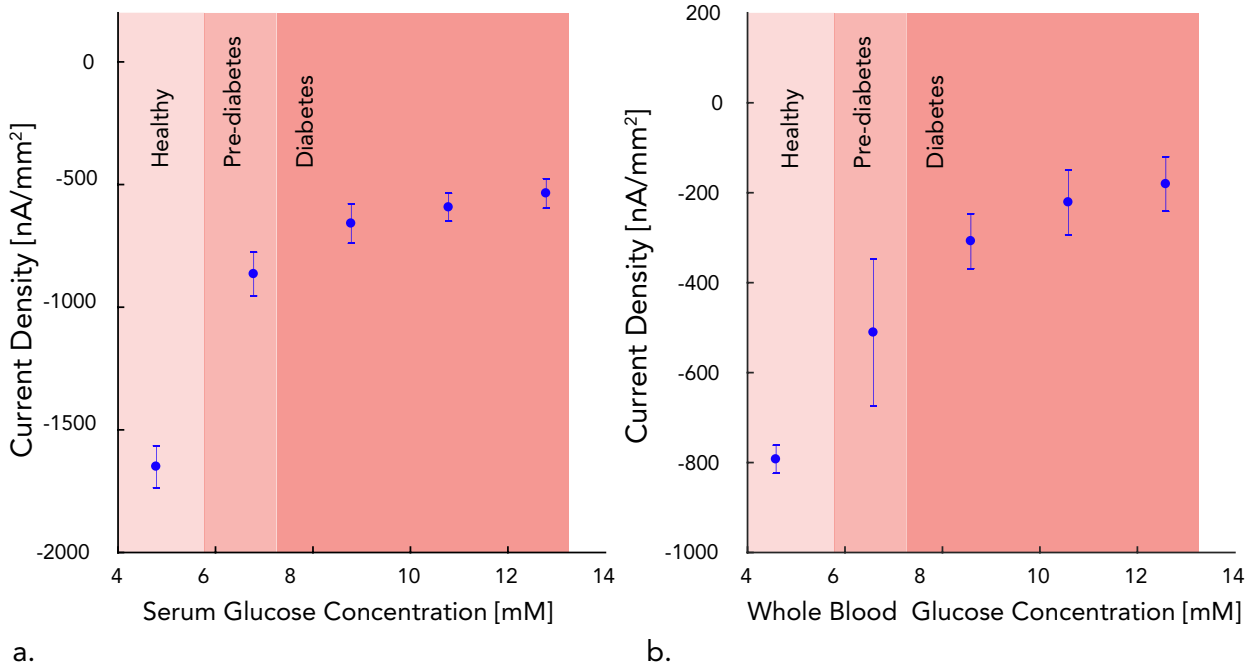


*Figure 5.13.* Non-linear feature of the steady-state response for glucose with Au-RuNPs-nanocomposite biosensor to different glucose concentration in (a) human serum and (b) porcine whole blood (n=4) with detection potential of −0.1 V vs. Ag/AgCl. The stabilization time of the chronoamperometry is 4 min. (Reprinted with permission from T. Nguyen et al. (2020). Copyright 2020 American Chemical Society).

*Table 5.5.* Detection performances of non-enzymatic glucose biosensors. (Reprinted with permission from T. Nguyen et al. (2020). Copyright 2020 American Chemical Society).

| Catalyst | Substrate | Sensitivity (nA $\mu M^{-1}$ $mm^{-2}$) | Limit of detection (mM) | Linear range (mM) | Operational Potential | Selectivity | Medium | Reference |
|---|---|---|---|---|---|---|---|---|
| Pt/Ru/MWCNTs/IL | GCE/FTO | 0.107 | 0.050 | 0.2-15 | -0.1 vs. SCE | AA, UA, AP, Fructose | PBS (pH 7.4) | Xiao et al. (2009) |
| PtRu NPs/MWCNTs | GCE | 0.282 | 0.025 | 1-15 | +0.55 vs. Ag/AgCl | AA, DA, UA | 0.1 M NaOH | L. H. Li, Zhang, and Ye (2008) |
| PtAu/MWCNT | Thin film Pt and Au | 0.107 | 0.010 | 24.4 | +0.3 vs. Ag/AgCl | AA,UA,AP | PBS (pH 7.4) | Ryu, Kim, Kim, Hahn, and Lashmore (2010) |
| PtAu/C nanocomposite | GCE | 0.047 | 0.002 | 0-10 | +0.35 vs. Ag/AgCl | AA,UA,AP, DA | PBS (pH 7.4) | Singh, Laffir, McCormac, and Dempsey (2010) |
| PtAu/C powder Nafion | GCE | 0.128 | 0.001 | 0.2-4.8 | +0.35 vs. Ag/AgCl | AA, DA, UA | PBS (pH 7.4) | J. Wang, Zhao, and Xu (2016) |
| PtAu/Nanofiber | BDD/Si wafer | N/A | 0.006 | 0.01-7.5 | -0.15 vs. Ag/AgCl | AA, AP, UA, NaCl | PBS (pH 7.4) | Nantaphol et al. (2017) |
| PtRu-PtSn | GCE | N/A | 0.700 | 0.0001-4 | -0.1 vs. Ag/AgCl | AA, UA | 0.1 M NaOH | Kwon, Kwen, and Choi (2012) |
| PtPd | GCE | 0.001 | 0.120 | 1-2.5 | -0.02 vs. Ag/AgCl | AA ,UA, AP | PBS (pH 7.4) | Bo, Bai, Yang, and Guo (2011) |
| PtAu nanocorals | GCE | 0.021 | 0.028 | 22 | +0.4 vs. Ag/AgCl | AA, UA | PBS (pH 7.4) | Y. Liu, Ding, Zhang, and Lei (2012) |
| Au-RuNPs | PtNPs-MWCNT nanocomposite | 0.234 | 0.068 | 10 | -0.1 vs. Ag/AgCl | AA, UA, AP, Fructose, Sucrose, Lactose | PBS (pH 7.4) | This work |

Note: N/A = not applicable, AA: ascorbic acid, UA: uric acid, AP: 4-acetamidophenol, DA: dopamine

*Table 5.6.* Estimate fabrication cost for one Au-RuNPs-nanocomposite non-enzymatic biosensor. (Reprinted with permission from T. Nguyen et al. (2020). Copyright 2020 American Chemical Society).

| Type of electrode | Fabrication method | Estimated cost |
|---|---|---|
| Au-RuNPs-PtNPs nanocomposite | Direct ink writing/Electrodeposition | $0.83/device |

*Table 5.7.* Break down fabrication cost for each ink batch. (Reprinted with permission from T. Nguyen et al. (2020). Copyright 2020 American Chemical Society).

| Chemical | Size (mg) | Cost ($) | Amount need for 1 batch (mg) | Cost for 1 batch ($) | Total cost for 1 batch ($) | Cost for each device ($) |
|---|---|---|---|---|---|---|
| $HAuCl_4$ | 1000 | 114.3 | 42 | 4.80 | 166.42 | 0.83 |
| $RuCl_3$ | 1000 | 43.2 | 77 | 3.33 | | |
| PtNPs | 250 | 283.5 | 126.58 | 143.54 | | |
| MWCNT | 1000 | 17 | 25 | 0.43 | | |
| PEDOT:PSS | 25000 | 179.1 | 2000 | 14.33 | | |

## 5.4 Conclusion

In summary, we have successfully developed a non-enzymatic glucose sensor using a one-step electrodeposition of Au-RuNPs on MWCNT-based nanocomposite. The nanocomposite electrodes was fabricated using a rapid and template-free method. In this study, direct glucose oxidation on the nanocomposite electrode was investigated both using voltammetric and amperometric methods. Additionally, a non-linear model was used to correlate the geometrical and chemical design parameters to the non-linear response of the glucose sensor. The Au-RuNPs electrode gave a good current response to glucose owing to its high active surface area and the synergistic effect of Au and Ru on the surface, as well as due to PtNPs and MWCNT underneath. The fabricated sensor also provided good reproducibility, selectivity, and stability for glucose determination, which are necessary attributes for future in vivo and other applications.

# CHAPTER 6. CONCLUSION AND FUTURE DIRECTIONS

## 6.1 Conclusion

The present doctoral thesis work attempts to overcome some of the challenges experienced by the fabrication process for implantable electrochemical biosensors. Notably, through this research, the first example of direct ink writing implantable glutamate biosensors have been demonstrated. This work has explored the synthesis and fabrication of different composite inks, the effect of different surface modifications, and their *ex vivo* and *in vivo* neurotransmitter sensing applications. Through this study, the electrode surface properties were characterized and then correlated to their electrochemical performance. These devices exhibited high electrocatalytic activity and good selectivity toward glutamate. They also possessed the necessary flexibility that we can use for implantation in biological tissues. As a result, these biosensors have significant implications in the rapid fabrication of electrochemical biosensors that we can use in different *in vitro* and *in vivo* applications.

### 6.1.1 Summary of results

In Chapter 2, we introduced and discussed the synthesis and characterization of nanocomposites electrodes made of PtNPs, MWCNTs, and a conductive polymer, PEDOT:PSS on a flexible substrate. We designed a sensor to measure the extracellular dynamics of glutamate and other potential biomarkers during a traumatic SCI event. Here we demonstrated good sensitivity and selectivity of these rapidly prototyped implantable that we can insert into a spinal cord ex vivo and measure extracellular glutamate concentration. We showed that our biosensors exhibit good flexibility, linear range, repeatability, and stability suitable for *in vivo* evaluation. In the future work, we plan to carry out additional *ex vivo* and *in vivo* work during SCI to verify the functionality in a more complex biological environment. We may be able to understand better the effects of GET in SCI *in vivo* at higher spatial and temporal resolution.

In Chapter 3, we demonstrated another type of composite ink that is even simpler and lower cost using commercially available activated carbon with Pt microparticles to fabricate highly sensitive glutamate biosensor using direct ink method. The fabricated biosensors are functionality superior compared to previously reported PtNPs nanocomposite ink. In this study, we utilized astrocyte cell culture to demonstrate our biosensor's ability to monitor the glutamate uptake process. We also presented a direct measurement of glutamate release from optogenetic stimulation in mouse primary visual cortex (V1) brain slices. In future work, we plan to print a multielectrode array to measure at specific distances simultaneously and to characterize the astrocyte-mediated glutamate concentration gradient better. Furthermore, we plan to apply similar fabrication techniques for other sensing applications using different recognition elements.

Chapter 4 presented the use of a perovskite nickelate-Nafion heterostructure as a promising glutamate sensor with a low detection limit in nano range and better response time. We designed and successfully tested the novel perovskite nickelate-Nafion electrodes for recording glutamate release *ex vivo* in electrically stimulated brain slices and *in vivo* from the primary visual cortex (V1) of awake mice exposed to visual stimuli. These results demonstrated the potential of perovskite nickelates as sensing media for brain-machine interfaces. In the future work, we intend to apply different types of permselective membranes such as m-phenylenediamine dihydrochloride to improve selectivity for these sensors. We will also include a final layer of ascorbate oxidase enzyme to prevent the interferences further. Additionally, we plan to print a multielectrode array with control electrodes combining with appropriate reference sensing methods to obtain a better selective signal for glutamate in biological tissues.

In Chapter 5, we demonstrated an amperometric non-enzymatic glucose biosensor fabricated using one-step electrodeposition of Au and Ru nanoparticles on the surface of our previously developed PtNPs nanocomposite. Using bench-top evaluations, we showed that the bimetallic catalyst of AuRu nanoparticles could enable non-enzymatic detection of glucose with superior performance, and stability. Furthermore, our biosensor exhibited good selectivity against other interferents with a non-linear dynamic range of 1–19 mM of glucose. The biosensor also displayed good repeatability and stability at 37 °C over a 3-week incubation period. We used a modified Butler-Volmer non-linear analytical model to evaluate the impact of geometrical and chemical design parameters on our

non-enzymatic biosensor performance. Finally, we measured glucose concentration from human serum and porcine whole blood samples directly using our biosensors. We saw substantial changes in current responses between different concentrations. We believe these results demonstrated the capability of our biosensors to differentiate physiologically-relevant glucose concentrations in biological media. By taking the non-linear responses of these non-enzymatic biosensors into account, we may also be able to improve the biosensors' range and performance for future *in vitro* and *in vivo* diagnostic applications.

## 6.2 Future Directions

### 6.2.1 *Ex vivo* and *in vivo* measurements of extracellular glutamate during spinal cord injury

As discussed above, we can apply the biosensors to monitor extracellular glutamate, particularly in SCI. GET's mechanism has been an area of interest for many basic medical scientists to prevent, delay, or even reverse the development of various neurodegenerations that can have an enormous impact on society's socioeconomic status. GET's fundamental basis is the prolonged glutamate elevation in the extracellular space after the neurons release it at the synapse. One particular condition that is well known to be closely related to GET is secondary SCI. After a physical trauma, there is an unusually high glutamate concentration in the cerebrospinal fluid of SCI patients, which leads to GET. As a result, it damages neurons and kills oligodendrocytes in the spinal cord and leads to demyelination of axon that survived the initial mechanical trauma Gonsette (2008); Platt (2007); G. Y. Xu, Hughes, Ye, Hulsebosch, and McAdoo (2004b). However, the mechanism leading to sustained high levels of glutamate remains unclear. Consequently, no established clinical treatment is available to suppress glutamate elevation and reduce post-SCI neurodegeneration.

New evidence has recently suggested that acrolein, an endogenously produced neurotoxin, and part of the post-impact secondary neurochemical reaction, is elevated weeks following SCI Y. Shi, Sun, McBride, Cheng, and Shi (2011). Acrolein may encourage extracellular glutamate elevation by damaging an astrocytic transporter glutamate uptake protein (GLT-1) responsible for glutamate reuptake Lauderback et al. (2001); R. Shi, Page, and Tully (2015).

Besides, post-SCI acrolein elevation correlates with GLT-1 damage: the highest levels of acrolein coincide with the lowest activity of GLT-1. Furthermore, microinjection of acrolein directly into the spinal cord in otherwise healthy rats can cause GLT-1 suppression, all indicative of a role of acrolein in damaging GLT-1. However, such a study has never been correlated with the extracellular glutamate concentration and consequent GET-instigated myelin damage Gonsette (2008). Therefore, it is desirable to develop a minimally invasive electrode that monitors the fluctuation of extracellular glutamate during the event of trauma to study the link between acrolein and GET.

Future work can utilize our recently developed implantable glutamate biosensor to examine glutamate release, *ex vivo*, from the excised spinal cord segment of a rat following a spinal cord injury. Furthermore, the biosensor can monitor the change of extracellular glutamate while microinjecting acrolein. On the other hand, future work should also focus on conducting *in vivo* experiments using clinically relevant contusive rat spinal cord injury models. The results from these experiments expect to shed additional insights on the critical link between the elevation of extracellular glutamate and acrolein, damage of GLT-1, and consequential tissue damage and functional loss due to GET. This study paves the way for future testing of the role of anti-acrolein treatment scavengers such as hydralazine. It is a feasible *in vivo* treatment that can potentially reduce the accumulation of glutamate, GET, and myelin damage Hamann, Nehrt, Ouyang, Duerstock, and Shi (2008); Y. Shi et al. (2011).

### 6.2.2 Integration of a wireless system for chronic *in vivo* neurotransmitter sensing

As discussed above, the ability to monitor extracellular glutamate *in vivo* during SCI is critical to establish the mechanism that causes GET and develop possible treatments. Additionally, the capability to monitor long-term molecular change in awake animals by implanting microelectrodes into the extracellular space of intact spinal cord or living brain can provide real-time correlations between neurochemical dynamics, real physiological conditions, and behavioral states. As a result, we can access the molecular basis information on neurological activities C. Pan, Wei, Han, Wu, and Mao (2020); Schultz et al. (2020).

Currently, our implantable sensors require bridging wire that is limited in readout distance and susceptible to damage during the implantation process Herbert, Mishra, Lim, Yoo, and Yeo (2019).

Therefore, it is desirable to develop a wireless communication platform for the current electrochemical biosensors C. Pan et al. (2020). Future work should focus on integrating a wireless system to enable chronically continuous monitoring of glutamate or other biological molecules *in vivo*. This platform's development could pave the way for a new generation of printable implanted electrochemical biosensors for different *in vivo* applications.

### 6.2.3 Direct ink writing of multielectrode arrays

#### 6.2.3.1 Multi-analyte detection

The multielectrode arrays of electrochemical biosensors can have multiple applications *in vitro* and *in vivo*. We can utilize our current direct ink writing technique to rapidly fabricate the multielectrode arrays and simultaneously monitor multiple biological molecules. For example, we can develop a glutamate and glutamine multielectrode arrays to quantify glutamate/glutamine ratio to detect chronic intestinal pseudo-obstruction Schultz et al. (2020); J. K. Yan et al. (2017). We can also employ the system to monitor the glutamate/glutamine ratio in the blood of patients with recent-onset schizophrenia Madeira et al. (2018); Schultz et al. (2020). Our lab has recently developed a multielectrode system to simultaneously monitor glutamate, glucose, and lactate in astrocyte cell culture Nolan et al. (2020). We can further develop the system to detect glucose, glutamate, acetylcholine, and adenosine with high-resolution in the brain. This technique can concurrently monitor the spatiotemporal heterogeneity of neurochemicals across different brain regions or at various depths. We can apply this system to investigate interactive molecular networks or neural communication by simultaneously measuring multiple analytes Bruno et al. (2006); Burmeister and Gerhardt (2001); Burmeister et al. (2002); C. Pan et al. (2020).

#### 6.2.3.2 Direct ink writing of multielectrode array for self-referencing

We can also use the multielectrode arrays as a self-referencing system to eliminate the interference from other electroactive species. As discussed in previous chapters, there is a set of criteria that we have to achieve for the biosensor to work in *ex vivo* and *in vivo* applications such as response time, sensitivity, selectivity, and appropriate size. For practical use, the biosensor must

selectively detect the physiological concentration of the desired analyte, such as glutamate, in the presence of other electroactive species such as serotonin, uric acid, and norepinephrine, ascorbic acid, acetaminophen. We have tried to utilize a semipermeable layer, Nafion, in order to improve the selectivity. By applying at room temperature, Nafion could not entirely exclude interferent species such as ascorbic acid or acetaminophen. Thus, we attempted to use a different method by annealing Nafion at 240 °C Qin, Van Der Zeyden, Oldenziel, Cremers, and Westerink (2008). Even though the sensors exhibited better selectivity against interferences, as shown in Chapter 3, the sensor experienced a decrease in sensitivity.

We are also investigating the application of another type of permselective membrane, m-phenylenediamine (mPD), and ascorbic oxidase to increase our biosensor's selectivity Scoggin et al. (2019); Weltin et al. (2014). The glutamate biosensor with a new type of permselective membrane may be used in our future work to measure extracellular glutamate in *ex vivo* and *in vivo* applications. It is worth noting that the biosensors' sensitivity and response time might decrease due to depositing multiple layers of mPD and ascorbate oxidase. Thus, we are developing and characterizing a multisite microelectrode array with other recording sites suitable for measuring other electroactive species such as hydrogen peroxide, ascorbic acid, acetaminophen, uric acid, or dopamine. An oxidase enzyme (glutamate oxidase) is applied to one electrode, while a chemically inert protein matrix, BSA and glutaraldehyde, is applied to the other recording site. Using an appropriate referencing method, we aim to create a dual-electrode system to demonstrate the ability to detect glutamate *in vivo* with high selectivity and sensitivity Burmeister and Gerhardt (2001). Additionally, we are constructing an array that consists of multiple dual-electrode systems in an attempt to characterize the diffusion of extracellular glutamate *in vivo*. Thus, future work should focus on using these multielectrode arrays to collect meaningful data of extracellular glutamate in *ex vivo* and *in vivo* during SCI.

### 6.2.4 Application of glutamate biosensors in clinical diagnosis

As discussed above, glutamate is an essential neurotransmitter in the nervous system responsible for cortical and cognitive functions. An elevation of glutamate in the extracellular space can lead to glutamate excitotoxicity in secondary SCI. Studies have shown that chronic activation of glutamate receptors can also lead to pathologies such as Alzheimer's disease,

amyotrophic lateral sclerosis, acute lung injury, autism, and schizophrenia Annesley (2003); Kuner (2010); Schultz et al. (2020); Wozniak, Rojas, Wu, and Slusher (2012). Thus, glutamate can perform as a potential biomarker for detecting and monitoring abnormalities such as neurodegenerative disorders, acute, chronic pain, and malignant diseases in biofluids. Biofluids such as cerebrospinal fluid, blood, urine, or saliva can serve as diagnostic tools for early detection or therapeutic monitoring C. Pan et al. (2020); Schultz et al. (2020). Electrochemical biosensors can offer as an alternative analytical method to conventional laboratory-based techniques to measure glutamate in these non-invasive biofluids. They can serve as a simple, low-cost, fast-response method for earlier detection of disease that can potentially improve the prognosis and lives of patients. As a consequence, future work can direct toward characterizing the biosensors to measure glutamate in biofluids reliably. By applying the suggested modifications above, we can develop a portable platform for rapid clinical tests with appropriate stability, selectivity, and applicable for commercial use.

# REFERENCES


Agnès, C., Arnault, J. C., Omnès, F., Jousselme, B., Billon, M., Bidan, G., & Mailley, P. (2009). XPS Study of Ruthenium Tris-bipyridine Electrografted from Diazonium Salt Derivative on Microcrystalline Boron Doped Diamond. *Physical Chemistry Chemical Physics*, *11*(48), 11647–11654.

Ahn, B. Y., Duoss, E. B., Motala, M. J., Guo, X., Park, S.-I., Xiong, Y., … Lewis, J. A. (2009). Omnidirectional Printing of Flexible, Stretchable, and Spanning Silver Microelectrodes. *Science*, *323*(5921), 1590–1593.

Alsaqqa, A. M., Singh, S., Middey, S., Kareev, M., Chakhalian, J., & Sambandamurthy, G. (2017). Phase coexistence and dynamical behavior in NdNiO3 ultrathin films. *Physical Review B*. doi: 10.1103/PhysRevB.95.125132

Ammam, M., & Fransaer, J. (2010). Highly sensitive and selective glutamate microbiosensor based on cast polyurethane/AC-electrophoresis deposited multiwalled carbon nanotubes and then glutamate oxidase/electrosynthesized polypyrrole/Pt electrode. *Biosens. Bioelectron.*, *25*(7), 1597–1602.

Annesley, T. M. (2003). Ion suppression in mass spectrometry. *Clinical Chemistry*, *49*(7), 1041–1044.

Armada-Moreira, A., Gomes, J. I., Pina, C. C., Savchak, O. K., Gonçalves-Ribeiro, J., Rei, N., … Vaz, S. H. (2020). Going the Extra (Synaptic) Mile: Excitotoxicity as the Road Toward Neurodegenerative Diseases. *Frontiers in Cellular Neuroscience*, *14*(April), 1–27.

Bach, A., & Semiat, R. (2011). The role of activated carbon as a catalyst in GAC/iron oxide/H2O2 oxidation process. *Desalination*, *273*(1), 57–63.

Bae, J. H., Han, J. H., & Chung, T. D. (2012). Electrochemistry at Nanoporous Interfaces: New Opportunity for Electrocatalysis. *Physical Chemistry Chemical Physics*, *14*(2), 448–463.

Bandodkar, A. J., Nuñez-Flores, R., Jia, W., & Wang, J. (2015). All-printed stretchable electrochemical devices. *Adv. Mater.*, *27*(19), 3060–3065. doi: 10.1002/adma.201500768

Batra, B., & Pundir, C. S. (2013). An amperometric glutamate biosensor based on immobilization of glutamate oxidase onto carboxylated multiwalled carbon nanotubes/gold nanoparticles/chitosan composite film modified Au electrode. *Biosens. Bioelectron.*, *47*, 496–501.

Behar, K. L., & Rothman, D. L. (2001). In Vivo Nuclear Magnetic Resonance Studies of Glutamate-$\gamma$-Aminobutyric Acid-Glutamine Cycling in Rodent and Human Cortex: the Central Role of Glutamine. *The Journal of Nutrition*, *131*(9), 2498S–2504S.

Biniak, S., Swiatkowski, A., & Pakuła, M. (2001). *Electrochemical studies of phenomena at active carbon-electrolyte solution interfaces* (Vol. 27). doi: 10.1007/s10291-009-0117-4

Bo, X., Bai, J., Yang, L., & Guo, L. (2011). The nanocomposite of PtPd nanoparticles/onion-like mesoporous carbon vesicle for nonenzymatic amperometric sensing of glucose. *Sensors Actuators, B Chem.*, *157*(2), 662–668.

Bouatra, S., Aziat, F., Mandal, R., Guo, A. C., Wilson, M. R., Knox, C., ... Wishart, D. S. (2013). The Human Urine Metabolome. *PLoS ONE*, *8*(9).

Boumezbeur, F., Petersen, K. F., Cline, G. W., Mason, G. F., Behar, K. L., Shulman, G. I., & Rothman, D. L. (2010). The contribution of blood lactate to brain energy metabolism in humans measured by dynamic 13C nuclear magnetic resonance spectroscopy. *J. Neurosci.*, *30*(42), 13983–91.

Bruno, J. P., Gash, C., Martin, B., Zmarowski, A., Pomerleau, F., Burmeister, J., ... Gerhardt, G. A. (2006). Second-by-second measurement of acetylcholine release in prefrontal cortex. *European Journal of Neuroscience*.

Burmeister, J. J., Davis, V. A., Quintero, J. E., Pomerleau, F., Huettl, P., & Gerhardt, G. A. (2013). Glutaraldehyde cross-linked glutamate oxidase coated microelectrode arrays: Selectivity and resting levels of glutamate in the CNS. *ACS Chemical Neuroscience*, *4*(5), 721–728.

Burmeister, J. J., & Gerhardt, G. A. (2001). Self-referencing ceramic-based multisite microelectrodes for the detection and elimination of interferences from the measurement of L-glutamate and other analytes. *Analytical Chemistry*, *73*(5), 1037–1042.

Burmeister, J. J., Palmer, M., & Gerhardt, G. A. (2005). L-lactate measures in brain tissue with ceramic-based multisite microelectrodes. *Biosensors and Bioelectronics*, *20*(9), 1772–1779.

Burmeister, J. J., Pomerleau, F., Palmer, M., Day, B. K., Huettl, P., & Gerhardt, G. A. (2002). Improved ceramic-based multisite microelectrode for rapid measurements of L-glutamate in the CNS. *J. Neurosci. Methods*, *119*(2), 163–171.

Burmeister, J. J., Price, D. A., Pomerleau, F., Huettl, P., Quintero, J. E., & Gerhardt, G. A. (2020). Challenges of simultaneous measurements of brain extracellular GABA and glutamate in vivo using enzyme-coated microelectrode arrays. *Journal of Neuroscience Methods*, *329*(June 2019), 108435.

Cao, H., Li, A. L., Nguyen, C. M., Peng, Y. B., & Chiao, J. C. (2012). An integrated flexible implantable micro-probe for sensing neurotransmitters. *IEEE Sens. J.*, *12*(5), 1618–1624.

Catalan, G. (2008). Progress in perovskite nickelate research. *Phase Transitions*, *81*(7-8), 729–749.

Catalan, G., Bowman, R. M., & Gregg, J. M. (2000). Transport properties of NdNiO3 thin films made by pulsed-laser deposition. *Journal of Applied Physics*.

Catalano, S., Gibert, M., Fowlie, J., Iñiguez, J., Triscone, J. M., & Kreisel, J. (2018). Rare-earth nickelates RNiO3: Thin films and heterostructures. *Reports on Progress in Physics*.

Caudle, W. M., & Zhang, J. (2009). Glutamate, excitotoxicity, and programmed cell death in parkinson disease. *Exp. Neurol.*, *220*(2), 230–233.

Chakraborty, S., & Retna Raj, C. (2007). Amperometric biosensing of glutamate using carbon nanotube based electrode. *Electrochem. commun.*, *9*(6), 1323–1330.

Chaurasia, C. S., Muller, M., Bashaw, E. D., Benfeldt, E., Bolinder, J., Bullock, R., ... Yeo, H. (2007). AAPS-FDA workshop white paper: Microdialysis principles, application and regulatory perspectives. *Pharm. Res.*, *24*(5), 1014–1025.

Cheng, M., Deivanayagam, R., & Shahbazian-Yassar, R. (2020). 3D Printing of Electrochemical Energy Storage Devices: A Review of Printing Techniques and Electrode/Electrolyte Architectures. *Batteries & Supercaps*, *3*(2), 130–146.

Cheng, M., Jiang, Y., Yao, W., Yuan, Y., Deivanayagam, R., Foroozan, T., ... Shahbazian-Yassar, R. (2018). Elevated-Temperature 3D Printing of Hybrid Solid-State Electrolyte for Li-Ion Batteries. *Advanced Materials*, *30*(39), 1–10.

Cifuentes Castro, V. H., López Valenzuela, C. L., Salazar Sánchez, J. C., Peña, K. P., López Pérez, S. J., Ibarra, J. O., & Villagrán, A. M. (2014a). An update of the classical and novel methods used for measuring fast neurotransmitters during normal and brain altered function. *Curr. Neuropharmacol.*, *12*(6), 490–508.

Cifuentes Castro, V. H., López Valenzuela, C. L., Salazar Sánchez, J. C., Peña, K. P., López Pérez, S. J., Ibarra, J. O., & Villagrán, A. M. (2014b). An update of the classical and novel methods used for measuring fast neurotransmitters during normal and brain altered function. *Current neuropharmacology*, *12*(6), 490–508.

Cinti, S., Arduini, F., Moscone, D., Palleschi, G., Gonzalez-Macia, L., & Killard, A. J. (2015). Cholesterol biosensor based on inkjet-printed Prussian blue nanoparticle-modified screen-printed electrodes. *Sensors Actuators B Chem.*, *221*, 187–190.

Clay, M., & Monbouquette, H. G. (2017). A Detailed Model of Electroenzymatic Glutamate Biosensors to Aid in Sensor Optimization and in Applications in vivo. *ACS Chem. Neurosci.*, acschemneuro.7b00262.

Clay, M., & Monbouquette, H. G. (2018). A Detailed Model of Electroenzymatic Glutamate Biosensors to Aid in Sensor Optimization and in Applications in Vivo. *ACS Chemical Neuroscience*, *9*(2), 241–251. doi: 10.1021/acschemneuro.7b00262

Connelly, C. A. (2011). Microdialysis update: optimizing the advantages. *Journal of Physiology*(1999), 2011–2011.

Cui, Y., Barford, J. P., & Renneberg, R. (2007). Development of an interference-free biosensor for l-glutamate using a bienzyme salicylate hydroxylase/l-glutamate dehydrogenase system. *Enzyme Microb. Technol.*, *41*(6-7), 689–693.

Daalkhaijav, U., Yirmibesoglu, O. D., Walker, S., & Mengüç, Y. (2018). Rheological Modification of Liquid Metal for Additive Manufacturing of Stretchable Electronics. *Advanced Materials Technologies*, *3*(4), 1–9.

Dai, H., Zhong, Y., Wu, X., Hu, R., Wang, L., Zhang, Y., … Yang, Z. (2018). Synthesis of perovskite-type SrTiO3 nanoparticles for sensitive electrochemical biosensing applications. *Journal of Electroanalytical Chemistry*, *810*(January), 95–99.

Dalkıran, B., Erden, P. E., & Kılıç, E. (2017). Graphene and tricobalt tetraoxide nanoparticles based biosensor for electrochemical glutamate sensing. *Artificial Cells, Nanomedicine and Biotechnology*. doi: 10.3109/21691401.2016.1153482

Danbolt, N. C. (2001). Glutamate uptake. *Prog. Neurobiol.*, *65*(1), 1–105.

De Graaf, R. A. (2007). *In Vivo NMR Spectroscopy: Principles and Techniques: 2nd Edition*.

Diabetes, D. O. F. (2009). *Diagnosis and classification of diabetes mellitus* (Vol. 32) (No. SUPPL. 1). doi: 10.2337/dc09-S062

Doble, A. (1999). The role of excitotoxicity in neurodegenerative disease: Implications for therapy. *Pharmacol. Ther.*, *81*(3), 163–221.

Dong, L., Youkey, S., Bush, J., Jiao, J., Dubin, V. M., & Chebiam, R. V. (2007). Effects of local Joule heating on the reduction of contact resistance between carbon nanotubes and metal electrodes. *J. Appl. Phys.*, *101*(2).

Duan, S., & Wang, R. (2013). Bimetallic Nanostructures with Magnetic and Noble Metals and their Physicochemical Applications. *Progress in Natural Science: Materials International*, *23*(2), 113–126.

Dzubay, J. A., & Jahr, C. E. (1999). The concentration of synaptically released glutamate outside of the climbing fiber-Purkinje cell synaptic cleft. *J. Neurosci.*, *19*(13), 5265–5274.

Economou, A., Kokkinos, C., & Prodromidis, M. (2018). Flexible plastic, paper and textile lab-on-a chip platforms for electrochemical biosensing. *Lab on a Chip*, *18*(13), 1812–1830.

Farooqui, a. a., & Horrocks, L. a. (1991). Excitatory amino acid receptors, neural membrane phospholipid metabolism and neurological disorders. *Brain Res. Brain Res. Rev.*, *16*(2), 171–191.

Featherstone, D. E., & Shippy, S. A. (2008). Regulation of synaptic transmission by ambient extracellular glutamate. *Neuroscientist*, *14*(2), 171–181.

Ferrando, R., Jellinek, J., & Johnston, R. L. (2008). Nanoalloys: From Theory to Applications of Alloy Clusters and Nanoparticles. *Chemical Reviews*, *108*(3), 845–910.

Foster Olive, M., Powell, G., McClure, E., & Gipson, C. D. (2018). Neurotransmitter systems: Glutamate. *The Therapeutic Use of N-Acetylcysteine (NAC) in Medicine*, 19–28.

Frey, O., Holtzman, T., Mcnamara, R. M., Theobald, D. E., van der Wal, P. D., de Rooij, N. F., … Koudelka-Hep, M. (2010). Enzyme-based choline and l-glutamate biosensor electrodes on silicon microprobe arrays. *Biosensors and Bioelectronics*, *26*(2), 477–484.

Gallego, J., Tapia, J., Vargas, M., Santamaria, A., Orozco, J., & Lopez, D. (2017). Synthesis of Graphene-coated Carbon Nanotubes-Supported Metal Nanoparticles as Multifunctional Hybrid Materials. *Carbon*, *111*, 393–401.

Ganesana, M., Trikantzopoulos, E., Maniar, Y., Lee, S. T., & Venton, B. J. (2019). Development of a novel micro biosensor for in vivo monitoring of glutamate release in the brain. *Biosensors and Bioelectronics*, *130*(October 2018), 103–109.

Gerwig, R., Fuchsberger, K., Schroeppel, B., Link, G. S., Heusel, G., Kraushaar, U., … Stelzle, M. (2012). PEDOT CNT Composite Microelectrodes for Recording and Electrostimulation Applications: Fabrication, Morphology, and Electrical Properties. *Front. Neuroeng.*, *5*.

Gollas, B., Elliott, J. M., & Bartlett, P. N. (2000). Electrodeposition and properties of nanostructured platinum films studied by quartz crystal impedance measurements at 10 MHz. *Electrochim. Acta*.

Gonsette, R. E. (2008). Neurodegeneration in multiple sclerosis: The role of oxidative stress and excitotoxicity. *J. Neurol. Sci.*, *274*(1-2), 48–53.

González-Gaitán, C., Ruiz-Rosas, R., Morallón, E., & Cazorla-Amorós, D. (2017). Effects of the surface chemistry and structure of carbon nanotubes on the coating of glucose oxidase and electrochemical biosensors performance. *RSC Adv.*, *7*(43), 26867–26878.

Govindarajan, S., McNeil, C. J., Lowry, J. P., McMahon, C. P., & O'Neill, R. D. (2013). Highly selective and stable microdisc biosensors for l-glutamate monitoring. *Sensors Actuators, B Chem.*, *178*, 606–614.

Govindasamy, M., Manavalan, S., Chen, S. M., Rajaji, U., Chen, T. W., Al-Hemaid, F. M., … Elshikh, M. S. (2018). Determination of Neurotransmitter in Biological and Drug Samples using Gold Nanorods Decorated f-MWCNTs Modified Electrode. *Journal of the Electrochemical Society*, *165*(9), B370–B377.

Gratson, G. M., García-Santamaría, F., Lousse, V., Xu, M., Fan, S., Lewis, J. A., & Braun, P. V. (2006). Direct-write assembly of three-dimensional photonic crystals: Conversion of polymer scaffolds to silicon hollow-woodpile structures. *Advanced Materials*, *18*(4), 461–465.

Guisbiers, G., Mejia-Rosales, S., Khanal, S., Ruiz-Zepeda, F., Whetten, R. L., & José-Yacaman, M. (2014). Gold-copper Nano-alloy, " Tumbaga ", in the Era of Nano: Phase Diagram and Segregation. *Nano Letters*, *14*(11), 6718–6726.

Hamann, K., Nehrt, G., Ouyang, H., Duerstock, B., & Shi, R. (2008). Hydralazine inhibits compression and acrolein-mediated injuries in ex vivo spinal cord. *J. Neurochem.*, *104*(3), 708–718.

Hamdi, N., Wang, J., Walker, E., Maidment, N. T., & Monbouquette, H. G. (2006). An electroenzymatic l-glutamate microbiosensor selective against dopamine. *J. Electroanal. Chem.*, *591*(1), 33–40.

Hao, L., Tang, D., Sun, T., Xiong, W., Feng, Z., Evans, K. E., & Li, Y. (2020). Direct Ink Writing of Mineral Materials: A review. *International Journal of Precision Engineering and Manufacturing - Green Technology*.

Hardin, J. O., Ober, T. J., Valentine, A. D., & Lewis, J. A. (2015). Microfluidic printheads for multimaterial 3D printing of viscoelastic inks. *Advanced Materials*, *27*(21), 3279–3284.

Harry Marsh, & Rodríguez-Reinoso, F. (2006). CHAPTER 4 - Characterization of activated carbon. In *Activated carbon* (pp. 143–242).

Hauser, A. J., Mikheev, E., Moreno, N. E., Hwang, J., Zhang, J. Y., & Stemmer, S. (2015). Correlation between stoichiometry, strain, and metal-insulator transitions of NdNiO3 films. *Applied Physics Letters*.

Herbert, R., Mishra, S., Lim, H. R., Yoo, H., & Yeo, W. H. (2019). Fully Printed, Wireless, Stretchable Implantable Biosystem toward Batteryless, Real-Time Monitoring of Cerebral Aneurysm Hemodynamics. *Advanced Science*.

Hertz, L. (2006). Glutamate, a neurotransmitter-And so much more. A synopsis of Wierzba III. *Neurochem. Int.*, *48*(6-7), 416–425.

Hoa, L. N. Q., Chen, H. R., & Tseng, T. T. (2018). An Arrayed Micro-glutamate Sensor Probe Integrated with On-probe Ag/AgCl Reference and Counter Electrodes. *Electroanalysis*, *30*(3), 561–570.

Holt-Hindle, P., Nigro, S., Asmussen, M., & Chen, A. (2008). Amperometric Glucose Sensor based on Platinum-Iridium Nanomaterials. *Electrochemistry Communications*, *10*(10), 1438–1441.

Hon, K. K. B., Li, L., & Hutchings, I. M. (2008). Direct writing technology-Advances and developments. *CIRP Ann. - Manuf. Technol.*, *57*(2), 601–620.

Hondred, J. A., Stromberg, L. R., Mosher, C. L., & Claussen, J. C. (2017). High-Resolution Graphene Films for Electrochemical Sensing via Inkjet Maskless Lithography. *ACS Nano*, *11*(10), 9836–9845.

Hrapovic, S., Liu, Y., Male, K. B., & Luong, J. H. T. (2004). Electrochemical Biosensing Platforms Using Platinum Nanoparticles and Carbon Nanotubes. *Analytical Chemistry*, *76*(4), 1083–1088.

Hsieh, H. H., Hsu, F. C., & Chen, Y. F. (2018). Energetically autonomous, wearable, and multifunctional sensor. *ACS Sensors*, *3*(1), 113–120.

Hsu, N. Y., Chien, C. C., & Jeng, K. T. (2008). Characterization and Enhancement of Carbon Nanotube-Supported PtRu Electrocatalyst for Direct Methanol Fuel Cell Applications. *Applied Catalysis B: Environmental*, *84*(1-2), 196–203.

Hu, Y., Mitchell, K. M., Albahadily, F. N., Michaelis, E. K., & Wilson, G. S. (1994). Direct measurement of glutamate release in the brain using a dual enzyme-based electrochemical sensor. *Brain Res.*, *659*(1-2), 117–125.

Huffman, M. L., & Venton, B. J. (2009). Carbon-fiber microelectrodes for in vivo applications. *Analyst*, *134*(1), 18–24.

Hwang, C. B., Fu, Y. S., Lu, Y. L., Jang, S. W., Chou, P. T., Wang, C. R., & Yu, S. J. (2000). Synthesis, Characterization, and Highly Efficient Catalytic Reactivity of Suspended Palladium Nanoparticles. *Journal of Catalysis*, *195*(2), 336–341.

Hwang, D. W., Lee, S., Seo, M., & Chung, T. D. (2018). Recent Advances in Electrochemical Non-enzymatic Glucose Sensors-A Review. *Analytica Chimica Acta*, *1033*, 1–34.

Isoaho, N., Peltola, E., Sainio, S., Wester, N., Protopopova, V., Wilson, B. P., ... Laurila, T. (2017). Carbon Nanostructure Based Platform for Enzymatic Glutamate Biosensors. *J. Phys. Chem. C*, *121*(8), 4618–4626.

Ispas, C. R., Crivat, G., & Andreescu, S. (2012). Review: Recent Developments in Enzyme-Based Biosensors for Biomedical Analysis. *Anal. Lett.*, *45*(2-3), 168–186.

Issberner, J. P., Schauer, C. L., Trimmer, B. A., & Walt, D. R. (2002). Combined imaging and chemical sensing of L-glutamate release from the foregut plexus of the Lepidopteran, Manduca sexta. *J. Neurosci. Methods*, *120*(1), 1–10.

Jabari, E., & Toyserkani, E. (2016). Aerosol-Jet printing of highly flexible and conductive graphene/silver patterns. *Materials Letters*, *174*, 40–43.

Jamal, M., Xu, J., & Razeeb, K. M. (2010). Disposable biosensor based on immobilisation of glutamate oxidase on Pt nanoparticles modified Au nanowire array electrode. *Biosens. Bioelectron.*, *26*(4), 1420–1424.

Jensen, J. M., & Shi, R. (2003). Effects of 4-aminopyridine on stretched mammalian spinal cord: the role of potassium channels in axonal conduction. *J Neurophysiol*, *90*, 2334 – 2340.

Jiao, X., Tanner, E. E., Sokolov, S. V., Palgrave, R. G., Young, N. P., & Compton, R. G. (2017). Understanding nanoparticle porosity: Via nanoimpacts and XPS: Electro-oxidation of platinum nanoparticle aggregates. *Physical Chemistry Chemical Physics*, *19*(21), 13547–13552.

Jin, X., & Alam, M. (2019). Generalized Modeling Framework of Metal Oxide-based Non-enzymatic Glucose Sensor: Concepts, Methods, and Challenges. *IEEE Transactions on Biomedical Engineering*, 1–1.

Kadara, R. O., Jenkinson, N., Li, B., Church, K. H., & Banks, C. E. (2008). Manufacturing electrochemical platforms: Direct-write dispensing versus screen printing. *Electrochem. commun.*, *10*(10), 1517–1519.

Kagedal, M., Cselenyi, Z., Nyberg, S., Raboisson, P., Stahle, L., Stenkrona, P., ... Karlsson, M. O. (2013). A positron emission tomography study in healthy volunteers to estimate mGluR5 receptor occupancy of AZD2066 - Estimating occupancy in the absence of a reference region. *Neuroimage*, *82*, 160–169.

Karyakin, A. A., Karyakina, E. E., & Gorton, L. (2000). Amperometric biosensor for glutamate using Prussian Blue-based 'artificial peroxidase' as a transducer for hydrogen peroxide. *Anal. Chem.*, *72*(7), 1720–1723.

Kergoat, L., Piro, B., Simon, D. T., Pham, M. C., Noël, V., & Berggren, M. (2014). Detection of glutamate and acetylcholine with organic electrochemical transistors based on conducting polymer/platinum nanoparticle composites. *Adv. Mater.*, *26*(32), 5658–5664.

Khan, R., Gorski, W., & Garcia, C. D. (2011). Nanomolar Detection of Glutamate at a Biosensor Based on Screen-Printed Electrodes Modified with Carbon Nanotubes. *Electroanalysis*, *10*(23), 2357–2363.

Kiedrowski, L., Wroblewski, J. T., & Costa, E. (1994). Intracellular sodium concentration in cultured cerebellar granule cells challenged with glutamate. *Mol. Pharmacol.*, *45*(5), 1050–4.

Kim, J. H., Nam, K. W., Ma, S. B., & Kim, K. B. (2006). Fabrication and Electrochemical Properties of Carbon Nanotube Film Electrodes. *Carbon*, *44*(10), 1963–1968.

Kingston, C., Zepp, R., Andrady, A., Boverhof, D., Fehir, R., Hawkins, D., … Wohlleben, W. (2014). Release Characteristics of Selected Carbon Nanotube Polymer Composites. *Carbon*, *68*, 33–57.

Kissinger, S. T., Pak, A., Tang, Y., Masmanidis, S. C., & Chubykin, A. A. (2018). Oscillatory encoding of visual stimulus familiarity. *Journal of Neuroscience*.

Kolesky, D. B., Truby, R. L., Gladman, A. S., Busbee, T. A., Homan, K. A., & Lewis, J. A. (2014). 3D bioprinting of vascularized, heterogeneous cell-laden tissue constructs. *Advanced Materials*, *26*(19), 3124–3130.

König, M., Thinnes, A., & Klein, J. (2018). Microdialysis and its use in behavioural studies: Focus on acetylcholine. *Journal of Neuroscience Methods*, *300*, 206–215.

Kotanen, C. N., Moussy, F. G., Carrara, S., & Guiseppi-Elie, A. (2012). Implantable enzyme amperometric biosensors. *Biosens. Bioelectron.*, *35*(1), 14–26.

Kulagina, N. V., Shankar, L., & Michael, A. C. (1999). Monitoring glutamate and ascorbate in the extracellular space of brain tissue with electrochemical microsensors. *Anal. Chem.*, *71*(22), 5093–5100.

Kuner, R. (2010). Central mechanisms of pathological pain. *Nature Medicine*, *16*(11), 1258–1266.

Kwon, S. Y., Kwen, H. D., & Choi, S. H. (2012). Fabrication of Nonenzymatic Glucose Sensors based on Multiwalled Carbon Nanotubes with Bimetallic Pt-M(M = Ru and Sn) Catalysts by Radiolytic Deposition. *Journal of Sensors*, *2012*, 784167.

Kwong, A. W., Gründig, B., Hu, J., & Renneberg, R. (2000). Comparative study of hydrogel-immobilized L-glutamate oxidases for a novel thick-film biosensor and its application in food samples. *Biotechnology Letters*, *22*(4), 267–272.

Lang, X., Hirata, A., Fujita, T., & Chen, M. (2014). Three-dimensional hierarchical nanoporosity for ultrahigh power and excellent cyclability of electrochemical pseudocapacitors. *Adv. Energy Mater.*.

Lau, A., & Tymianski, M. (2010). Glutamate receptors, neurotoxicity and neurodegeneration. *Pflugers Arch. Eur. J. Physiol.*, *460*(2), 525–542.

Lauderback, C. M., Hackett, J. M., Huang, F. F., Keller, J. N., Szweda, L. I., Markesbery, W. R., & Butterfield, D. a. (2001). The glial glutamate transporter, GLT-1, is oxidatively modified by 4-hydroxy-2-nonenal in the Alzheimer's disease brain: the role of Abeta1-42. *J Neurochem*, *78*(2), 413–416.

Lee, H., Yoo, J. K., Park, J. H., Kim, J. H., Kang, K., & Jung, Y. S. (2012). A stretchable polymer-carbon nanotube composite electrode for flexible lithium-ion batteries: Porosity engineering by controlled phase separation. *Advanced Energy Materials*, *2*(8), 976–982.

Lee, W. C., Kim, K. B., Gurudatt, N. G., Hussain, K. K., Choi, C. S., Park, D. S., & Shim, Y. B. (2019). Comparison of enzymatic and non-enzymatic glucose sensors based on hierarchical Au-Ni alloy with conductive polymer. *Biosensors and Bioelectronics*, *130*(July), 48–54.

Lein, E. S., Hawrylycz, M. J., Ao, N., Ayres, M., Bensinger, A., Bernard, A., … Jones, A. R. (2007). Genome-wide atlas of gene expression in the adult mouse brain. *Nature*.

Lewis, J. A. (2006). Direct ink writing of 3D functional materials. *Adv. Funct. Mater.*, *16*(17), 2193–2204.

Li, L. H., Zhang, W. D., & Ye, J. S. (2008). Electrocatalytic Oxidation of Glucose at Carbon Nanotubes Supported PtRu Nanoparticles and its Detection. *Electroanalysis*, *20*(20), 2212–2216.

Li, Q., & Lewis, J. A. (2003). Nanoparticle Inks for Directed Assembly of Three-Dimensional Periodic Structures. *Advanced Materials*, *15*(19), 1639–1643.

Li, R. Z., Hu, A., Zhang, T., & Oakes, K. D. (2014). Direct writing on paper of foldable capacitive touch pads with silver nanowire inks. *ACS Applied Materials and Interfaces*, *6*(23), 21721–21729.

Li, S., & Huang, Y. (2014). In vivo imaging of the metabotropic glutamate receptor 1 (mGluR1) with positron emission tomography: recent advance and perspective. *Curr. Med. Chem.*, *21*(1), 113–23.

Li, Y., Wu, P., Luo, Z., Ren, Y., Liao, M., Feng, L., … He, L. (2015). Rapid fabrication of microfluidic chips based on the simplest LED lithography. *J. Micromechanics Microengineering*, *25*(5).

Li, Z., Leung, C., Gao, F., & Gu, Z. (2015). Effects of nanowire length and surface roughness on the electrochemical sensor properties of nafion-free, Vertically aligned pt nanowire array electrodes. *Sensors (Switzerland)*, *15*(9), 22473–22489.

Lim, C. S., Tan, S. M., Sofer, Z., & Pumera, M. (2015). Impact Electrochemistry of Layered Transition Metal Dichalcogenides. *ACS Nano*.

Liu, D., Thangnipon, W., & McAdoo, D. (1991). Excitatory amino acids rise to toxic levels upon impact injury to the rat spinal cord. *Brain Res.*, *547*(X), 344–348.

Liu, H., Song, C., Zhang, L., Zhang, J., Wang, H., & Wilkinson, D. P. (2006). A Review of Anode Catalysis in The Direct Methanol Fuel Cell. *Journal of Power Sources*, *155*(2), 95–110.

Liu, Y., Ding, Y., Zhang, Y., & Lei, Y. (2012). Pt-Au Nanocorals, Pt Nanofibers and Au Microparticles Prepared by Electrospinning and Calcination for Nonenzymatic Glucose Sensing in Neutral and Alkaline Environment. *Sensors and Actuators, B: Chemical*, *171-172*, 954–961.

Lowry, J. P., & O'Neill, R. D. (1994). Partial characterization in vitro of glucose oxidase-modified poly(phenylenediamine)-coated electrodes for neurochemical analysis in vivo. *Electroanalysis*.

Ma, M., Liu, K., Shen, J., Kas, R., & Smith, W. A. (2018). In Situ Fabrication and Reactivation of Highly Selective and Stable Ag Catalysts for Electrochemical CO2 Conversion. *ACS Energy Letters*, *3*(6), 1301–1306.

Ma, P. C., Tang, B. Z., & Kim, J. K. (2008). Effect of CNT decoration with silver nanoparticles on electrical conductivity of CNT-polymer composites. *Carbon N. Y.*, *46*(11), 1497–1505.

Madeira, C., Alheira, F. V., Calcia, M. A., Silva, T. C. S., Tannos, F. M., Vargas-Lopes, C., … Panizzutti, R. (2018). Blood Levels of Glutamate and Glutamine in Recent Onset and Chronic Schizophrenia. *Frontiers in Psychiatry*.

Maity, D., & Kumar, R. T. (2019). Highly sensitive amperometric detection of glutamate by glutamic oxidase immobilized Pt nanoparticle decorated multiwalled carbon nanotubes(MWCNTs)/polypyrrole composite. *Biosensors and Bioelectronics*, *130*(August 2018), 307–314.

Márquez, A., Jiménez-Jorquera, C., Domínguez, C., & Muñoz-Berbel, X. (2017). Electrodepositable alginate membranes for enzymatic sensors: An amperometric glucose biosensor for whole blood analysis. *Biosensors and Bioelectronics*, *97*(May), 136–142.

Mattinson, C. E., Burmeister, J. J., Quintero, J. E., Pomerleau, F., Huettl, P., & Gerhardt, G. A. (2011). Tonic and phasic release of glutamate and acetylcholine neurotransmission in sub-regions of the rat prefrontal cortex using enzyme-based microelectrode arrays. *J. Neurosci. Methods*, *202*(2), 199–208.

McAdoo, D. J., Xu, G.-Y., Robak, G., & Hughes, M. G. (1999). Changes in Amino Acid Concentrations over Time and Space around an Impact Injury and Their Diffusion Through the Rat Spinal Cord. *Exp. Neurol.*, *159*(2), 538–544.

McLamore, E. S., Mohanty, S., Shi, J., Claussen, J., Jedlicka, S. S., Rickus, J. L., & Porterfield, D. M. (2010). A self-referencing glutamate biosensor for measuring real time neuronal glutamate flux. *J. Neurosci. Methods*, *189*(1), 14–22.

McMahon, C. P., & O'Neill, R. D. (2005). Polymer-enzyme composite biosensor with high glutamate sensitivity and low oxygen dependence. *Anal. Chem.*, *77*(4), 1196–1199.

Melorose, J., Perroy, R., & Careas, S. (2015). *Neurochemical Aspects of Excitotoxicity* (Vol. 1).

Middey, S., Chakhalian, J., Mahadevan, P., Freeland, J., Millis, A., & Sarma, D. (2016). Physics of Ultrathin Films and Heterostructures of Rare-Earth Nickelates. *Annual Review of Materials Research*.

Miele, M., Berners, M., Boutelle, M. G., Kusakabe, H., & Fillenz, M. (1996). The determination of the extracellular concentration of brain glutamate using quantitative microdialysis. *Brain Res.*, *707*(1), 131–133.

Moraes, E. R. d. S., Grisolia, A. B. A., Oliveira, K. R. M., Picanço-Diniz, D. L. W., Crespo-López, M. E., Maximino, C., … Herculano, A. M. (2012). Determination of glutamate uptake by high performance liquid chromatography (HPLC) in preparations of retinal tissue. *Journal of Chromatography B: Analytical Technologies in the Biomedical and Life Sciences*, *907*, 1–6.

Moussawi, K., Riegel, A., Nair, S., & Kalivas, P. W. (2011). Extracellular glutamate: functional compartments operate in different concentration ranges. *Front. Syst. Neurosci.*, *5*(November), 94.

Muehllehner, G., & Karp, J. S. (2006). Positron emission tomography. *Phys. Med. Biol.*, *51*(13), R117—-37.

Mueller, J. E., Krtil, P., Kibler, L. A., & Jacob, T. (2014). Bimetallic Alloys in Action: Dynamic Atomistic Motifs for Electrochemistry and Catalysis. *Physical Chemistry Chemical Physics*, *16*(29), 15029–15042.

Müller, C. A., Hundshammer, C., Braeuer, M., Skinner, J. G., Berner, S., Leupold, J., … Hövener, J. B. (2020). Dynamic 2D and 3D mapping of hyperpolarized pyruvate to lactate conversion in vivo with efficient multi-echo balanced steady-state free precession at 3 T. *NMR in Biomedicine*, *33*(6), 1–16.

Nair, P. R., & Alam, M. A. (2006). Performance Limits of Nanobiosensors. *Applied Physics Letters*, *88*(23), 10–13.

Nair, P. R., & Alam, M. A. (2013). A Compact Analytical Formalism for Current Transients in Electrochemical Systems. *Analyst*, *138*(2), 525–538.

Nantaphol, S., Watanabe, T., Nomura, N., Siangproh, W., Chailapakul, O., & Einaga, Y. (2017). Bimetallic Pt–Au Nanocatalysts Electrochemically Deposited on Boron-doped Diamond Electrodes for Nonenzymatic Glucose Detection. *Biosensors and Bioelectronics*, *98*, 76–82.

Naylor, E., Aillon, D. V., Gabbert, S., Harmon, H., Johnson, D. A., Wilson, G. S., & Petillo, P. A. (2011). Simultaneous real-time measurement of EEG/EMG and l-glutamate in mice: A biosensor study of neuronal activity during sleep. *Journal of Electroanalytical Chemistry*, *656*(1-2), 106–113.

Nguyen, T., Jin, X., Nolan, J. K., Xu, J., Le, K. V. H., Lam, S., … Lee, H. (2020). Printable non-enzymatic glucose biosensors using carbon nanotube-ptnps nanocomposite modified with auru for improved selectivity. *ACS Biomaterials Science & Engineering*, *0*(ja), null.

Nguyen, T. N., Nolan, J., Cheng, X., Park, H., Wang, Y., Lam, S., … Lee, H. (2020). Fabrication and ex vivo evaluation of activated carbon–Pt microparticle based glutamate biosensor. *Journal of Electroanalytical Chemistry*, *866*, 114136.

Nguyen, T. N., Nolan, J. K., Park, H., Lam, S., Fattah, M., Page, J. C., … Lee, H. (2019a). Facile fabrication of flexible glutamate biosensor using direct writing of platinum nanoparticle-based nanocomposite ink. *Biosensors and Bioelectronics*, *131*, 257–266.

Nguyen, T. N., Nolan, J. K., Park, H., Lam, S., Fattah, M., Page, J. C., … Lee, H. (2019b). Facile Fabrication of Flexible Glutamate Biosensor using Direct Writing of Platinum Nanoparticle-based Nanocomposite Ink. *Biosensors and Bioelectronics*, *131*, 257–266.

Nguyen, T. N. H., Jin, X., Nolan, J. K., Xu, J., Le, K. V. H., Lam, S., … Lee, H. (n.d.). Printable non-enzymatic glucose biosensors using carbon nanotube-based nanocomposite modified with AuRu-PtNPs for improved selectivity. *Under Revision*.

Nicholls, D., & Attwell, D. (1990). The release and uptake of excitatory amino acids. *Trends Pharmacol. Sci.*, *11*(11), 462–468.

Nichols, S. P., Koh, A., Storm, W. L., Shin, J. H., & Schoenfisch, M. H. (2013). *Biocompatible materials for continuous glucose monitoring devices.* doi: 10.1021/cr300387j

Nolan, J. K., Nguyen, T. N., Le, K. V. H., DeLong, L. E., & Lee, H. (2020). Simple Fabrication of Flexible Biosensor Arrays Using Direct Writing for Multianalyte Measurement from Human Astrocytes. *SLAS Technology*, *25*(1), 33–46.

Oh, C., Jo, M., & Son, J. (2019). All-Solid-State Synaptic Transistors with High-Temperature Stability Using Proton Pump Gating of Strongly Correlated Materials. *ACS Applied Materials and Interfaces*, *11*(17), 15733–15740.

Okumoto, S., Looger, L. L., Micheva, K. D., Reimer, R. J., Smith, S. J., & Frommer, W. B. (2005). Detection of glutamate release from neurons by genetically encoded surface-displayed FRET nanosensors. *Proc. Natl. Acad. Sci. U. S. A.*, *102*(24), 8740–5.

Oldenziel, W. H., Van Der Zeyden, M., Dijkstra, G., Ghijsen, W. E. J. M., Karst, H., Cremers, T. I. F. H., & Westerink, B. H. C. (2007). Monitoring extracellular glutamate in hippocampal slices with a microsensor. *J. Neurosci. Methods*, *160*(1), 37–44.

Olivé-Monllau, R., Esplandiu, M. J., Bartrolí, J., Baeza, M., & Céspedes, F. (2010). Strategies for the optimization of carbon nanotube/polymer ratio in composite materials: Applications as voltammetric sensors. *Sensors and Actuators, B: Chemical*, *146*(1), 353–360.

Olney, J. W., & Sharpe, L. G. (1969). Brain lesions in an infant rhesus monkey treated with monsodium glutamate. *Science*, *166*(903), 386–388.

O'Neill, R. D., Chang, S. C., Lowry, J. P., & McNeil, C. J. (2004). Comparisons of platinum, gold, palladium and glassy carbon as electrode materials in the design of biosensors for glutamate. *Biosens. Bioelectron.*, *19*(11), 1521–1528.

Oyinbo, C. A. (2011). Secondary injury mechanisms in traumatic spinal cord injury: A nugget of this multiply cascade. *Acta Neurobiol. Exp. (Wars).*, *71*(2), 281–299.

Özel, R. E., Ispas, C., Ganesana, M., Leiter, J. C., & Andreescu, S. (2014). Glutamate oxidase biosensor based on mixed ceria and titania nanoparticles for the detection of glutamate in hypoxic environments. *Biosensors and Bioelectronics*.

Pachitariu, M., Steinmetz, N., Kadir, S., Carandini, M., & Harris, K. (2016). Fast and accurate spike sorting of high-channel count probes with KiloSort. In *Advances in neural information processing systems.*

Page, J., Park, J., Chen, Z., Cao, P., & Shi, R. (2017). Parallel evaluation of two potassium channel blockers in restoring conduction in mechanical spinal cord injury in rat. *Journal of Neurotrauma*, *9*(35), 1057–1068.

Pan, C., Wei, H., Han, Z., Wu, F., & Mao, L. (2020). Enzymatic electrochemical biosensors for in situ neurochemical measurement. *Current Opinion in Electrochemistry*, *19*, 162–167.

Pan, S., & Arnold, M. A. (1996). Selectivity enhancement for glutamate with a Nafion/glutamate oxidase biosensor. *Talanta*, *43*(7), 1157–1162.

Park, E., Velumian, A. a., & Fehlings, M. G. (2004). The role of excitotoxicity in secondary mechanisms of spinal cord injury : a review with an emphasis on the implications for white matter degeneration. *J. Neurotrauma*, *21*(6), 754–774.

Park, H., Raffiee, A. H., John, S. W. M., Ardekani, A. M., & Lee, H. (2018). Towards Smart Self-Clearing Glaucoma Drainage Device. *Microsystems Nanoeng.*.

Park, J., Lee, A., Yim, Y., & Han, E. (2011). Electrical and thermal properties of PEDOT:PSS films doped with carbon nanotubes. *Synth. Met.*, *161*(5-6), 523–527.

Park, S., Boo, H., & Chung, T. D. (2006). Electrochemical non-enzymatic glucose sensors. *Anal. Chim. Acta*, *556*(1), 46–57. doi: 10.1016/j.aca.2005.05.080

Patole, A., & Lubineau, G. (2015). Carbon nanotubes with silver nanoparticle decoration and conductive polymer coating for improving the electrical conductivity of polycarbonate composites. *Carbon N. Y.*, *81*(1), 720–730.

Pellerin, L., & Magistretti, P. J. (2004). Neuroenergetics: Calling Upon Astrocytes to Satisfy Hungry Neurons. *Neurosci.*, *10*(1), 53–62.

Peng, L., Hertz, L., Huang, R., Sonnewald, U., Petersen, S. B., Westergaard, N., ... Schousboe, A. (1993). Utilization of glutamine and of TCA cycle constituents as precursors for transmitter glutamate and GABA. *Dev Neurosci*, *15*(3-5), 367–377.

Peng, Y., Pan, W., Wang, N., Lu, J. E., & Chen, S. (2018). Ruthenium Ion-Complexed Graphitic Carbon Nitride Nanosheets Supported on Reduced Graphene Oxide as High-Performance Catalysts for Electrochemical Hydrogen Evolution. *ChemSusChem*, *11*(1), 130–136.

Perry, M., Li, Q., & Kennedy, R. T. (2009). Review of recent advances in analytical techniques for the determination of neurotransmitters. *Anal. Chim. Acta*, *653*(1), 1–22.

Perry, S. C., Gateman, S. M., Sifakis, J., Pollegioni, L., & Mauzeroll, J. (2018). Enhancement of the enzymatic biosensor response through targeted electrode surface roughness. *Journal of The Electrochemical Society*, *165*(12), G3074–G3079.

Platt, S. R. (2007). The role of glutamate in central nervous system health and disease - A review. *Veterinary Journal*, *173*(2), 278–286.

Pospíšilová, M., Kuncová, G., & Trögl, J. (2015). Fiber-Optic Chemical Sensors and Fiber-Optic Bio-Sensors. *Sensors*, *15*(10), 25208–25259.

Qin, S., Van Der Zeyden, M., Oldenziel, W. H., Cremers, T. I. F. H., & Westerink, B. H. C. (2008). Microsensors for in vivo measurement of glutamate in brain tissue. *Sensors*, *8*(11), 6860–6884.

Rahman, M. A., Kwon, N. H., Won, M. S., Choe, E. S., & Shim, Y. B. (2005). Functionalized conducting polymer as an enzyme-immobilizing substrate: An amperometric glutamate microbiosensor for in vivo measurements. *Anal. Chem.*, *77*(15), 4854–4860. doi: 10.1021/ac050558v

Ramadan, S., Lin, A., & Stanwell, P. (2013). Glutamate and glutamine: A review of in vivo MRS in the human brain. *NMR in Biomedicine*, *26*(12), 1630–1646.

Rathod, D., Dickinson, C., Egan, D., & Dempsey, E. (2010). Platinum nanoparticle decoration of carbon materials with applications in non-enzymatic glucose sensing. *Sensors Actuators, B Chem.*, *143*(2), 547–554.

Rivera, J. F., Sridharan, S. V., Nolan, J. K., Miloro, S. A., Alam, M. A., Rickus, J. L., & Janes, D. B. (2018). Real-time characterization of uptake kinetics of glioblastoma: Vs. astrocytes in 2D cell culture using microelectrode array. *Analyst*, *143*(20), 4954–4966.

Rossant, C., Kadir, S. N., Goodman, D. F., Schulman, J., Hunter, M. L., Saleem, A. B., … Harris, K. D. (2016). Spike sorting for large, dense electrode arrays. *Nature Neuroscience*, *19*(4), 634–641. doi: 10.1038/nn.4268

Rothman, D. L., Sibson, N. R., Hyder, F., Shen, J., Behar, K. L., & Shulman, R. G. (1999). In vivo nuclear magnetic resonance spectroscopy studies of the relationship between the glutamate-glutamine neurotransmitter cycle and functional neuroenergetics. *Philos. Trans. R. Soc. Lond. B. Biol. Sci.*, *354*(1387), 1165–1177.

Rutherford, E. C., Pomerleau, F., Huettl, P., Strömberg, I., & Gerhardt, G. A. (2007). Chronic second-by-second measures of L-glutamate in the central nervous system of freely moving rats. *Journal of Neurochemistry*, *102*(3), 712–722.

Ryan, M. R., Lowry, J. P., & O'Neill, R. D. (1997). Biosensor for neurotransmitter L-glutamic acid designed for efficient use of L-glutamate oxidase and effective rejection of interference. *Analyst*, *122*(11), 1419–1424.

Ryu, J., Kim, K., Kim, H. S., Hahn, H. T., & Lashmore, D. (2010). Intense Pulsed Light Induced Platinum-gold Alloy Formation on Carbon Nanotubes for Non-enzymatic Glucose Detection. *Biosensors and Bioelectronics*, *26*(2), 602–607.

Salazar, P., Martín, M., O'Neill, R. D., & González-Mora, J. L. (2016). Glutamate microbiosensors based on Prussian Blue modified carbon fiber electrodes for neuroscience applications: In-vitro characterization. *Sensors Actuators, B Chem.*, *235*, 117–125.

Salazar, P., Martín, M., O'Neill, R. D., & González-Mora, J. L. (2016). Glutamate microbiosensors based on Prussian Blue modified carbon fiber electrodes for neuroscience applications: in-vitro characterization. *Sensors Actuators B Chem.*, *235*, 117–125.

Scherwitzl, R., Zubko, P., Lezama, I. G., Ono, S., Morpurgo, A. F., Catalan, G., & Triscone, J. M. (2010). Electric-field control of the metal-insulator transition in ultrathin NdNiO3 films. *Advanced Materials*. doi: 10.1002/adma.201003241

Schultz, J., Uddin, Z., Singh, G., & Howlader, M. M. (2020). Glutamate sensing in biofluids: Recent advances and research challenges of electrochemical sensors. *Analyst*, *145*(2), 321–347.

Scoggin, J. L., Tan, C., Nguyen, N. H., Kansakar, U., Madadi, M., Siddiqui, S., ... Murray, T. A. (2019). An enzyme-based electrochemical biosensor probe with sensitivity to detect astrocytic versus glioma uptake of glutamate in real time in vitro. *Biosensors and Bioelectronics*, *126*, 751–757.

Secor, E. B., Ahn, B. Y., Gao, T. Z., Lewis, J. A., & Hersam, M. C. (2015). Rapid and Versatile Photonic Annealing of Graphene Inks for Flexible Printed Electronics. *Advanced Materials*, *27*(42), 6683–6688.

Seland, F., Tunold, R., & Harrington, D. A. (2008). Impedance Study of Formic Acid Oxidation on Platinum Electrodes. *Electrochimica Acta*, *53*(23), 6851–6864.

Shaw, J. E., Sicree, R. A., & Zimmet, P. Z. (2010). Global Estimates of The Prevalence of Diabetes for 2010 and 2030. *Diabetes Research and Clinical Practice*, *87*(1), 4–14.

Shen, J. (2010). Impaired neurotransmitter release in Alzheimer's and Parkinson's diseases. *Neurodegenerative Diseases*.

Shi, J., Zhou, Y., & Ramanathan, S. (2014). Colossal resistance switching and band gap modulation in a perovskite nickelate by electron doping. *Nature Communications*, *5*, 1–9.

Shi, R., & Blight, A. (1996). Compression injury of mammalian spinal cord in vitro and the dynamics of action potential conduction failure. *Journal of neurophysiology*, *76*(3), 1572–1580.

Shi, R., Page, J. C., & Tully, M. (2015). Molecular mechanisms of acrolein-mediated myelin destruction in CNS trauma and disease. *Free Radic. Res.*, *49*(7), 888–895.

Shi, Y., Sun, W., McBride, J. J., Cheng, J. X., & Shi, R. (2011). Acrolein-mediated injury in nervous system trauma and diseases. *Molecular Nutrition and Food Research*, *55*(9), 1320–1331.

Shin, S. R., Farzad, R., Tamayol, A., Manoharan, V., Mostafalu, P., Zhang, Y. S., ... Khademhosseini, A. (2016). A Bioactive Carbon Nanotube-Based Ink for Printing 2D and 3D Flexible Electronics. *Advanced Materials*, *28*(17), 3280–3289.

Si, P., Huang, Y., Wang, T., & Ma, J. (2013). Nanomaterials for Electrochemical Non-enzymatic Glucose Biosensors. *RSC Advances*, *3*(11), 3487.

Silver, I. A. (1965). Some observations on the cerebral cortex with an ultramicro, membrane-covered, oxygen electrode. *Medical Electronics & Biological Engineering*, *3*(4), 377–387.

Singh, B., Laffir, F., McCormac, T., & Dempsey, E. (2010). PtAu/C based Bmetallic Nanocomposites for Non-enzymatic Electrochemical Glucose Detection. *Sensors and Actuators, B: Chemical*, *150*(1), 80–92.

Sirca, D., Vardeu, A., Pinna, M., Diana, M., & Enrico, P. (2014). A robust, state-of-the-art amperometric microbiosensor for glutamate detection. *Biosensors and Bioelectronics*, *61*, 526–531.

Soares, D. P., & Law, M. (2009). Magnetic resonance spectroscopy of the brain: review of metabolites and clinical applications. *Clin. Radiol.*, *64*(1), 12–21.

Sokolov, S. V., Tschulik, K., Batchelor-McAuley, C., Jurkschat, K., & Compton, R. G. (2015). Reversible or Not? Distinguishing Agglomeration and Aggregation at the Nanoscale. *Analytical Chemistry*, *87*(19), 10033–10039.

Sridharan, S. V., Rivera, J. F., Nolan, J. K., Alam, M. A., Rickus, J. L., & Janes, D. B. (2018). On-chip microelectrode array and in situ transient calibration for measurement of transient concentration gradients near surfaces of 2D cell cultures. *Sensors and Actuators B: Chemical*.

Steigerwalt, E. S., Deluga, G. A., & Lukehart, C. M. (2002). Pt-Ru/carbon fiber nanocomposites: Synthesis, characterization, and performance as anode catalysts of direct methanol fuel cells. A search for exceptional performance. *Journal of Physical Chemistry B*, *106*(4), 760–766.

Stephens, M. L., Quintero, J. E., Pomerleau, F., Huettl, P., & Gerhardt, G. A. (2011). Age-related changes in glutamate release in the CA3 and dentate gyrus of the rat hippocampus. *Neurobiology of Aging*, *32*(5), 811–820.

Sun, A., Venkatesh, A. G., & Hall, D. A. (2016). A Multi-Technique Reconfigurable Electrochemical Biosensor: Enabling Personal Health Monitoring in Mobile Devices. *IEEE Transactions on Biomedical Circuits and Systems*, *10*(5), 945–954.

Sun, H., Jia, Y., Dong, H., Dong, D., & Zheng, J. (2020). Combining additive manufacturing with microfluidics: an emerging method for developing novel organs-on-chips. *Current Opinion in Chemical Engineering*, *28*, 1–9.

Sun, K., Wei, T. S., Ahn, B. Y., Seo, J. Y., Dillon, S. J., & Lewis, J. A. (2013). 3D printing of interdigitated Li-ion microbattery architectures. *Advanced Materials*, *25*(33), 4539–4543.

Sun, W., Smith, D., Fu, Y., Cheng, J.-X., Bryn, S., Borgens, R., & Shi, R. (2010). Novel potassium channel blocker, 4-AP-3-MeOH, inhibits fast potassium channels and restores axonal conduction in injured guinea pig spinal cord white matter. *J. Neurophysiol.*, *103*, 469 –478.

Sun, Z., Li, Z., Huang, C., Zhao, Y., Zhang, H., Tao, R., & Liu, Z. (2011). Ultrasonication-assisted Uniform Decoration of Carbon Nanotubes by Various Particles with Controlled Size and Loading. *Carbon*, *49*(13), 4376–4384.

Tian, K., Prestgard, M., & Tiwari, A. (2014). A Review of Recent Advances in Nonenzymatic Glucose Sensors. *Materials Science and Engineering C*, *41*, 100–118.

Tiwari, J. N., Vij, V., Kemp, K. C., & Kim, K. S. (2016). Engineered carbon-nanomaterial-based electrochemical sensors for biomolecules. *ACS Nano*, *10*, 46–80.

Toghill, K. E., & Compton, R. G. (2010). Electrochemical Non-enzymatic Glucose Sensors: A perspective and an evaluation. *International Journal of Electrochemical Science*, *5*(August), 1246 – 1301.

Tolosa, V. M., Wassum, K. M., Maidment, N. T., & Monbouquette, H. G. (2013). Electrochemically deposited iridium oxide reference electrode integrated with an electroenzymatic glutamate sensor on a multi-electrode array microprobe. *Biosens. Bioelectron.*, *42*(1), 256–260.

Tseng, T. T. C., & Monbouquette, H. G. (2012). Implantable microprobe with arrayed microsensors for combined amperometric monitoring of the neurotransmitters, glutamate and dopamine. *J. Electroanal. Chem.*, *682*, 141–146.

Tseng, T. T. C., Yao, J., & Chan, W. C. (2013). Selective enzyme immobilization on arrayed microelectrodes for the application of sensing neurotransmitters. *Biochem. Eng. J.*, *78*, 146–153.

Tseng, W. C., Hsu, K. C., Shiea, C. S., & Huang, Y. L. (2015). Recent trends in nanomaterial-based microanalytical systems for the speciation of trace elements: A critical review. *Anal. Chim. Acta*, *884*, 1–18.

Van Der Zeyden, M., Oldenziel, W. H., Rea, K., Cremers, T. I., & Westerink, B. H. (2008). Microdialysis of GABA and glutamate: Analysis, interpretation and comparison with microsensors. *Pharmacology Biochemistry and Behavior*, *90*(2), 135–147.

van der Zeyden, M., Oldenziel, W. H., Rea, K., Cremers, T. I., & Westerink, B. H. (2008). Microdialysis of GABA and glutamate: Analysis, interpretation and comparison with microsensors. *Pharmacology Biochemistry and Behavior*, *90*(2), 135–147.

Villagrán, A. M., Pérez, S. J. L., & Ibarra, J. O. (2008). Electrochemical Biosensors to Monitor Extracellular Glutamate and Acetylcholine Concentration in Brain Tissue. *Biosens. Heal. Environ. Biosecurity*.

Wang, B., Gu, S., Ding, Y., Chu, Y., Zhang, Z., Ba, X., … Li, X. (2013). A novel route to prepare LaNiO3 perovskite-type oxide nanofibers by electrospinning for glucose and hydrogen peroxide sensing. *Analyst*, *138*(1), 362–367. doi: 10.1039/c2an35989h

Wang, J. (2005). Carbon-Nanotube Based Electrochemical Biosensors: A Review. *Electroanalysis*, *17*(1), 7–14.

Wang, J., Thomas, D. F., & Chen, A. (2008). Nonenzymatic electrochemical glucose sensor based on nanoporous PtPb networks. *Anal. Chem.*, *80*(4), 997–1004. doi: 10.1021/ac701790z

Wang, J., Zhao, D., & Xu, C. (2016). Nonenzymatic Electrochemical Sensor for Glucose Based on Nanoporous Platinum-Gold Alloy. *Journal of Nanoscience and Nanotechnology*, *16*(7), 7145–7150.

Wang, L., Li, J., Feng, M., Min, L., Yang, J., Yu, S., … Yang, Z. (2017). Perovskite-type calcium titanate nanoparticles as novel matrix for designing sensitive electrochemical biosensing. *Biosensors and Bioelectronics*.

Wang, L., Stoerzinger, K. A., Chang, L., Yin, X., Li, Y., Tang, C. S., … Du, Y. (2019). Strain Effect on Oxygen Evolution Reaction Activity of Epitaxial NdNiO 3 Thin Films. *ACS Applied Materials and Interfaces*, *11*(13), 12941–12947.

Wang, L., Stoerzinger, K. A., Chang, L., Zhao, J., Li, Y., Tang, C. S., ... Du, Y. (2018). Tuning Bifunctional Oxygen Electrocatalysts by Changing the A-Site Rare-Earth Element in Perovskite Nickelates. *Advanced Functional Materials*.

Wang, X., Zhu, Y., Vasileff, A., Jiao, Y., Chen, S., Song, L., ... Qiao, S. Z. (2018). Strain Effect in Bimetallic Electrocatalysts on the Hydrogen Evolution Reaction. *ACS Energy Letters*, *5*(3), 1198–1204.

Wang, Y., Mishra, D., Bergman, J., Keighron, J. D., Skibicka, K. P., & Cans, A. S. (2019). Ultrafast Glutamate Biosensor Recordings in Brain Slices Reveal Complex Single Exocytosis Transients. *ACS Chemical Neuroscience*, *10*(3), 1744–1752. doi: 10.1021/acschemneuro.8b00624

Wassum, K. M., Tolosa, V. M., Tseng, T. C., Balleine, B. W., Monbouquette, H. G., & Maidment, N. T. (2012). Transient extracellular glutamate events in the basolateral amygdala track reward-seeking actions. *J Neurosci*, *32*(8), 2734–2746.

Wassum, K. M., Tolosa, V. M., Wang, J., Walker, E., Monbouquette, H. G., & Maidment, N. T. (2008). Silicon wafer-based platinum microelectrode array biosensor for near real-time measurement of glutamate in vivo. *Sensors*, *8*(8), 5023–5036.

Wei, G., Xu, F., Li, Z., & Jandt, K. D. (2011). Protein-promoted synthesis of Pt nanoparticles on carbon nanotubes for electrocatalytic nanohybrids with enhanced glucose sensing. *J. Phys. Chem. C*, *115*(23), 11453–11460.

Wei, M., Zhang, F., Wang, W., Alexandridis, P., Zhou, C., & Wu, G. (2017). 3D direct writing fabrication of electrodes for electrochemical storage devices. *Journal of Power Sources*, *354*, 134–147.

Wei, W., Song, Y., Wang, L., Zhang, S., Luo, J., Xu, S., & Cai, X. (2015). An implantable microelectrode array for simultaneous L-glutamate and electrophysiological recordings in vivo. *Microsystems Nanoeng.*, *1*(April), 15002.

Weltin, A. (2015). Multiparametric , Flexible Microsensors for In Vivo Application.

Weltin, A., Kieninger, J., Enderle, B., Gellner, A. K., Fritsch, B., & Urban, G. A. (2014). Polymer-based, flexible glutamate and lactate microsensors for in vivo applications. *Biosens. Bioelectron.*, *61*, 192–199.

Weltin, A., Kieninger, J., & Urban, G. A. (2016). Microfabricated, amperometric, enzyme-based biosensors for in vivo applications. *Analytical and bioanalytical chemistry*, *408*(17), 4503–21.

Weltman, A., Yoo, J., & Meng, E. (2016). Flexible, penetrating brain probes enabled by advances in polymer microfabrication. *Micromachines*, *7*(10), 180.

Wen, D., Guo, S., Zhai, J., Deng, L., Ren, W., & Dong, S. (2009). Pt Nanoparticles Supported on TiO 2 Colloidal Spheres with Nanoporous Surface: Preparation and Use as an Enhancing Material for Biosensing Applications. *J. Phys. Chem. C*, *113*, 13023–13028.

Wilson, G. S., & Gifford, R. (2005). Biosensors for real-time in vivo measurements. *Biosens. Bioelectron.*, *20*(12), 2388–2403.

Wilson, R., & Turner, A. P. F. (1992). Glucose Oxidase: an Ideal Enzyme. *Biosensors and Bioelectronics*, *7*(3), 165–185.

Wong, K. C. (1996). NMR spectroscopy: Basic principles, concepts, and applications in chemistry. *Spectrochim. Acta Part A Mol. Biomol. Spectrosc.*, *52*(4), 479–481.

Wozniak, K. M., Rojas, C., Wu, Y. W., & Slusher, B. S. (2012). The Role of Glutamate Signaling in Pain Processes and its Regulation by GCP II Inhibition. *Current Medicinal Chemistry*, *19*(9), 1323 – 1334.

Wu, Q., Kolb, I., Callahan, B. M., Su, Z., Stoy, W., Kodandaramaiah, S. B., ... Chubykin, A. A. (2016). Integration of autopatching with automated pipette and cell detection in vitro. *Journal of Neurophysiology*, *116*(4), 1564–1578.

Xiao, F., Zhao, F., Mei, D., Mo, Z., & Zeng, B. (2009). Nonenzymatic Glucose Sensor based on Ultrasonic-electrodeposition of Bimetallic PtM (M = Ru, Pd and Au) Nanoparticles on Carbon Nanotubes-ionic Liquid Composite Film. *Biosensors and Bioelectronics*, *24*(12), 3481–3486.

Xu, G. Y., Hughes, M. G., Ye, Z., Hulsebosch, C. E., & McAdoo, D. J. (2004a). Concentrations of glutamate released following spinal cord injury kill oligodendrocytes in the spinal cord. *Exp. Neurol.*, *187*(2), 329–336.

Xu, G. Y., Hughes, M. G., Ye, Z., Hulsebosch, C. E., & McAdoo, D. J. (2004b). Concentrations of glutamate released following spinal cord injury kill oligodendrocytes in the spinal cord. *Experimental Neurology*, *187*(2), 329–336. doi: 10.1016/j.expneurol.2004.01.029

Xu, G. Y., Hughes, M. G., Zhang, L., Cain, L., & McAdoo, D. J. (2005). Administration of glutamate into the spinal cord at extracellular concentrations reached post-injury causes functional impairments. *Neurosci. Lett.*, *384*(3), 271–276.

Xu, G. Y., Liu, S., Hughes, M. G., & McAdoo, D. J. (2008). Glutamate-induced losses of oligodendrocytes and neurons and activation of caspase-3 in the rat spinal cord. *Neuroscience*, *153*(4), 1034–1047.

Xu, G. Y., McAdoo, D. J., Hughes, M. G., Robak, G., & De Castro, R. (1998). Considerations in the determination by microdialysis of resting extracellular amino acid concentrations and release upon spinal cord injury. *Neuroscience*, *86*(3), 1011–1021.

Xu, Q., Lv, Y., Dong, C., Sreeprased, T. S., Tian, A., Zhang, H., ... Li, N. (2015). Three-dimensional micro/nanoscale architectures: fabrication and applications. *Nanoscale*, *7*(25), 10883–10895.

Xue, J., Ma, S., Zhou, Y., Zhang, Z., & He, M. (2015). Facile Photochemical Synthesis of Au/Pt/g-$C_3N_4$ with Plasmon-enhanced Photocatalytic Activity for Antibiotic Degradation. *ACS Applied Materials and Interfaces*, *7*(18), 9630–9637.

Yan, J. K., Zhou, K. J., Huang, J. H., Wu, Q. Q., Zhang, T., Wang, C. C., & Cai, W. (2017). Urinary glutamine/glutamate ratio as a potential biomarker of pediatric chronic intestinal pseudo-obstruction. *Orphanet Journal of Rare Diseases*, *12*(1), 10–13.

Yan, R., Page, J. C., & Shi, R. (2010). Effects of 4-aminopyridine on stretched mammalian spinal cord: the role of potassium channels in axonal conduction. *J Neurophysiol*, *90*(4), 469–478.

Yang, G., Kampstra, K. L., & Abidian, M. R. (2014). High-performance conducting polymer nanofiber biosensors for detection of biomolecules. *Advanced Materials*, *26*(29), 4954–4960.

Yang, J., Chen, X., Yang, X., & Ying, J. Y. (2012). Stabilization and Compressive Strain Effect of AuCu Core on Pt Shell for Oxygen Reduction Reaction. *Energy and Environmental Science*, *5*(10), 8976–8981.

Yang, J., Jiang, L. C., Zhang, W. D., & Gunasekaran, S. (2010). A Highly Sensitive Non-enzymatic Glucose Sensor based on a Simple Two-step Electrodeposition of Cupric Oxide (CuO) Nanoparticles onto Multi-walled Carbon Nanotube Arrays. *Talanta*, *82*(1), 25–33.

Yao, T., Yano, T., & Nishino, H. (2004). Simultaneous in vivo monitoring of glucose, L-lactate, and pyruvate concentrations in rat brain by a flow-injection biosensor system with an on-line microdialysis sampling. *Anal. Chim. Acta*, *510*(1), 53–59.

Yi, Q., Yu, W., & Niu, F. (2010). Novel Nanoporous Binary Au-Ru Electrocatalysts for Glucose Oxidation. *Electroanalysis*, *22*(5), 556–563.

You, T., Niwa, O., Kurita, R., Iwasaki, Y., Hayashi, K., Suzuki, K., & Hirono, S. (2004). Reductive H2O2 Detection at Nanoparticle Iridium/Carbon Film Electrode and Its Application asL-Glutamate Enzyme Sensor. *Electroanalysis*, *16*(12), 54–59.

Zhang, H. T., Zuo, F., Li, F., Chan, H., Wu, Q., Zhang, Z., ... Ramanathan, S. (2019). Perovskite nickelates as bio-electronic interfaces. *Nature Communications*, *10*(1), 1–7.

Zhang, J., Gao, L., Sun, J., Liu, Y., Wang, Y., & Wang, J. (2012). Incorporation of single-walled carbon nanotubes with PEDOT/PSS in DMSO for the production of transparent conducting films. *Diam. Relat. Mater.*, *22*, 82–87.

Zhang, M., Mullens, C., & Gorski, W. (2006). Amperometric glutamate biosensor based on chitosan enzyme film. *Electrochim. Acta*, *51*(21), 4528–4532.

Zhang, Y., Shi, G., Qin, J., Lowe, S. E., Zhang, S., Zhao, H., & Zhong, Y. L. (2019). Recent Progress of Direct Ink Writing of Electronic Components for Advanced Wearable Devices. *ACS Applied Electronic Materials*, *1*(9), 1718–1734.

Zhang, Y., & Wilson, G. S. (1993). In vitro and in vivo evaluation of oxygen effects on a glucose oxidase based implantable glucose sensor. *Anal. Chim. Acta*, *281*(3), 513–520.

Zhang, Z., Schwanz, D., Narayanan, B., Kotiuga, M., Dura, J. A., Cherukara, M., ... Ramanathan, S. (2018). Perovskite nickelates as electric-field sensors in salt water. *Nature*, *553*(7686), 68–72.

Zhao, S., Zhang, K., Bai, Y., Yang, W., & Sun, C. (2006). Glucose oxidase/colloidal gold nanoparticles immobilized in Nafion film on glassy carbon electrode: Direct electron transfer and electrocatalysis. *Bioelectrochemistry*, *69*(2), 158–163.

Zhou, J., & Lubineau, G. (2013). Improving electrical conductivity in polycarbonate nanocomposites using highly conductive PEDOT/PSS coated MWCNTs. *ACS Appl. Mater. Interfaces*, *5*(13), 6189–6200.

Zhu, C., Yang, G., Li, H., Du, D., & Lin, Y. (2015). Electrochemical Sensors and Biosensors Based on Nanomaterials and Nanostructures. *Analytical Chemistry*, *87*(1), 230–249.

# APPENDIX A. PROGRAM TO ANALYZE DATA

## A.1 Program to analytically calculate the amperomatric response of enzymatic biosensor

```
%%Final Concentration at each time point when glutamate was added
load('concentration_data');
load('Data_file');
format long;
cdir = pwd;
data1       = data_name;
%% Change to nA/mm^2 from uA (multichannel potentiostat)
data1_1     = (data1(:,2).*(1e3))/(surface_area);
interval = 10;
%% Glutamate was added every 2 min
waiting  = 2; % minute
%% Period of where increment of glutamate concentrations were added
points = [300:waiting*60:780];
average_value = zeros(length(points),1);
for i = 1:length(points)
index1   = sum(data1(:,1)<points(i)) + 1;
average_value(i) = mean(data1_1(index1+interval:index1+waiting*200-1-interval,1));
end

%%-----------------------plot-----------------------------

%% Parameters for graphs
fontsize   = 16;
linewidth  = 1.5;
```

```
markerSize = 4;
scaleMax   = 1.02;
scaleMin   = .98;
driver  = '-dpng';
driver1 = '-depsc2';
driver2  = '-dpng';
driver3 = '-depsc2';

y = average_value;
X = [ones(length(average_value),1) concentration_data(1:length(average_value))];
B = regress(y,X);
fitted_y = X*B;

%%-------------------------------------------------------------
% Graph staircase figure

figure('Units','inches','Position',[0 0 8 8],'PaperPositionMode','auto');
figure(1);
axes1 = axes('Parent',figure(1),'FontWeight','bold','FontSize',20,'FontName',
'Helvetica Bold*','linewidth',2);
box(axes1,'off');
hold(axes1,'on');
plot(data1(:,1),data1_1,'linewidth',1,'color',[0 0 1]);
xlabel('Time (s)','fontweight','bold','fontsize',30,'fontname','Helvetica Bold*')
ylabel('Current Density (nA/mm^2)','fontweight','bold','fontsize',30,'fontname',
'Helvetica Bold*');
lname = legend('show','Location','Northwest');
legend boxoff;
set(lname,'fontsize',20,'fontweight','bold','fontname','Helvetica Bold*');
```

```
%x and y limit
ylim([0,1000]);
xlim([0,930]);

%%-------------------------------------------------------------
% % % Save graph
graph_name = '';
graph_directory  = '';
cd(graph_directory);
print(driver,graph_name);
print(driver1,graph_name);
saveas(gcf,graph_name,'fig');
cd(cdir);

%%-------------------------------------------------------------
%% Graph in separated sensitive slope figure 2
figure('Units','inches','Position',[0 0 8 8],'PaperPositionMode','auto');
figure(2);
axes2 = axes('Parent',figure(2),'fontweight','bold','fontsize',20,'fontname',
'Helvetica Bold*', 'linewidth',2);
box(axes2,'off');
hold(axes2,'on');
plot(Conc_01_31_18(1:length(average_value)), average_value,'rs',
'LineWidth',2,'Color',[0 0 1]);
xlabel('Concentration (\muM)','fontweight','bold','fontsize',30,'fontname',
'Helvetica Bold*');
ylabel('Current Density (nA/mm^2)','fontweight','bold','fontsize',30,'fontname',
'Helvetica Bold*');
hold on;
```

```
if (sign(B(1)) == -1)
equation_name = ['y =  ',num2str(B(2),'%2.4f'),'x - ',num2str(abs(B(1)),'%2.4f')];
else
equation_name = ['y =  ',num2str(B(2),'%2.4f'),'x + ',num2str(B(1),'%2.4f')];
end

plot(concentration_data(1:length(average_value)), fitted_y,'-b','linewidth',2,
'MarkerSize',1)
lname = legend('show',equation_name,'Location','Northwest');
legend boxoff;
set(lname,'fontsize',20,'fontweight','bold','fontsize',20,'fontname',
'Helvetica Bold*');
xlim([48,350]);
ylim([0,1000]);

%%-------------------------------------------------------
% % Save graph
graph_name_2 = '';
graph_directory_2  = '';
cd(graph_directory_2);
print(driver2,graph_name_2);
print(driver3,graph_name_2);
saveas(gcf,graph_name_2,'fig');
cd(cdir);
```

A.2 Program to analytically calculate the average sensitivity with more samples

```
load('concentration_data');
%% Device 1
filename = '';
data1       = read_data_mpt(filename);
data1_1     = (data1(:,11).*(1e6))/(surface_area);   %% Change to nA/mm^2
data1(:,11) = data1(:,11)./(surface_area);
data1_2     = data1_1(:,1) - data1_1(3834);           %% Normalize data
interval    = 10;
waiting  = 3; % minute
points = [1800:waiting*60:2520];

average_value_1 = zeros(length(points),1);
for i = 1:length(points)
index1   = sum(data1(:,8)<points(i)) + 1;
average_value_1(i) = mean(data1_1(index1+interval:index1+waiting*200-1-interval,1));
end
%% Device 2
filename = '';
data2       = read_data_mpt(filename);
data2_1     = (data2(:,11).*(1e6))/(surface_area);   %% Change to nA/mm^2
data2(:,11) = data2(:,11)./(surface_area);
data2_2     = data2_1(:,1) - data2_1(3834);          %% Normalize data
interval = 10;
waiting  = 3; % minute
points = [1800:waiting*60:2520];
```

```
average_value_2 = zeros(length(points),1);
for i = 1:length(points)
index1   = sum(data2(:,8)<points(i)) + 1;
average_value_2(i) = mean(data2_2(index1+interval:index1+waiting*200-1-interval,1));
end
%% Device 3
filename = '';
data3      = read_data_mpt(filename);
data3_1     = (data3(:,11).*(1e6))/(surface_area);   %% Change to nA/mm^2
data3(:,11) = data3(:,11)./(surface_area);
data3_2     = data3_1(:,1) - data3_1(3834);          %% Normalize data
interval = 10;
waiting  = 3; % minute
points = [1800:waiting*60:2520];

average_value_3 = zeros(length(points),1);
for i = 1:length(points)
index1   = sum(data3(:,8)<points(i)) + 1;
average_value_3(i) = mean(data3_2(index1+interval:index1+waiting*200-1-interval,1));
end

%% Graph
%% Parameters for graphs
fontsize   = 24;
linewidth  = 1.5;
markerSize = 1;
driver  = '-dpng';
driver1 = '-depsc2';
```

```
%%-----------------------fit-----------------------------------------------
y1 = average_value_1*1e6;
y1 = average_value_1;
X1 = [ones(length(average_value_1),1) Conc_01_31_18(1:length(average_value_1))];
B1 = regress(y1,X1);
fitted_y1 = X1*B1;
%%-------------------------------------------------------------------------
y2 = average_value_2*1e6;
y2 = average_value_2;
X2 = [ones(length(average_value_2),1) Conc_01_31_18(1:length(average_value_2))];
B2 = regress(y2,X2);
fitted_y2 = X2*B2;
%%-------------------------------------------------------------------------
y3 = average_value_3*1e6;
y3 = average_value_3;
X3 = [ones(length(average_value_3),1) Conc_01_31_18(1:length(average_value_3))];
B3 = regress(y3,X3);
fitted_y3 = X3*B3;

%% Average total for 3 device of Flat Pt with Glutamate
y_average = (y1 + y2 + y3)/3;
data = [y1 y2 y3];
y_err = zeros(length(y1));
for indx = 1:length(y1)
y_err(indx,:) = std(data(indx,:))/sqrt(3);
end
X = [ones(length(average_value_1),1) Conc_01_31_18(1:length(average_value_1))];
B = regress(y_average,X);
fitted_y_average = X*B;
```

```
figure('Units','inches','Position',[0 0 8 8],'PaperPositionMode','auto');
figure(1);
axes1 = axes('Parent',figure(1),'fontweight','bold','fontsize',20,'fontname'
,'Helvetica Bold*','linewidth',2);
box(axes1,'off');
hold(axes1,'on');
xlabel('Concentration (\muM)','fontweight','bold','fontsize',30,'fontname',
'Helvetica Bold*');
ylabel('Current Density (nA/mm^2)','fontweight','bold','fontsize',30,'fontname',
'Helvetica Bold*');

hold on;
if (sign(B(1)) == -1)
equation_name = ['y =  ',num2str(B(2),'%2.4f'),'x - ',num2str(abs(B(1)),'%2.4f')];
else
equation_name = ['y =  ',num2str(B(2),'%2.4f'),'x + ',num2str(B(1),'%2.4f')];
end
plot1 = plot(Conc_01_31_18(1:length(average_value_1)), fitted_y_average,'-k',
'linewidth',3,
'MarkerSize',5,'Color',[1 0 0],'Displayname',equation_name);
hold on
x = Conc_01_31_18(1:length(average_value_1));
for indx = 1:length(y1)
errorbar(x(indx),y_average(indx),y_err(indx),'-ok','linewidth',linewidth,
'MarkerSize',5,'Color',[1 0 0])
end
```

```
%%-----------------------------------------------------------
% % Save graph
graph_name = '';
graph_directory  = '';
(graph_directory);
print(driver,graph_name);
print(driver1,graph_name);
saveas(gcf,graph_name,'fig');
cd(cdir);
```

## A.3 Filtering data

```
filename = '';
data1       = read_data_mpt(filename);
data1_1     = (data1(:,11).*(1e6))/(surface_area);       %% Change to nA/mm^2
data1(:,11) = data1(:,11)./(surfacez_area);
data1_2     = data1_1(:,1) - (data1_1(1834)+12000);  %% Normalize to 0
interval = 10;
waiting  = 2; %% minute
points = [600:waiting*60:1680];
average_value_1 = zeros(length(points),1);
for i = 1:length(points)
index1   = sum(data1(:,8)<points(i)) + 1;
average_value_1(i) = mean(data1_2(index1+interval:index1+waiting*200-1-interval,1));
end
%% Low pass filter
Fs=500;
Ts=1/Fs;
t=-0:Ts:100;
X1 =  data1_2;
n=1;
Wn=20;
Fn=Fs/2;
ftype='low';
[b,a]=butter(n,Wn/Fn,ftype);
y1=filter(b,a,X1);
z1 = data1(:,8);
% plot(z,y)
```

A.4 Program to analytically calculate the amperomatric response of nonenzymatic glucose biosensor

```
%%
%Parameter Specification
%%Simulation Physical Constants
k=8.6173324e-5;  %%%% Boltzmann constant (eV.K^-1)
q=1.6022e-19;         %%%% Electronic charge e (C)
NA=6.02e23;   %%%% Avogadro's Number (1/mol)

%% Exp. data
G0_exp = [X1 X2...Xn]'*10;  % Unit: mM
i_exp = [Y1 Y2...Yn]'*1e-3;  % Unit: A/m^2

% Linear fit
fit_ord=1;  %% Fitting order (1: linear)
p= polyfit(G0_exp,i_exp,fit_ord);
i_linear = polyval(p,G0_exp);

%% Simulation Parameters
H=2e-4*2/3;   %%%% Height of the unit cell (m)
W=1e-4;         %%%% Width of the unit cell (m)
L=1.9;             %%%% Length of the unit cell (m)
r=8e-5;          %%%% Radius of NW electrode (m)
s=100e-9;      %%%% Radius of Pt NPs (m)
% G0=[0:0.1:30]';         %%%% Bulk glucose concentration (mol/m^3 or mM)
G0=G0_exp;                 %%%% Bulk glucose concentration (mol/m^3 or mM)
Wd=H;                         %%%% Diffusion width (m)
Dg=6e-10;                    %%%% Glucose diffusion coefficient (m^2/s)
```

```
% Fitting parameters
k_F=2.6e-2;     %%%% Glucose forward rate constant (m^3/s/mol)
k_R=3e-1;        %%%% Reverse reaction rate constant  (1/s)
k_RP=k_R/8;     %%%% Reverse reaction rate constant prime (1/s)
N0=2.5e-5;      %%%% Initial metal oxide surface density  (mol/m^2)

%% Calculation
% Diffusion Capacitance
% C_P=Dg*W*L/H;   %%%% Diffusion capacitance of planar sensor (m^3/s)

%% Diffusion capacitance of NW array (m^3/s)
C_NW=2*pi*Dg*L/(log(sinh((2*pi*(Wd+r))/W)/sinh(pi*r/W))+pi/s*L/2/(N0*NA*2*pi*r*L));

%% NW array
% Intermediate parameters
alpha = k_R./(k_F*G0);
beta = k_RP./(k_F*G0);
sigma = C_NW/(W*L*k_F*N0);

gamma = alpha+beta;
X = gamma*sigma + sigma - alpha;
Y = alpha*sigma;

%% Exact solution

%% Surface concentration of CuII (mol/m^2)
N3_P = 1/2./gamma.*(-X + sqrt(X.^2 + 4*gamma.*Y)).*N0;
```

```
%% Surface concentration of CuIII (mol/m^2)
N2_P = N0 - N3_P;

%% Current density (A/m^2)
i_P = q*NA*2*pi*r*L*(k_R*N2_P - k_RP*N3_P)/(W*L);

% Approximate solution
Beta=2*pi*r*L*k_R*N0/C_NW;

%% Current density (A/m^2)
i_P_approx = q*NA*2*pi*r*L*N0*(k_R+k_RP)*((G0+k_RP/k_F)./
(G0+(k_R+k_RP)/k_F)-(k_RP/(k_R+k_RP)))/(W*L);

%% Fitting
x1=G0_exp;
y1=i_exp;
fo = fitoptions('Method','NonlinearLeastSquares',...
'Robust','LAR',...
'Algorithm','Trust-Region',...
'Lower',[q*NA*2*pi*r*L/(W*L)*N0/1000,k_R/1000,k_RP/1000,k_F/1000],...
'Upper',[q*NA*2*pi*r*L/(W*L)*N0*1000,k_R*100,k_RP*1000,k_F*1000],...
'StartPoint',[q*NA*2*pi*r*L/(W*L)*N0,k_R,k_RP,k_F]);
ft = fittype('A*(k_R+k_RP)*((x+k_RP/k_F)./
(x+(k_R+k_RP)/k_F)-(k_RP/(k_R+k_RP)))','options',fo);
[curve,gof] = fit(x1,y1,ft);
```

```
Coeff=coeffvalues(curve);
A_Fitted=Coeff(1);
k_F_Fitted=Coeff(2);
k_R_Fitted=Coeff(3);
k_RP_Fitted=Coeff(4);
i_P_approx_fit=A_Fitted*(k_R_Fitted+k_RP_Fitted)*((G0+k_RP_Fitted/k_F_Fitted)./
(G0+(k_R_Fitted+k_RP_Fitted)/k_F_Fitted)-(k_RP_Fitted/(k_R_Fitted+k_RP_Fitted)));

%% Plotting
%% Plot curve color
LINE={'-b','-r','-g','-m','-c','-k','-y','ks-','ko','r^-',
'mv-','go-','cs-','y*-','mp-','kp-','b*-','rs-','mo-',
'bv-','c^-','rx-','ms-','ks-.','bx-.'};
figure(1)
plot(G0_exp,i_exp*1e3,LINE{9},'markersize',12.0,'linewidth',3.0);
hold on;
plot(G0,i_P*1e3,LINE{1},'markersize',12.0,'linewidth',3.0);
hold on;
plot(G0,i_P_approx*1e3,LINE{4},'markersize',12.0,'linewidth',3.0);
hold on;
plot(G0,i_P_approx_fit*1e3,LINE{5},'markersize',12.0,'linewidth',3.0);
hold on;
plot(G0_exp,i_linear*1e3,LINE{2},'markersize',12.0,'linewidth',3.0);

set(gca,'linewidth',2.5,'fontname','Helvetica','Fontsize',24,'ticklength',
[0.025 0.025],'PlotBoxAspectRatio',[1 0.85 1],...
```

```
%% Linewidth of the box and tick
'xgrid','off','ygrid','off');
%% mA/m^2 = nA/mm^2
xlabel('Glucose concentration [mM]');ylabel('Current [nA/{mm^2}]');
%axis([0 11 0 max(i_P*1e3)*1.2]);
%set(gca,'XTick',[0 0.5 1 1.5 2],'YTick',[0:0.02:0.14]);
legend('Exp','Ana.','Ana approx','Ana approx fit','Linear')

%% Evaluate curve fitting
%% [r2_model rmse_model] = rsquare(i_exp,i_P);
%% [r2_linear rmse_linear] = rsquare(i_exp,i_linear);

% SST=sum((i_exp-mean(i_exp)).^2);
% SSR_model=sum((i_exp-i_P).^2);
% SSR_linear=sum((i_exp-i_linear).^2);
% r2_model=1-SSR_model/SST;
% r2_linear=1-SSR_linear/SST;

% n=length(i_exp);
% m_model=4;
% m_linear=fit_ord+1;

% r2_adj_model=((n-1)*r2_model-(m_model))/(n-m_model-1);
% r2_adj_linear=((n-1)*r2_linear-(m_linear))/(n-m_linear-1);

% AIC_model=n*log(SSR_model/n)+2*m_model;
% AIC_linear=n*log(SSR_linear/n)+2*m_linear;
```